Search for Unstable Neutral and Charged Heavy Leptons in e^+e^- Collisions above Z^0 Resonance at LEP

Shuji Tanaka

The Graduate School of Science and Technology

KOBE University

Acknowledgement

I would like to thank Professor H. Takeda, who gave me the chance to join the OPAL Collaboration. I am also grateful to Professor S. Komamiya and my colleagues of ICEPP, International Center of Elementary Particle Physics, the University of Tokyo; their encouragement and inspiring discussions were invaluable throughout this work.

I am indebted to all the members of the OPAL Collaboration, for their construction of the beautiful detector and more than seven years of its successful operation. They are also very helpful to a newcomer, and I was helped by many of them in understanding the experiment. Among all, I would like to express my special gratitude to several persons who have directly helped my work or suggested some useful comments: Drs. S. Asai, K. Kawagoe. M. Nozaki, G. Hanson, R. Mcpherson, D.R. Ward, D. Charlton and D. Heuer (Spokesman of the OPAL Collaboration). Finally, I would like to thank the SL Division of CERN for the efficient operation of the LEP accelerator, and other CERN staffs for their support.

Preface

The LEP project has been one of the most successful undertakings in the history of high energy physics. Shortly after it was commissioned in July 1989, it started producing a large number of Z^0's, enabling studies of the electroweak interaction at the very energy of its symmetry breaking. A lot of important results have been obtained with an unprecedented accuracy, including the measurement of the Z^0 mass and the determination of the number of light neutrino species. Also the heavy lepton searches were performed at LEP1, and the lower mass limits were estimated [1].

I became a member of the OPAL Collaboration, one of the four experiments at LEP, in January 1996. At the time of my visit to CERN, the OPAL detector had already been in stable operation for nearly seven years. The LEP1.5 data ($\sqrt{s} = 130$ and 136 GeV) has been already collected after the LEP upgrading by installing the super-conducting RF cavities, so I started analysing the charged heavy lepton signals using the LEP1.5 data. Firstly I studied the Monte Carlo simulation of the heavy leptons by the JETSET7.3 Monte Carlo generator. But this simulator was not up to date and also not included the spin correlations, so I tried to use the TIPTOP Monte Carlo simulator, which included spin correlations, and adopted the JETSET7.4 for the fragmentation and hadronization of the W boson decay products. I wrote two reports, one describing the charged lepton search [2] and the other describing the neutral lepton search [3]. Based on these reports I wrote a paper on the heavy lepton search at $\sqrt{s} = 130$ GeV and 136 GeV [4].

In July 1996, LEP2 ($\sqrt{s} = 161$ GeV) phase was started. I nearly completed the study of the analysis method by Monte Carlo samples and wrote the report [5] before data taking. After the full collection of the data, I applied the analysis method to the real data and summarized the analysis as a paper [6].

This thesis is based on all my works done for the OPAL Collaboration. The main part of the thesis will be published in the above-mentioned paper. It also contains contribution from Sachio Komamiya and Shoji Asai, who kindly trained me not only about the methods of analyses but also English.

Contents

Abstract

Searches for unstable neutral and charged heavy leptons (L^0, $L^{\pm}$) have been performed at centre-of-mass energies of $\sqrt{s}$ = 130, 136 and 161 GeV. The data were collected with the OPAL detector at LEP during October 1995 and July 1996. Two candidate events were observed after the selection procedure, which were consistent with the expected total background of 1.57 events, and the lower limits have been derived on heavy lepton masses for various models. If an unstable Dirac neutral heavy lepton L^0 decays only into eW^*, μW^* or τW^*, the lower limits on its mass at 95% C.L. are 69.3 GeV, 72.0 GeV and 66.0 GeV, respectively. The limits are modified for a Majorana L^0 to 59.5 GeV, 60.5 GeV and 55.7 GeV, respectively. For charged heavy leptons, a mass limit at 95% C.L. of 73.5 GeV was obtained, if the $L^{\pm}$ decays into a stable heavy neutrino ν_L and $W^{*\pm}$, and if $m_{L^{\pm}} - m_{\nu_L} > 13$ GeV. If the $L^{\pm}$ decays through lepton flavour mixing into a massless neutrino ν_ℓ and $W^{*\pm}$, the lower limit on $m_{L^{\pm}}$ was determined to be 76.7 GeV at 95% C.L..

Chapter 1

Introduction

This paper presents searches for the pair production of unstable neutral heavy leptons $L^0\bar{L}^0$ and unstable charged heavy leptons L^+L^- in e^+e^- collisions[1]. The data used in this analysis were collected with the OPAL detector at a centre-of-mass energy ($\sqrt{s}$) of 130, 136 (LEP1.5) and 161 GeV (LEP2). This was the first chance to search for the new particles above the Z^0 resonance.

The precise measurements of the Z^0 boson parameters by the LEP1 ($\sqrt{s} \sim M_Z$) and SLC experiments have determined the number of species of light neutrinos to be three [20]. Also the lower mass limits of the sequential charged and neutral heavy lepton were estimated to be $\sim M_Z/2$. However, this does not exclude the fourth generation in which all the fermions are heavy. Many theories beyond the Standard Model (SM) of the electroweak and the strong interactions predict the existence of new fermion. In most of the cases, these new fermions have non canonical $SU(2)_L \times U(1)_Y$ quantum numbers, e.g. the left-handed components are in weak isodoublets and the right-handed components in weak isosinglets. Examples of extension models are the following:

1) Sequential fermion [7]: this is the simplest extension of the SM, one simply has to add to the known fermionic spectrum with its three-fold replica a fourth family with the same quantum numbers.

2) Left-right symmetric model [9]: The simplest such model employs the gauge group $SU(2)_L \times SU(2)_R \times U(1)_{B-L}$ and contains each of left-handed and right-handed lepton doublet per generation.

3) Mirror fermions [10]: they have chiral properties which are opposite to those of ordinary fermions, i.e. the right-handed components are in weak isodoublets and the left-handed ones are in weak isosinglets; there is also a left-handed heavy neutrino. These fermions appear in many extensions of

[1]Throughout this paper, charge conjugation is implicitly assumed. L^- denotes an unstable charged heavy lepton, L^0 denotes an unstable neutral heavy lepton and ν_L denotes a stable heavy neutrino.

the Standard Model and provide a possible way to restore left-right symmetry at the scale of the electroweak symmetry breaking; they naturally occur in lattice gauge theories.

In this paper the heavy leptons were assumed to be sequential 4th generation leptons, which was the simplest possibility to search for new physics. The theoretical overview is described in Chapter. 2, and the experimental environments are in Chapter. 3, the detailed analysis methods are described in Chapter. 4, 5 and 6.

Chapter 2

Theory and Overview

The theoretical and phenomenological frameworks necessary for this work are described in this chapter. The Standard Model of the electroweak theory, which enables us to predict the physical quantities in concern, is briefly reviewed.

2.1 The Standard Model

The so-called 'Standard Model' of the electroweak theory is a quantum field theory based on the gauge group $SU(2)_L \times U(1)_Y$. The SU(2) part represents weak isospin symmetry, and the U(1) part is for hyper-charge. The symmetry is spontaneously broken by the Higgs mechanism, which gives masses to weak gauge bosons.

The model includes three generations of 12 spin-1/2 fermions and corresponding anti-fermions as players of the electroweak theory:

- neutral leptons (neutrinos): $\nu_{\rm e}(\overline{\nu_{\rm e}})$, $\nu_\mu(\overline{\nu_\mu})$, $\nu_\tau(\overline{\nu_\tau})$;
- charged leptons: $\rm e^-(e^+)$, $\mu^-(\mu^+)$, $\tau^-(\tau^+)$;
- charge +2/3 quarks: $\rm u(\overline{u})$, $\rm c(\overline{c})$, $\rm t(\overline{t})$;
- charge -1/3 quarks: $\rm d(\overline{d})$, $\rm s(\overline{s})$, $\rm b(\overline{b})$.

They are listed above in the order of increasing masses, whereas the neutrinos are massless. The Standard Model does not restrict the number of generations to be three; it has been experimentally confirmed for the case of light neutrinos.

The boson fields mediating the interactions can be derived by the local gauge invariance of the Lagrangian. Requiring the Lagrangian density to be invariant under local $SU(2)_L$ transformations in the isospin space, minimum interaction Lagrangian including an isospin triplet of gauge fields, $A_\mu^{1,2,3}$, is obtained. Similarly, requirement of the local U(1) invariance results in a gauge field B_μ. The

four gauge fields represents massless vector bosons, which do not correspond to physically observed electroweak bosons.

The Higgs mechanism gives masses to three of the four gauge bosons. Introducing a complex isodoublet scalar field

$$\phi = \frac{1}{\sqrt{2}} \begin{pmatrix} \phi_1 + i\phi_2 \\ \phi_3 + i\phi_4 \end{pmatrix}, \tag{2.1}$$

and requiring the local $\mathrm{SU}(2)_L \times \mathrm{U}(1)_Y$ gauge invariance, three of the four degrees of freedom of ϕ transform into the longitudinal components of the SU(2) gauge bosons. The remaining one degree of freedom corresponds to an undiscovered massive scalar boson, the Higgs particle. The physically observed gauge bosons correspond to linear combinations of the SU(2) and U(1) gauge bosons:

$$W_\mu^+ = \frac{1}{\sqrt{2}}(A_\mu^1 - iA_\mu^2), \tag{2.2}$$

$$W_\mu^- = \frac{1}{\sqrt{2}}(A_\mu^1 + iA_\mu^2), \tag{2.3}$$

$$Z_\mu = \cos\theta_{\mathrm{W}} A_\mu^3 - \sin\theta_{\mathrm{W}} B_\mu, \tag{2.4}$$

$$A_\mu = \sin\theta_{\mathrm{W}} A_\mu^3 + \cos\theta_{\mathrm{W}} B_\mu, \tag{2.5}$$

where θ_{W} is an adjustable parameter called the Weinberg angle.

The couplings of the fermions to the gauge fields are obtained from the gauge invariance and the known electromagnetic and weak couplings at low energies. However, the experimental fact that the charged current interaction takes place in left-handed forms must be taken into account. This fact is included into the model by hand: the Standard Model doesn't explain why the charged current has V−A form. Left-handed fermions are written as the isospin doublets

$$\begin{pmatrix} \nu_{\mathrm{e}L} \\ e_L \end{pmatrix} \quad \begin{pmatrix} \nu_{\mu L} \\ \mu_L \end{pmatrix} \quad \begin{pmatrix} \nu_{\tau L} \\ \tau_L \end{pmatrix}$$
$$\begin{pmatrix} \mathrm{u_L} \\ \mathrm{d_L} \end{pmatrix} \quad \begin{pmatrix} \mathrm{c_L} \\ \mathrm{s_L} \end{pmatrix} \quad \begin{pmatrix} \mathrm{t_L} \\ \mathrm{b_L} \end{pmatrix}, \tag{2.6}$$

while right-handed fermions stay isospin singlets

$$\mathrm{e_R} \quad \mu_{\mathrm{R}} \quad \tau_{\mathrm{R}}$$
$$u_R \quad \mathrm{c_R} \quad \mathrm{t_R} \quad \mathrm{d_R} \quad \mathrm{s_R} \quad \mathrm{b_R}.$$

The left-handed and right-handed fields for a fermion f are defined by

$$f_L = \frac{1}{2}(1 - \gamma_5) f, \tag{2.7}$$

$$f_R = \frac{1}{2}(1 + \gamma_5) f. \tag{2.8}$$

There are no right-handed neutrinos in the minimal Standard Model.

The Lagrangian describing the interactions between fermions and gauge bosons has three terms. The first, charged current term is

$$\frac{\mathrm{g}}{\sqrt{2}}(J^{\mu-}_{\mathrm{cc}}\, W^{+}_{\mu} + J^{\mu+}_{\mathrm{cc}}\, W^{-}_{\mu} + \mathrm{h.c.}), \tag{2.9}$$

where the charged current J^{μ}_{cc} is given by

$$J^{\mu+}_{\mathrm{cc}} = \left(\begin{array}{ccc} \overline{\mathrm{u}}_{\mathrm{L}} & \overline{\mathrm{c}}_{\mathrm{L}} & \overline{\mathrm{t}}_{\mathrm{L}} \end{array} \right) \gamma^{\mu} U \left(\begin{array}{c} d_L \\ s_L \\ b_L \end{array} \right) \quad \text{for quarks,} \tag{2.10}$$

and by

$$J^{\mu+}_{\mathrm{cc}} = \left(\begin{array}{cc} \overline{\nu_{\mathrm{eL}}} & \overline{\mathrm{e}}_{\mathrm{L}} \end{array} \right) \gamma^{\mu} \tau^{+} \left(\begin{array}{c} \nu_{\mathrm{eL}} \\ e_{\mathrm{L}} \end{array} \right) \quad \text{for electrons and other leptons,} \tag{2.11}$$

where τ^{+} stands for the raising operator formed by the Pauli matrices. The unitary matrix U describes the mixing of the weak couplings of quarks, and is often called as the Cabibbo-Kobayashi-Maskawa (CKM) matrix. Comparing the coupling constant in equation (2.9) with the Fermi-type 4-vertex Lagrangian for muon decays, a relationship

$$\frac{g^2}{8m^2_{\mathrm{W}}} = \frac{G_{\mu}}{\sqrt{2}}, \tag{2.12}$$

is obtained, where G_{μ} is the Fermi constant

$$G_{\mu} = 1.16637(2) \times 10^{-5}\,\mathrm{GeV}^{-2}. \tag{2.13}$$

The second, electromagnetic term is

$$\mathrm{g}\sin\theta_{\mathrm{W}}(\mathrm{J}^{\mu}_{\mathrm{em}}\mathrm{A}_{\mu} + \mathrm{h.c.}), \tag{2.14}$$

where the electromagnetic current J^{μ}_{em} is given by

$$J^{\mu}_{\mathrm{em}} = q_f \overline{f} \gamma^{\mu} f \tag{2.15}$$

for any fermion f with charge q_f. Comparing equation (2.14) with the usual electromagnetic interaction Lagrangian,

$$e = g \sin\theta_{\mathrm{W}} \tag{2.16}$$

is obtained. It follows from equations (2.12) and (2.16) that the mass of $\mathrm{W}^{\pm}$ is given by

$$m_{\mathrm{W}} = \sqrt{\frac{\pi\alpha}{\sqrt{2}G_{\mu}\sin^2\theta_{\mathrm{W}}}} \tag{2.17}$$

$$= \frac{37.280\,\mathrm{GeV}}{\sin\theta_{\mathrm{W}}}. \tag{2.18}$$

Table 2.1: Electroweak coupling constants of fermions

Fermion	q	c_{V}	c_{A}
ν	0	$\frac{1}{2}$	$\frac{1}{2}$
e, μ, τ	-1	$-\frac{1}{2}+2\sin^2\theta_{\mathrm{W}}$	$-\frac{1}{2}$
u, c, t	$\frac{2}{3}$	$\frac{1}{2}-\frac{4}{3}\sin^2\theta_{\mathrm{W}}$	$\frac{1}{2}$
d, s, b	$-\frac{1}{3}$	$-\frac{1}{2}+\frac{2}{3}\sin^2\theta_{\mathrm{W}}$	$-\frac{1}{2}$

The Z^0 mass is related to m_{W} as

$$m_{\mathrm{Z}} = \frac{m_{\mathrm{W}}}{\cos\theta_{\mathrm{W}}}. \tag{2.19}$$

The third, weak neutral current term is

$$\frac{\mathrm{e}}{\sin\theta_{\mathrm{W}}\cos\theta_{\mathrm{W}}}(\mathrm{J}^{\mu}_{\mathrm{nc}}\mathrm{Z}_{\mu}+\mathrm{h.c.}), \tag{2.20}$$

where the neutral current J^{μ}_{nc} is given by

$$J^{\mu}_{\mathrm{nc}} = c^f_{\mathrm{V}}\overline{f}\gamma^{\mu}f - c^f_{\mathrm{A}}\overline{f}\gamma^{\mu}\gamma_5 f \tag{2.21}$$

for any fermion f. The vector and the axial-vector coupling constants c^f_{V} and c^f_{A} are given by

$$c^f_{\mathrm{V}} = I_3 - 2q_f\sin^2\theta_{\mathrm{W}}, \tag{2.22}$$

$$c^f_{\mathrm{A}} = I_3, \tag{2.23}$$

where I_3 is the third component of the weak isospin. The coupling constants q_f, c^f_{V} and c^f_{A} are summarized in table 2.1.

2.2 Extension of the Standard Model and constraints

So far, no contradictions have been found between the experimental results and the predictions from the Standard Model. However, there are many open issues in neutrino (and also charged lepton) sector:

(a) Are there right-handed neutrinos?

(b) Are the neutrinos a Majorana type or a Dirac?

(c) Are there further sequential generations?

(d) Why are observed neutrino masses so small?

(e) Do neutrino decay?

(f) What is the origin of parity violation in the weak interaction?

(g) What is the pattern of neutrino mixing? (such as a CKM or $L-R$ type?)

The above subjects are important guides for the theoretical models at higher energy scale.

In this analysis the fourth generation leptons, which are just an analogue of the lighter three generations, were searched for at the new higher energy scale ($M_{\rm Z} < \sqrt{s} \leq 2M_{\rm W}$) by the $\rm e^+e^-$ collider experiments. The number of light neutrino generations for $m_\nu < M_{\rm Z}/2$ was already measured to be three by the LEP line-shape measurements. So the mass of the fourth generation neutrino ($\rm L^0$) should be considered to be heavy: $m_{\rm L^0} > M_{\rm Z}/2$. As the neutrinos are massless and there is no right-handed component of ν_ℓ in the minimal standard $\rm SU(2)_L{\times}U(1)_Y$ gauge theory, some expansion of this model must be required.

The ways to get a non-zero neutrino mass are:

(1) Include the right-handed singlet ν_R term. While this provides the simplest way to get a non-zero neutrino mass, it is usually not considered as the sole origin of neutrino mass because it provides no information about the smallness of neutrino mass.

(2) Do not include ν_R, but add a Higgs triplet that has a Yukawa coupling to leptons [11]. This provides a Higgs mechanism for producing the Majorana mass (see equation 2.28).

(3) Consider the effects of new physics at a large mass scale M, causing the violation of lepton number which results in Majorana mass terms. In this model the mixing between right-handed and left-handed neutrino term was expected, namely the *flavour changing neutral current (FCNC)* could be occurred on the production and decay of the heavy neutral lepton. In particular, famous solution of this model is 'See-Saw' mechanism [7], but there are too many versions of this model.

We consider the cases (1) and (3), then right-handed neutrinos were added in the isosinglet group for each generation The left-handed isospin doublet of fourth generation is represented as

$$\begin{pmatrix} \rm L^0_L \\ \rm L^-_L \end{pmatrix}, \tag{2.24}$$

while right-handed fermions stay in two isospin singlets

$$\rm L^-_R, \quad L^0_R$$

The correlation between the weak and mass eigenstates of leptons could be considered to be just the analogue as the quark sector (such as CKM matrix). The weak eigenstates L^0 are mixtures of the mass eigenstates ($\nu'_\ell = \nu'_e, \nu'_\mu, \nu'_\tau$ or $L^{0'}$),

$$L^0 \;=\; \sum_{\ell=1}^{4} V_{L\ell}\nu'_\ell, \tag{2.25}$$

where $V_{L\ell}$ is the flavour mixing parameter between a heavy (left-handed) lepton and a light (left-handed) lepton(e', μ' or τ'). The square of mixing parameter ($|V_{L\ell}|^2$) between a fourth generation and a light lepton(e, μ or τ) in terms of its leptonic branching ratio is given by

$$\sum_{\ell\neq L} |V_{L\ell}|^2 = (\frac{m_\mu}{m_{L^0}})^5 \; \frac{\tau_\mu \; \sum_{\ell\neq L} \mathrm{Br}(L^0 \to \ell^- e^+ \nu_e)}{f \; \tau_{L^0}}, \quad (\ell \;=\; e,\; \mu \text{ or } \tau),$$

where m_μ and τ_μ are the muon mass and the muon lifetime, τ_{L^0} is the lifetime of the neutral heavy lepton, and f is a phase-space suppression factor for final state particles, which differs appreciably from unity when the mass difference between the neutral lepton and its decay products is small [12]. The mean decay length ℓ of the heavy lepton is given by

$$\ell = \beta\gamma\tau_{L^0} c$$

where c is the velocity of the light, $\gamma \equiv (1-\beta^2)^{-1/2}$ and $\beta \equiv \sqrt{1-4m_{L^0}^2/s}$. So the decay length could be written as a function of the flavour mixing parameter and heavy lepton mass. The lifetime of a Majorana L^0 is half of a Dirac L^0, since the decays $L^0 \to \ell^- W^{*+}$ and $L^0 \to \ell^+ W^{*-}$ occur with equal probability for a Majorana neutral heavy lepton and not for Dirac.

Neutrinos are very special elementary fermions, since their uniqueness lies in not having any electromagnetic charge. This enables massive neutrinos to be either Dirac fermions with distinct particles and anti-particles or, giving up lepton conservation, self-conjugate Majorana fermions. (The distinction becomes meaningless in the massless case when a Dirac fermion simply becomes a linear superposition of two Majorana ones.) It is convenient to consider along with a neutrino (ν) the *'c-conjugated field'* $\nu^C \equiv (\bar{\nu}C)^T$ where C is the c-conjugation matrix in spinor space and T is transpose. For Dirac neutrino $\nu \neq \nu^C$ whereas Majorana ones obey the condition $\nu = \nu^C$, actually $\nu^C = e^{i\Theta}\nu$, where $e^{i\Theta}$ is sometimes called Majorana creation phase factor [13]. The mass term for a Dirac neutrino can be written as

$$\mathcal{L}^D_{\mathrm{mass}} = -m\overline{\nu}\nu = -m(\overline{\nu_L}\nu_R + \overline{\nu_R}\nu_L), \tag{2.26}$$

where $\nu_{L,R} \equiv \frac{1}{2}(1 \mp \gamma_5)\nu$. There are four independent chiral components in this case:$\nu_L,\ \nu_R,\ (\nu_L)^C = (\nu^C)_R$ and $(\nu_R)^C = (\nu^C)_L$.

In contrast, a massive Majorana neutrino admits a term such as

$$-\frac{1}{2}M_L\overline{\nu}\nu = -\frac{1}{2}M_L(\overline{\nu_L}(\nu_L)^C + \overline{(\nu_L)^C}\nu_L), \tag{2.27}$$

where $\nu \equiv \nu_L + (\nu_L)^C$ More generally, Lorentz invariance allows separate Majorana masses $M_{L,R}$ for $\nu_{L,R}$ so that one can take

$$\mathcal{L}^M_{\rm mass} = -\frac{1}{2}M_L\overline{\nu_L}(\nu_L)^C - \frac{1}{2}M_R\overline{(\nu_R)^C}\nu_R + h.c. \tag{2.28}$$

The most general mass term would be sum of the (2.26) and (2.28). If ν_L transforms as a doublet and ν_R as a singlet of the electroweak $\mathrm{SU}(2)_L\times\mathrm{U}(1)_Y$ gauge group, $M_L(M_R)$ would have to arise from the vacuum expectation value of a Higgs field transforming as a triplet (singlet). Since a triplet representation usually has a problem with a unit value of the ρ-parameter ($\equiv \frac{M_{\rm W}^2}{M_{\rm Z}^2\cos^2\theta_{\rm w}}$), it is customary to take $M_L = 0$, but having the possibility that high scale physics may induce a tiny M_L. On the other hand, a Higgs singlet - being outside the electroweak gauge theory - could only be a relic of high scale physics so that one expects $M_R = M \gg M_W$. The general mass term for L can then be written in matrix from as (using $\overline{\nu_L}\nu_R = \overline{(\nu_L)^C}(\nu_R)^C$)

$$\mathcal{L}_{\rm mass} = -\frac{1}{2}\begin{pmatrix} \overline{\nu}_L & \overline{(\nu_R)^C} \end{pmatrix}\begin{pmatrix} 0 & m_i \\ m_i^T & M_i \end{pmatrix}\begin{pmatrix} (\nu_L)^C \\ \nu_R \end{pmatrix} + h.c. \tag{2.29}$$

In the mass-matrix ($\mathcal{M}$) of (2.29) the off-diagonal element m_i is the Dirac mass matrix of i-th generation. Now we consider the one generation, then $m_i = m$, $M_i = M$ and $m_i^T = m$ are numerical numbers. It may be expected to be typically of the order of the known charged fermion masses of the concerned family in the Standard Model. Moreover, for the sake of simplicity, let us assume that both m and M are real and $M > 0$. Now choose an orthogonal matrix

$$\mathcal{O} = \begin{pmatrix} \cos\theta & -\sin\theta \\ \sin\theta & \cos\theta \end{pmatrix} \tag{2.30}$$

with $\tan 2\theta = 2m/M$. Then

$$\mathcal{O}\mathcal{M}\mathcal{O}^{\mathcal{T}} = \begin{pmatrix} -m_1 & 0 \\ 0 & m_2 \end{pmatrix}, \tag{2.31}$$

where

$$m_{1,2} = \frac{1}{2}(\sqrt{M^2 + 4m^2} \mp M). \tag{2.32}$$

Since $m_{1,2} \geq 0$, we still have a little problem, i.e., the elements of the diagonal matrix in Eq. 2.31 are not all non-negative and therefore cannot be interpreted as the masses of physical fields. So this matrix is redefined as:

$$\mathcal{O}\mathcal{M}\mathcal{O}^{\mathcal{T}} = \begin{pmatrix} -m_1 & 0 \\ 0 & m_2 \end{pmatrix} = \begin{pmatrix} m_1 & 0 \\ 0 & m_2 \end{pmatrix} \begin{pmatrix} -1 & 0 \\ 0 & 1 \end{pmatrix} = \mathcal{A}\mathcal{K}^2 \tag{2.33}$$

Then,

$$\mathcal{M} = \mathcal{O}^{\mathcal{T}}\mathcal{A}\mathcal{K}^2\mathcal{O}$$

Now, if we define the column vectors

$$\begin{pmatrix} \nu_L' \\ (\nu_R)^{C'} \end{pmatrix} \equiv \mathcal{O} \begin{pmatrix} \nu_L \\ (\nu_R)^{C} \end{pmatrix} = \begin{pmatrix} \cos\theta & -\sin\theta \\ \sin\theta & \cos\theta \end{pmatrix} \begin{pmatrix} \nu_L \\ (\nu_R)^{C} \end{pmatrix} \tag{2.34}$$

and

$$\begin{pmatrix} (\nu_L)^{C'} \\ \nu_R{}' \end{pmatrix} \equiv \mathcal{K}^2\mathcal{O} \begin{pmatrix} (\nu_L)^{C} \\ \nu_R \end{pmatrix} = \begin{pmatrix} -\cos\theta & \sin\theta \\ \sin\theta & \cos\theta \end{pmatrix} \begin{pmatrix} (\nu_L)^{C} \\ \nu_R \end{pmatrix} \tag{2.35}$$

then,

$$\mathcal{L}_{\text{mass}} = -\frac{1}{2}m_1\overline{\nu_L'}(\nu_L)^{C'} - \frac{1}{2}m_2\overline{(\nu_R)^{C'}}\nu_R' + h.c. \tag{2.36}$$

Thus, for a single generation, we obtain two eigenstates:

$$\nu_1 = \nu_L' + (\nu_L)^{C'} = (\nu_L - (\nu_L)^{C})\cos\theta - ((\nu_R)^{C} - \nu_R)\sin\theta \tag{2.37}$$

$$\nu_2 = \nu_R' + (\nu_R)^{C'} = (\nu_R + (\nu_R)^{C})\cos\theta + ((\nu_R)^{C} + \nu_R)\sin\theta \tag{2.38}$$

The ν_2 is the Majorana neutrinos by definition $((\nu_{L,R})^{C})^{C} = \nu_{L,R}$ and ν_1 could also be with the Majorana creation phase factor $e^{i\Theta}$ = -1. If the constraint $m \ll M$ (namely $sin\theta \approx \frac{m}{M}$ and $cos\theta \approx 1$) on the mass matrix was satisfied, **one**

($\sim M$) of the two eigenvalues is therefore expected to be heavy and the other ($\sim m^2/M$) light. This model is called "See-Saw" mechanism [7], which can explain the smallness of the neutrino of the light three generations if generally the observed neutrinos were the Majorana type (for case (3)). Note that the physical low mass state is purely left-handed:

$$\nu'_L = \cos\theta\nu_L - \sin\theta(\nu_R)^c \approx \nu_L - \frac{m}{M}(\nu_R)^c, \tag{2.39}$$

while the heavy state is right-handed:

$$\nu'_R = \cos\theta\nu_R + \sin\theta(\nu_L)^c \approx \nu_R + \frac{m}{M}(\nu_L)^c. \tag{2.40}$$

This additional mixing spoils the unitarity of the lepton CKM matrix to order m/M and leads to off-diagonal Z^0 coupling of this order, in other words the *flavour changing neutral current (FCNC)* could be possible in this order. In this simplest of See-Saws the physical particles are Majorana fermion, however more complicated See-Saws models [14] could form the Dirac type neutrino.

Since the constraints for m and M depend on the models, a rough guide to the lower limit on M is shown, with assuming that there exist 4th generation leptons and that the Dirac neutrino mass for each generation corresponds to the charged lepton mass ($m = m_{\nu_\ell}$). We consider the ratio m_ℓ^2/m_ν for each generation, where m_ℓ is the charged lepton mass and $m_{\nu\ell}$ is the upper limit on the corresponding neutrino mass. Using $m_{\nu_e} < 5$ eV, $m_{\nu_\mu} < 270$ keV and $m_{\nu_\tau} < 31$ MeV [20], one finds

$$M \geq \frac{m_e^2}{m_{\nu_e}} > 50 \text{ GeV}, \tag{2.41}$$

$$M \geq \frac{m_\mu^2}{m_{\nu_\mu}} > 41 \text{ GeV}, \tag{2.42}$$

$$M \geq \frac{m_\tau^2}{m_{\nu_\tau}} > 102 \text{ GeV}. \tag{2.43}$$

Hence, using the LEP1 experimental mass limit of the Majorana m_{L^0}:

$$m_{L^0} \approx \frac{m_{L^-}^2}{M} \geq 39.5 \text{ GeV},$$

then m_{L^-} is expected to be larger than 63.5 GeV on this simple calculations, when the neutrino flavour mixing (through eq. 2.25) is not included. One of most strong limits of the See-Saw mixing amplitude $U_\ell \approx m/M$ for three light generations has been determined by the direct search of the isosinglet heavy lepton N_R ($= \nu'_R$ see eq. 2.40). The N_R could be produced with its associated isodoublet neutrino from Z^0 decay:

$$e^+e^- \to Z^0 \to N_R\bar{\nu}_\ell \text{ or } \bar{N}_R\nu_\ell,$$

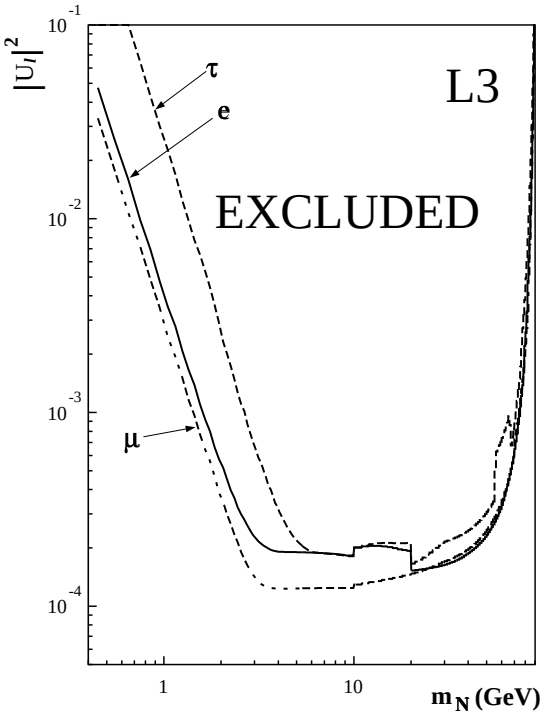

Figure 2.1: The 95% C.L. upper limit on the See-Saw mixing amplitude $|U_\ell|^2$ as a function of the mass of the isosinglet heavy lepton for three generations from the L3 analysis [15] at LEP1.

where $\nu_\ell = \nu_{\rm e}, \nu_\mu$ or ν_τ. The production cross-section is reduced from the neutrino pair production cross-section by a phase-space factor and by the square of a mixing amplitude. It can be written as

$$\mathrm{Br}(\mathrm{Z}^0 \to \nu_\ell \mathrm{N}_\ell) = \mathrm{Br}(\mathrm{Z}^0 \to \nu_\ell \bar{\nu}_\ell) |\, U_\ell|^2 (1 - \frac{m_{\rm N}^2}{M_{\rm Z}^2})^2 (1 + \frac{1}{2}\frac{m_{\rm N}^2}{M_{\rm Z}^2}), \qquad (2.44)$$

where $m_{\rm N}$ is the mass of N_R and $M_{\rm Z}$ the Z^0 mass. The $|U_\ell|^2$ limits as a function of $m_{\rm N}(< M_{\rm Z})$ have been already obtained by the LEP1 analysis and the result that the $|U_\ell|^2$ should be lower than 10^{-4} for a $m_{\rm N}$ between a few GeV and 80 GeV was obtained [15]. Of course, eq. 2.41, eq. 2.42 and eq. 2.43 satisfy these constraints ($|U_{\rm e}|^2 < 10^{-10}$, $|U_\mu|^2 < 10^{-6}$ and $|U_\tau|^2 < 10^{-3}$ with $m_{\rm N} > 102$ GeV). Therefore the See-Saw mechanism allows the possibility of the sequential generations because of the unknown mass parameters of the m and M. For instance, Ref. [16] allows the Dirac neutrino mass m up to 178 GeV by computing the one-loop radiative corrections. Fig. 2.1 shows the $|U_\ell|^2$ limits as a function of $m_{\rm N}$ from the LEP1 analysis. In the present analysis, the $\mathrm{e}^+\mathrm{e}^- \to \mathrm{Z}^0 \to \mathrm{N}_R \bar{\nu}_\ell$ process was not searched for because of the small expected numbers of events, (a few hundred events for each flavour both with LEP1.5 and LEP2 data), where significant upper $|U_\ell|^2$ limits were no longer expected than the current limit from the LEP1 experiment

on the mass range below $M_{\rm Z}$ and from the CHARM experiment [17] or the limit from the "weak universality" requirement [18] on the mass range above $M_{\rm Z}$. The cross-section of the $\rm N_{\it R}$ pair production is suppressed relatively to the single production cross-section by an additional $|U_\ell|^2$ factor. By this constraint the expected cross-section of the $\rm N_{\it R}$ pair production at LEP1.5 and LEP2 would be very small and these processes were also not considered.

The further more extension candidate of the $\rm SU(2)_{\it L}{\times}U(1)_{\it Y}$ is the left-right symmetric model. The simplest such model employs the gauge group $\rm SU(2)_{\it L}\times$ $\rm SU(2)_{\it R}\times$ $\rm U(1)_{\it B-L}$ and contains one left-handed and one right-handed lepton doublet per generation, which is described in Ref. [9]. Also the mirror fermion models [10] may be expected to be another candidate of new heavy leptons. They have chiral properties which are opposite to those of ordinary fermions, i.e. the right-handed components are in weak isodoublets and the left-handed ones are in weak isosinglets; there is also a left-handed heavy neutrino. As the light three generations whichever of the left-right symmetric model or the mirror model can be detected by the single production ($\rm e^+e^- \to Z^0 \to N_{\it R}\bar{\nu}_\ell$) rather than the pair production with the the reason described before, I concentrated to analyze the sequential 4th generation lepton.

As a result, the investigation of the existence for the heavy leptons is very important subject not only to know the possibility for the extension of the Standard Model but also to resolve the neutrino mass problem. In this paper, the pair production of an unstable sequential heavy neutral lepton and charged lepton was searched for at new energy scale ($M_{\rm Z} < \sqrt{s} \leq 2M_{\rm W}$). The production and decay patterns searched for were:

(A) $\rm e^+e^- \to L^0\bar{L}^0$ with $\rm L^0 \to \ell W^*$
The $\rm L^0$ allows either a Dirac type or a Majorana type neutrino. For the Majorana case, the left-handed (light mass eigenstate in the See-Saw model) was searched for.

(B) $\rm e^+e^- \to L^+L^-$ with $\rm L^- \to \nu_L W^{*-}$,
where $\nu_{\rm L}$ is a stable heavy neutrino (> 39.5 GeV).

(C) $\rm e^+e^- \to L^+L^-$ with $\rm L^- \to \nu_\ell W^{*-}$,
where ν_ℓ is a light neutrino ($\ell =$ e, μ or τ). This case was considered with the condition $m_{\rm L^-} \leq m_{\rm L^0}$.

The details are described in the next section.

2.3 The production and decay of unstable heavy lepton

The production of a heavy neutral lepton pair ($\rm L^0\bar{L}^0$) at LEP1.5 and LEP2 proceeds primarily through a Drell-Yan-like mechanism (namely, exchange of

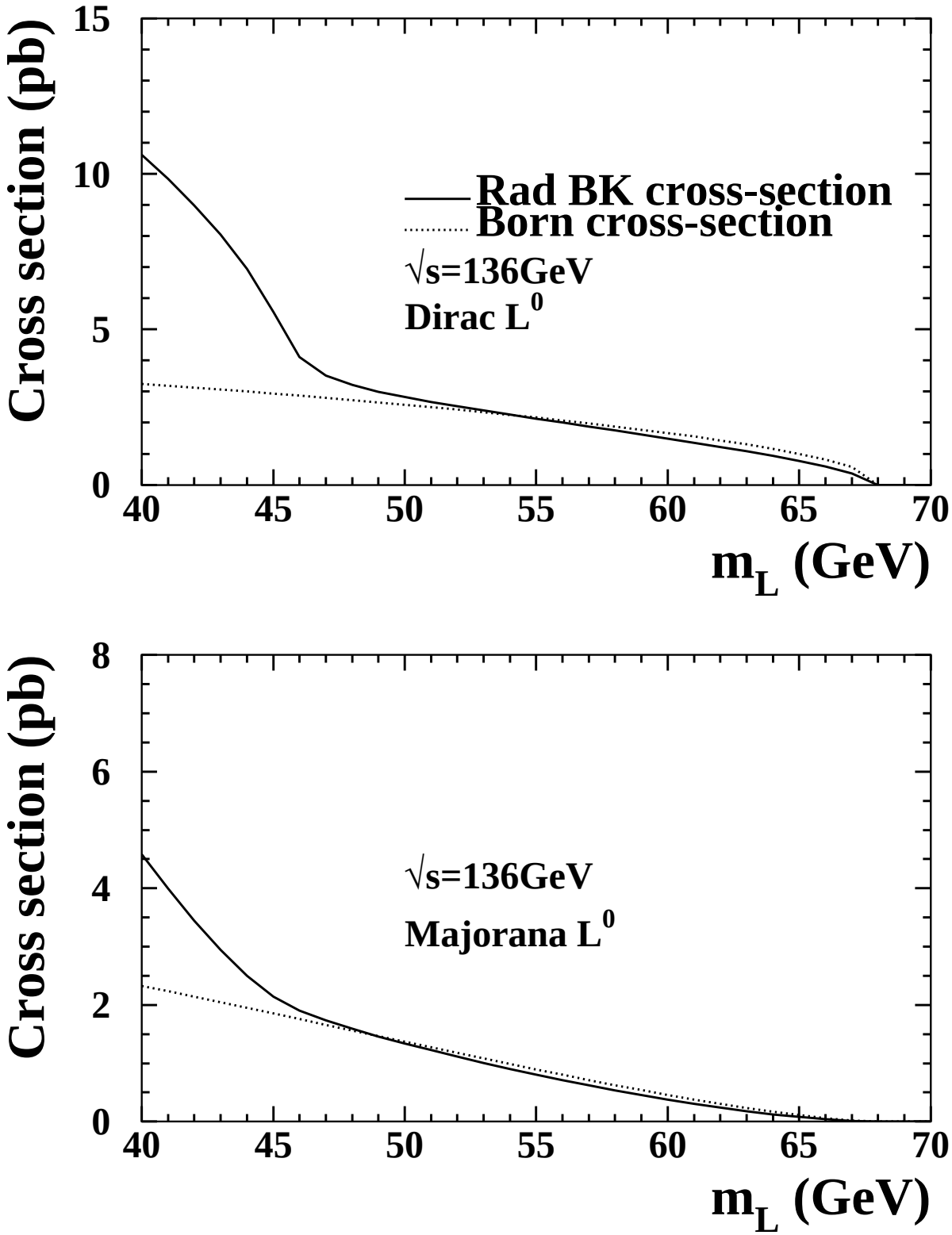

Figure 2.2: The cross-section for $L^0\bar{L}^0$ pair production at a centre-of-mass energy = 136 GeV.

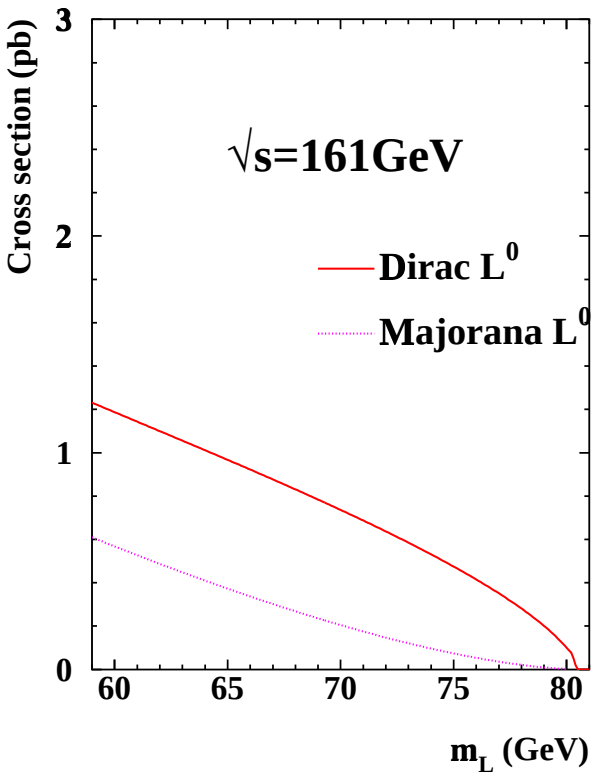

Figure 2.3: The cross-section for $L^0\bar{L}^0$ pair production including the initial state radiation at a centre-of-mass energy = 161 GeV.

s-channel Z^0). For the $L^0\bar{L}^0$ production, the γ channel is obviously absent. There is an additional diagram through a t-channel W exchange. Since the latter contribution to the amplitude involves the eL^0 mixing, which is already restricted to be very small, t-channel exchange can be essentially neglected. The Born level cross section of neutral heavy lepton pair production in e^+e^- annihilation is calculated as follows [19]:

$$\sigma_{e^+e^-\to L^0\bar{L}^0} = \frac{\beta(3+\beta^2)}{4}\cdot\sigma_{\nu\bar{\nu}} \quad \text{for a Dirac neutral heavy lepton,}$$

$$\sigma_{e^+e^-\to L^0\bar{L}^0} = \beta^3\cdot\sigma_{\nu\bar{\nu}} \quad \text{for a Majorana neutral heavy lepton,}$$

where $\beta \equiv \sqrt{1-4m^2_{L^0}/s}$, m_{L^0} is the heavy neutral lepton mass and $\sigma_{\nu\bar{\nu}}$ is the massless $\nu_\mu\bar{\nu}_\mu$ pair production cross section. The total cross-sections are shown in Fig. 2.2 and Fig. 2.3 as a function of L^0 mass at $\sqrt{s} = 136$ GeV and 161 GeV, respectively. The corrected cross-sections with initial state radiation are shown by solid lines, based on the calculations of Berends *et al.* [21]. The differential cross section for L^0 pair production is given by

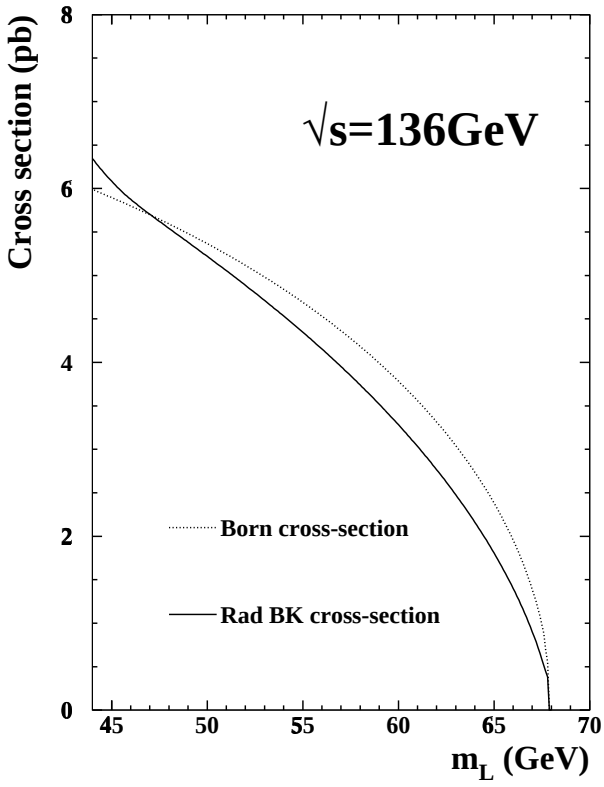

Figure 2.4: The cross-section for L^+L^- pair production at a centre-of-mass energy = 136 GeV.

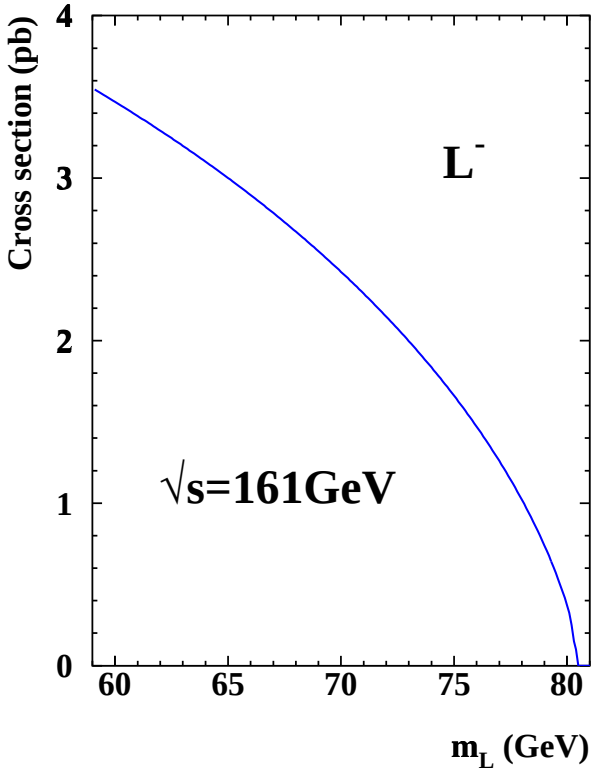

Figure 2.5: The cross-section for L^+L^- pair production including the initial state radiation at a centre-of-mass energy = 161 GeV.

$$\frac{\sigma_{\mathrm{L^0\bar{L}^0}}}{d(\cos\theta)} \propto (1+\cos^2\theta)$$

for a Majorana $\mathrm{L^0}$, where θ is the polar angle of the $\mathrm{L^0}$ momentum vector. For a Dirac $\mathrm{L^0}$, the differential cross section is given by

$$\frac{\sigma_{\mathrm{L^0\bar{L}^0}}}{d(\cos\theta)} \propto (1+\beta^2\cos^2\theta + \frac{2(1-4\sin^2\theta_{\mathrm{w}})}{1-4\sin^2\theta_{\mathrm{w}}+8\sin^4\theta_{\mathrm{w}}}\beta\cos\theta) ,$$

Since an absolutely stable heavy lepton is disfavoured on astrophysical/ cosmological grounds [22], any such new particles must necessarily decay. Although this bound can not be applied to particles with a very small (but finite) decay width, such particles would be effectively stable as far as the collider experiments are concerned. While a stable $\mathrm{L^0}$ would be directly undetected in the LEP1 experiments, it is still possible to detect a stable $\mathrm{L^0}$ through a invisible width, Γ_{inv}, measurement but there was no signal yet.

The following decay mode was considered for $\mathrm{L^0}$:

(A) $\mathrm{L^0} \to \ell\mathrm{W^*}$ via lepton flavour mixing, where ℓ is e, μ or τ, and $\mathrm{W^*}$ is a virtual W boson.

A Majorana $\mathrm{L^0}$ can decay into either $\ell^-\mathrm{W^{*+}}$ or $\ell^+\mathrm{W^{*-}}$. Therefore the charge correlation between the two light leptons was not used in the analysis, in order to be sensitive both to a Dirac and a Majorana $\mathrm{L^0}$. The visible energy of these events is expected to be large and there should be at least four charged particles, including at least two light leptons (e, μ or τ) in an event.

Charged heavy lepton pairs $\mathrm{L^+L^-}$ could be produced in $\mathrm{e^+e^-}$ annihilation via a virtual $\mathrm{Z^0}$ boson or a virtual photon. Assuming that the $\mathrm{Z^0}$ couples to $\mathrm{L^+L^-}$ in the same way as it couples to lighter charged leptons, the Born-level cross-section is as follows:

$$\sigma_{\mathrm{e^+e^-\to L^+L^-}} = \frac{4\pi\alpha^2}{3s}\beta\frac{3-\beta^2}{2}\Big[1+\frac{(1-4\sin^2\theta_{\mathrm{w}})^2}{8\cos^2\theta_{\mathrm{w}}\sin^2\theta_{\mathrm{w}}}\frac{s(s-M_{\mathrm{Z}}^2)}{(s-M_{\mathrm{Z}}^2)^2+M_{\mathrm{Z}}^2\Gamma_{\mathrm{Z}}^2}$$

$$+\frac{(1-4\sin^2\theta_{\mathrm{w}})^2+1}{256\cos^4\theta_{\mathrm{w}}\sin^4\theta_{\mathrm{w}}}\Big((1-4\sin^2\theta_{\mathrm{w}})^2+\frac{2\beta^2}{3-\beta^2}\Big)\frac{s^2}{(s-M_{\mathrm{Z}}^2)^2+M_{\mathrm{Z}}^2\Gamma_{\mathrm{Z}}^2}\Big] ,$$

Here, s is the square of the centre-of-mass energy, M_{Z} and Γ_{Z} are the mass and width of the $\mathrm{Z^0}$ boson, θ_{w} is the weak mixing angle, and β is the velocity of the heavy leptons in the final state: $\beta \equiv \sqrt{1-4m_{\mathrm{L^-}}^2/\mathrm{s}}$. As shown in Fig. 2.4 and 2.5, the total cross section including the correction of the first order initial state radiation [21] has been calculated as a function of the charged heavy lepton mass.

The following two cases were studied for the decay of $\mathrm{L^-}$:

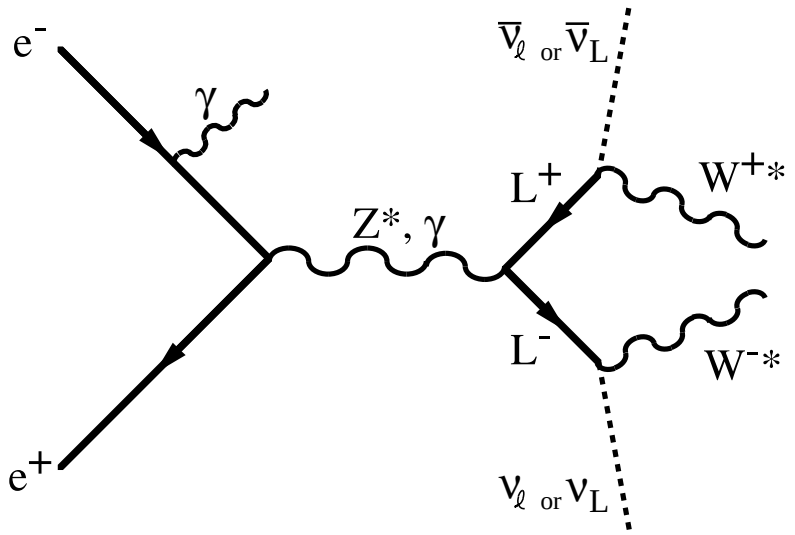

Figure 2.6: Feynman diagrams for the charged heavy lepton production.

(B) $L^- \to \nu_L W^{*-}$, where ν_L is a stable heavy neutrino: neutral partner of L^- in the fourth generation lepton doublet. The lower mass limit based on data from LEP1 for the heavy stable neutrino (ν_L) was 45.0 GeV for a Dirac neutrino and 39.5 GeV for a Majorana neutrino [1, 20]. In this case, the ν_L is therefore assumed to be heavier than 39.5 GeV.

(C) $L^- \to \nu_\ell W^{*-}$, where ν_ℓ is ν_e, ν_μ or ν_τ. The decay occurs via lepton flavour mixing.

The ordinary V–A coupling was assumed for the $L^-\nu_L W^{*-}$ and $L^-\nu_\ell W^{*-}$ decay vertices. In Fig. 2.6, Feynman diagrams for the charged heavy lepton production is shown. The expected experimental signature for L^+L^- events for both cases is that of a multijet[1] event with a large unbalanced transverse momentum with respect to the beam axis. If all the visible decay products of L^- and L^+ happened to be in the same hemisphere, the event topology could be a monojet. The events in case (B) are expected to have a smaller visible energy than for case (C), because the two heavy neutrinos carry away more energy and momentum.

Cascade decays ($L^0 \to L^- \to \nu_\ell$, $L^- \to L^0 \to \ell$ with $\tau_{L^0,L^-} \ll 10^{-10}$ sec) of heavy leptons were not considered in this analysis. Because $L^0 \to L^- \to \nu_\ell$ type cascade decay would be detected by case (C) analysis and also $L^- \to L^0 \to \ell$ type by case (A). The analysis was designed to have a good sensitivity for heavy leptons with a decay length shorter than a few cm. Namely, the mixing parameters of

[1] An isolated lepton is treated as a jet.

L^0–ℓ^- and L^-–ν_ℓ were assumed to satisfy the condition $\sum_\ell |V_{L\ell}|^2 > \mathcal{O}(10^{-11})$. Of course, these requirements satisfy the constraints explained in Sec. 2.2.

2.4 Mass limits from LEP1 data

2.4.1 Neutral Heavy Lepton

Lower mass limit for neutral heavy leptons depends on the mixing angle $|V_{L\ell}|^2$ (ℓ = e, μ or τ). If all the mixing angles between the neutral heavy lepton and light three leptons were larger than 10^{-10} in terms of $|V_{L\ell}|^2$, namely if the heavy leptons decay within the detector at $\sqrt{s} \approx M_Z$, the signal could be detected by the direct search. On the other hand, when the mixing angle would be lower, namely if the neutral heavy lepton would not decay within the detector, the mass limit could be estimated by invisible width from the Z^0 line-shape data, Γ_{inv} = Γ_{Z^0} - Γ_{had} - $3\Gamma_{\ell\ell}$, where Γ_{Z^0} is the Z^0 total width, Γ_{had} the partial width of $q\bar{q}$ hadronic final states obtained from the observed cross-section, $\Gamma_{\ell\ell}$ the partial width of the leptonic final states (e^+e^-, $\mu^+\mu^-$ and $\tau^+\tau^-$). An additional type of leptons would increase the total decay width of the Z^0 by the following amount:

$$\Gamma_{L^+L^-} = \frac{G_\mu M_Z^3}{12\pi\sqrt{2}}[\beta(3-\beta^2)c_V^2 + 2\beta^3 c_A^2] \tag{2.45}$$

for sequential charged leptons,

$$\Gamma_{L^0\bar{L}^0} = \frac{G_\mu M_Z^3}{12\pi\sqrt{2}}\frac{1}{4}\beta(3+\beta^2) \tag{2.46}$$

for Dirac neutrinos,

$$\Gamma_{L^0\bar{L}^0} = \frac{G_\mu M_Z^3}{12\pi\sqrt{2}}\frac{1}{4}\beta^3 \tag{2.47}$$

for Majorana neutrinos. Based on the possible deviation of the measured Γ_{inv} from the Standard Model expectation, the following mass limits have been obtained with 95% C.L. from LEP1 data;

(1) 45.0 GeV (for a Dirac L^0, if L^0 is a stable and undetected within the detector),

(2) 39.5 GeV (for a Majorana L^0, if L^0 is a stable and undetected within the detector[2]) and

Fig. 2.7 and 2.8 show the 95% C.L. lower mass limit contours in the parameter plane of m_{L^0} and $|V_{L\ell}|^2$ for a Dirac and a Majorana case, respectively.

[2]In this paper this case L^0 is quoted as ν_L.

2.4.2 Charged Heavy Lepton

The lower L^- mass region of the $L^- \rightarrow \nu_L W^*$ case has been already excluded by the ν_L mass limit (> 39.5 GeV). Therefore m_{L^-} is considered to be larger than 39.5 GeV in $L^- \rightarrow \nu_L W^*$ case. In the case of $L^- \rightarrow \nu_\ell W^*$ ($m_{L^-} < m_{L^0}$), however, the lower limit is determined by the Γ_{had} and Γ_{inv} measurements as described above.

In summary the mass limits for L^- are as follows:

(1) In the case of $m_{L^-} > m_{L^0}$, ($L^- \rightarrow \nu_L W^*$), the mass limit of L^- is the same as ν_L mass limit. Namely, m_{L^-} is larger than 39.5 GeV.

(2) In the case of $m_{L^-} < m_{L^0}$, ($L^- \rightarrow \nu_\ell W^*$), $m_{L^-} > 42.7$ GeV.

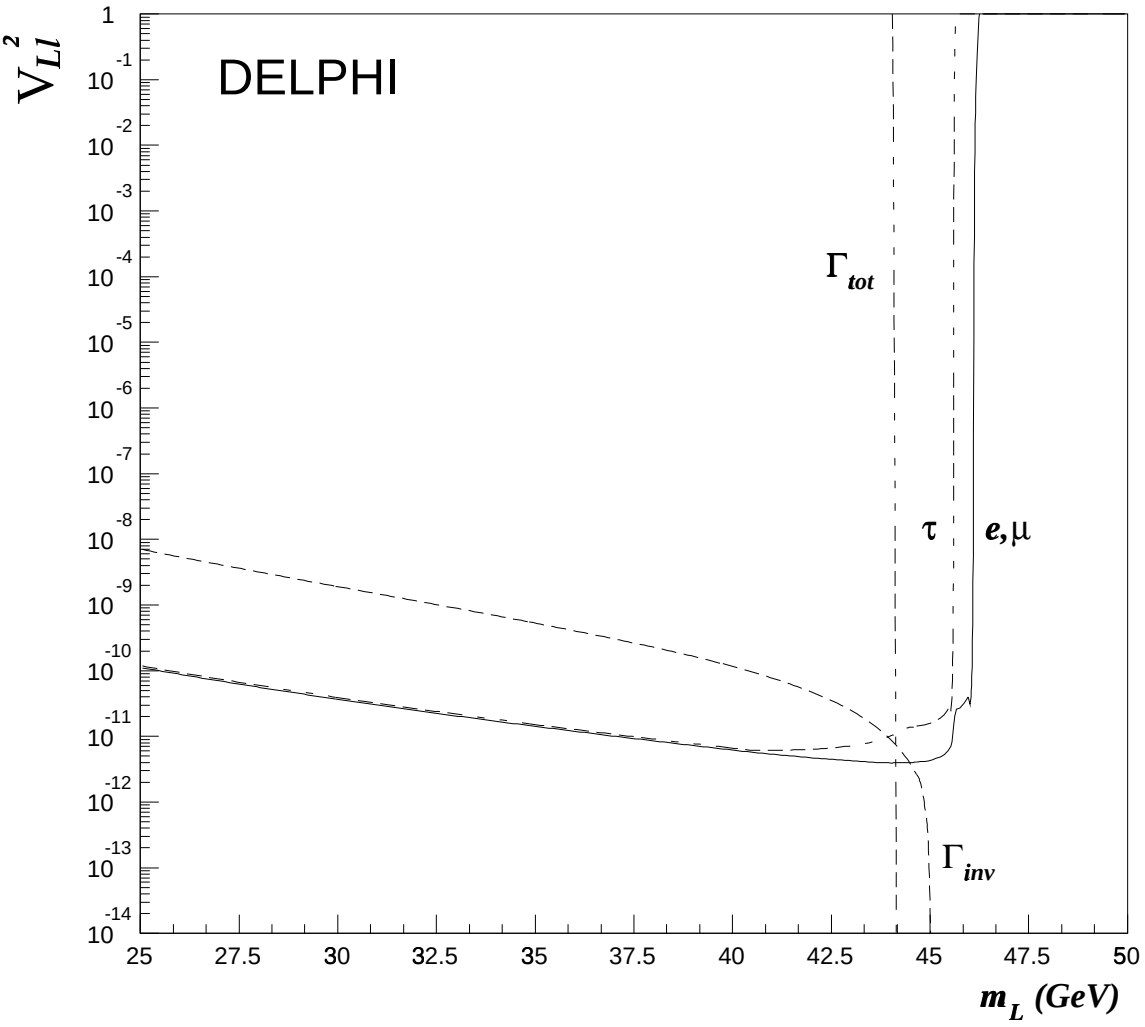

Figure 2.7: The 95% C.L. lower limit contours in the plane of the m_{L^0} and $|V_{\mathrm{L}\ell}|^2$ for a Dirac case using the DELPHI detector [23], where e, μ and τ show the direct search mass limits for each decay modes and Γ_{tot} and Γ_{inv} show the mass limits from the total Z^0 width measurement and the invisible width measurement, respectively.

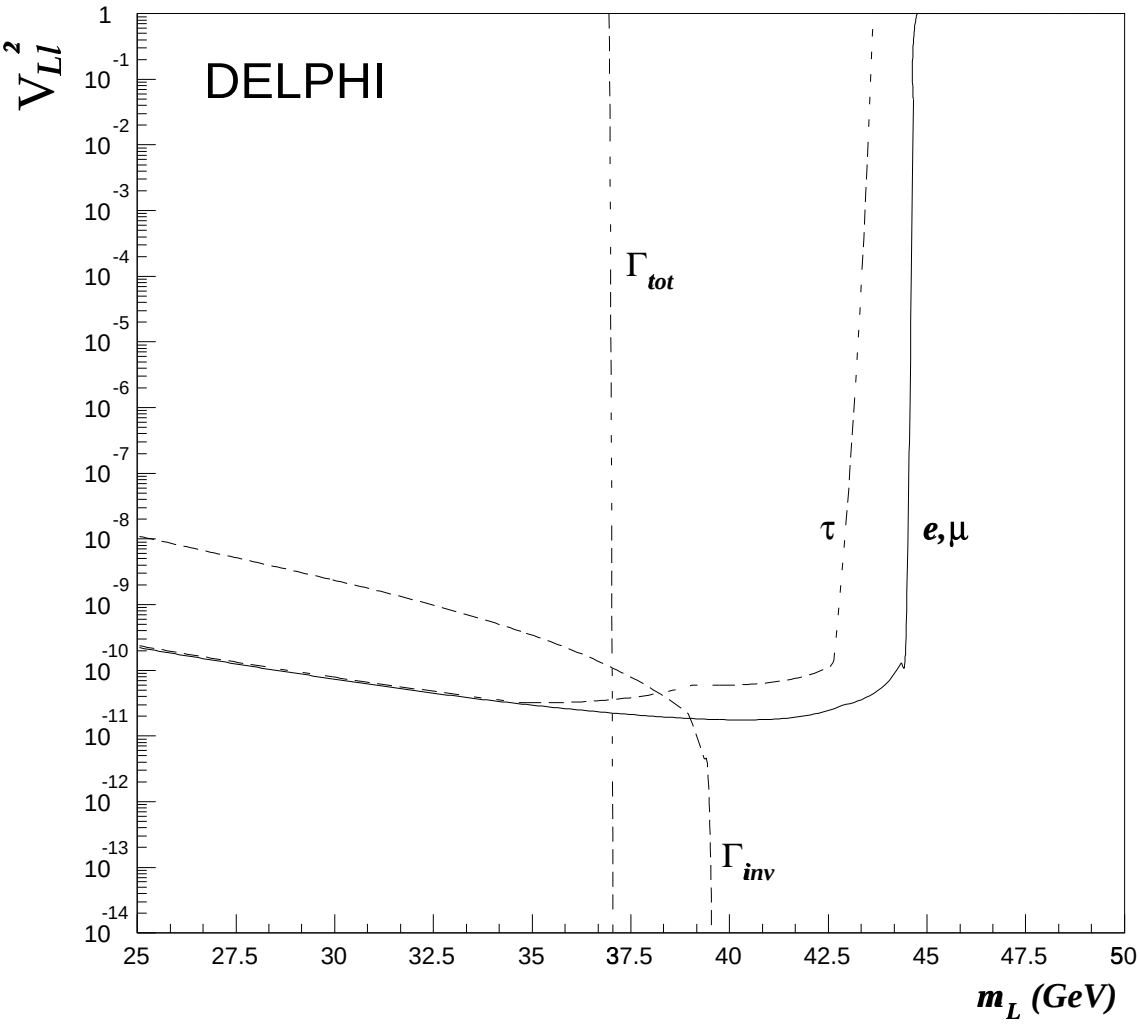

Figure 2.8: The 95% C.L. lower limit contours in the plane of m_{L^0} and $|V_{\mathrm{L}\ell}|^2$ for a Majorana case. The figure definitions are the same as in Fig. 2.7.

Chapter 3

Experimental Apparatus

This chapter describes the experimental apparatus used in this study. An overview of the accelerator, the LEP storage ring, is given in section 3.1. Section 3.2 describes the OPAL detector and its components critical to this study, followed by description of the data acquisition system in section 3.3.

3.1 LEP Storage Ring

The CERN Large Electron-Positron collider, known as LEP, is a storage ring designed to investigate e^+e^- collision at centre-of-mass energies up to 200 GeV. Electrons and positrons are stored in a ring-shaped vacuum chamber as several counter-rotating 'bunches', and collide at 'interaction points' where experiments observe the events.

3.1.1 Basic Design

Beam Energy

The design of the LEP electron-positron collider was motivated by a very clear physics target: direct investigation of the Standard Model of the electroweak interaction at the energy scale of its symmetry breaking. The collider is operated, in its first phase (LEP1), at the energy of the e^+e^- to Z^0 resonance, producing a large number of Z^0's. In the second phase (LEP2), the energy is raised above the threshold of the $e^+e^- \to W^+W^-$ process, which was achieved at $\sqrt{s} = 161$ GeV in July 1996. Before reaching the LEP2, the machine was operated at the intermediate energy points ($\sqrt{s} = 130$ and 136 GeV: LEP1.5 phase), starting in October 1995.

The maximum energy reached by an electron storage ring is limited by the energy loss due to the synchrotron radiation. For an electron of energy E_b running

in a circle of radius ρ, the radiation energy loss per turn is given by

$$U_0 = c_\gamma \frac{E_\mathrm{b}^4}{\rho}, \tag{3.1}$$

where

$$c_\gamma = \frac{4\pi}{3} \frac{r_\mathrm{e}}{(m_\mathrm{e}c^2)^3} = 8.85 \times 10^{-5}\,\mathrm{m/GeV^3}, \tag{3.2}$$

with r_e being the classical electron radius and m_e the mass of the electron. To maintain beams in the orbit, this energy loss must be compensated by the radio-frequency (RF) acceleration system. The radius of LEP was decided to be $\sim$3.5 km by the optimization between the available RF power and the building cost of the ring.

Luminosity

The second important parameter of a colliding-type accelerator is the luminosity $\mathcal{L}$. For a physical process of cross-section σ, the event rate is given by

$$\frac{\mathrm{dN}}{\mathrm{dt}} = \sigma\mathcal{L}. \tag{3.3}$$

In the case of a head-on collider like LEP, the luminosity is given by

$$\mathcal{L} = \frac{N_\mathrm{e} N_\mathrm{p} k_\mathrm{b} f_\mathrm{rev}}{4\pi\sigma_x^*\sigma_y^*}, \tag{3.4}$$

where N_e and N_p are the numbers of electrons and positrons per bunch respectively, k_b is the number of bunches per beam, and $\sigma_x^*\sigma_y^*$ is the cross-section of the bunches at the interaction point. It is obvious from equation (3.4) that better luminosity is attained by:

- increasing N_e and N_p, i.e., increasing the current per bunch,
- increasing the number of bunches k_b, and
- decreasing $\sigma_x^*\sigma_y^*$, i.e., focussing the beam to a smaller spot at the interaction point.

The design value of the initial beam current is 0.75 mA per bunch, which is limited by the *transverse-mode coupling instability* [24] of the bunches. When a bunch of particles circulate in a conductive cavity like the vacuum chamber of LEP, they generate high-frequency transverse electromagnetic field, often referred to as 'wake field'. The strength of the field depends on the *transverse mode coupling impedance* determined by the geometry and electrical property of the surrounding components, as well as on the bunch current and the transverse

spread of the particles. The wake field generated by the particles in the front part of the bunch excites the particles in the tail of the bunch. This results in increase of the transverse oscillation amplitude, and eventually loss of the particles.

Increasing the number of bunches introduce additional, and unwanted, interaction points where the bunches collide. It is necessary to equip those interaction points with beam separating devices, such as electrostatic plates, to avoid excessive beam-beam effect and faster loss of the beam intensity. Increase in the required RF power, beam instability caused by the coupling between adjacent bunches, and reduction of the data acquisition time allowed for the experimental detectors should also be considered. The number of bunches was chosen to be four until the autumn of 1992, when eight-bunch operation started.

The transverse size of the beam at an interaction point can be reduced using a pair of very strong superconducting quadrupole magnets. The magnets are called 'low-β quadrupoles' because they decrease the betatron amplitude β_y^* locally. The minimum beam size is limited by the spread in the focussing power due to the natural momentum spread of the beam. This effect, called 'tune spread' or 'chromaticity', can be corrected by a set of sextupoles; but the remaining higher-order effects still limits the minimum attainable β_y^*. The design value for the betatron amplitude at the interaction points is $\beta_y^* = 7.0\,\mathrm{cm}$.

The design luminosity of LEP with four bunches and 3 mA per beam is $1.6 \times 10^{31}\,\mathrm{cm}^{-2}\mathrm{s}^{-1}$ for each interaction point.

3.1.2 Structure and Components

The LEP storage ring consists of eight straight sections connected by the same number of curved sections. The circumference is 26.67 km. The ring is situated underground, in a tunnel of 3.8 m inner diameter, crossing the border between France and Switzerland near Geneva. The plane of the tunnel is inclined by 1.4% to ensure that it is contained in solid rock while keeping the depth of the access shafts less than 150 m. The average depth of the tunnel is about 100 m from the surface. In spite of the large scale of the construction, the actual LEP circumference has been measured to be accurate within 1 cm. There are eight major access points located in the middle of each straight sections, numbered clockwise from P1 to P8. Four even-numbered points are occupied by the experiments: L3, ALEPH, OPAL and DELPHI in this order.

Electrons and positrons are constrained in the vacuum chamber along the nominal orbit by the electromagnetic guide field system. The system consists of dipole, quadrupole and sextupole magnets, dipole correctors in horizontal and vertical directions, rotated quadrupoles, and electrostatic deflectors. Each of the eight curved sections are occupied by seven sets of standard cells consisting of two groups of six bending dipoles supplemented by two quadrupoles, two sextupoles and a horizontal and a vertical orbit correctors. The beams are bent by the dipole

field of about 0.1 T, which is unusually low as a circular accelerator in order to reduce the radiative energy loss. The quadrupoles produce alternating-gradient focussing, and the sextupoles are used to compensate the energy dependence of the focussing strength.

In the middle of the eight straight sections are the interaction points. Four of them are surrounded by solenoidal magnets used by the detectors of the experiments. As mentioned in the previous section, beams are focussed tightly at the interaction points by the strong quadrupole field generated by a set of superconducting magnets called 'low-β' magnets to obtain maximum luminosity. Typical transverse dimension of the beam at an interaction point is about $10\,\mu\mathrm{m} \times 250\,\mu\mathrm{m}$ in the vertical and horizontal plane respectively. The longitudinal dimension is typically $\sim$2 cm. In addition, a pair of quadrupole magnets rotated by 45° about their axes are installed around each solenoid, to compensate coupling effect introduced by the solenoid between horizontal and vertical betatron oscillations.

When LEP is operated with four bunches per beam, there are four more interaction points other than the four that are instrumented by experiments. It is important in view of the stability and the storage lifetime of the beam to keep them from colliding at the unwanted places. Four sets of electrostatic separators are installed to accomplish this by deflecting electrons and positrons in opposite directions. The beam instability caused by the electromagnetic force between colliding bunches is parametrized by the beam-beam strength parameter ξ_y, which varies inversely proportional to the third power of beam energy. The maximum current allowed by this instability (the beam-beam limit) is therefore much lower at lower energies, and letting beams collide at the injection energy, 20 GeV, permits the beam current of only $\sim$0.03 mA. Thus, the beams are separated by electrostatic separators also around experimental points during injection and energy ramping.

The number of bunches per beam has been increased from four to eight in the autumn of 1992. This change has introduced eight more interaction points in the middle of the curved sections, where the beams must be separated by some means. A new mode of operation called 'pretzel scheme' was adopted. In this scheme, horizontal modulation is given to the orbit of beams using additional electromagnetic separators installed in two straight sections around P2 and P6. The orbits of the electron and positron beams oscillate horizontally in opposite directions around the average orbit, and are separated from each other at the new interaction points.

It is very important for a storage ring to maintain high vacuum to minimise particle losses due to collisions with residual gas. The LEP vacuum chamber is also subject to severe heating coming from synchrotron radiation. In addition, it must be capable of effectively shielding the radiation to prevent damage caused to the materials of various equipments in the tunnel. The vacuum chamber is therefore made of aluminium covered with a lead cladding. The static pressure achieved without beams is 8×10^{-12} torr. It rises to $\sim 10^{-9}$ torr in the presense

of beams, due to gas desorption from the inner wall provoked by the radiation. With this level of vacuum, a typical LEP fill can last ∼12 hours before a refilling becomes necessary.

The energy lost by synchrotron radiation is replenished by the RF acceleration system. Initially, the RF system consisted of 128 RF cavities made of copper, powered by sixteen 1 MW klystrons. Each cavity has an effective length of 2.128 m and can produce peak accelerating field of 1.47 MeV/m. Total accelerating voltage at peak is therefore 400 MV per revolution. The system operates at a frequency of 352.21 MHz, which corresponds to 31 320 times the beam revolution frequency of LEP. During the shutdown between 1991 and 1992, eight of the cavities were removed to make room for electrostatic separators necessary for the eight-bunch 'pretzel scheme' operation. They were followed, between 1992 and 1993, by eight more cavities to install more separators.

At the beam energy of 50 GeV, the power absorbed by the full-intensity beams (3 mA per beam) is only 1.2 MW. With the conventional copper cavities, however, the power dissipated as heat in the cavities dominates the power consumption, resulting in the total required RF power of 16 MW. For the second phase of LEP, when the beam energy is raised to 90 GeV, the power consumption will reach 100 MW, while only 12 MW of it will be used by the beams. RF cavities made of superconducting material is developed to reduce power dissipation. Two modules of different designs, each containing four cavities, are currently installed at the straight sections around P2 and P6. Each cavity has an effective length of 1.7 m and is capable of handling accelerating field up to 6 MV/m. It is planned to install 46 more modules, making the total number of superconducting cavities 192. This will increase the total RF voltage to 2300 MV per revolution, which is sufficient to study e^+e^- collisions beyond the W^+W^- threshold.

3.1.3 Injectors

Electrons and positrons are injected into LEP from a chain of five accelerators: two linacs of 200 MeV and 600 MeV, a 600 MeV Electron-Positron Accumulator (EPA), and the CERN Proton Synchrotron (PS) and the CERN Super Proton Synchrotron (SPS) operating as 3.5 GeV and 20 GeV e^+e^- synchrotrons respectively. The existing CERN proton synchrotrons, the PS and the SPS, were modified to accelerate electrons and positrons to serve as the LEP injectors. When LEP is to be filled, the PS and the SPS operate in multicycle mode, using a supercycle in which four cycles of electron and positron acceleration take place followed by one cycle of protons. By this mode of operation, filling LEP has little effect on the other experiments that run parallel with LEP using the 450 GeV proton beam from the SPS.

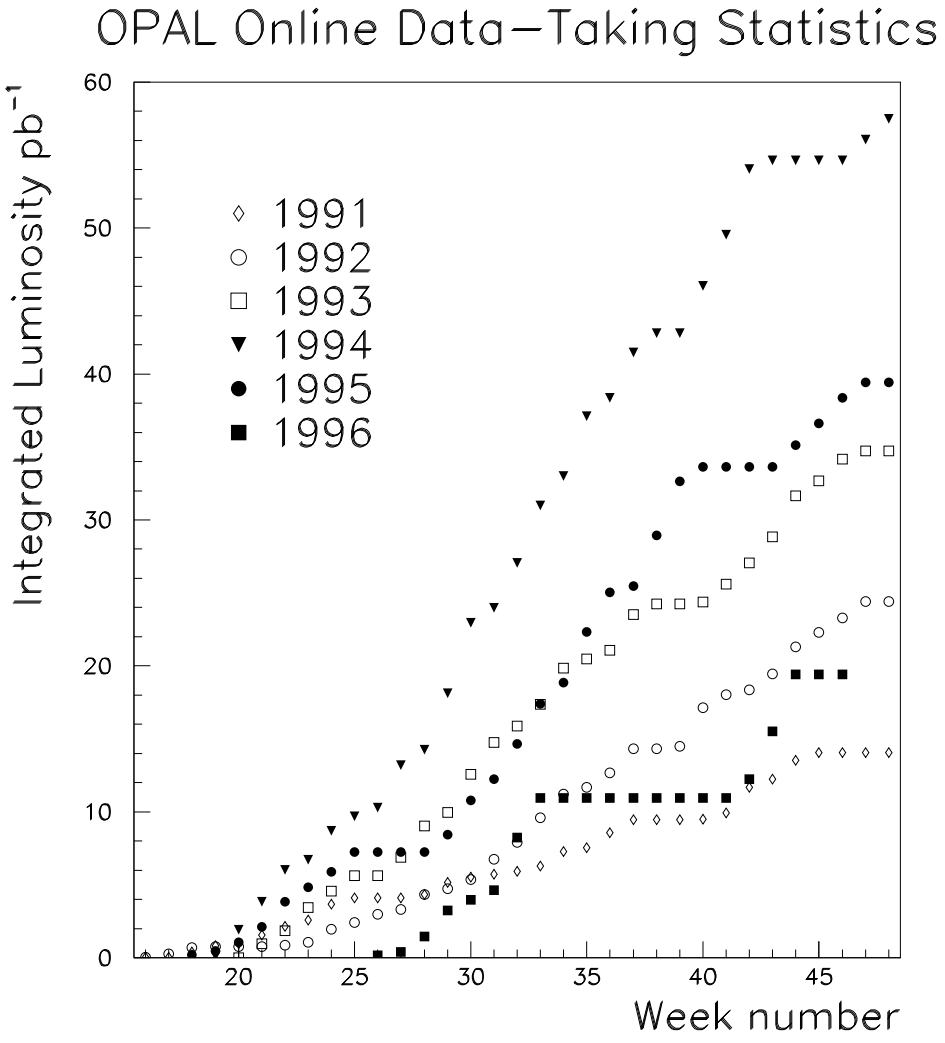

Figure 3.1: Integrated luminosities seen by experiments in 1990–1996

3.1.4 Operation and Performance

The first positron beam was injected into LEP on 14 July 1989. About one month later, first collisions were recorded on 13 August. Stable physics runs started on 20 September 1989. The LEP1.5 phase was started at 31 October 1995 and LEP2 was at 7 July 1996. Fig. 3.1 shows the evolution of integrated luminosity delivered to each experiment in each year since 1990.

Steady improvement in luminosity is clearly seen.

3.2 OPAL Detector

The OPAL detector [65, 67], one of the four large detectors installed at the LEP e^+e^- storage ring, is a multipurpose apparatus to detect decay products of Z^0's. In order to detect all types of visible events expected from e^+e^- collisions with high efficiency, and to classify them without ambiguity, the detector has been built to provide excellent measurement of charged particles and electromagnetic energies. The solid angle acceptance is very close to 4π, giving very accurate measurements of the total, leptonic, and hadronic cross-sections.

The main part of the detector consists of many subdetectors which can conveniently be classified into five elements:

- A central detector which measures the positions, directions and momenta of charged tracks as well as their energy losses in the filled gas.
- An electromagnetic calorimeter which identifies electrons and photons by measuring their energies.
- A hadron calorimeter which measures the energies of hadrons.
- A muon detector which identifies muons by measuring their positions and directions behind the hadron calorimeter.
- A forward detector which measures the luminosity by counting very forward Bhabha scattering events.

The whole detector surrounds the beam pipe with the centre of the detector at the nominal interaction point. Surrounding the central detector is a solenoidal coil which provides the detector with a uniform magnetic field of 0.435 T parallel to the beam. The iron return yoke of the magnet serves also as the absorption material of the hadron calorimeter. A schematic view of the general layout of the detector is shown in Fig. 3.2 The abbreviations of the OPAL subdetector is summarized in Appendix A. Fig. 3.3 shows cross-sections of the detector by the x-y and z-x planes.

The coordinate system used in describing the OPAL detector is a right-handed Cartesian system defined as follows:

- The origin is at the nominal interaction point.
- The z axis lies along the nominal direction of the electron beam.
- The x axis points horizontally towards the centre of LEP.
- The y axis is normal to the z-x plane.

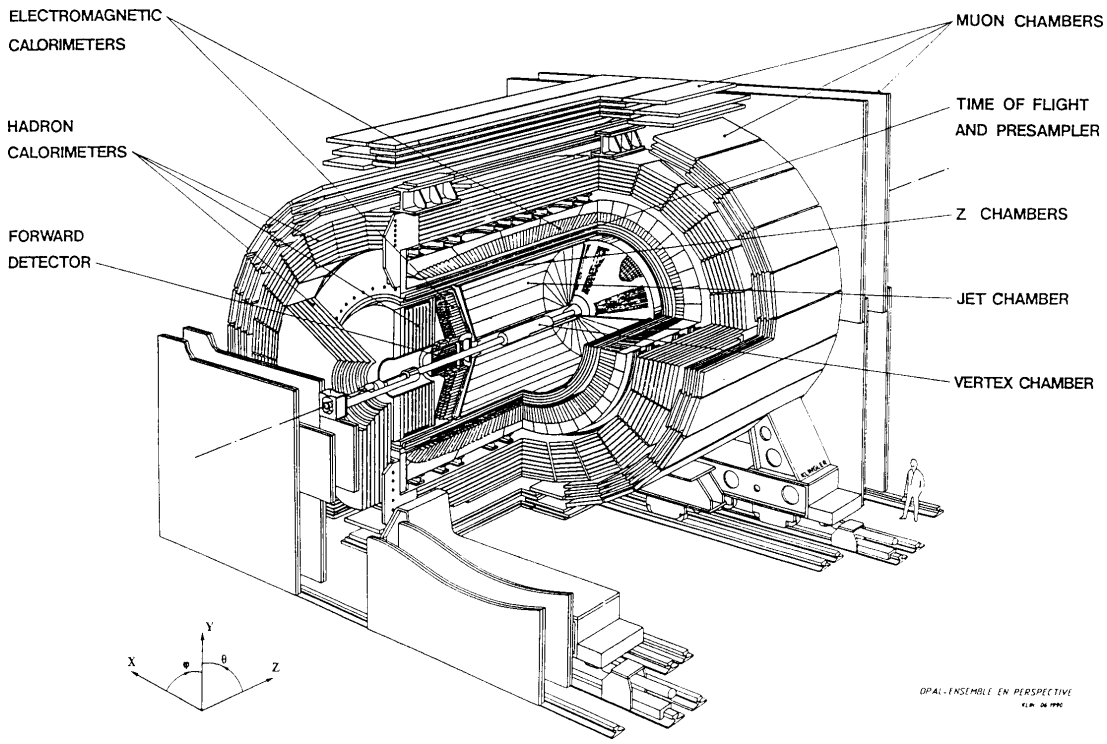

Figure 3.2: Schematic view of the OPAL detector

The electron beam runs counter-clockwise in LEP when viewed from above. The direction of the beam is inclined by 13.9 mrad with respect to the horizontal at the centre of OPAL, so is the OPAL z axis. As a consequence, the y axis is also inclined with respect to the vertical. The polar angle θ is measured from the z axis, and the azimuthal angle ϕ from the x axis.

Each part of the detector is described in more detail, from inside to outside, in the following sections.

3.2.1 Beam Pipe

The beam pipe runs through the OPAL detector at an angle of 13.9 mrad with respect to the horizontal. As it constitutes a part of the vacuum chamber of LEP, the beam pipe must be able to keep a high level of vacuum inside while coping with the 4 bar outside gas pressure needed by the central detector. The material of the beam pipe should have good transparency in terms of the radiation length. Employment of light, high-strength material is essential to fulfil the conflicting requirements.

In the initial installation, a carbon fibre composite construction was chosen. The radius of the beam pipe should be as small as permitted by the background consideration. The actual inner radius was chosen to be 78 mm. The pipe was

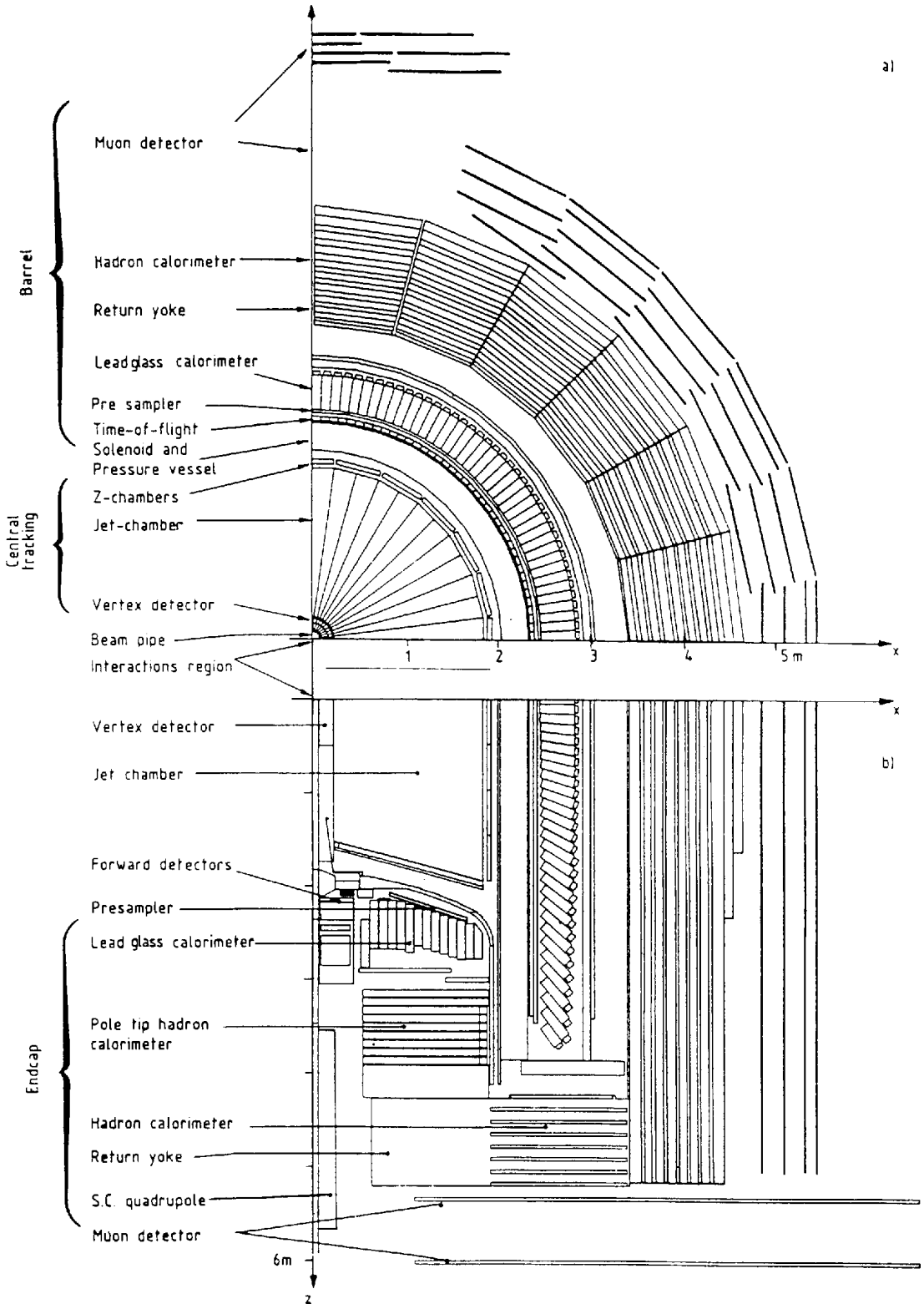

Figure 3.3: Cross-sections of a quadrant of the OPAL detector (a) perpendicular to the beam and (b) parallel to the beam

made by applying overlapping layers of epoxy-dipped carbon fibre onto a 0.1 mm thick aluminium tube. The total thickness of the carbon fibre layer was 1.3 mm, which corresponds to 0.55% of a radiation length. The aluminium inner skin, which amounted to additional 0.11% radiation length, was necessary to provide a continuous conductive surface seen by the LEP beams. This is important to decrease the transverse mode coupling impedance which limits the maximum beam current per bunch. The aluminium also provided electromagnetic shielding for the detector and a vacuum tight surface with minimum outgassing.

An upgrade of the beam pipe was made during the LEP shutdown period between 1990 and 1991. The new pipe consists of two coaxial tubes: an inner tube made of 1.1 mm thick beryllium, and an outer of 2 mm thick carbon fibre epoxy composite. The beryllium inner pipe, with a minimum inner radius of 53 mm, serves as a part of the vacuum chamber of LEP. The outer pipe has an 80 mm inner radius and holds the 4 bar absolute gas pressure of the surrounding central detector. The space between two pipes is used by the silicon microvertex detector. The amount of the material of the new beam pipe is about 1.16% of a radiation length: a 0.31% due to the beryllium pipe in addition to a 0.85% due to the carbon fibre pipe.

3.2.2 Central Detector

The central detector is the innermost part of the OPAL detector. The primary function of the central detector is to measure positions, directions and momenta of passing tracks. The ionization losses of the tracks are also measured. The central detector consists of four subdetectors:

- A silicon microvertex detector which measures the position and the direction of the track with very high accuracy at small radii. Its main function is to locate decay vertices of short-lived particles.

- A vertex detector which measures the position and the direction of the track with high accuracy. It occupies the space between the beam pipe and the jet chamber and improves the spatial and momentum resolution. It also helps to connect reconstructed track segments between the microvertex detector and the jet chamber.

- A jet chamber which measures the position, direction and the energy loss of the track. It provides most of the momentum resolution of the central detector and particle identification.

- A set of z-chambers which measure the position and the direction of the track, especially in z, at large radii. It surrounds the jet chamber and improves the θ angle resolution.

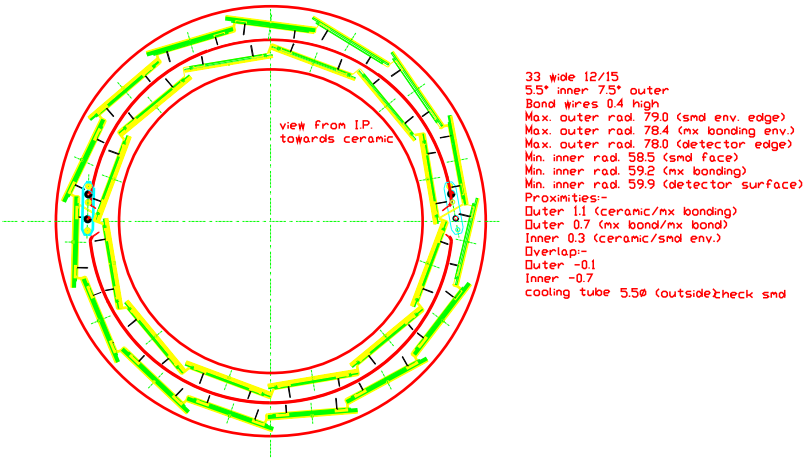

Figure 3.4: Layout of the silicon microvertex detector in the r-ϕ plane

The detectors are held inside a pressure vessel which keeps them under a pressure of 4 bar. The pressure vessel has a cylindrical structure with its ends closed by bell-shaped covers (pressure bells). An axial magnetic field of 0.435 T, which is nearly uniform within the volume of the central detector, is supplied by a solenoidal magnet surrounding the pressure vessel.

Silicon Microvertex Detector

The silicon microvertex detector (SI) [28] was installed between 1990 and 1991, and became operational in the middle of 1991. Fig. 3.4 shows the layout of the detector in the r-ϕ plane. In 1993 an upgraded detector was installed that had $r-\phi$ and $r-z$ wafers glued back to back. For 1995, the detector was further upgraded. The number of ladders was increased to 12 and 15 and the ladders tilted to close ϕ gaps. The outer layer was also extended from 3 to 5 wafers by the addition of a layer of 2 wafer ladders at the $-z$ end. The interaction point was still at the centre of the 3 ladder detector. In 1996, 2 wafer ladders were added to the inner layer as well so for 1996 onwards, both layers contained of 3 wafer plus 2 wafer ladders with interaction point in the centre of the five wafers. The detector consists of two cylindrical layers of single-sided silicon microstrip detectors situated between the two coaxial beam pipes. The radii of the two layers of the detector are 60 and 78 mm. The inner layer of the detector covers a polar angle range of $|\cos\theta| < 0.83$. The amount of material traversed by a track at $\cos\theta = 90°$ corresponds to 0.6% of a radiation length. The inner layer is made up of 12 rectangular structures called 'ladders', and the outer of 15. The overlap region in the r-ϕ plane is 0.1° for outer ladders and 0.7° for inner ladders. Each

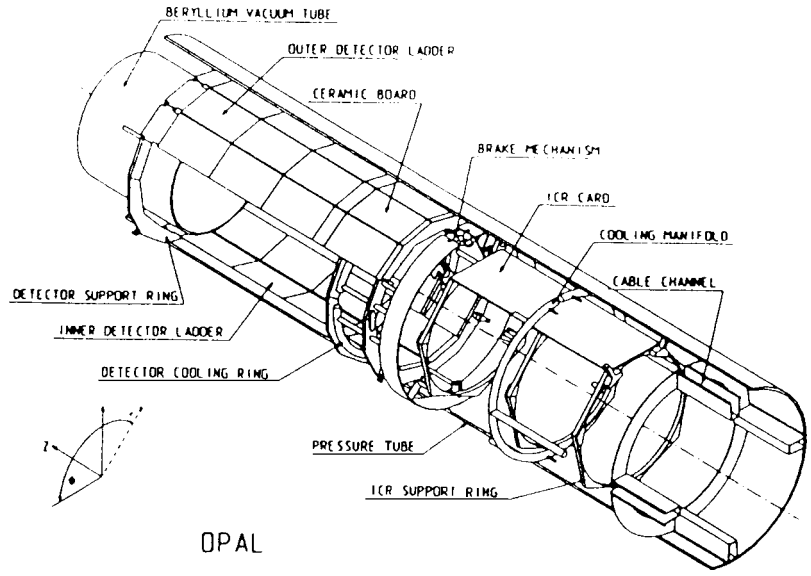

Figure 3.5: Schematic view of the silicon microvertex detector

ladder carries three silicon microstrip detectors daisy-chained together. Fig. 3.5 shows a schematic view of the detector.

The microstrip detectors were developed in collaboration with Micron Semiconductor Ltd. A new 'FoxFET' biasing scheme enabled tuning of the dynamic bias resistance for optimum signal-to-noise performance while being simple to fabricate. Each detector has an active area of 33 mm × 60 mm. The thickness of the the high-resistivity n^- substrate is 300 μm. Narrow strips of p^+ implant run on the substrate parallel to its longer side in 25 μm pitch. Every second strip is read out through capacitive coupling to an aluminium strip running above an oxide insulation layer. The number of readout strips is 629 per detector. The position of a passing track is determined with an intrinsic resolution of 6 μm using the charge division between adjacent strips. The Z readout strips are positionned every 100 microns, while the Phi readout strips are at a 50 micron pitch. Notice in the picture that the Phi type strips are directly daisy chained. The Z type strips are also daisy chained, by using a conductor called a Z Print.

Fig. 3.6 shows the structure of a ladder and its readout components. Three microvertex detectors are positioned end-to-end and glued onto a 0.5 mm thick epoxy-Kevlar composite plate. The expansion coefficient of the plate is 7 ppm/°C, while that of silicon is 3 ppm/°C. The 629 readout channels are daisy-chained by aluminium wire bondings, and are connected to five MX7 Microplex chips [76] through a pitch-adjusting glass adaptor.

The readout is done using the MX7 Chip. This chip is approximately .7 cm on a side and contains 128 separate channels using analog amplifiers and shift registers. The inputs are spaced 47 microns apart - connections are made using wire bonding technology. Each side of a ladder is readout by five MX7 chips,

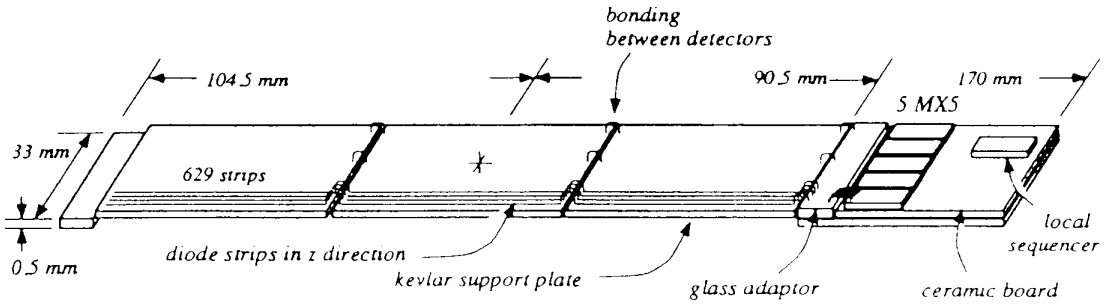

Figure 3.6: Assembly of a silicon microvertex detector ladder

each set of which is controlled by a local sequencer (shown in the picture) which coordinates the action of over 600 readout channels on each side of every ladder. These local electronics are mounted on a Beryllium oxide subtrate which is used for its excellent thermal conduction properties.

Twenty-five ladders are mounted on three split polygonal aluminium rings to form the complete detector as shown in figure 3.5. One of the rings that positions closest to the readout MX7 chips is equipped with a water cooling circuit to carry off the heat from the 256 mW power dissipation per chip. The readout end of the detector is equipped with a brake mechanism, followed by the interconnect ring (ICR) assembly which carries additional electronics, busses and connectors. The aluminium cable channels are also shown in the figure.

Vertex Detector

The vertex detector (CV) [44] is a small cylindrical drift chamber using a jet-type cell geometry. The chamber is 1 m long and has an outer radius of 235 mm. It is divided into two layers, each consisting of 36 small sectors. Each sector in the inner, or axial, layer has a plane of twelve sense wires strung parallel to the beam direction, at radii ranging from 103 to 162 mm. In the outer, or stereo, layer, each sector includes six sense wires inclined by an angle of $\sim 4^\circ$ to allow measurement of the z coordinate. The radial positions of the stereo wires range between 188 and 213 mm. The maximum drift distance is 14 mm.

Fig. 3.7 shows a schematic view of the vertex chamber. The wires are strung between two 32 mm thick end plates made of glass fibre epoxy composite. A 1.5 mm thick carbon fibre tube forms the outer shell of the detector and holds the end plates at a distance of 1 m from each other. At the inner radius, 88 mm, of the detector is a cylinder of thin aluminised mylar which defines the separated gas volume of the chamber from other parts of the central detector. The sense wires are read out from both ends. The preamplifiers and the high voltage distribution components are placed on the end plates. They are cased in gas-tight aluminium cylinders attached to the ends of the chamber as extensions of the gas volume.

Fig. 3.8 shows the layout of the wires at one of the end plates. Each anode

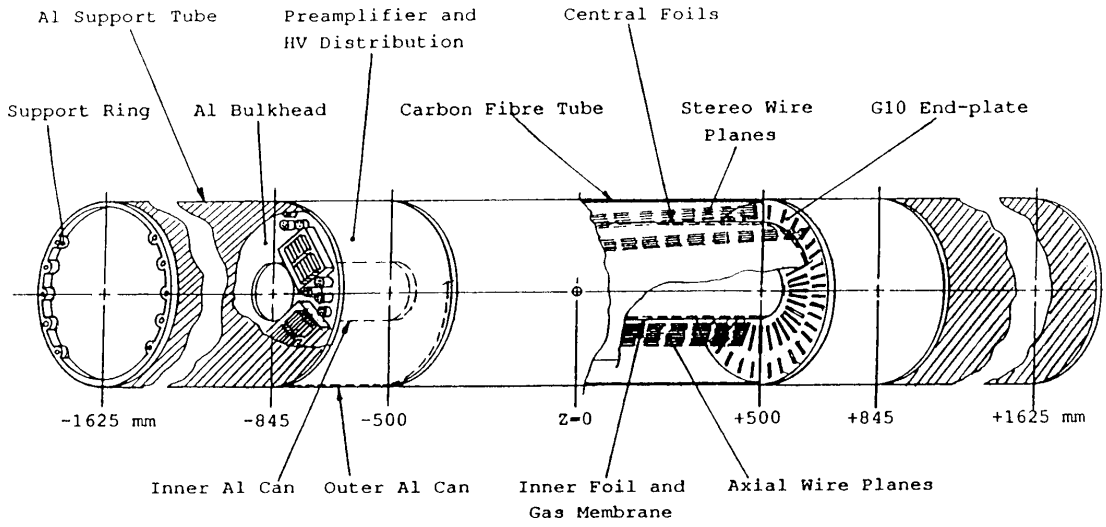

Figure 3.7: Schematic view of the vertex chamber

plane consists of 20 μm diameter anode wires and 200 μm diameter potential wires alternating each other. The anode wires are offset by 41 μm from the wire plane in alternating directions to resolve left-right ambiguity. The displacement of the anode wires increase by 50–100 μm when the operating high-voltage is applied to the chamber. The chamber works with the anode wires at ground potential. Register networks mounted on the chamber supplies the cathode and potential wires with appropriate voltage which determines the gas gain and the drift field.

The signals from the both ends of the anode wires are fed into preamplifiers followed by a crosstalk-cancelling network. The timing of each pulse is found by a constant fraction discriminator. The circuit is capable of handling multiple hits. The r-ϕ position of a track is measured by the drift time sensed by the axial wires. Good spatial resolution, $\sigma \approx 50\,\mu$m, is obtained by the use of the 4 bar gas pressure and the short drift distance. The z position is measured by combining the information from axial and stereo wires. In addition, a fast, but course measurement of the z position is given by the time difference between signals seen at either end of the wires. This information is used by the trigger system and the pattern recognition program.

Since the resolution for the track nearest to a wire plane is better than that for the rest of the tracks, the signal that arrived to a wire first is often referred to as the 'first hit', and other signals are collectively called 'second hits'.

Jet Chamber

The jet chamber (CJ) [41, 51, 56] is a large cylindrical drift chamber filling most of the volume of the central detector. It has a length of 4 m with outer and inner radii of 1850 mm and 250 mm respectively. The chamber consists of 24 radial

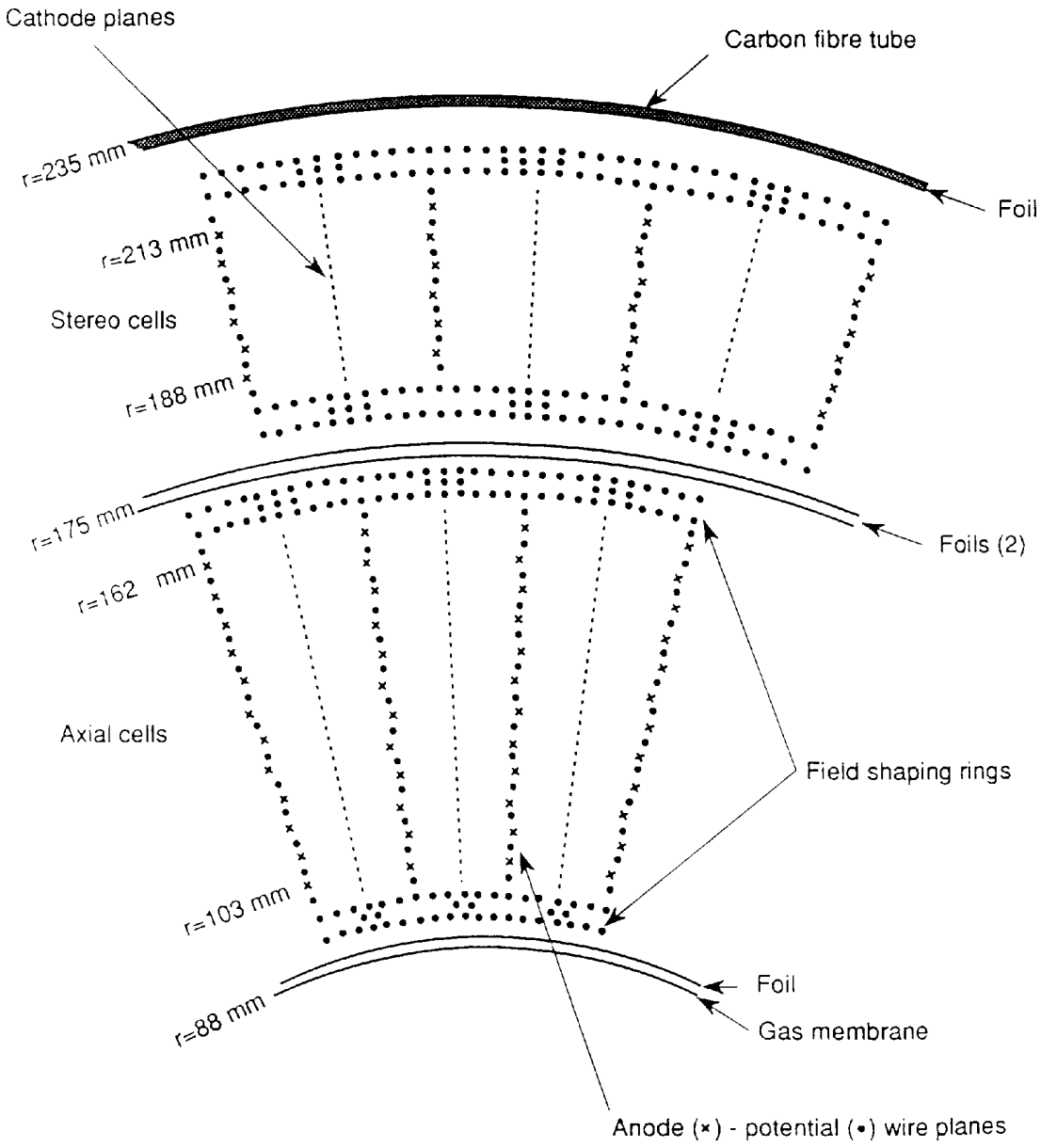

Figure 3.8: Wire layout of the vertex chamber at one end plate

sectors, in the centre of which is a plane of 159 sense wires strung parallel to the beam direction. The maximum drift length is 3 cm at the innermost sense wire, and is 25 cm at the outermost. Tracks in the range of $|\cos\theta| < 0.73$ are measured at 159 points. At least 8 points are measured for tracks in 98% of the full solid angle. The track position in the r-ϕ plane is obtained by the measurement of the drift time. The ratio of the charge measured at each end of the wires provides the measurement of the z coordinate. The energy loss, dE/dx, of the track is given by the sum of the measured charge [55].

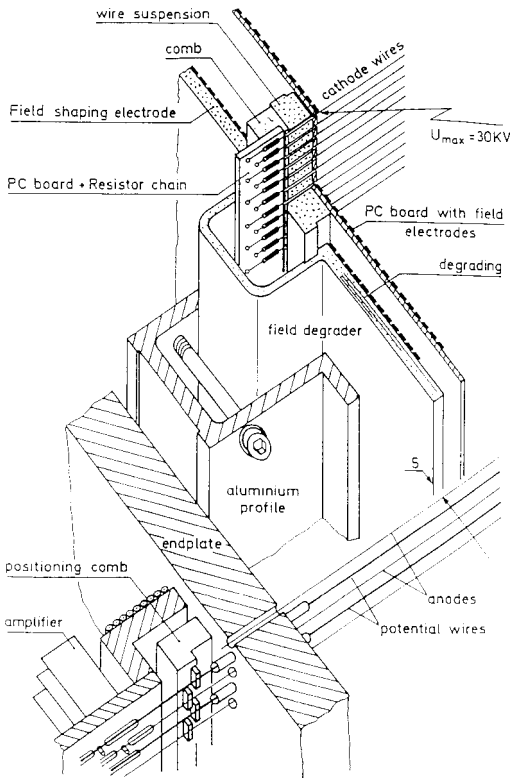

Figure 3.9: Wire support structure of the jet chamber

Each sector is separated from the adjacent one with a radial plane of cathode wires on each side. In the middle of each sector is an anode plane. The signal wires are positioned at radii between 255 mm and 1835 mm with a 10 mm spacing, alternating with potential wires. The signal wires are staggered alternately by $\pm 100\,\mu$m to resolve left-right ambiguity. The gas gain is determined by the voltage of the potential wires, normally set to -2.38 kV, while the signal wires are working at ground potential. The cathode wires are supplied with varying high voltage by a resistor network to provide uniform electric field in the drift region. The maximum cathode voltage is about -25 kV. The drift field is terminated by a field cage of wires, a foil and field shaping electrodes at the boundaries that are not covered by the cathode wires.

Wires are strung between two conical end plates made of aluminium. The end plates are held apart by 24 hollow aluminium panels at the outer radius of the chamber. Fig. 3.9 shows a perspective view of the wire support structure at the end plates. The signal and potential wires run through holes in the end plate, positioned by accurately machined combs, and connected to the read out circuits or the high-voltage distribution network. The cathode wires are supported by aluminium profiles running inside of the end plate, which also supports printed-circuit boards with the field shaping electrodes and the resistor network.

The signal wires are read out at both ends. A resistor network is used to compensate capacitive crosstalk between neighbouring wires. The signals are fed into the preamplifiers mounted on the end plates, then sent to 100 MHz flash analogue-to-digital converters (FADCs). This allows recognition of multiple hits with good timing and double-hit resolution. The FADCs have a 6-bit resolution extended effectively to 8-bit using a nonlinear response function.

For a long drift length chamber like the OPAL jet chamber, it is of critical importance to keep the drift velocity under good control. The gas gain should also be monitored to maintain good resolution of the energy loss measurement. The chamber gas used is a three-component mixture of 88.2% argon, 9.8% methane and 2.0% isobutane. A closed system with recirculation and purification is employed to achieve stable mixture and to eliminate oxygen contamination to a level of a few ppm. A small fraction of water vapour, (500 ± 50) ppm, is added for the benefit of the chamber lifetime. A calibration system [40] based on a Nd-Yag laser is used to monitor the drift velocity and the gas gain. The chamber is illuminated with a pair of parallel beams split by a dielectric beam splitter. The time separation between the two signal generated by the beams with precisely known distance gives a measurement of the drift velocity with an accuracy of 0.1%.

Fig. 3.10 shows the intrinsic coordinate resolution in the r-ϕ plane obtained from the data. The average resolution is 135 μm. The resolution of the z measurement, obtained from charge division, is about 6 cm. The resolution of the momentum component transverse to the beam, p_{xy}, is $\sigma_{p_{xy}}/p_{xy} = 1.5 \times 10^{-3} p_{xy}$ for p_{xy} in GeV/c for muon tracks in the $e^+e^- \to \mu^+\mu^-$ events. For tracks with less than 159 hits, the resolution follows Gluckstern form [53] as

$$\sigma_{p_{xy}}/p_{xy} = 6.94 \times 10^{-4} \sqrt{\frac{720}{N_{\mathrm{CJ}} + 4}},$$

where N_{CJ} is the number of hits.

For each hit associated to a track, a measurement of the energy loss dE/dx is obtained by the sum of the integrated charge seen at the both ends of the wire. A truncated mean of the measured energy loss is calculated for each track rejecting 30% of the largest hits. Fig. 3.11 shows the distribution of the measured dE/dx as a function of the momentum p for tracks in a sample of multihadron events and of $e^+e^- \to \mu^+\mu^-$ events. The resolution for tracks in $e^+e^- \to \mu^+\mu^-$ events with at least 139 samples is $\sigma_{\mathrm{dE/dx}}/(\mathrm{dE/dx}) = 3.8\%$.

The number of hits actually used for the measurement of the position and momentum of a track, N_{CJ}, is usually smaller than 159 due to a few reasons: signals can be too small to be recognised by the hit finding program; signals are rejected if they are too close to any of the wires to avoid local distortion of the drift field; signals are also rejected if they are too close to the adjacent hits from neighbouring tracks to avoid pile-up effect. It is also possible that a track crosses the cathode plane in the chamber volume, resulting in the different

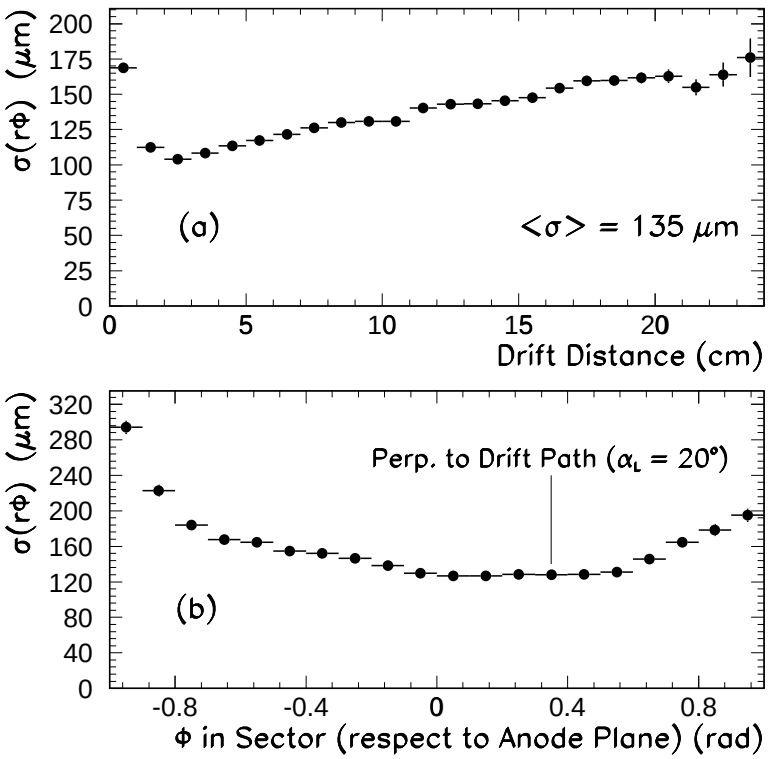

Figure 3.10: Spatial resolution of the jet chamber in the r-ϕ plane as a function of (a) drift distance, and (b) local ϕ angle of the track with respect to the anode wire plane

number of wires reachable by the drifting electrons depending on the Lorentz angle. Once the track is recognised and the position is determined, small hits can also be used in the measurement of dE/dx since the position of the hit is known. In the calculation of dE/dx, however, the hits must satisfy tighter criterion in terms of the closeness to the nearest neighbour, to ensure the measurement is not degraded by the crosstalk effect. This usually results in smaller number of hits used in the dE/dx measurement, N_{DX}, than N_{CJ}.

Crosstalk occurs not only between signals from nearby tracks, but also between signals from one track on different wires. Even after the crosstalk cancellation using the resistor network, inductive coupling between parallel wires causes a non-negligible amount of crosstalk. The effect of this crosstalk is discussed in the later chapter.

Z-Chambers

The z-chambers (CZ) [61] are a set of thin drift chambers which provides a precise measurement of the z coordinate of tracks as they leave the jet chamber. They consist of a layer of 24 drift chambers with 4 m length and 0.5 m width, ar-

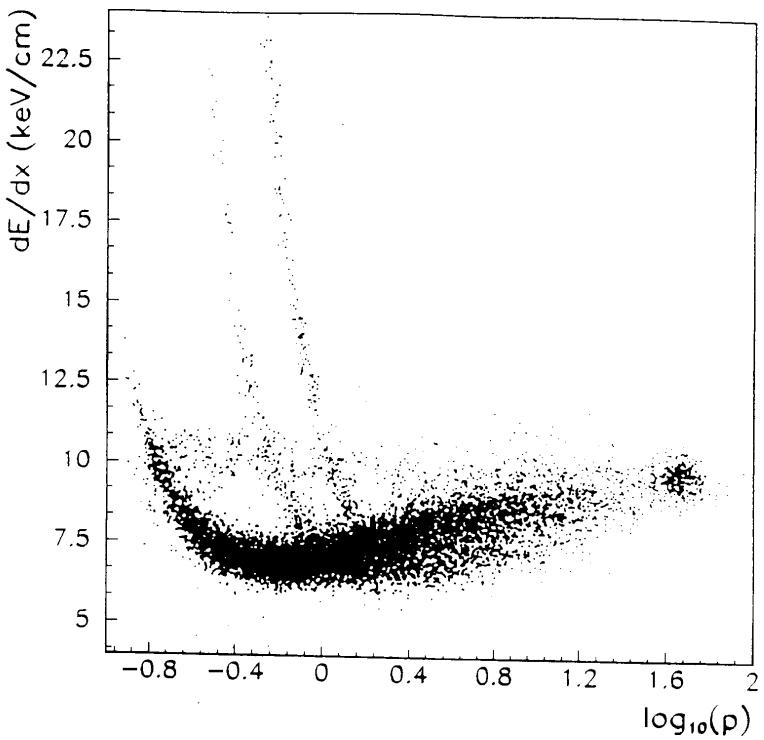

Figure 3.11: Energy loss measured in the jet chamber

ranged to form a barrel. The thickness of the chambers is 59 mm. The chambers cover 94% of the azimuthal angle within the polar angle range $|\cos\theta| < 0.72$.

Each chamber is divided in z into eight cells, each covering 50 cm × 50 cm. Fig 3.12 shows a cross-section of a cell. In the middle of each cell is a plane of six sense wires strung in the ϕ direction. The maximum drift distance is 25 cm in the z direction. The sense wires are positioned with 4 mm spacing, staggered by ±250 mm to resolve left-right ambiguity. Two planes of wire grids isolate the sense wires from the drift region, ensuring a linear time-to-position relationship.

Each sense wire is implemented with two amplifiers at both ends. Signals are multiplexed and fed into FADCs, allowing recognition of multiple hits within jets. The intrinsic z resolution is better than 100 μm for the shortest drift length, to 200 μm for the longest. Installed in the OPAL detector, a θ angle resolution of 3 mrad is obtained. The resolution in ϕ, obtained using the charge division, is about 1.5 cm.

3.2.3 Magnet

The magnet consists of a solenoidal coil surrounding the central detector and an iron return yoke. Since the coil is inside of the electromagnetic calorimeter, it is important for it to be transparent to the passing electrons and photons in terms of the radiation length. The coil is therefore made as an aluminium self-supporting

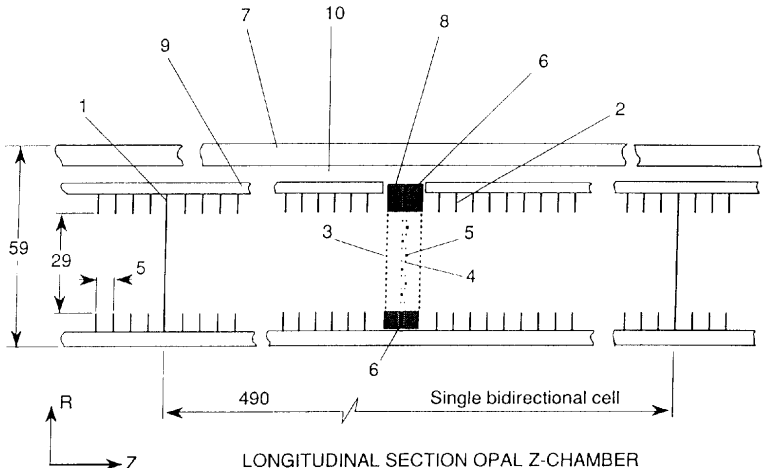

Figure 3.12: Cross-section of a z-chamber cell. The numbered elements are: (1) cathode (2) drift field electrodes (3) grid wires (4) guard wires (5) anode wires (6) inner electrodes (7) Lexan box and cover (8) G10 anode module (9) HV distribution board (10) space for electronic components. The stagger of the anode wires are exaggerated. All dimensions are in mm

water-cooled solenoid, thus eliminating the need of a coil-supporting structure. The amount of material corresponds to $1.7X_0$. The coil is wound as a single long unit without interruption instead of being divided into shorter sections. This construction, though it is more difficult to build, provides less stray field around the solenoid where photomultipliers are used. The magnetic field in the central detector volume is 0.435 T and is measured to be uniform within $\pm 0.5\%$. The design parameters of the magnet is summarized in table 3.1.

The return yoke is made of soft iron plates. It consists of five parts: a central part, two side-barrel parts called 'C's, and two pole tips. Fig. 3.13 shows an isometric view of the magnet in the open position where the return yoke is

Table 3.1: Parameters of the magnet

Central field	0.435 T
Mean coil diameter	4.36 m
Distance between pole faces	6.3 m
Solenoid thickness	96 mm Al + 54 mm glass epoxy
Maximum current	7000 A
Maximum power	5 MW
Coil weight	25 t
Barrel return yoke thickness	0.8–1.0 m
Overall magnet weight	2800 t

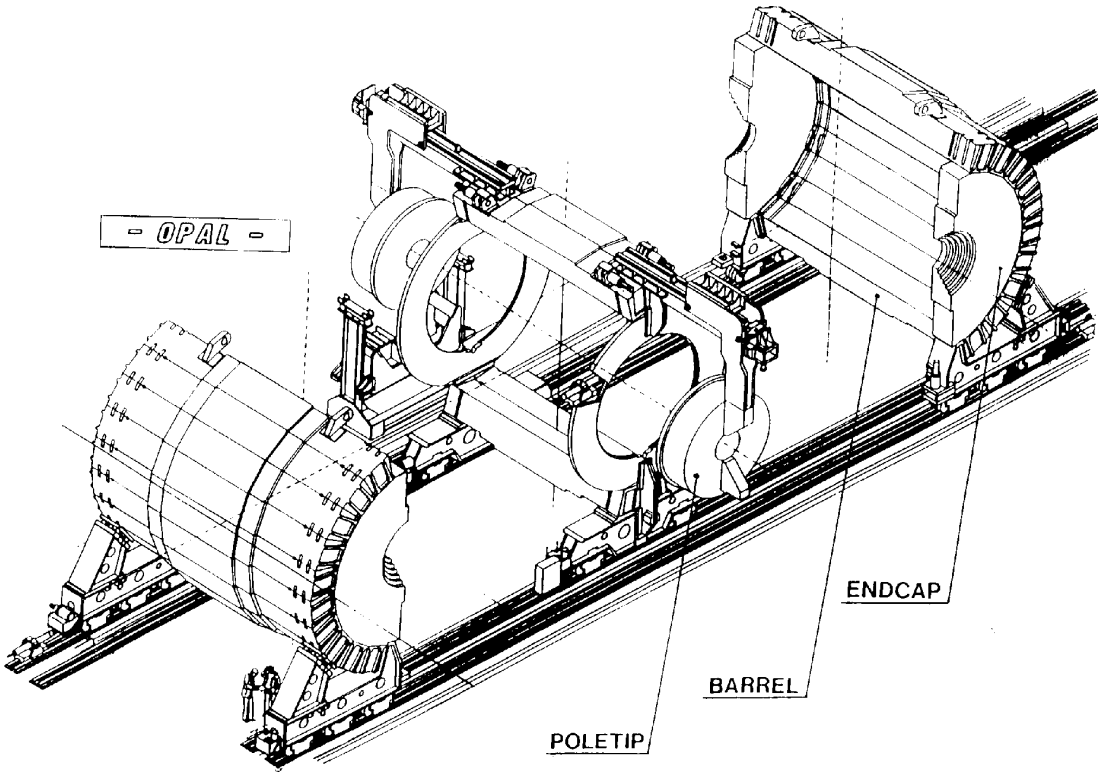

Figure 3.13: Isometric view of the magnet in the open position

disassembled for accesses to the detectors inside.

3.2.4 Electromagnetic Calorimeter

The electromagnetic calorimeter provides detection and identification of electrons and photons. The main component is a lead glass total absorption calorimeter split into a barrel and two endcap arrays. Lead glass was chosen because of its excellent intrinsic energy resolution, linearity, spatial resolution, granularity, electron-hadron discrimination, hermeticity and gain stability. In front of the lead glass, there are $\sim 2.1\, X_0$ of material mainly due to the coil and the pressure bell of the central detector. Consequently, most electromagnetic showers start developing before entering the lead glass. Presampling detectors, which are also split into a barrel and two endcaps, are installed in front of the lead glass to improve the energy and spatial resolution by measuring the position and multiplicity of the shower. In front of the barrel presampler is a time-of-flight detector to provide additional particle identification and fast trigger signals.

Fig. 3.14 shows the profile of the total number of radiation length at a typical ϕ, in front of and inside the electromagnetic calorimeter as a function of $|\cos\theta|$. The peaks in the material in front of the calorimeter around $|\cos\theta| = 0.8$ and 0.96 are due to the structure of the pressure vessel of the central detector.

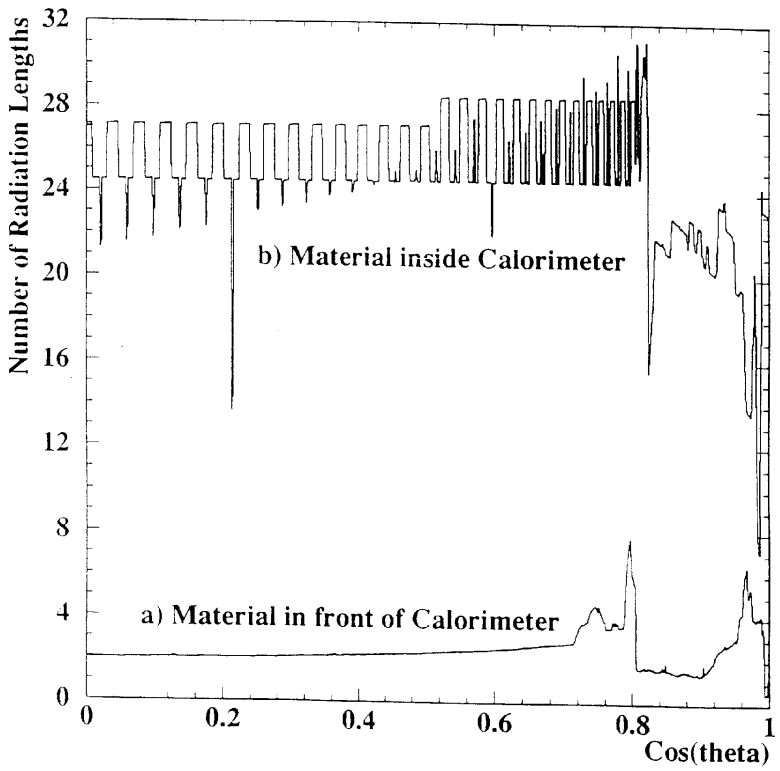

Figure 3.14: Radiation lengths in front of and inside the electromagnetic calorimeter

The structures in the material inside the calorimeter near $|\cos\theta| = 0.8$ and 0.975 arise from the barrel-to-endcap and endcap-to-forward calorimeter transitions. The repetitive structure seen in the calorimeter material for $|\cos\theta| < 0.8$ arises from the geometry of the barrel lead glass counters described later.

Time-of-Flight Counters

The time-of-flight counters (TB), installed at a mean radius of 2.36 m, covers an acceptance of $|\cos\theta| < 0.82$. It provides fast trigger signals and allows identification of charged particles in the momentum range of 0.6 to 2.5 GeV/c. They also contribute to the rejection of cosmic rays.

The system consists of 160 scintillation counters forming a barrel surrounding the OPAL solenoid. The counters have a length of 6.84 m and a trapezoidal cross-section, 45 mm thick and 89 to 91 mm wide. The maximum gap between adjacent counters is 2.6 mm. The scintillation light is collected at both ends by a pair of phototubes through 300 mm long Plexiglas light guides. The Signal from each phototube is split into two; one is digitized by a 12-bit charge integrating ADC, the other goes to a constant fraction discriminator. The output from the discriminator is sent to an 11-bit, 50 ps/count TDC, as well as a meantimer which

generates a fast trigger signal. A calibration system with a pulsed nitrogen laser is used to monitor the response of the counters and the associated electronics.

The timing resolution of the counters, measured using $e^+e^- \to \mu^+\mu^-$ events, is 460 ps. The z resolution is measured to be 7.5 cm by comparing the measured z coordinate with that of the barrel electromagnetic calorimeter.

Barrel Electromagnetic Presampler

The barrel electromagnetic presamplers (PB) consists of 16 chambers forming a 6623 mm long cylinder at a radius of 2388 mm. The polar angle acceptance is $|\cos\theta| < 0.81$. Fig. 3.15 shows the structure of the detector. Each chamber consists of two layers of limited streamer mode tubes with the anode wires running in the z direction. Each layer of a chamber has four units of 24 cells made of PVC extrusions. Each cell has an internal size of 9.6 mm square and separated from the adjacent cells by 1 mm thick walls. The inner surfaces of the cells are coated with graphite to have a surface resistivity of $\sim$1 MΩ/square. The anode wires are 75 μm diameter stainless steel. The chambers operates with a gas mixture of 32% n-pentane and 68% CO_2. High voltage is applied to the resistive cathodes with the anode wire at ground potential.

On both side of each layer of tubes are 1 cm wide cathode strips running at $\pm 45°$ to the wire direction. The position of hits are measured by reading these strips using charge sensitive amplifiers. The signals are multiplexed and digitized by two sets of 12-bit ADCs for high- and low-gain measurement. The amounts of charge collected at each end of the wire also provide a measurement of the z coordinate by the charge division.

In a beam test performed prior to the installation, a position resolution of 1–2 mm was obtained for single charged particles. The resolution for electromagnetic showers after 2.1 radiation lengths of material varies from 6 to 4 mm as the energy of the incident electrons changes from 6 to 50 GeV. The resolution in z obtained by the charge division of anode signals is $\sim$10 cm.

Barrel Lead Glass Calorimeter

The barrel lead glass calorimeter (EB) is a cylindrical array of 9440 lead glass blocks surrounding the magnet coil and the barrel presamplers at a radius of 2455 mm. It covers a polar angle range of $|\cos\theta| < 0.82$. Each block has a depth of 37 cm, corresponding to $24.6X_0$. The area of the top surface is about $10 \times 10\,\mathrm{cm}^2$.

The calorimeter is segmented into 59×160 blocks in z and ϕ respectively. The blocks are arranged in a nearly-pointing geometry shown in figure 3.16. The longitudinal axis of each block points at the interaction region with slight offset. This geometry ensures that particles coming from the interaction region usually traverse only one block, while keeping them from escaping in the gaps between the blocks. In the z direction, each block points to different z positions ($|z| = 55.5$–

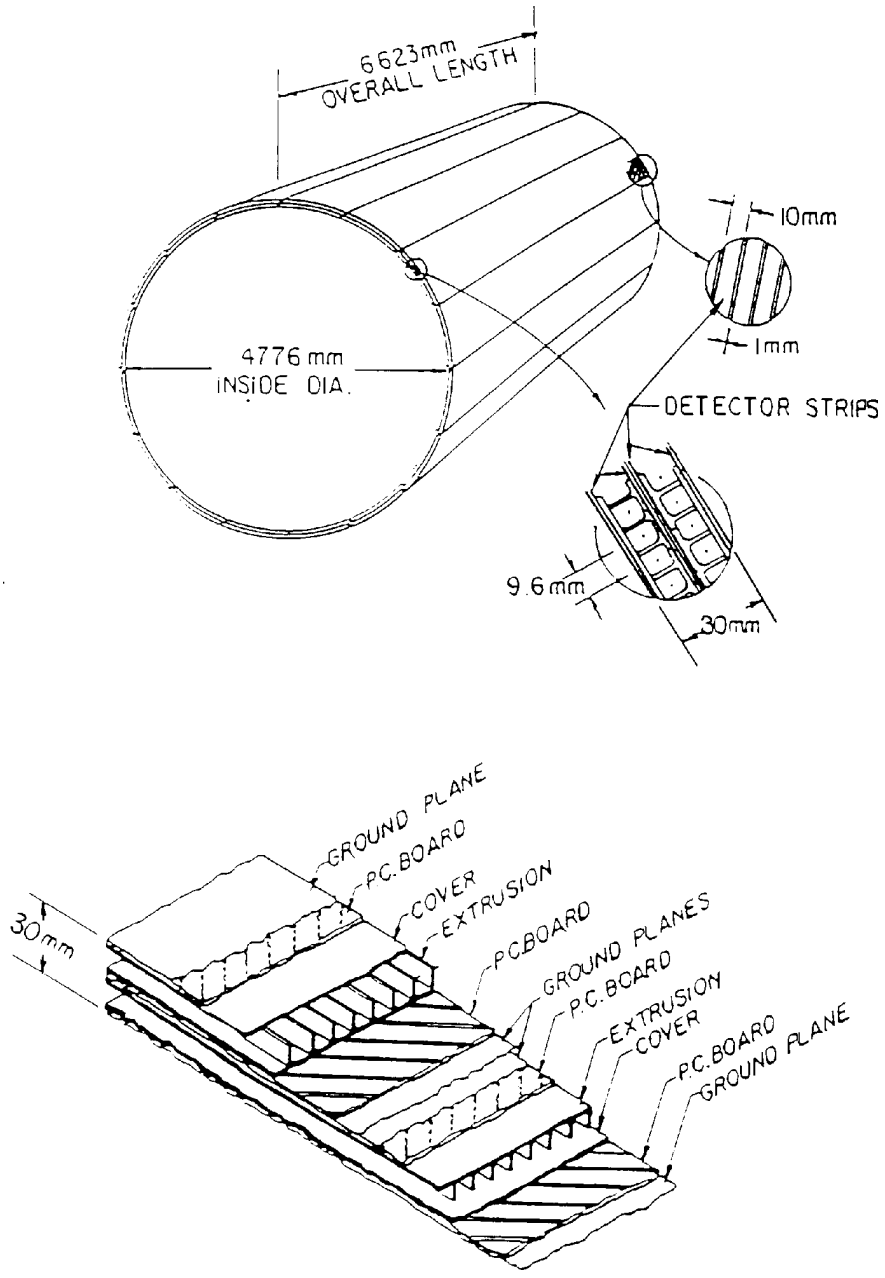

Figure 3.15: Structure of the barrel electromagnetic presampler

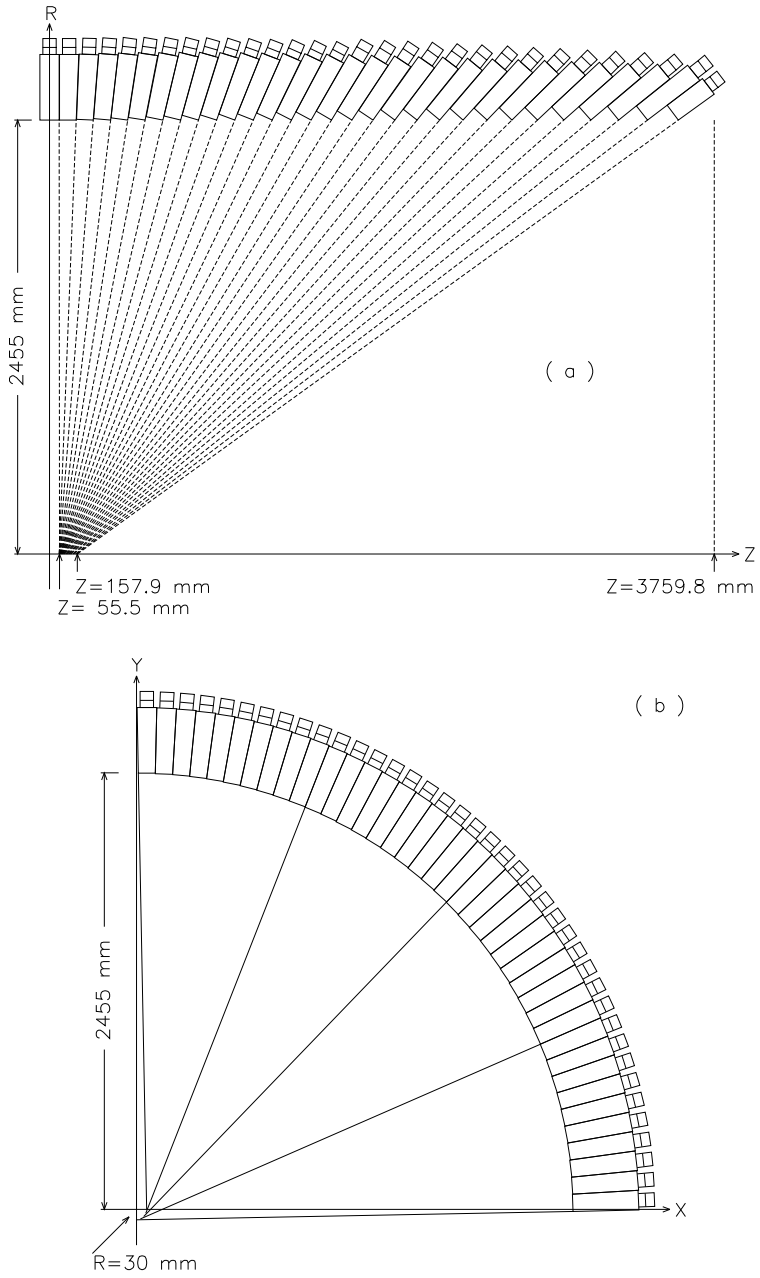

Figure 3.16: Geometry of the barrel electromagnetic calorimeter array (a) in r-z and (b) in r-ϕ view

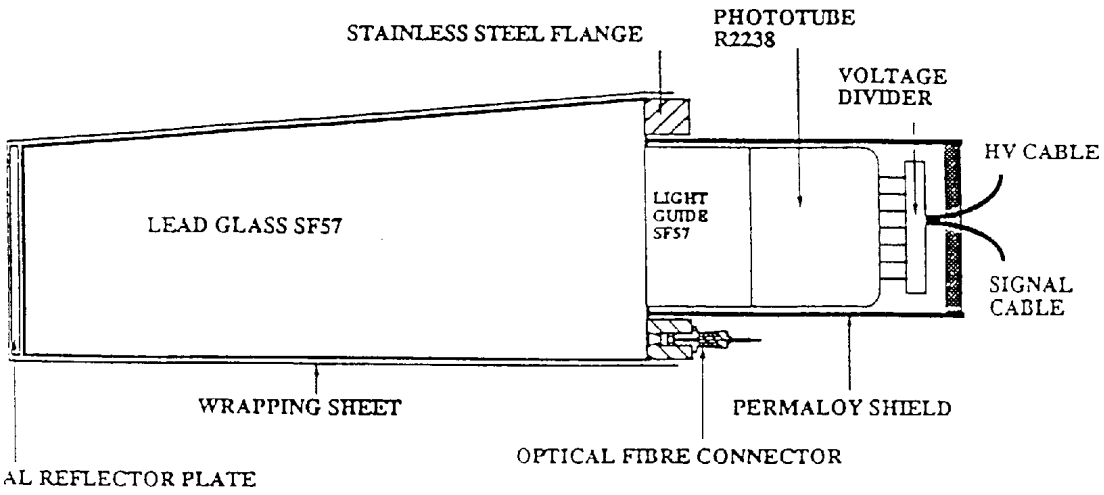

Figure 3.17: Assembly of a barrel electromagnetic calorimeter block

157.9 mm) along the beam axis depending on its position. In the ϕ direction, the blocks are tilted by 0.574° so that they miss the beam axis by 30 mm. The blocks were fabricated in 16 different shapes to achieve this geometry. In terms of the mechanical support structure, the calorimeter is divided into two halves by the y-z plane, each having five half-rings containing 12 (or 11 for the middle ring) $\times$ 80 blocks in z and ϕ respectively.

A newly developed heavy lead glass, SF57 [75], is used to maximise the effective counter thickness. The glass contains 75% by weight of PbO, giving it a density of 5.54 g/cm^3 and a radiation length X_0 = 1.50 cm. The refractive index is 1.8467 at the wave length λ = 586 nm. Fig. 3.17 shows the assembly of a block. Each block is polished and wrapped for optical isolation with a black sheet of vinyl fluoride laminated between two sheets of polyester films. The inner surface of the sheet is coated with aluminium to improve light transmission. The total thickness of the wrapping is 70 μm. On the top surface of each block is a 1 mm thick aluminium plate coated with white paint, providing better controlled reflection which is important for a good gain monitoring.

The Čerenkov light generated by passage of relativistic particles in a block is collected through a 4 or 6 cm long light guide made of SF57. The extra material due to the light guides is clearly seen in figure 3.14 as periodic rises of the upper curve. The figure also shows narrow dips due to the gaps between blocks, with two gaps between half-rings (around $|\cos\theta| = 0.2$ and 0.6) being especially noticeable. Each block is equipped with an R2238 photomultiplier tube [71] with 3 inch diameter, which is supported by a stainless steel flange glued to the block. The phototube has a bialkali photocathode with an effective diameter of 70 mm, followed by 12-stage mesh dynodes which make the tube less susceptive to weak magnetic field. The phototube is guarded by a 2 mm thick Permalloy metal tube from the stray field of the magnet. With this shielding, the phototube can operate

in an external field of up to 100 gauss with a gain deviation of less than 1%. Each phototube is supplied with independent high voltage, typically $-1.0\,\mathrm{kV}$, which can be controlled in 2 V steps. The nominal gain of the phototubes is about 10^5.

The signals from phototubes are digitized by 96-channel 12-bit charge integrating ADCs. Each channel contains two front-ends with different sensitivities, 30 fC/count and 225 fC/count, to provide high precision for a wide range of energies.

The gains of all lead glass counters were calibrated absolutely using a 50 GeV electron beam from the CERN SPS. The high voltage for each counter is adjusted so that a 50 GeV electron produces a signal of 500 pC. The nonlinearity was measured to be less than 1% for electrons in the energy range of 6–7 GeV.

A gain monitoring system is used to maintain the gain calibration over years of operation. Each counter is equipped with an optical fibre through which light from a xenon flash lamp illuminates the block. Xenon lamps provide similar light spectrum to that of the Čerenkov light considering the light attenuation in the lead glass and the quantum efficiency of the of the photocathode. One Xe lamp is installed for each of the ten half-rings. A bundle of 80 optical fibres distribute the light from each Xe lamp to 80 ϕ-segment modules of 12 counters, where each fibre branches to the fibres of individual counters. The light output of each flash lamp is monitored by a PIN photodiode, which also provides a trigger signal to the ADCs.

The final calibration of the counter gains is provided by the $e^+e^- \to e^+e^-$ process at the Z^0 resonance. By the end of 1992, about 70% of the counters ($\sim 50\%$ for the outermost half rings, $\sim 80\%$ for the rest) have recorded at least two 'good' beam-energy electrons and calibrated using them, where a 'good' electron must deposit more than 80% of its energy in one counter. Counters with one or no such electron are calibrated using the average gain of the counters in the same module served by an optical fibre of the monitoring system.

The energy resolution obtained in a beam test is expressed as

$$\sigma_E/E = 0.2\% + 6.3\%/\sqrt{E}$$

with no material in front of the counters. For 50 GeV electrons injected normal to the counters, a position resolution of 2.4 mm was obtained.

Endcap Electromagnetic Presampler

Each endcap electromagnetic presampler (PE) [39] consists of 32 multiwire proportional counters arranged in 16 ϕ sectors, or wedges, to form an umbrella located between the pressure bell and the endcap electromagnetic calorimeter. Fig. 3.18 shows schematic views of the endcap presampler and calorimeter. The polar angle acceptance is $0.83 < |\cos\theta| < 0.95$.

The detector consists of thin multiwire chambers operating at a high gain. The design of the chamber is similar to that used for the hadron pole tip calorimeter,

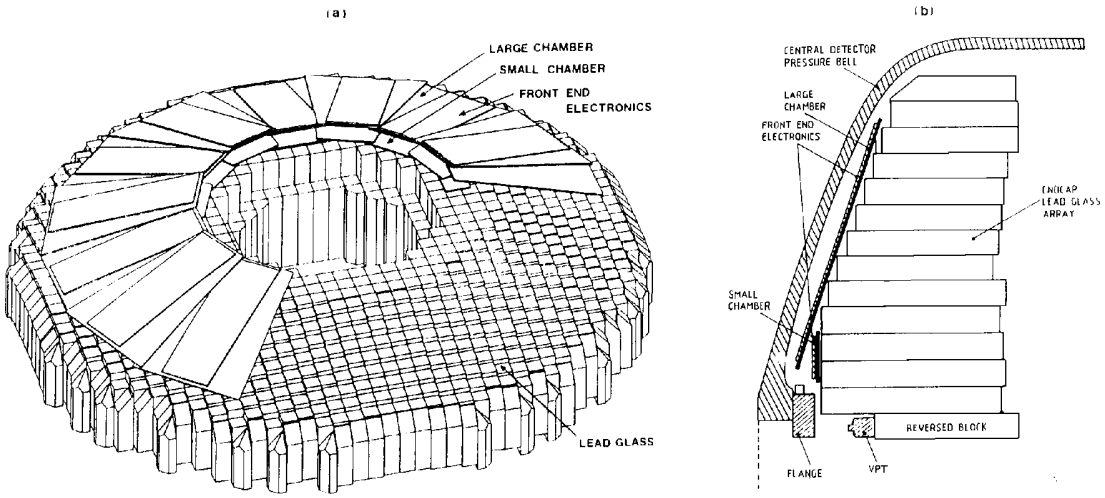

Figure 3.18: Schematic views of the endcap electromagnetic calorimeter (a) in 3-D view, and (b) in a cross-section parallel to the beam direction.

and is explained in more detail in section 3.2.5. Each sector consists of two trapezoidal chambers. The larger one, covering most of the acceptance of the detector, is inclined by 18° with respect to the r-ϕ plane. The smaller one, covering the innermost (large $|\cos\theta|$) region, is at 90° to the beam direction. Neighbouring sectors overlap each other.

The anode wires and the cathode strips are read out in groups of four, providing measurements of the position for showers and single tracks. The cathode pad readouts provide better measurements of energy correction for electromagnetic showers. They also help resolving ambiguities of the position measurement by the wires and strips.

Endcap Lead Glass Calorimeter

The endcap electromagnetic calorimeter (EE) [25] consists of two dome-shaped arrays of 1132 lead glass counters. They are located behind the pressure bell of the central detector, as shown in figure 3.18, and covers the full azimuthal angle in the region of $0.81 < |\cos\theta| < 0.98$. The lead glass blocks are mounted with their axes parallel to the beam direction.

Fig. 3.19 shows a schematic view of a counter assembly. The lead glass used is CEREN-25 [45] which contains 55% by weight of PbO and has a density of $4.06\,\mathrm{g/cm^3}$. One radiation length is 2.51 cm and the refractive index is 1.708 at the wavelength $\lambda = 400\,\mathrm{nm}$. Each block is polished, wrapped with aluminium foil and mylar, and housed in a can of 0.45 mm thick brass. The aluminium wrapping improves the light reflection efficiency. The blocks were manufactured in three lengths, 380, 420 and 520 mm, and arranged so that the total depth of the counter seen by particles from the interaction region is at least $20.5X_0$, and

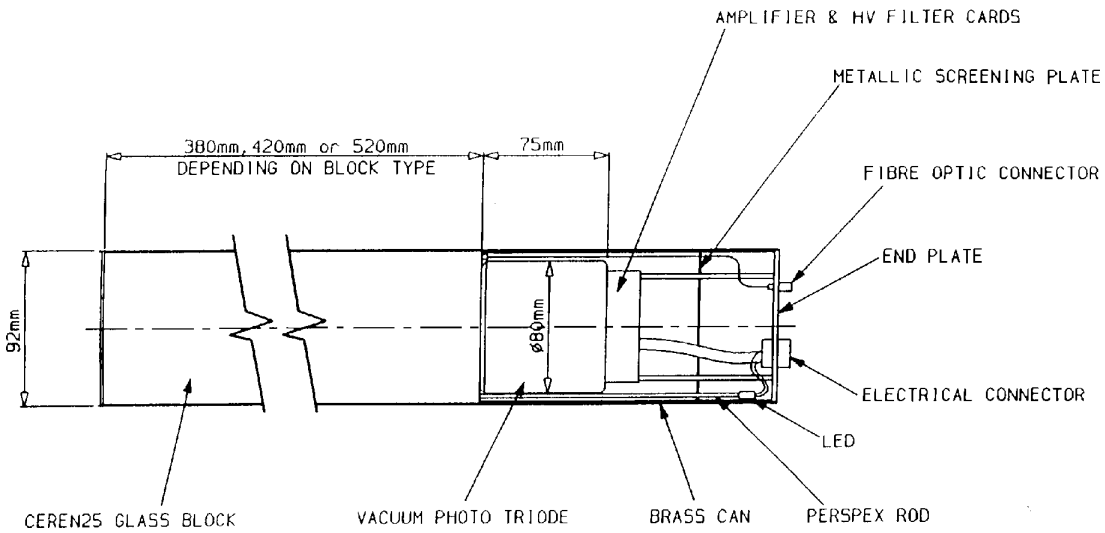

Figure 3.19: Assembly of an endcap electromagnetic calorimeter block

typically $22X_0$.

The lead glass blocks are equipped with novel single-stage multipliers called vacuum photo triodes (VPTs) [72]. This device is capable of operating in a strong magnetic field, which is an important advantage for the endcap calorimeter. The tubes used, XP1501/FL [80], have an average gain of 12.3 at the external field of $\sim$0.4 T. The operating voltage is -1.0 kV for all tubes. The VPTs have an average photocathode diameter of 3 inches and an average quantum efficiency of 26%. The tubes are glued to the lead glass by an epoxy resin with good optical transparency and high refractive index. A high gain, low noise amplifier installed at the bottom of each VPT provides additional amplification. Special care was taken for filtering ripples from the high voltage supply at the VPT bases.

The signal from each counter is digitized by a charge integrating ADC. The mean number of photoelectrons produced by an electromagnetic shower is measured to be 1.8×10^3 per GeV. The noise is dominated by that from amplifiers, and is equivalent to an energy of 14 MeV.

Two systems of reference light sources are used to monitor the performance of the counters. Each block assembly has an optical fibre through which light from a liquid scintillator excited by a pulsed ultraviolet nitrogen laser is sent to the lead glass. In addition, a green light emitting diode (LED) is mounted on a Perspex rod glued to the block. The laser and LED systems produce signals equivalent to $\sim$10 GeV and $\sim$20 GeV electrons respectively.

The energy resolution of the endcap calorimeter at low energies, studied in pion and electron beams, is $\sigma_E/E = 5\%/\sqrt{E}$ for E in GeV. The response was measured to be linear within errors of $\sim$1% in the energy range of 3 to 50 GeV. A spatial resolution of 8–14 mm was obtained for a 6 GeV electron beam incident at 15° to the longitudinal block axes.

3.2.5 Hadron Calorimeter

The hadron calorimeter measures the energy of the hadrons that penetrate through the electromagnetic calorimeter, and helps to identify muons. The iron return yoke of the magnet, which represents at least 4 interaction lengths of material over a solid angle of 97% of 4π, is instrumented with several layers of detectors. The detector consists of three parts: the barrel, the endcaps and the pole tips. The barrel and endcap calorimeters use limited streamer tubes with essentially the same design. The pole tip calorimeters use thin high-gain multiwire chambers.

Barrel and Endcap Hadron Calorimeter

The barrel hadron calorimeter (HB) and the endcap hadron calorimeters (HE) share essentially the same design [35]. The barrel, covering an angular acceptance $|\cos\theta| < 0.81$, consists of 9 layers of chambers alternating with 8 iron slabs. The two doughnut-shaped endcaps cover each end of the barrel, $0.81 < |\cos\theta| < 0.91$, with 8 layers of chambers and 7 slabs of iron. Each iron slab has a 100 mm thickness, and the gap between adjacent slabs is 25 mm in the barrel and 35 mm in the endcaps. The total thickness of the iron absorber corresponds to 4.8 interaction lengths in the barrel and 4.2 interaction lengths in the endcaps.

The active elements of the calorimeter cover a total area of 2400 m^2. To reduce the building cost, limited streamer tubes made of PVC extrusions are chosen. The detector consists of 9 mm × 9 mm cells with a 100 μm diameter anode wire at the centre. The distance between two wires is 10 mm. The inner surface of the PVC walls are coated with graphite and a stabiliser, giving a surface resistance of 0.1–5 $\mathrm{M}\Omega$/square. Signals are read out by aluminium strips and pads covering the inner and outer faces of the detector layers respectively. The strips are 4 mm wide and centred over the wires, which are running in the beam direction for the barrel and horizontal for the endcaps. There are 57 000 strips in total, which give precise tracking and shower profile information. The pads, each covering typically 500 mm × 500 mm, are grouped to form 976 towers. Each tower covers a solid angle of $\sim 7.5^\circ \times 5^\circ$ in ϕ and θ respectively. Fig. 3.20 shows the layout of the barrel and endcap calorimeters.

The chambers use a gas mixture of 75% isobutane and 25% argon, flowing through the entire volume of the detector once per day. The applied high voltage varies between 4.65 and 4.85 kV depending on the atmospheric pressure, to keep the detector operating in limited streamer mode with approximately constant gain.

Two readout systems are used for signals from the towers (HT) and from the strips (HS) of the hadron calorimeter. Signals from the strips are latched by locally-mounted shift registers. Signals from the pad towers are digitized by two sets of charge integrating ADCs with gains different by a factor of about 8. The innermost pad of each tower has a separate readout to assist interpretation

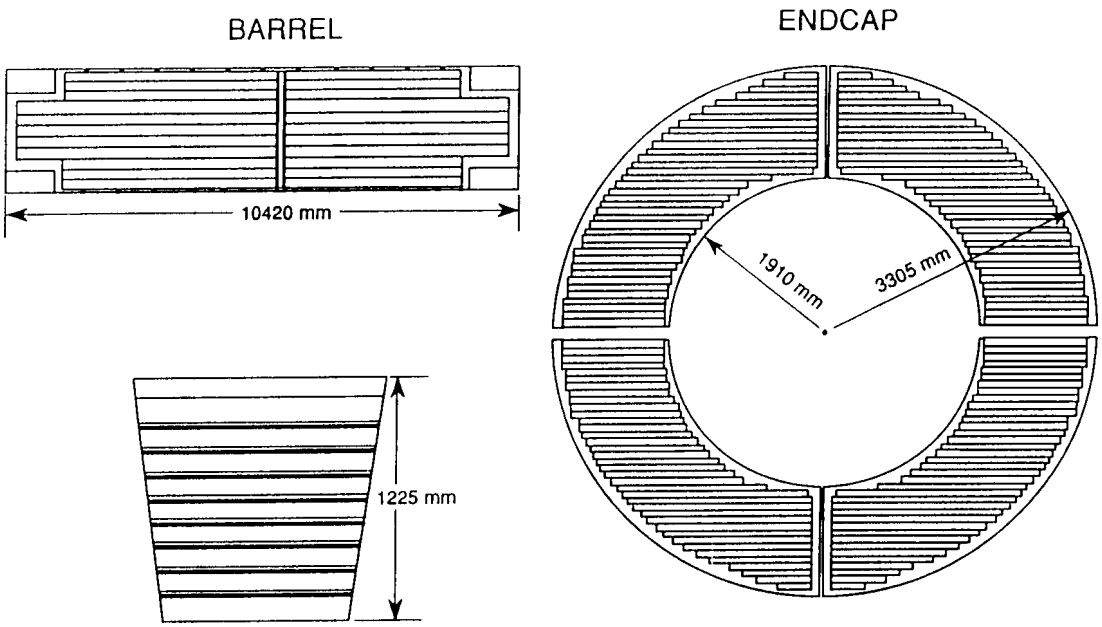

Figure 3.20: Layout of the barrel and endcap hadron calorimeters

of anomalously high signals in the electromagnetic calorimeter due to charge exchange interactions of hadrons near the back end of the lead glass blocks. In addition, 92 trigger signals are generated by summing signals from 4×4 towers.

The energy resolution of a unit of 3×3 towers was measured in pion beams at an incident energy of 10 GeV, and found to be $\sigma_E/E = 120\%/\sqrt{E}$ for E in GeV. Since there is 2.2 interaction lengths of material in the electromagnetic calorimeter, the total hadronic energy must be determined by combining signals from the electromagnetic and hadron calorimeters.

Hadron Pole Tip Calorimeter

The pole tip hadron calorimeter (HP) [48] covers the polar angle range $0.91 < |\cos\theta| < 0.99$ to extend the solid angle coverage of the hadron calorimeter. In this region, the available gaps between iron plates are reduced to 10 mm to avoid perturbing the magnetic field. Thin multiwire proportional chambers, 7 mm in thickness, operating in a high-gain mode were chosen to fit the detector in this geometrical constraint.

The calorimeter consists of 10 active layers alternating with 9 iron slabs of an 80 mm thickness. Fig. 3.21 shows a cross-section of the chamber. A plane of 50 μm diameter anode wires, strung 2 mm apart, is placed in the middle of a 3.2 mm gas gap between cathode planes. Signals are read out from copper strips and pads behind the cathode planes. The chamber is operated with the anode wires at a voltage of 3.5 kV. The gas mixture is 55% CO_2 and 45% n-pentane.

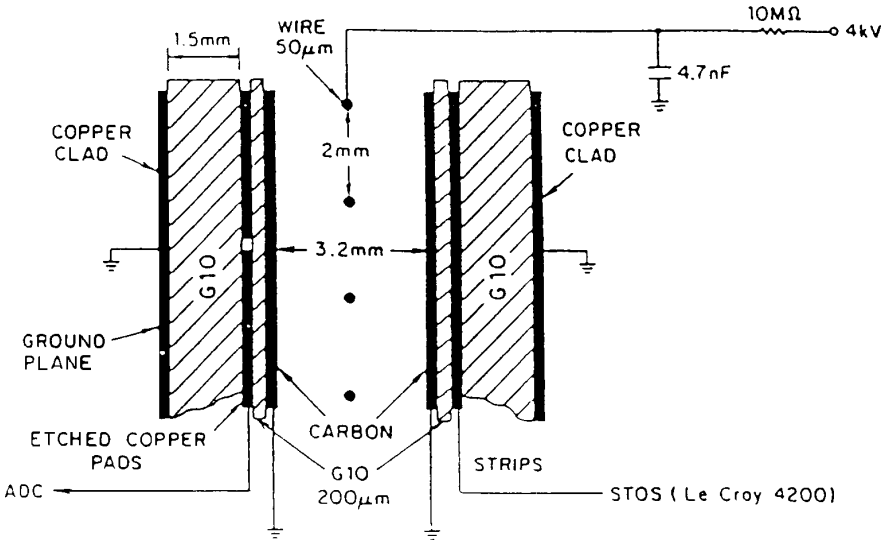

Figure 3.21: Cross-section of the pole tip hadron calorimeter

Fig. 3.22 shows the layout of the wires, strips and pads of the chamber. The pads have a typical area of 500 cm^2 to match the expected spread of hadronic showers. The pad size varies from one layer to another, forming towers pointing the the interaction region. The signals from 10 pads of each tower are summed and the pulse height is digitized by an ADC. The strips run radially, perpendicular to the wire directions, are read out at the outer ends of the chambers and recorded digitally.

One eighth of a pole tip calorimeter module was tested using a hadron beam of energies between 6 and 50 GeV. The energy resolution at energies below 15 GeV was measured to be $\sigma_E/E = 100\%/\sqrt{E}$ for E in GeV. At higher energies, the resolution deteriorated to $120\%/\sqrt{E}$ due to shower leakage.

3.2.6 Muon Detector

The muon detector is designed to identify muons in over 93% of the full solid angle. Before entering the muon detector, most particles from the interaction region traverse more than 7 interaction lengths of material as shown in figure 3.23. The probability of a pion penetrating the absorber without interacting strongly is less than 0.1%. Particles with less than 2 GeV of energy usually stop in the absorber, while muons above 3 GeV emerge from it. There are, however, inevitable acceptance holes due to the beam pipe, the detector support legs, and the cables. The detector legs are responsible for $2 \times 2.2\%$ of detector gaps, and is also seen in figure 3.23 as a dip in the amount of material between $|\cos\theta| = 0.7$ and 0.9.

The muon detector is divided into a barrel and two endcaps. The barrel part covers $|\cos\theta| < 0.68$ and the endcaps cover $0.67 < |\cos\theta| < 0.98$. Fig. 3.24 shows the geometrical acceptance of the muon detector.

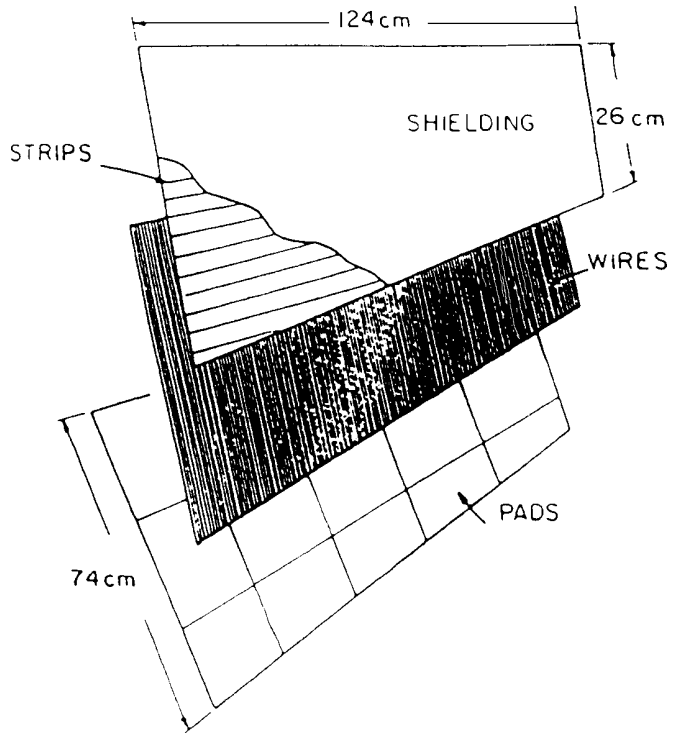

Figure 3.22: Layout of the pole tip hadron calorimeter

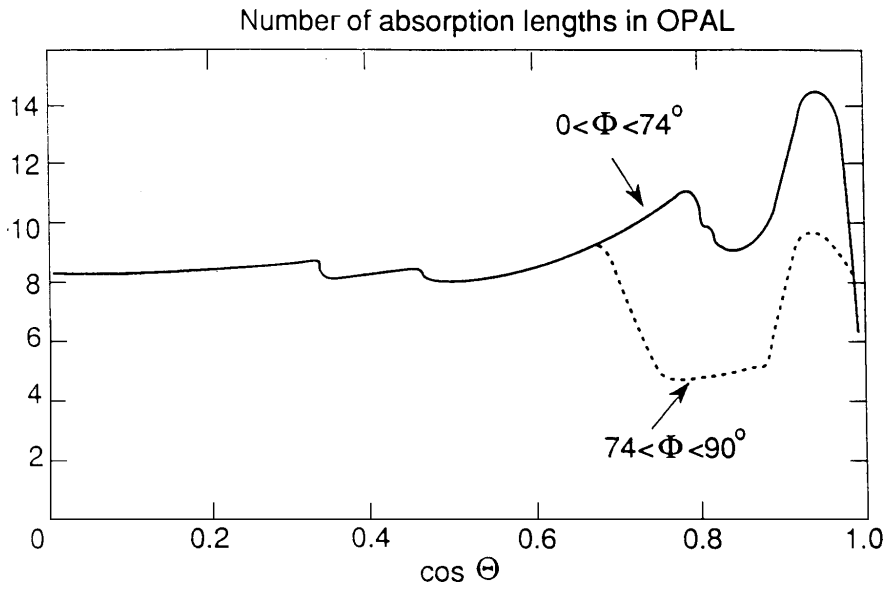

Figure 3.23: Number of absorption lengths seen by a particle from the interaction region before reaching the muon detector, as a function of θ and averaged over the indicated ϕ ranges

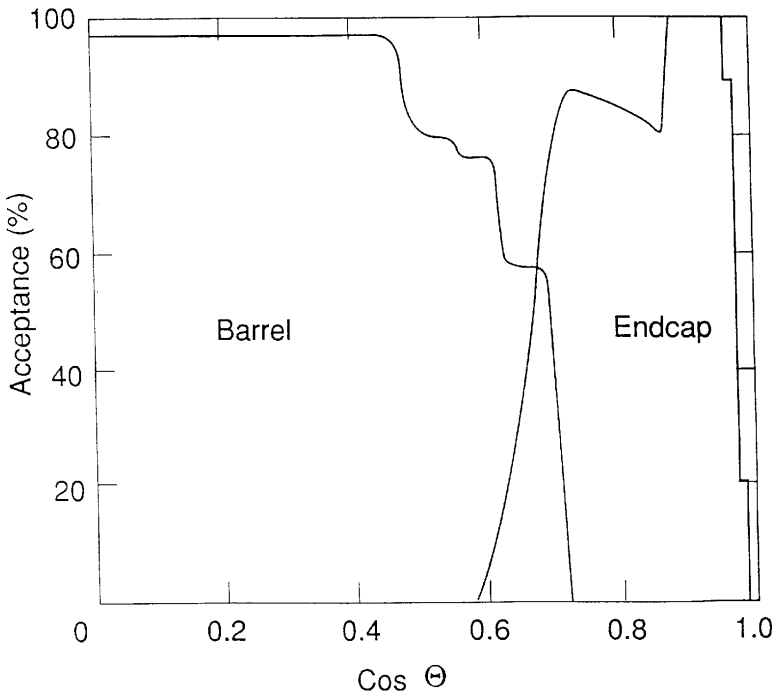

Figure 3.24: Geometrical acceptance of the barrel and endcap muon detector as functions of the polar angle θ

Muons are identified by extrapolating the tracks detected in the central detector to the muon detector allowing for energy loss and multiple scattering in the absorber. Track segments detected in the muon detector are tested for consistency with the extrapolated tracks, both in the position and in the direction. The position and angular resolution required for the muon detector is determined by the multiple scattering of the highest momentum muons of interest, and are about 2 mm and 3 mrad respectively.

Barrel Muon Detector

The barrel muon detector (MB) consists of 110 drift chambers, each having a 1.2 m width and a 90 mm thickness including the supporting frame. Of the 110 chambers, 2×44 are mounted on each side of the barrel, 10 on the top and 12 at the bottom between the legs of the detector. The lengths of the chambers are 10.4, 8.4 and 6.0 m for the side, top and the bottom modules respectively. The chambers are arranged in four layers, staggering in the ϕ direction by typically 50 mm from each other. This layout solves the left-right ambiguity, and provides self-calibration of the drift velocity.

Fig. 3.25 shows a cross-sectional view of a chamber. Each chamber consists of two cells, arranged side by side, each having a 50 μm diameter anode wire. The wires run in the z-direction and are supported at every 1.4 m. The maximum drift

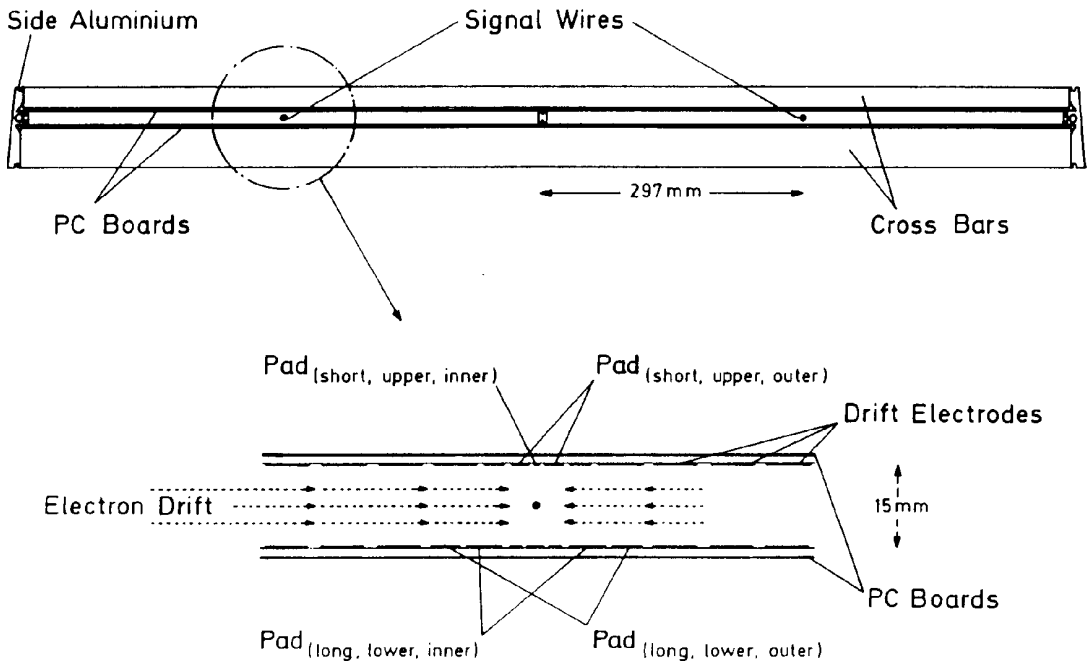

Figure 3.25: Cross-section of a barrel muon drift chamber

length is 297 mm. The inner and outer walls of the chamber are printed circuit boards, held 15 mm apart by a pair of side support and a central divider made of extruded aluminium. The inner surface of the PC boards are etched to have 7.5 mm wide strips with 2.5 mm spacing to define the drift field. Within 20 mm of the wires, the strips are replaced by diamond-shaped cathode pads [26] shown in figure 3.26, which provides measurement of the position along the wire. The cathode pads operate at +4.0 kV, and the nominal voltage of the anode wire is +1.85 kV relative to the pads. The outside layer of the PC boards and aluminium supports are at ground potential.

For each cell, two signals are read out from both ends of each wire, and four from cathode pads. The signals are read out by preamplifiers installed at the chamber and are digitized by 8-bit, 12.5 MHz FADC modules called time projection digitizer (TPD) developed by ALEPH [59].

The ϕ-coordinate is determined by the drift time to an accuracy of better than 1.5 mm. The z-coordinate is determined to an accuracy of 2 mm by three steps: course, medium and fine z measurements. The course z measurement is provided by the amplitude and time difference between signals from either side of the wires. The medium and fine z measurements are given by induced signals on the diamond-shaped cathode pads. The long pads, which repeats itself at a 1710 mm interval, gives the medium z measurement with an accuracy of about 30 mm. The short pads, with the 171 mm repeat interval, gives the fine z measurement to an accuracy of 2 mm. The ambiguity of the fine z measurement at every 171 mm is

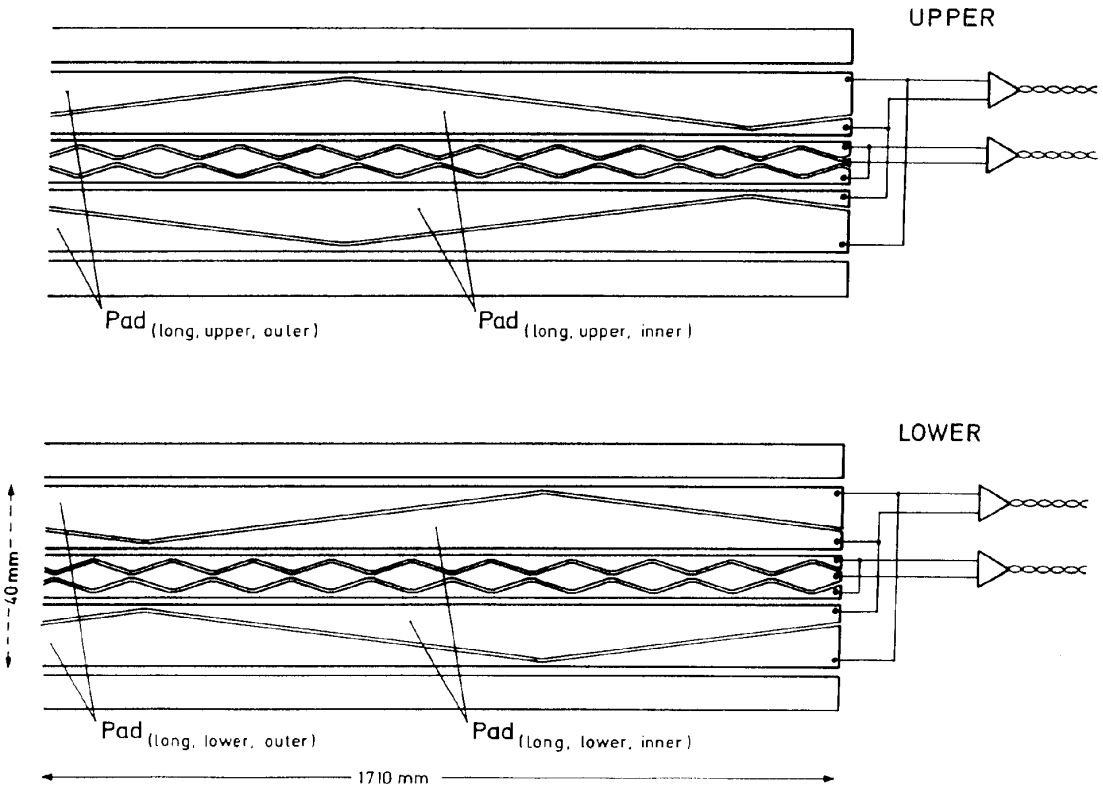

Figure 3.26: Schematic layout of the diamond-shaped cathode pads of the barrel muon drift chambers

resolved by the medium and course measurements. The medium z measurement is calibrated by the fine measurement, and the course by the medium. The positions of the wires are surveyed to an accuracy of 1 mm.

Endcap Muon Detector

The endcap muon detector (ME) [34] consists of four layers of limited streamer tubes covering a polar angle range of $0.67 < |\cos\theta| < 0.985$. Fig. 3.27 shows the layout of the detector. Each endcap consists of 8 quadrant chambers complemented by 4 patch chambers. The size of a quadrant chamber is 6 m × 6 m and a patch chamber covers 3 m × 2.5 m. The chambers are overlapped with each other to ensure good geometrical acceptance as shown in figure 3.24.

Each chamber has two layers of streamer tubes, spaced by 19 mm, with wires running horizontally in one layer and vertically in the other. The streamer tubes are made of fire-resistant plastic [64] which forms 1 mm thick walls of 8 square cells, each having a 9 mm × 9 mm inner cross-section. The inner walls of the extrusion are coated with a water-based carbon suspension, giving them a surface resistivity of about 5 MΩ/square. The wires, 100 μm diameter, run the full length of the chambers, supported at every 500 mm. The tubes are filled with a gas

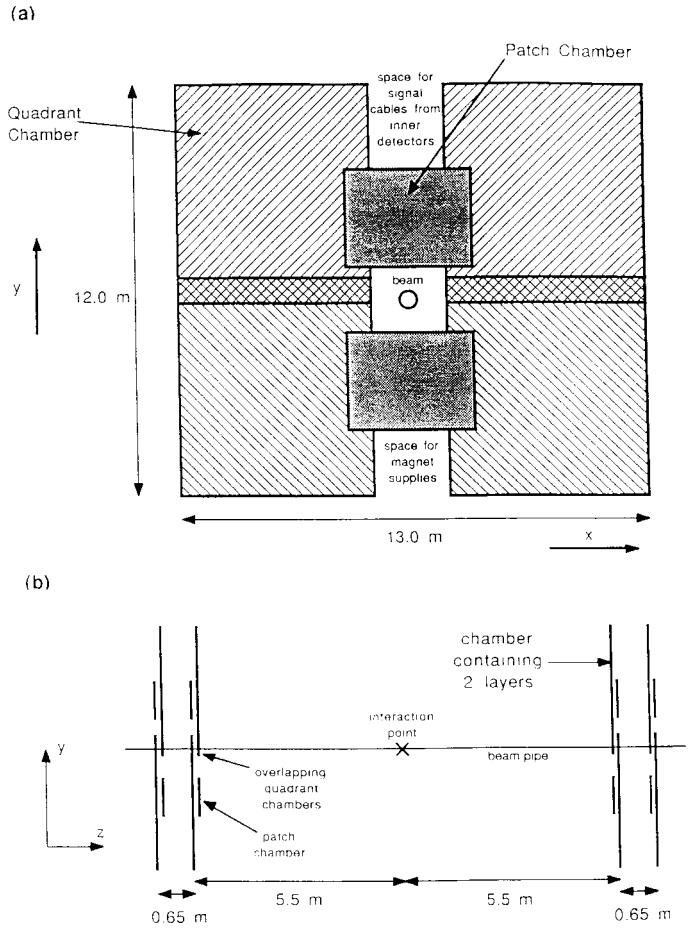

Figure 3.27: Schematic layout of the endcap muon detector (a) in the end view, and (b) in the side view

mixture of 25% argon and 75% isobutane. High voltage of typically +4.3 kV is applied to the wires, with the cathodes at ground potential.

The outside of the tubes are covered by aluminium strips, 8 mm wide with a 2 mm spacing. The charge induced on the strips are read out to detect position of the streamers. The signals are integrated for 5 μs after a beam crossing and digitized by 12-bit ADCs. The strips on one side of the chamber run parallel to the wires, determining which cell is hit. The strips on the other side are perpendicular to the wires and the weighted average of the signals, shared by typically 4 to 5 strips, gives a position measurement accurate to better than 1 mm. The positions of the strips are surveyed to an accuracy of about 1 mm.

3.2.7 Forward Detector

The forward detector is a combination of six detectors—a calorimeter (FD), tube chambers, drift chambers, a fine luminosity monitor, a gamma catcher (GC) and

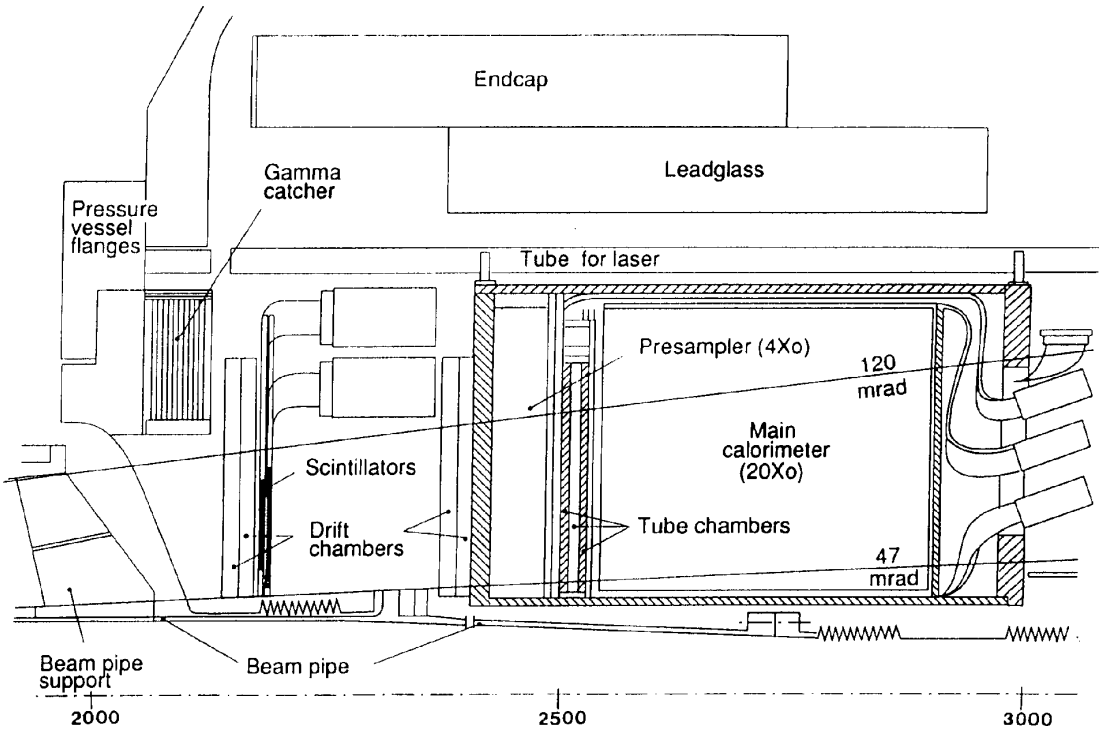

Figure 3.28: Cross-section of the forward detector

a far-forward monitor—which measures the luminosity by detecting small-angle Bhabha scatterings. Fathermore The silicon tungsten detector (SW SW) is a installed in order to detect the very low angle Bhabha scattering with an angular acceptance of 25 mrad to 59 mrad.

It also complements the other detectors, mainly the electromagnetic calorimeters, to give a near 4π acceptance to the OPAL detector. Fig. 3.28 shows a cross-sectional view of the forward detector between 2 and 3 m from the interaction point.

The detector has a clean acceptance between 47 and 120 mrad from the beam axis, where the only material between the detector and the interaction region is a 2 mm thick aluminium window of the central detector's pressure vessel and the beam pipe, with aluminium webs supporting the beam pipe in the horizontal and vertical planes.

The forward calorimeter consists of sixteen segments of 35-layer lead-scintillator sandwiches. They are read out by vacuum phototetrodes with charge-sensitive amplifiers through wavelength shifters. The thickness of the calorimeter corresponds to $24X_0$. The first $4X_0$, called presampler, is read out separately from the rest. Three planes of proportional tube chambers are installed between the presampler and the main section of the calorimeter to improve the resolution of the shower position measurement. The energy resolution obtained from well-contained Bhabha events is $\sigma_E/E = 17\%/\sqrt{E}$ for E in GeV. The radial

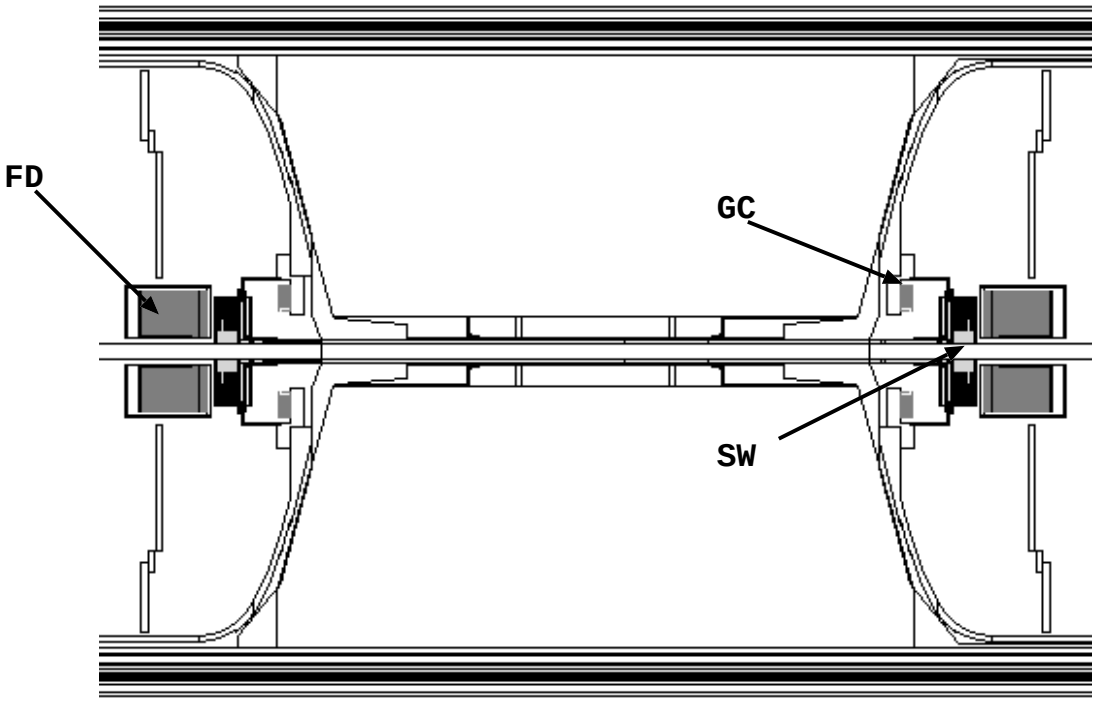

Figure 3.29: Cross-section of the forward detector

position resolution, obtained by the ratio of the signal amplitudes from the inner and outer edges of the detector, is ± 2 mm near the inner edge. The azimuthal resolution is $\pm 1.5°$ or less. The cross-section for Bhabha scattering at the Z^0 peak into the acceptance of the main calorimeter is about 57 nb.

The drift chambers, measuring the position of the incident particles before entering the calorimeter, are divided into four azimuthal sectors. Each sector has two chambers, front and rear, with two gas gaps for each chamber. Two anode wires are strung azimuthally, providing a radial position measurement from the drift time. The position along the wire is measured by the charge division as well as by the induced signals from pads of an intersecting diamond pattern. A position resolution of 300 μm in the radial direction, and 1 mm along the wires, is obtained.

The fine luminosity monitor consists of four pairs of 6 mm thick scintillation counters, positioned to cover an angular region of 50 to 109 mrad from the beam axis. The counters have a timing resolution of 300 ps necessary for the rejection of backsplash from showers in the forward calorimeter.

The gamma catcher is a ring-shaped module of lead-scintillator sandwich which covers the acceptance gap, 142 to 200 mrad from the beam axis, between the endcap electromagnetic calorimeter and the forward calorimeter. The detector is 7 radiation lengths thick and is read out by silicon photodiodes through wavelength shifters. Charge sensitive amplifiers are used and the signals are

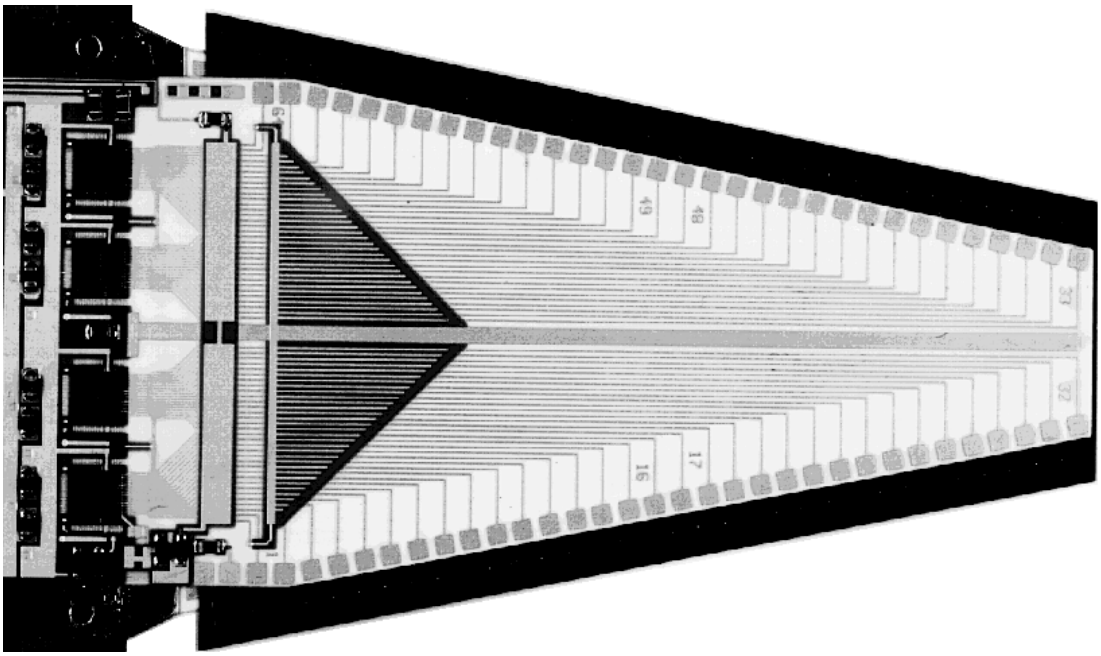

Figure 3.30: Cross-section of the silicon layer in the silicon tungsten detector

digitized by charge integrating ADCs. The detector has a linear response to electromagnetic showers with energies up to 5 GeV. Any electrons or photons with more than 2 GeV of energy can be detected, thus providing an efficient veto for radiative events.

The far forward luminosity monitor, mounted on either side of the beam pipe at 7.85 m from the interaction point, consists of a pair of small lead-scintillator calorimeters. They are segmented into six readout sections to give shower position information. Electrons scattered into angles between 5 and 10 mrad from the beam axis near the horizontal plane are bent outwards by the low-β quadrupoles and detected by these counters. The effective cross-section for Bhabha scattering at Z^0 is about 460 nb.

The silicon tungsten detector (SW) is a sampling calorimeter designed to detect low angle Bhabha scattering events in order to measure the luminosity. There are 2 calorimeters at $\pm$238.94cm in z from the interaction point with an angular acceptance of 26 mrad to 59 mrad. Each calorimeter consists of 19 layers of silicon detectors and 18 layers of tungsten. At the front of each calorimeter is a bare layer of silicon to detect preshowering, the next 14 silicon layers are each behind 1 radiation length (3.8mm) of tungsten and the final 4 layers are behind 2 radiation lengths (7.6 mm) of tungsten.

Each silicon layer consists of 16 wedge shaped silicon detectors. The wedges cover 22.5 o in ϕ with an inner radius at 6.2 cm and an outer one at 14.2 cm. The wedges are subdivided into 64 pads (32 in r and 2 in ϕ) giving a total of 38912 channels which are read out individually. Adjacent wedges in a layer are

offset by 800μm in z and positioned in such a way that there is no gap in the active area of the silicon. Consecutive layers in the detector are offset in ϕ by half a wedge (11.25°) so that any cracks between the tungsten half–rings do not line up.

3.3 OPAL Data Acquisition System

The OPAL data acquisition (DAQ) system [36] has three functions: trigger, data acquisition and control. When LEP is operating in the four-bunch mode, the bunches of electrons and positrons collide near the centre of the OPAL detector every 22.2 μs; or twice as often in the eight-bunch mode. The trigger system collects fast information from the subdetectors to select interesting events within this time, thereby reducing the 45–90 kHz bunch crossing rate to an acceptable data-acquisition rate of 1–5 Hz. When the trigger system decided to record an event, the data acquisition system collects the full information belonging to the event from the subdetectors and merge the data to build an event record. A first-level on-line analysis is performed for each event and clearly unwanted events are discarded. The data are then processed by an on-line event reconstruction system, and recorded in magnetic tape cartridges and optical disks. All the data flow processes are controlled by an on-line VAX cluster. In addition, a slow control system monitors the status of subdetectors and associated electronics, mainly to provide safety operation.

The OPAL data acquisition system has been continuously evolving since its first operation in 1989. The largest change during 1989–1993 was the introduction of the pretrigger system necessitated by the commissioning of the eight-bunch operation of LEP. The description given in this section is based on the configuration in 1991, and in 1992 for the pretrigger system. Most of the data used in this study were taken in this configuration.

The data acquisition system has a multilevel tree structure through which the data are collected, buffered, processed and recorded. Figure 3.31 shows the overall scheme of the triggering and the data acquisition. The lowest level of the structure consists of 14 local system crates used by the subdetectors, the trigger and track-trigger subsystems, and one station of the slow control system. There are more than 150 000 analogue signals from the subdetectors, producing several megabytes of data after digitization. The size of the data is reduced in each ascending step of the data acquisition, to an average of 46 kbyte per multihadronic event before the recording to the storage media.

Most of the system components run on 68000-series microprocessors [60], running the OS9 operating system [69] in VMEbus [78] based hardwares. The VME crates are interconnected using a fast parallel link called VICbus. Trigger information is broadcast via dedicated trigger bus. The Ethernet [50] local area network provides the connection between all computers and all VME crates. The

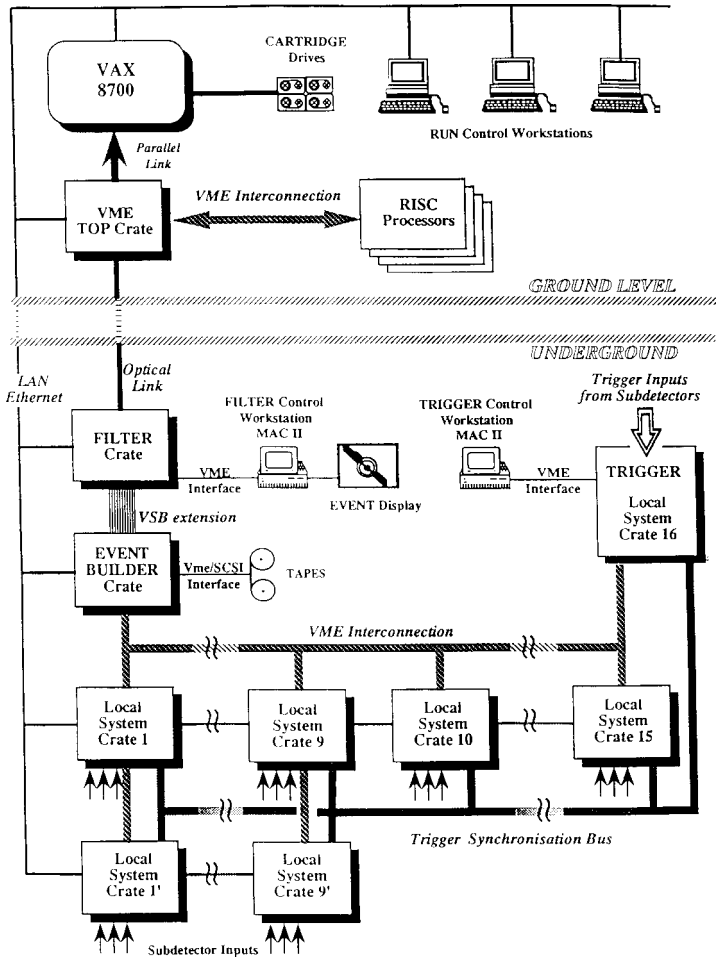

Figure 3.31: Overall scheme of event triggering and data acquisition

following sections describe the functions of each components of the data acquisition system.

3.3.1 Local System Crates

Each subdetector has one or two local system crates (LSCs) which collects and processes the data from the detector. If the configuration of the subdetector requires two LSCs, usually one on each side of the detector, only one of the LSC (master) is directly connected to the central trigger and event builder crate, and the other (slave) crate is connected to the master LSC and controlled by it. There are two more LSCs which do not belong to the subdetectors: one for the global trigger system (TR) and another for the track trigger system (TT). A list of LSCs and the numbers of the detector channels they handle is summarized in table 3.2.

During data taking runs, the LSCs are responsible for all the local activities

Table 3.2: Local system crates and numbers of detector channels

Subdetector		LSCs	Channels
Central detector	SI	1	15 725
	CV	1	648
	CJ	1	7 680
	CZ	1	1 152
Time-of-flight counters	TB	1	320
Electromagnetic calorimeter	PB	1	21 504
	EB	2	9 440
	PE	2	6 080
	EE	2	2 264
Hadron calorimeter	HT	2	1 696
	HS	2	56 146
	HP	2	10 576
Muon detector	MB	2	1 320
	ME	1	42 496
Forward detectors	FD	2	1 176
Trigger system	TR	1	
	TT	1	

of the subdetector, including:

- Collecting the digitized data from the detector. Pedestal subtraction, zero suppression and other data compression may be done if the front-end electronics do not have these capabilities.

- Reconstructing the sub-event from the data. First level processing, e.g., pattern recognition for tracks, may be provided by some LSCs.

- Sending the data to the event builder.

- Synchronising the trigger with the central trigger system. This is done by the local trigger unit (LTU) as explained in the next section.

- Calibrating and monitoring the detector.

In addition, the LSCs can conduct local runs independently from central activity of the data acquisition system, to perform other local activities such as detector calibration, testing and debugging.

Table 3.3: Theta-phi segmentation of the trigger system

θ bin	$\cos\theta$	ϕ bin	ϕ (degree)
1	$-0.980 - -0.596$	1	$0 - 30$
2	$-0.823 - -0.213$	2	$15 - 45$
3	$-0.596 - 0.213$	3	$30 - 60$
4	$-0.213 - 0.596$	$\cdots$	$\cdots$
5	$0.213 - 0.823$	23	$330 - 360$
6	$0.596 - 0.980$	24	$345 - 15$

3.3.2 Trigger

The trigger system [31] is designed to provide high efficiency for the various physics reactions, and good rejection for backgrounds. Several independent trigger conditions are used for most of the physics reactions, resulting in not only a high efficiency but also an enough redundancy to determine the efficiency to a good precision. The efficiency for multihadronic events, for example, within the 98% solid angle accepted by offline selection exceeds 99.9%.

Until the beginning of 1992, the OPAL trigger system consisted of a single stage. On every bunch crossing, each subdetector generates two kinds of trigger signals, namely, 'θ-ϕ' and 'stand-alone' signals. The full solid angle covered by the OPAL detector is divided into 144 overlapping bins, defined as in table 3.3. The θ-ϕ signals from the subdetectors are binned so that they reproduce table 3.3 as closely as possible. The subdetector triggers are generated by six trigger processors:

- Track trigger (TT) [42] generates 144 θ-ϕ triggers indicating the detection of tracks by the jet chamber and the vertex detector. The triggers are based on the hits on the axial wires of the vertex detector, and on the wires of the jet chamber in three 'rings' at variable radii. The z coordinate of the hits are determined, in the vertex chamber, by the time difference of the signals seen at the two ends of the wire, and by the charge division in the jet chamber. It also provides 6 stand-alone signals for $\geq$1, 2, 3 barrel tracks that lie within $|\cos\theta| < 0.82$, and for $\geq$1, 2, 3 tracks in the full detector.

- Time-of-flight trigger (TOF) generates 25 ϕ triggers based on coincidences of the signals from the phototubes at the both ends of each counter. No θ-segmentation is provided.

- Electromagnetic calorimeter trigger (EM) generates 144 θ-ϕ triggers based on analogue sums of typically 48 lead glass counters. The signals from the barrel and endcap calorimeters are combined to form overlapping θ-ϕ signals, which are then discriminated at two thresholds. The low-threshold

signals, corresponding roughly to 1 GeV, are used by central θ-ϕ matrix; the high-threshold signals, corresponding to $\sim$2.5 GeV, generates a stand-alone signal by taking the logical-OR of them. The total energy sums are also formed in the barrel and the endcaps, to provide additional stand-alone triggers.

- Hadron calorimeter trigger (HA) generates triggers based on analogue sums of 12 or 16 towers. As in the case of the EM trigger, multiple thresholds are used to generate 144 θ-ϕ triggers as well as stand-alone signals.

- Muon detector trigger (MU) generates 120 θ-ϕ triggers based on the hits in the barrel and endcap muon detectors. The signals are formed independently in the barrel and the endcaps, and the barrel signals have no segmentation in θ. The muon detector triggers are not overlapping in ϕ as in table 3.3.

- Forward detector trigger (FD) generates only stand-alone triggers based on the energy sums of the presamplers and the calorimeter. Signals from the fine luminosity scintillators are also available. Triggers are formed by back-to-back coincidences of these signals. In addition, 'accidental' triggers are formed by concidences between signals from two different bunch crossings separated by one LEP revolution.

These trigger signals are combined in the central trigger logic (CTL), installed in a purpose-built Eurocrate with a special trigger bus in addition to the standard VME/VSB bus. Figure 3.32 shows an overview of the trigger generation. Trigger signals are generated from θ-ϕ matrix according to four conditions:

- At least one θ-ϕ bin being set in the left endcap, in the right endcap, and in the barrel at the same time.

- Multiplicity counting: $\geq$1 or 2 ϕ bins being set after projection on ϕ. Three adjacent ϕ bins count as one because of the overlap.

- Back-to-back hits in θ-ϕ, except for those in muon detectors.

- At least one θ-ϕ coincidences between two of the five detectors, except for those between the electromagnetic and hadron calorimeters.

These signals are logically combined with stand-alone triggers by the pattern arrangement module (PAM), which derives the trigger decision from the 120 input signals using look-up memories and programmable array logics (PALs).

When a trigger decision is made, the global trigger unit (GTU) broadcasts the information to the local trigger units (LTUs) of all subdetectors. If the event is not accepted by the trigger, a reset pulse is sent 6 μs before the next beam crossing. If the event is accepted, a trigger pulse is sent along with the central

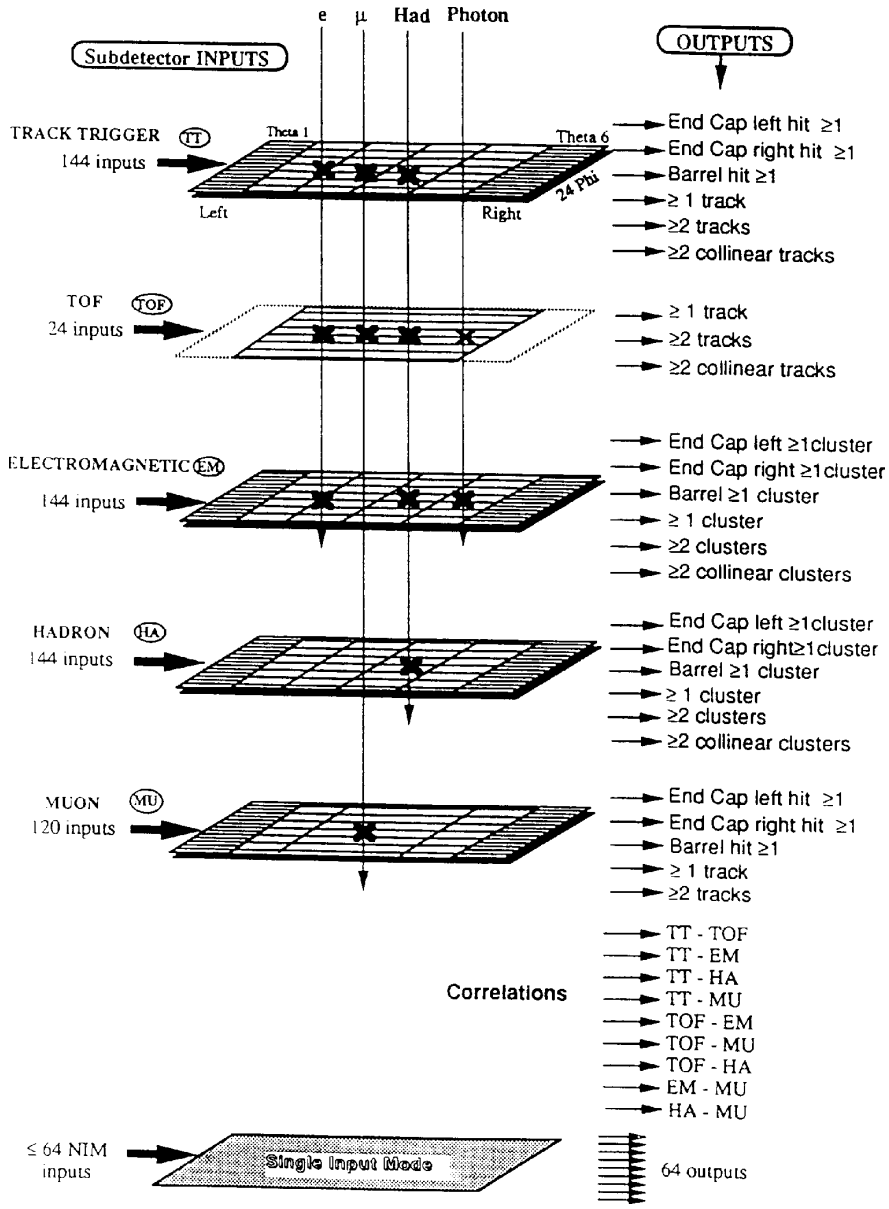

Figure 3.32: Overview of the trigger generation by the θ-ϕ matrix

event number and the PAM input pattern. The LTUs generate a wired-OR busy signal to inhibit further triggers during the readout process of each subdetector.

3.3.3 Pretrigger

Since the beginning of 1992, a pretrigger system [32] has been installed to cope with the increased bunch crossing rate introduced by the 8×8 bunch mode operation. Figure 3.33 shows an overview the new trigger scheme. The pretrigger

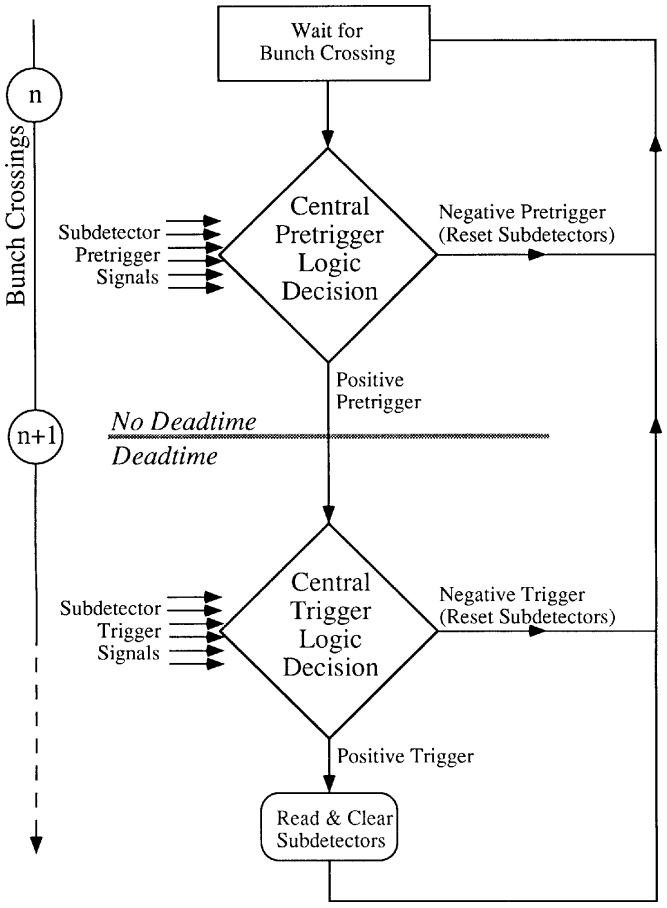

Figure 3.33: Overview of the two-stage trigger system

system is added on top of the existing trigger system with minimum modification. The central pretrigger logic (CPL) takes fast pretrigger inputs from the subdetectors and generates positive or negative pretrigger. If the pretrigger is negative, the subdetectors are reset 4.5 μs before the next bunch crossing, causing no deadtime. On positive pretriggers, the original trigger system starts its decision, which causes deadtime of at least one bunch crossing.

The design of the pretrigger system is similar to the trigger system. Six subdetectors, CV, CJ, TB, EB, EE and ME, send pretrigger signals for 12 overlapping ϕ segments and stand-alone signals. Unlike the trigger system, the pretrigger signals are not segmented in θ. The coverage in θ is $|\cos\theta| < 0.98$. The hadron calorimeters and the barrel muon detector are not used because of their long drift times. The vertex chamber and the jet chamber provides independent signals to make up for the reduced redundancy.

Typical positive pretrigger rate during the eight-bunch operation of LEP is 1–2 kHz, corresponding to 1–2% deadtime.

3.3.4 Event Builder

The data collected by the LSCs are transferred to the event builder via VICbus VME crate interconnections. The lengths of the VICbus cables vary from a few metres to 100 m, and the maximum transfer rate is 6 Mbyte/s for the shortest cable. The event builder merges the sub-events from 16 subsystems to form a complete event record. It is responsibility of the event builder to ensure the integrity of the event record while allowing the LSCs to spend varying processing time. Sub-events from LSCs may not arrive in the chronological order of the events. A large multi-event buffer consisting of two 16 Mbyte dual-ported memories is used to allow for latencies of several seconds. After merging, the event data is transferred to a triple-ported memory connected to the VICbus interface of the filter processor.

The event builder has five processors providing parallelism: two copy processors for sub-event input, a merge processor for event building, a copy processor for event output, and a supervisor processor for controlling the event building process. This system can handle a sustained rate of 25 Hz for 100 kbyte events.

3.3.5 Filter

The filter [46] is an HP Apollo DN10000 RISC-based workstation acting as a software trigger. The workstation is interfaced to VMEbus which houses the VICbus module connected to the event builder. Substantial CPU resources provided by the four CPU board configuration enables a fast on-line analysis to classify each event in the multi-event buffers into various categories of physics candidates. The events flagged as backgrounds are rejected leaving only 64-word event headers. About 30% reduction of the number of events is achieved. The data size of the accepted events are compressed by a factor of five to reduce the data transfer bandwidth and the storage media. The CPU power of the filter is sufficient to handle event rates up to 10 Hz, limited by the data compression process. The filter also manages histograms for on-line monitoring purposes, enabling fast checking of the data quality and diagnosis of possible hardware/software problems.

The output files from the filter is stored in a large staging disk from which the files are written onto 630 Mbyte rewritable optical disks. The optical disk library stores 32 removable optical disks, providing a continuous storage of 20.8 Gbyte without operator intervention. The staging disk also serves as the data buffer for the on-line event reconstruction.

3.3.6 On-line Event Reconstruction

The event records accepted by the filter are reconstructed, i.e., the raw detector data are converted into physical quantities such as particle energies or momenta. This process requires considerable computing resources, and was

traditionally performed on mainframe computers; however, RISC-based high-performance workstations made it possible to integrate such task in the DAQ system. The on-line event reconstruction system provides reconstructed data of sufficient quality to begin physics analysis, and also a quick feedback concerning the operation of the detector.

The data files are buffered in the large storage of the filter, which can accommodate 12 hours of data acquisition at the nominal LEP luminosity. The large buffer is necessary firstly because the event reconstruction requires access to calibration data which become available after a delay of typically 30 minutes. It also helps to reduce the amount of required CPU power because the LEP luminosity, hence the data acquisition rate, changes over several hours; the system should cope with only the average data rate. The reconstruction system is based on three HP Apollo workstations each having four CPU boards. Reconstruction of a hadronic event takes 26 CPU seconds on a DN10000 processor. The throughput of the system is typically 4 events/second.

3.3.7 DAQ Control

The DAQ control system takes routine control of the DAQ subsystems (the LSCs, event builder, filter, etc.), conducts recovery procedures in case of hardware/software malfunction, and maintains databases containing configuration and run-time parameters. The system also communicate with the LEP control system via CERN-wide Ethernet network to obtain information concerning the accelerator status, and to send information about the beam condition seen by the detector. The system consists of several programs running on the on-line VAX cluster:

- A control engine which perform the above tasks.
- A communication process which handles network messages between the engine and the DAQ subsystems.
- A communication process which handles the operator interaction with the engine.
- An ORACLE [68] based database server.

The system is implemented using an object-oriented approach. The control engine consists of a number of finite state machines which naturally reflects the modular and hierarchical structure of the DAQ subsystems. Any change in the DAQ operating status is reflected by the state change of one or more of the finite state machines, which can be initiated by the DAQ subsystems or by the operator action via graphic user interface. The original system was written using the Prolog language [62], which has been replaced by a C++ implementation which provides higher efficiency.

3.3.8 Slow Control

The slow control system [30] monitors the status of the detector and associated hardwares to ensure safe operation. It works independently from the DAQ system, and is implemented on seven dedicated VME stations located in the electronics rooms and a supervising station in the control room. Each station monitors typically 500 analogue and 300 digital channels representing, for example, gas flow rate, high voltage, power supply status and temperature. Some of the subdetectors also has the slow control software running in their LSCs or dedicated VME systems to communicate detector status information with the slow control system. The communication between the slow control stations and the LSCs is based on OS9Net over Ethernet.

The monitored signals are compared with their nominal values and are recorded at regular intervals. Any anomalies are notified to the operator by the graphic interface provided by a Macintosh II computer connected to the main station. Automatic corrective action is taken when possible.

Chapter 4

Analysis environment

This chapter describes the analysis environment and also the main cuts used in this analysis and the expected event signals.

4.1 Data Sample

At LEP, physics data are taken in periods of typically two weeks. The data used in this study have been recorded in the data-taking periods summarized in table 4.1. Each subdetector defines 2-bits of detector status flag for each event, indicating the operating condition of the detector at the moment the event was recorded. The status values are defined as

0 The subdetector status is unknown.

1 The subdetector was not operational.

2 The subdetector was partially operational.

3 The subdetector was fully operational.

The status flag is determined firstly by the local system crate of each subdetector as the event is recorded. Off-line processing may reveal a hidden problem, or be

Table 4.1: Summary of data-taking periods

Year	Period ($\sqrt{s}$)	Date
1995	76 (130 GeV)	31 Oct – 10 Nov
	76 (136 GeV)	11 Nov – 22 NoV
	76 (130 GeV)	22 Nov – 25 Nov
1996	78 (161 GeV)	8 Jul – 25 Jul
	79 (161 GeV)	27 Jul – 16 Aug

able to recover data quality for events with a bad on-line status. In such a case, the status flag is updated in the process of event reconstruction.

4.2 Event Reconstruction

The event reconstruction is a process which takes raw data from the detector as the input and produces physics quantities, e.g., the energy, momentum and the position of each particle, as the output. The reconstruction program used by OPAL is called ROPE. The main function of ROPE is to generate *data summary tapes* (DSTs) from raw data. ROPE can also read DSTs and provides a standard framework for physics analyses.

ROPE is a collection of software modules called *processors*. Each processor has a well-defined set of functions and is referred to by a two-letter name. Most of the processors analyse information from one subdetector after which the processor is named; for example, the EB processor takes raw data from the electromagnetic barrel calorimeter and reconstructs electromagnetic clusters. Some processors take inputs from more than one subdetectors and compute less detector-specific quantities.

SI takes raw data from the silicon microvertex detector and computes hit coordinates.

CV takes raw data from the vertex detector, computes hit coordinates and performs stand-alone pattern recognition and track fitting.

JC (Jet chamber Calibration) takes raw data from the jet chamber and computes hit coordinates.

CJ takes the hit coordinates of the jet chamber and performs stand-alone pattern recognition and track fitting.

OP (On-line Pattern recognition) takes raw data from the jet chamber and performs fast on-line pattern recognition and track fitting.

CZ takes raw data from the z-chambers, computes hit coordinates and performs stand-alone pattern recognition and track fitting.

CT (Central Tracking) takes the track segments found by CV, CJ and CZ processors and performs overall track fitting.

DX (dE/dx) takes the hit information of the jet chamber and performs a dE/dx analysis.

CX (Central verteX) reconstructs secondary vertices using the CT track information.

CS (Central Silicon) associates SI hits to CT tracks.

CE (Central Extrapolation) extrapolates CT tracks to the outer detectors.

CA (Central Association) associates extrapolated tracks to hits and track segments in the outer detectors.

TB takes raw data from the time-of-flight counters and computes time and position of the hits.

PB takes raw data from the barrel presampler and forms reconstructed clusters.

EB takes raw data from the barrel electromagnetic calorimeter and forms energy clusters.

PE takes raw data from the endcap presampler and forms reconstructed clusters.

EE takes raw data from the endcap electromagnetic calorimeter and forms energy clusters.

EM (Electromagnetic calorimeter Merging) merges the energy clusters separately found by PB, EB, PE and EE processors.

HB takes raw data from the barrel hadron calorimeter and forms energy clusters.

HE takes raw data from the endcap hadron calorimeter and forms energy clusters.

HP takes raw data from the pole-tip hadron calorimeter and forms energy clusters.

HM (Hadronic calorimeter Merging) merges the energy clusters separately found by HB, HE and HP processors.

MB takes raw data from the barrel muon detector and forms muon track segments.

ME takes raw data from the endcap muon detector and forms muon track segments.

MM (Muon Merging) merges the muon track segments found by MB and ME processors.

FD takes raw data from the forward detectors and performs analysis.

SW takes raw data from the silicon tangsten detectors and forms energy.

In addition, there are processors with more general purposes and various utilities. Two of them are of special importance for this study:

MT (Mathing method between charged tracks and calorimeter clusters)

ID (particle IDentification) subroutine library for particle identification.

MT is a package of codes, which provides momentum of each particle observed by Central Tracker (CT), by ECAL (EB+EE), and by HCAL (HB+HE+HP). MT removes double-counting of energy by using matching algorithm.

The ID library defines various algorithms of identifying particles, especially electrons and muons, using the OPAL detector.

4.3 Tracks and Clusters

The "good" charged track selection criteria are as follows:
Tracks were required to have at least 20 measured spatial hits, more than 50% of the hits geometrically expected, and a transverse momentum exceeding 50 MeV. Backgrounds from cosmic rays and beam gas interactions were suppressed by requiring each event to have at least one hit in the time-of-flight counter. The spatial distance of closest approach from track to the beam axis in the x-y plane, $|d_0|$, was required to be less than 8.0 cm, recovering acceptance for long lived L^- and L^0 candidates whose decay lengths are up to 10 cm. The distance along the beam with respect to the interaction point, $|z_0|$, was required to be less than 30 cm.

The "good" neutral cluster selection criteria are as follows:
Electromagnetic clusters in the barrel region were required to have an energy of at least 100 MeV, and the clusters in the endcaps to have an energy of at least 250 MeV and to contain at least two adjacent lead glass blocks. Clusters in the hadron calorimeters were required to have an energy of at least 0.6 GeV in the barrel and endcaps, and at least 2 GeV in the pole tip detectors. The silicon tungsten calorimeter clusters were required to have at least 2 GeV of deposited energy. Furthermore, clusters in the forward calorimeter were required to have at least 1.5 GeV and in the gamma-catcher at least 5 GeV.

Event observables such as the total visible energy or hemisphere momenta were calculated as follows. The track momenta and the momentum vectors of EM or HCAL calorimeter clusters not associated with charged tracks were first summed. When a calorimeter cluster was associated with charged tracks, the scalar sum of the associated charged track momenta was subtracted from the cluster energy to reduce double counting. If the energy of a cluster was smaller than the scalar sum of the associated track momenta, the cluster energy was not used. The masses of all charged particles were set to the charged pion mass and the meutral clusters were assumed to be caused by photons.

4.4 Cut parameters

On the selection of the expected signals, the effective reduction of the Standard Model process background is a main task. Therefore the choice of the cut variable in order to distinguish the expected topology from the background processes is important. In this section, the most important cut parameters are described. In Fig. 4.1 cross-sections of the Standard Model process backgrounds are shown as a function of $\sqrt{s}$.

4.4.1 Good track requirement $N_{\rm ch}$

Normally the requirement of the number of charged tracks, $N_{\rm ch}$, depends on the final states of the expected signals. For example in the $L^0\bar{L}^0$ search $N_{\rm ch}$ was required to be at least 4, then the almost dilepton events $\ell^+\ell^-(\gamma)$ events were rejected by this requirement. The ratio of the number of tracks which satisfied the good track selection criteria to the total number of reconstructed tracks was required to be greater than 0.2 in order to reject beam-gas and beam-wall backgrounds. This requirement is very loose not to make some discrepancy of the statistics between the real data and Monte Carlo samples.

4.4.2 Forward Detectors (FD, SW, GC) veto

The forward veto cut was applied in order to distinguish the expected signals from two-photon process background. As in the hard two-photon process the electron (positron) beam should recoil to transverse direction with respect to z direction, it is important to detect the recoiled electron (positron). The coverage of the forward detectors is down to the polar angle of 26 mrad. If the polar angle of the recoiled electron (positron) direction is larger than 26 mrad, the forward detectors could detect the two-photon signals as a large energy deposit from electron or positron. Fig. 4.2 shows Feynman diagram of the two-photon process. And in Fig. 4.3 the typical event sample rejected by the forward detector veto is shown.

4.4.3 Transverse Missing momentum (P_t, $P_t^{\rm HCAL}$)

The two-photon events remaining after the forward detector vetoes can be efficiently removed from the data by investigating the transverse momentum (P_t) in the event, excluding the hadron calorimeter, and also the transverse momentum including the hadron calorimeter ($P_t^{\rm HCAL}$).

The definition of the transverse missing momentum is

$$\overrightarrow{P} \;=\; \sum_{i=1}^{Nch} \overrightarrow{P}_i, \;\; \overrightarrow{P}_{mis} \;=\; -\,\overrightarrow{P}$$

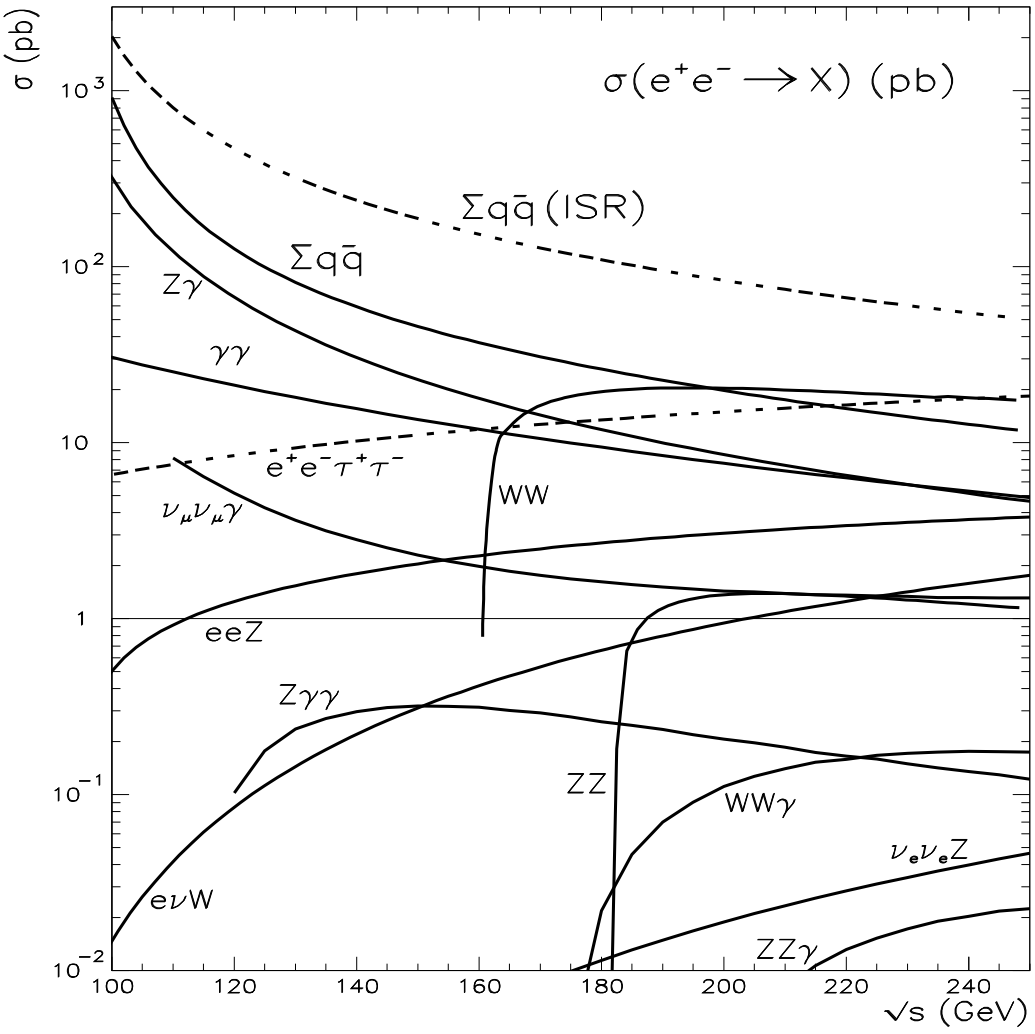

Figure 4.1: Cross-sections of the Standard Model process backgrounds as a function of $\sqrt{s}$.

$$P_t \;=\; \sqrt{P_{mis}(x)^2 \;+\; P_{mis}(y)^2}.$$

Since the polar angle of the recoiled electron (positron) in these events should be less than 26 mrad, the maximum transverse momentum for two-photon processes can be roughly estimated as $\mathrm{E_{beam}} \times 0.026 \times 2$. For $\sqrt{s} = 136$ GeV (161 GeV) the maximum transverse momentum for two-photon events will be 3.5 GeV (4.2 GeV) in the ideal detector. Thus by demanding the P_t value to be greater than certain threshold, which depends on $\sqrt{s}$, most of the two-photon events can be removed.

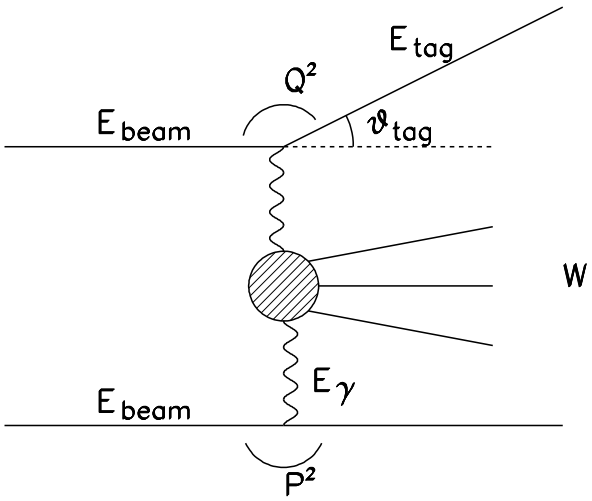

Figure 4.2: Feynman diagram of the two-photon process. $\theta_{\rm tag}$ is the angle of the recoiled electron.

Fig. 4.4 shows a real event sample removed by the P_t cut.

In the case of $\mathrm{L}^- \to \nu_{\mathrm{L}}\mathrm{W}^{*-}$, P_t and P_t^{HCAL} values compared with the visible energy were expected to be large due to the undetectable heavy neutrino ν_{L} whose mass should be larger than 39.5 GeV (the LEP1 limit [20]).

Although most of the events from two-photon processes were rejected by the P_t cut, the P_t^{HCAL} cut was additionally applied to reject occasional two-photon events with a high transverse momentum neutral hadron. On the other hand the events overlapped with an accidental cosmic-ray or accidental HCAL noise could only be rejected by P_t cut. Therefore both of P_t and P_t^{HCAL} cuts were needed. Fig. 4.5 shows a real event sample rejected by the P_t cut, but not by P_t^{HCAL}.

4.4.4 $|\cos\theta_{\mathrm{miss}}|$

"Radiative return" events from $\mathrm{e}^+\mathrm{e}^- \to \mathrm{Z}\gamma$ have a potential of the background source since the direction of large fraction of the initial state radiative photons tends to parallel with the beam direction; these photons escape into the beam

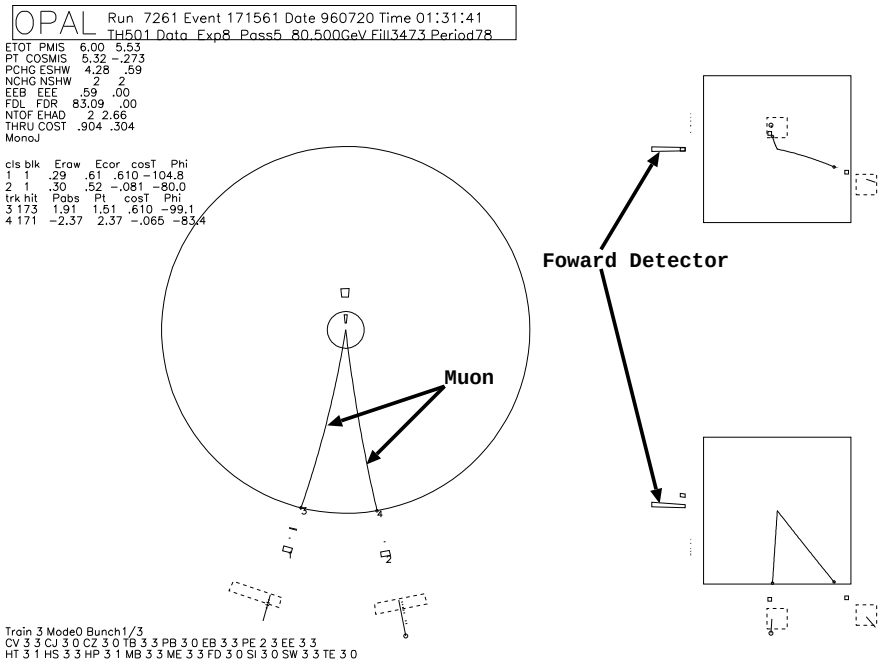

Figure 4.3: Typical event sample $e^+e^-\mu^+\mu^-$ two-photon process background. This background has an acoplanar event topology, but there is a large energy deposit on forward detector by a recoiled electron. The description of the event figure is summarized in Appendix B.

pipe. In this process the almost final state particles produced through real Z boson would lie on the forward/backward region ($|\cos\theta| > 0.8$) in the detector. Fig. 4.6 shows the $|\cos\theta|$ distribution of the the initial state radiative photon. Fig. 4.7 shows one of the typical "Radiative return" events.

As the fraction of the forward region particles is larger, the reliability of information on tracks would be lower, because of the worse track momentum resolution. In order to reject "radiative return" events and also two-photon process, the polar angle of the missing momentum direction $\theta_{\rm miss}$ is calculated, where $|\cos\theta_{\rm miss}| = 1$ means that the missing momentum direction is parallel with the beam direction.

The definition of $|\cos\theta_{\rm miss}|$ is

$$|\cos\theta_{\rm miss}| = \frac{|P_{mis}(z)|}{|\overrightarrow{P}_{mis}|}$$

4.4.5 Thrust and $|\cos\theta_{\rm thrust}|$

Thrust cut is important to reject $\tau^+\tau^-(\gamma)$ and two-photon process backgrounds. The definition of thrust and $|\cos\theta_{\rm thrust}|$ are as follows:

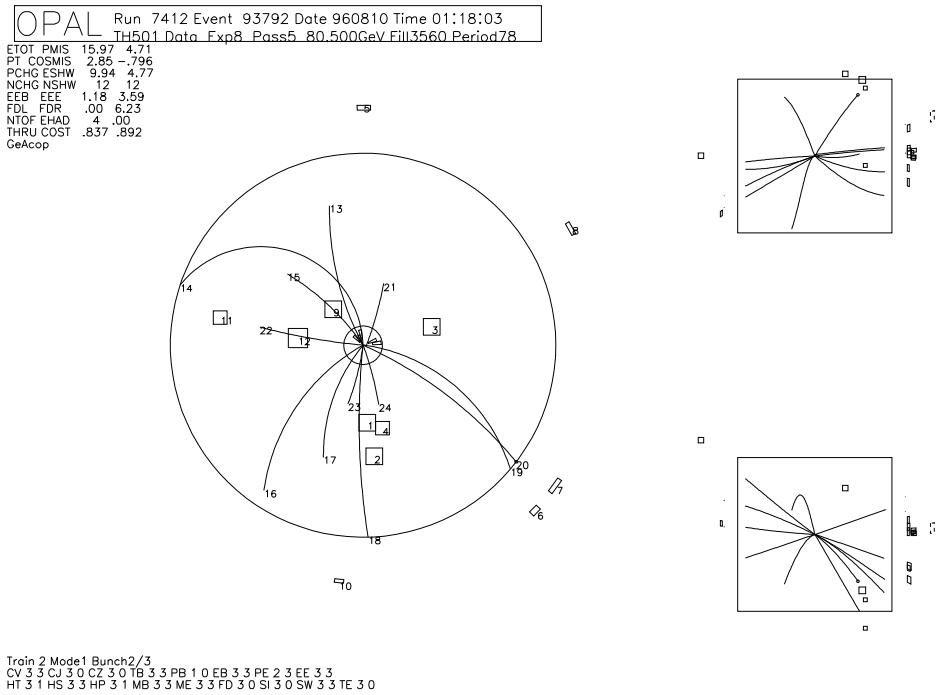

Figure 4.4: A sample event rejected by the transverse momentum cut. This event is considered as two-photon process background. Events due to this background process have relatively low missing transverse momentum because scattered high energy electron tends to escape into the beam pipe.

$$Thrust \;=\; max\frac{\sum_i |\,\vec{n}\cdot\vec{P_i}\,|}{\sum_i |\,\vec{P_i}\,|}, \quad |\,\vec{n}\,| \;=\; 1$$

$$|\cos\theta_{\rm thrust}| \;=\; \frac{|v(z)|}{|\,\vec{v}\,|},$$

where the thrust axis $\vec{v}$ is given by the $\vec{n}$ vector for which maximum is attained. The allowed range of thrust is between 0.5 and 1.0, with a 2-jet event corresponding to Thrust ≈ 1 and an isotropic event to Thrust ≈ 0.5. Thus the back-to-back or collinear events can be efficiently removed by the requirement Thrust < 0.9, for example. Fig. 4.8 and Fig. 4.9 show two sample events rejected by the thrust requirement.

Normally, a back-to-back event is rejected by acoplanarity angle cut (described below). But if there were not significant energy deposits in the both thrust hemispheres, which are separated by the plane perpendicular to the thrust axis, the acoplanarity angle will not be a reliable cut parameter.

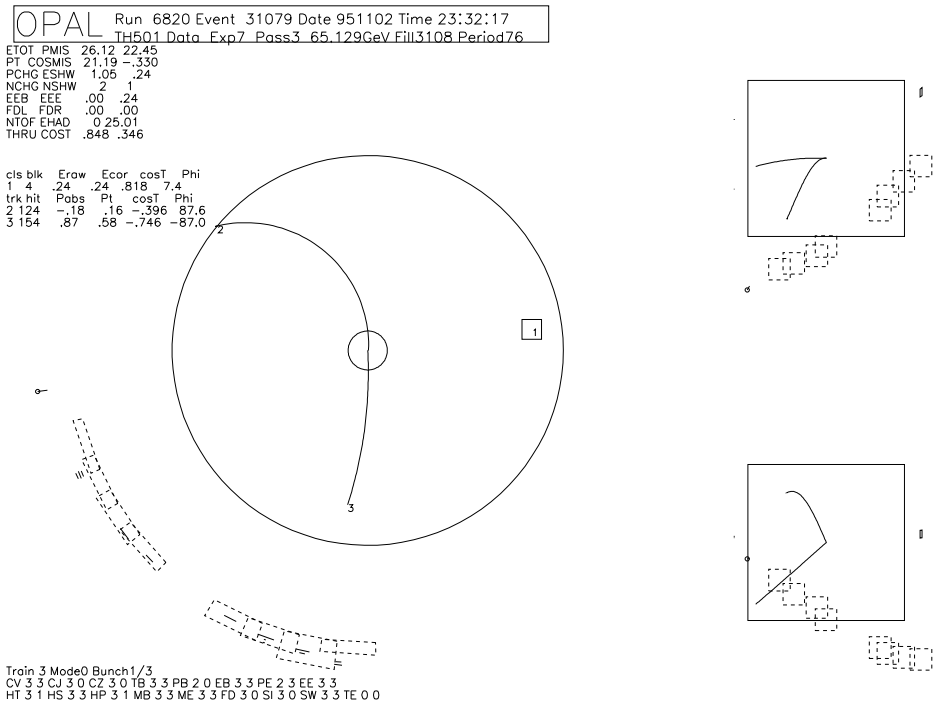

Figure 4.5: Event sample rejected by the transverse momentum cut. This event could be two-photon process overlapped with an accidental cosmic-ray. The P_t was less than 1 GeV but P_t^{HCAL} was larger than 20 GeV by the large energy deposit of the accidental cosmic-ray.

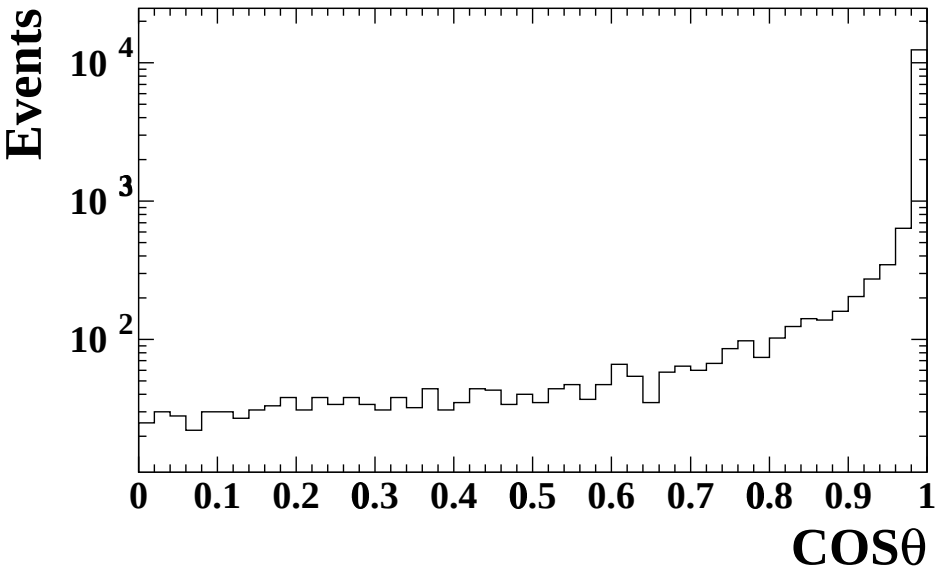

Figure 4.6: Distribution of $|\cos\theta|$ of the initial state radiative photon in the "Radiative return" lepton pair events at the centre-of-mass energy = 161 GeV.

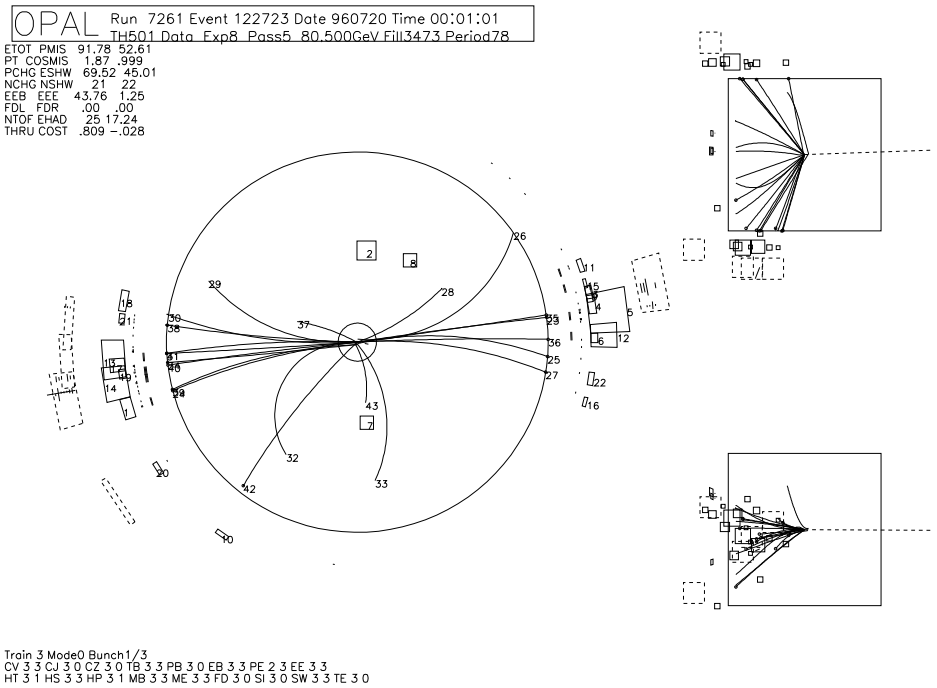

Figure 4.7: Typical event sample of "Radiative return" process background. This background has large ambiguity of the acoplanarity angle. Dashed line indicates the missing momentum direction.

4.4.6 Further rejection of two-photon process

The typical event topologies of the two photon process are shown in Fig. 4.4 and Fig. 4.10. The characteristics of two-photon process events remaining after the forward veto and P_t cut are large fractional energy deposits in the forward region $|\cos\theta| > 0.8$ and large missing momentum with respect to the beam direction by the undetected electron. In order to reject these backgrounds the following cuts were used:

$$\frac{E(|\cos\theta|>0.8)}{E_{\rm vis}} < 1.5\ \frac{\rm E_{vis}}{\sqrt{\rm s}},$$

$$|P^{\rm mis}_{\rm (z)}| < 0.4\ {\rm E_{vis}},$$

where $E(|\cos\theta|>0.8)$ is the sum of the visible energy over $|\cos\theta| > 0.8$ and $|P^{\rm mis}_{\rm (z)}|$ is the missing momentum along the beam direction. Fig. 4.10 shows a real event removed by these two-photon process rejections.

4.4.7 Backcone Energy ($E_{\rm back}$)

For $\rm L^- \to \nu_\ell W^{*-}$ search a serious background comes primarily from hadronic events in which a mismeasurement of the energy of a jet leads to an artificial

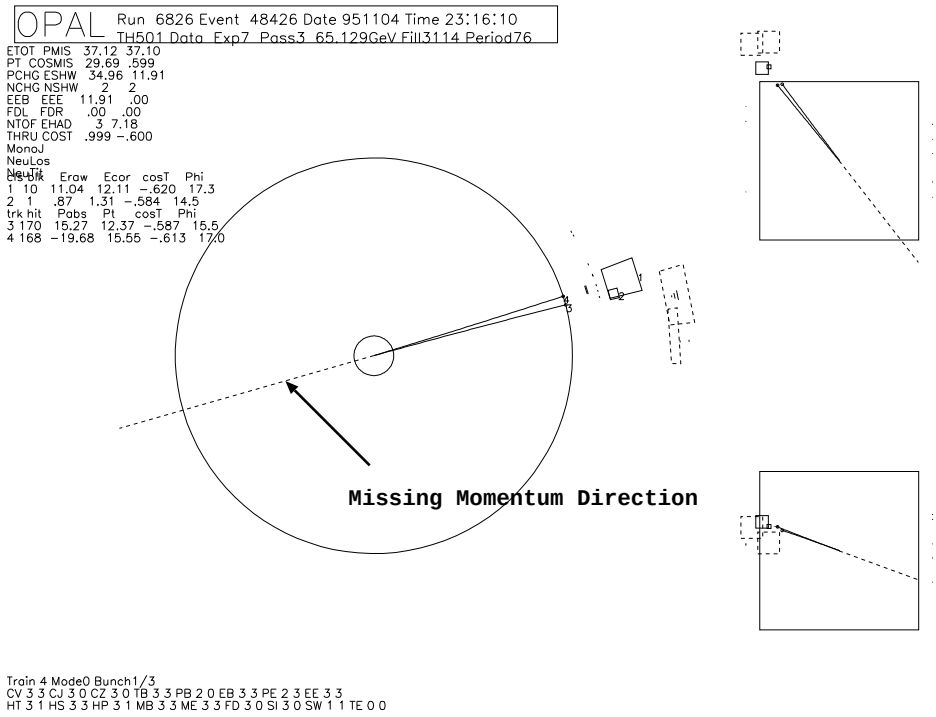

Figure 4.8: A sample of $e^+e^- \rightarrow Z\gamma^* \rightarrow \nu\bar{\nu}\tau^+\tau^-$ or $\nu\bar{\nu}q\bar{q}$ four-fermion process background. This background was significantly rejected by thrust cut. Dashed line indicates the missing momentum direction.

missing momentum. This missing momentum may produce a large acoplanarity angle and tends to lie along the direction of jets in ordinary multihadron events. We defined the total energy sum ($E_{\rm back}$) within a cone of half-angle of θ_1 around the direction of the missing momentum.

$$E_{\rm back} \;=\; \sum_{i=1}^{N} E_i,\;\; (if\;\; \theta_{ik} \;<\; \theta_1)$$

where k means the missing momentum direction and i is the ith track or cluster direction.

4.4.8 Acoplanarity Angle ($\phi_{\rm acop}$)

The acoplanarity angle $\phi_{\rm acop}$ was defined as $\pi - \phi_{\rm open}$, where $\phi_{\rm open}$ was the azimuthal opening angle between the directions of the momentum sums of the particles in the two thrust hemispheres separated by the plane perpendicular to the thrust axis, i.e.

$$\cos\phi_{\rm open} = \frac{(\overrightarrow{P_1}\times\hat{z})\cdot(\overrightarrow{P_2}\times\hat{z})}{|\overrightarrow{P_1}\times\hat{z}|\cdot|\overrightarrow{P_2}\times\hat{z}|},$$

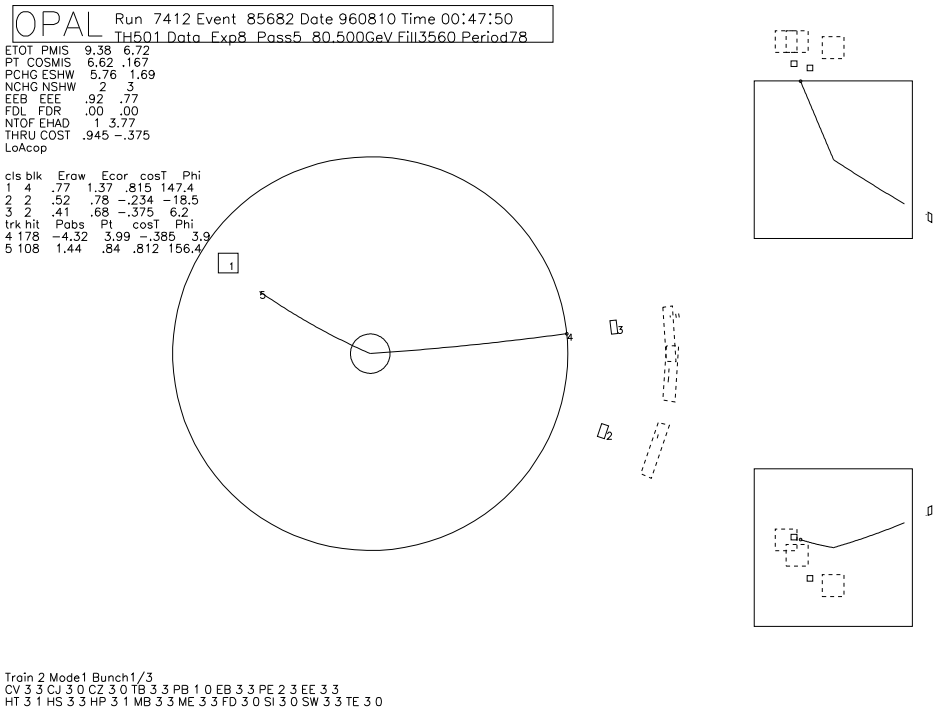

Figure 4.9: A sample of $e^+e^- \rightarrow e^+e^-\tau^+\tau^-$ two-photon process background. This event topology tends to be an acoplanar, but rejected by thrust cut.

where $\hat{z}$ is the electron-beam direction vector, $\overrightarrow{P_1}$ and $\overrightarrow{P_2}$ are the two hemisphere momenta. In this definition, the significant energy deposits for both hemispheres are needed; in case of no energy deposit on one hemisphere, the event is recognized as a monojet. If the energy deposit of the one hemisphere is much lower than that of the other hemisphere, the ambiguity of the $\phi_{\rm acop}$ will be large and the event might be recognized as one with a large $\phi_{\rm acop}$, which is searched for. This kind of event, however, tends to have a large thrust value and can be rejected by thrust cut, since the thrust value is predominantly determined by one hemisphere with a large energy deposit. The typical event is shown in Fig. 4.9, which has large $\phi_{\rm acop}$ and can be rejected by thrust cut.

4.4.9 Jet Finding

Jets were formed using the Durham algorithm [94] with a jet resolution parameter of $y_{\rm cut} = 0.006$ for LEP1.5 analysis and 0.004 for LEP2 analysis.

$$y_{ij} = \frac{2\ min(E_i^2, E_j^2)(1-\cos\theta_{ij})}{E_{\rm cm}^2}$$

If a calculated y_{ij} of two clusters or tracks is smaller than cut-off values $y_{\rm cut}$ and also has a minimum among all the combinations, two particles are joined into

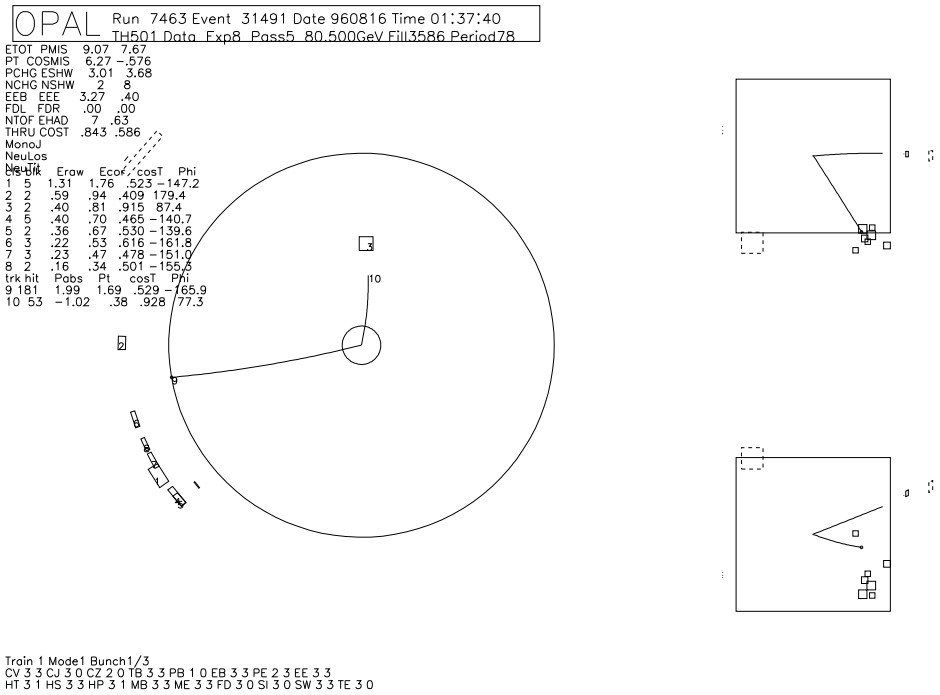

Figure 4.10: A sample event rejected by two-photon cut (rejected by both requirements). This event was considered as a $e^+e^- \rightarrow e^+e^-\tau^+\tau^-$ two-photon process in which e^+e^- escaped into beam pipe.

one. In this algorithm lower energy particles are joined first, and so on until all clusters and tracks are separated by a "distance" larger than the cut-off $y_{\rm cut}$. The clusters remaining at the end of the procedure are called "jets". The number of "jets" explicitly depends on the $y_{\rm cut}$ value. Fig. 4.11 shows the $y_{\rm cut}$ dependence of the number of events, where $N_{\rm jet} \geq 4$ is required in each event.

4.4.10 Isolated Lepton Tagging

The selection criteria for isolated leptons are the following:

The momentum of the lepton candidate was required to be less than 40 GeV and larger than 2 GeV.

Electron

The output of the neural network described in [95] was greater than 0.95. There were no other tracks within a cone of half angle 15° around an electron track.

Muon

The point of closest approach of each extrapolated track to the track segment reconstructed independently in the muon detectors was examined. The angular separation of these points and the muon segments was calculated in azimuthal

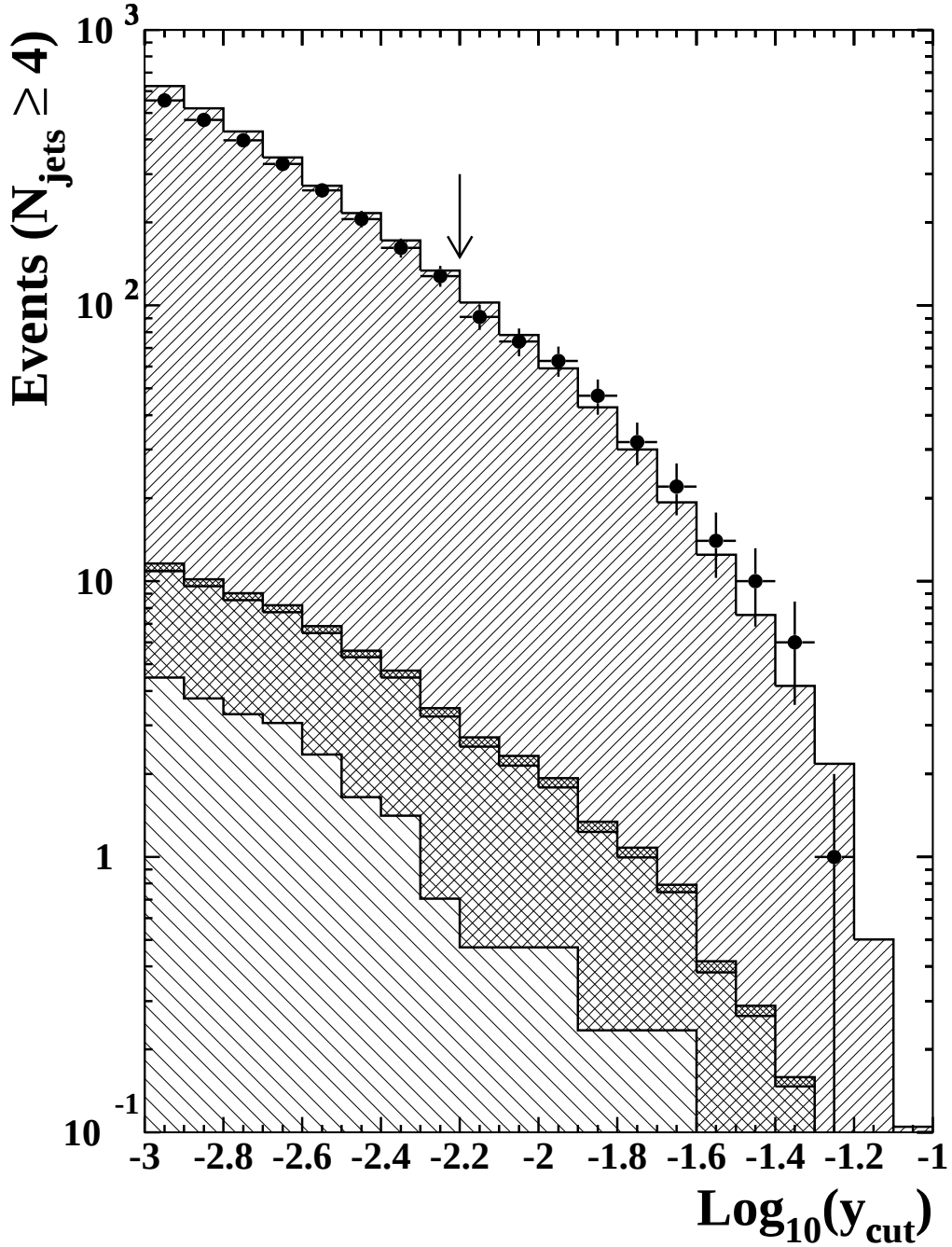

Figure 4.11: Number of events which cantain at least four jets using the Durham algorithm [94] as a function of the jet resolution parameter $y_{\rm cut}$. The arrow indicates the cut value ($y_{\rm cut} = 10^{-2.2}$) used in LEP1.5 analysis.

and polar angle. The sum χ_{pos} in quadrature of these deviations, normalized by their errors, was calculated [96]. The track was identified as a muon when χ_{pos} was less than three. In regions outside the muon chamber acceptance, muons were identified by an algorithm including the hadron calorimeters as described in [98]. There were no tracks within a cone of half angle 15° around the muon track.

Tau 1-prong
All the following requirements should be satisfied for a reconstructed jet. The reconstructed jets described above were used to identify taus.
1. There was only one track in the jet with momentum larger than 3 GeV, and the momenta of other tracks in the same jet must be less than 1 GeV.
2. There were no other tracks within a cone of half angle 15° around the high momentum track.
3. The invariant mass of the track and neutral clusters within the cone should be less than 2.5 GeV. These requirements also have a sensitivity for prompt electron or muon tracks.

Tau 3-prong
A reconstructed jet was taken as a tau three prong decay, if the following three conditions were satisfied.
1. There were only three tracks in the jet.
2. These three tracks must be inside a cone of half angle 15° around the jet axis.
3. The invariant mass of the three tracks and neutral clusters within the cone should be less than 2.5 GeV. The vector sum of the three charged particle momenta should be greater than 3 GeV.

Since the reconstructed jet was used for a τ lepton identification, the efficiency and the probability of the mis-identification depend on the chosen $y_{\rm cut}$ value in Durham jet-finding algorithm.

4.5 Expected Event topology

This section describes the decay properties of the heavy lepton and the expected event topologies.

4.5.1 $L^0\bar{L}^0$

In this analysis the heavy neutral lepton $L^0\bar{L}^0$ was assumed to decay into a light lepton (e, μ or τ) and a virtual W boson, which decays into $q\bar{q}'$ or $\ell\nu_\ell$, through the flavour changing charged current. The flavour changing neutral current was not taken into account in this analysis, since this coupling depends on the theoretical models.

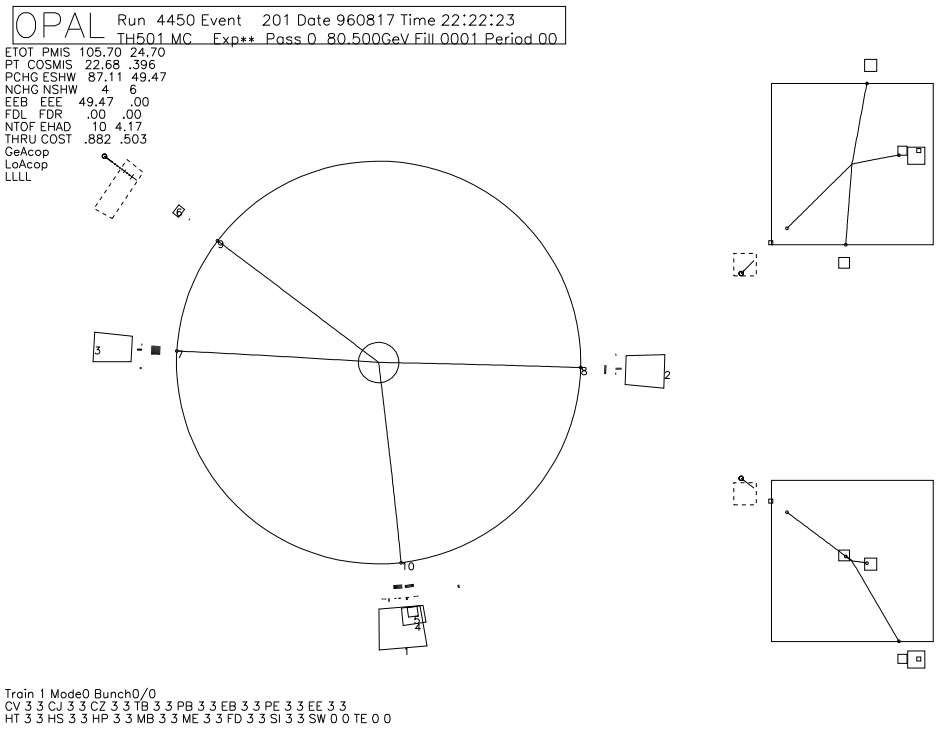

Figure 4.12: $L^0\bar{L}^0 \rightarrow eW^*eW^* \rightarrow e\nu\mu e\nu\tau$ (Monte Carlo)

The expected final states are as follows:

$L^0\bar{L}^0 \rightarrow \ell W^*\ell W^* \rightarrow$

- $\ell\ell\nu_\ell\ell\nu_\ell\ell$ (1) (Fig. 4.12)
- $\ell\ell\nu_\ell\ell qq^{'}$ (2) (Fig. 4.13)
- $\ell\ell qq^{'}q^{''}q^{'''}$ (3) (Fig. 4.14)

The expected event topology of the final state (1) is 4 leptons (satisfying automatically 4 jets requirement[1]) with large missing momentum and missing energy. In this case, the main background is $e^+e^- \rightarrow Z^0Z^*/\gamma^* \rightarrow \ell^+\ell^-\ell'\bar{\ell}'$ four-fermion process. The difference between the expected signal and the this background process is the total visible energy. The expected signal tends to have a lower visible energy by the undetectable two neutrinos but the $\ell^+\ell^-\ell^{'+}\ell^{'-}$ background should have a full visible energy. However the $\tau\tau\ell^{'+}\ell^{'-}$ background has a possibility not to be eliminated in the analysis, but this was not so serious because of the lower cross-section.

[1]In this analysis isolated leptonsare counted as jets

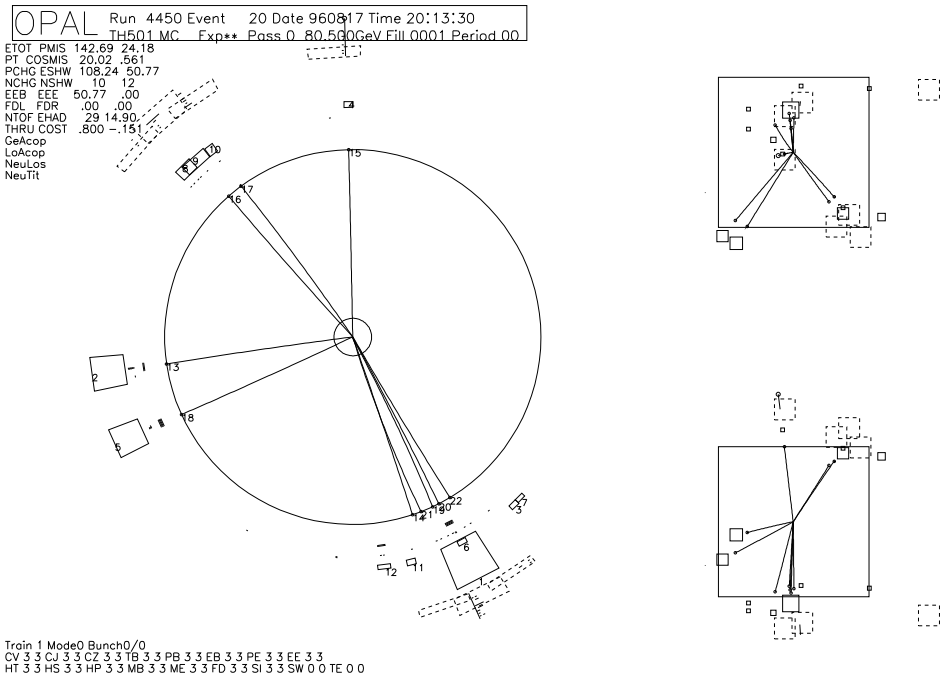

Figure 4.13: $L^0\bar{L}^0 \rightarrow eW^*eW^* \rightarrow e\nu\mu eqq'$ (Monte Carlo)

Secondly the expected event of the final state (2) has normally 5 jets (3 leptons + 2 hadron jets) with missing momentum. In this case the number of the reconstructed jets could be mainly four or five, because of the large possibility of overlapping of the two adjacent jets which depends on the jet reconstruction algorithm and the $y_{\rm cut}$ value. Therefore if the number of the reconstructed jets happened to be four, heavy quark multihadron events and $e^+e^- \rightarrow Z^0Z^{0*}/\gamma^* \rightarrow \ell^+\ell^-q\bar{q}$ process, or $\ell\nu cs$ process (including WW events at LEP2) could be the main background.

Finally, the final state (3) has a 6 jets event topology including 2 leptons with no missing momentum (for $\ell = \tau$ case, some missing momentum is expected). This final state event topology mostly has a clear $L^0\bar{L}^0$ signal. In this case the background process is negligible.

The common feature for all the final states is that the expected signal have at least 2 isolated leptons and at least 4 jets (including leptons). In selecting $L^0\bar{L}^0$ candidates, this feature is most important. Hence on the optimisation of this analysis procedure, the choice of the value $y_{\rm cut}$ and the algorithm of isolated leptons were main subjects.

4.5.2 $L^+L^- \rightarrow \nu_L W^*\nu_L W^*$

The process $L^+L^- \rightarrow \nu_L W^*\nu_L W^*$ occurs if the mass of the heavy neutral lepton ($\nu_L \equiv$ stable L^0) lies between 39.5 GeV (the lower mass limit from LEP1) and

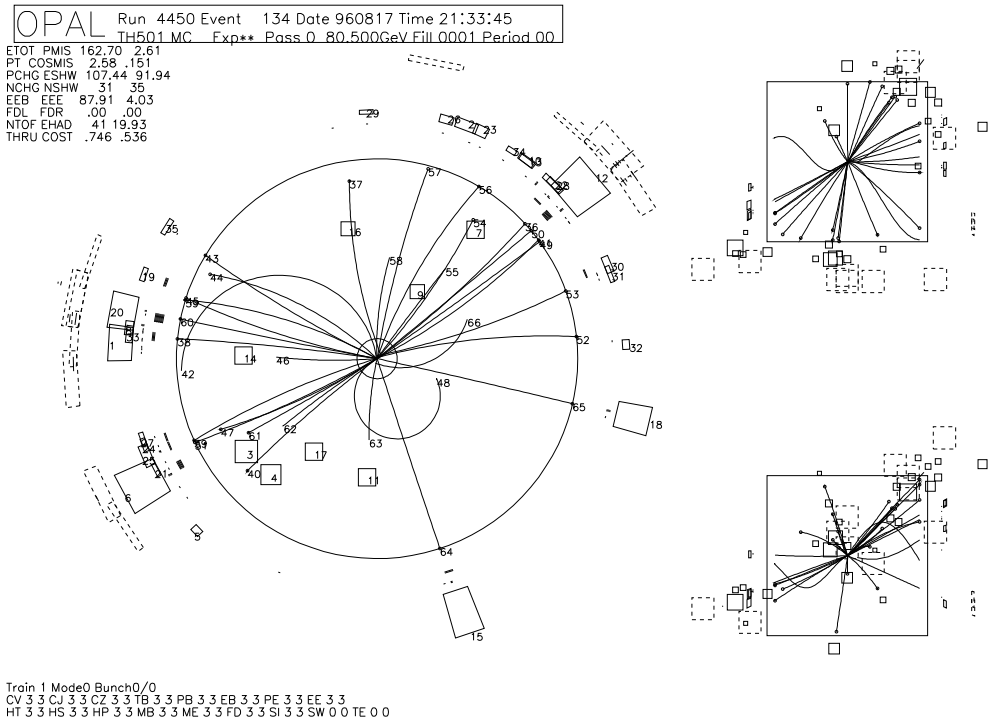

Figure 4.14: $L^0\bar{L}^0 \rightarrow eW^*eW^* \rightarrow eqq'eq''q'''$ (Monte Carlo)

the produced heavy charged lepton mass, and if the heavy neutral leptons do not decay within the detector ($|V_{L^0\ell}|^2 < 10^{-13}$). If $|V_{L^0\ell}|^2$ is larger than 10^{-11}, the heavy neutral lepton can be detected in the detector.

The expected decay products in this case are:

$L^+L^- \rightarrow \nu_L W^* \nu_L W^* \rightarrow$

- $\nu_L \nu_L \nu_\ell \ell \nu_\ell \ell$ (Fig. 4.15)
- $\nu_L \nu_L \nu_\ell \ell qq'$ (Fig. 4.16)
- $\nu_L \nu_L qq'q''q'''$ (Fig. 4.17)

The available information in the event is less than that of $L^0\bar{L}^0$ case because of the two undetectable neutrinos. However these two neutrinos provide the following characteristic features:

- large missing transverse momentum with respect to the visible energy,
- large acoplanarity angle.

The main Standard Model background for this topology depends on the mass difference between m_{L^-} and m_{ν_L}. For the small mass difference case, the serious

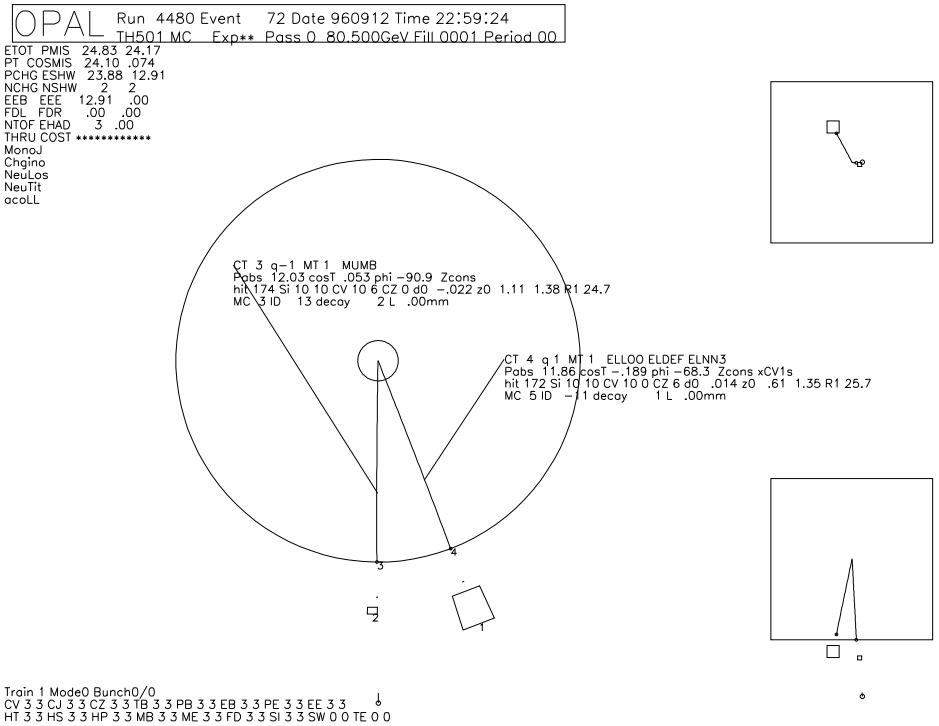

Figure 4.15: $L^+L^- \rightarrow \nu_L W^* \nu_L W^* \rightarrow \nu_L \nu \mu \nu_L \nu e$ (Monte Carlo)

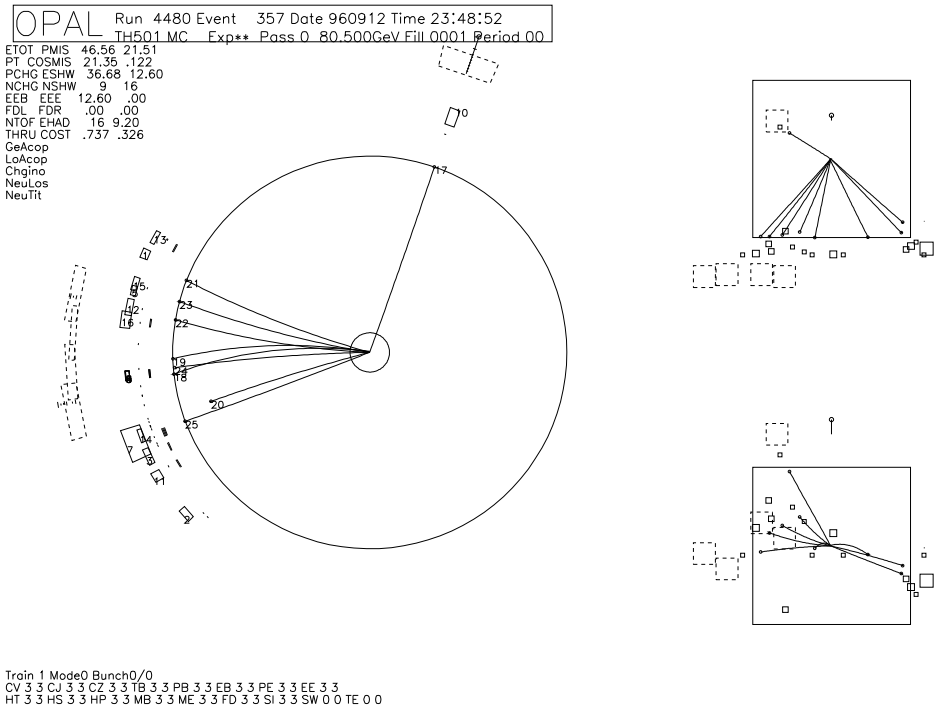

Figure 4.16: $L^+L^- \rightarrow \nu_L W^* \nu_L W^* \rightarrow \nu_L \nu \mu \nu_L q q'$ (Monte Carlo)

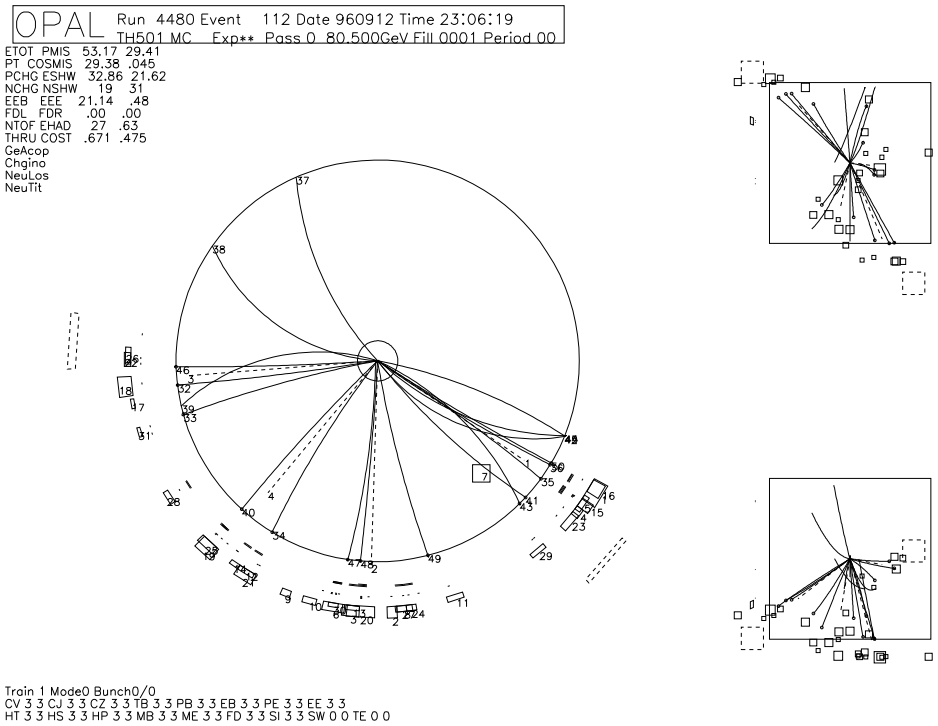

Figure 4.17: $L^+L^- \rightarrow \nu_L W^* \nu_L W^* \rightarrow \nu_L q q' \nu_L q'' q'''$ (Monte Carlo)

background is the two-photon process. This background tends to have a large energy deposit in the forward region ($|\cos\theta| > 0.8$) and to have a peak at $|\cos\theta_{\rm miss}| = 1.0$ because of the high energy electron (positron) escaping into the beam pipe. For the large mass difference case, the main backgrounds are four-fermion processes such as $\nu_\ell\nu_\ell q\bar{q}$ or $\ell\nu_\ell q\bar{q}$ (including WW events). The $\nu_\ell\nu_\ell q\bar{q}$ background is very serious especially at $\sqrt{s} = 161$ GeV and could be an irreducible background. On the other hand, the $\ell\nu_\ell q\bar{q}$ four-fermion background can be rejected by removing the event with high momentum track, because the $L^+L^- \rightarrow \nu_L\nu_L\nu_\ell\ell\nu_\ell\ell$ and $\nu_L\nu_L\nu_\ell\ell q q'$ signals tend to have lower track momenta.

4.5.3 $L^+L^- \rightarrow \nu_\ell W^* \nu_\ell W^*$

The process $L^+L^- \rightarrow \nu_\ell W^* \nu_\ell W^*$ occurs if m_{L^-} was smaller than m_{L^0}.

The expected signals are:

$L^+L^- \rightarrow \nu_\ell W^* \nu_\ell W^* \rightarrow$

- $\nu_\ell\nu_\ell\nu_\ell\ell\nu_\ell\ell$ (Fig. 4.18),
- $\nu_\ell\nu_\ell\nu_\ell\ell q q'$ (Fig. 4.19),

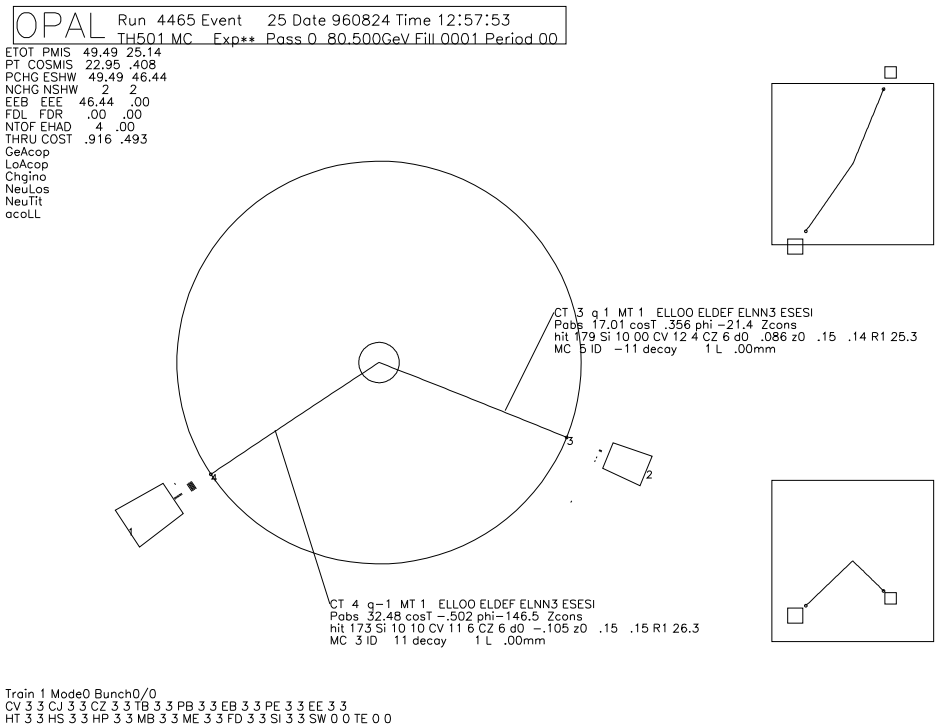

Figure 4.18: $L^+L^- \rightarrow \nu_\ell W^* \nu_\ell W^* \rightarrow \nu_\ell \nu e \nu_\ell \nu e$ (Monte Carlo)

- $\nu_\ell \nu_\ell q q' q'' q'''$ (Fig. 4.20).

The expected topology is similar to the decay $L^+L^- \rightarrow \nu_L W^* \nu_L W^*$ but with larger transverse missing momentum. The main background processes are $\nu_\ell \nu_\ell q\bar{q}$ and $\ell \nu_\ell q\bar{q}$ final state events (also W^+W^-'s at $\sqrt{s} = 161$ GeV). The $q\bar{q}$ multihadron events could be serious background when the mismeasurement of the energy cluster or track momentum occurred, because this kind of mismeasurement could cause a large missing transverse momentum or large acoplanarity angle.

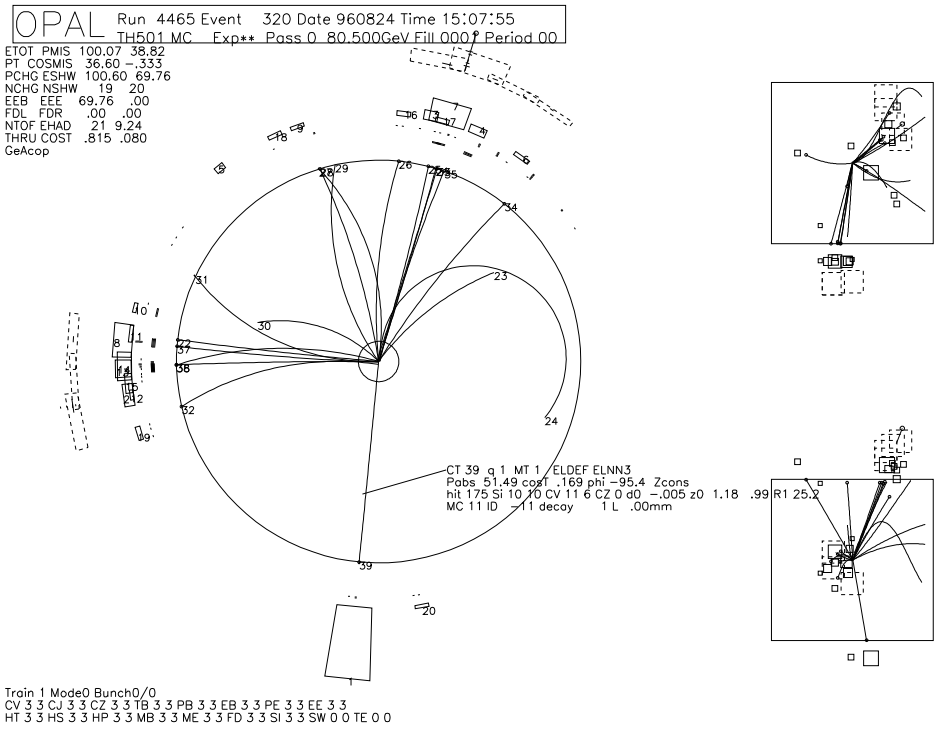

Figure 4.19: $L^+L^- \rightarrow \nu_\ell W^* \nu_\ell W^* \rightarrow \nu_\ell \nu e \nu_\ell q q'$ (Monte Carlo)

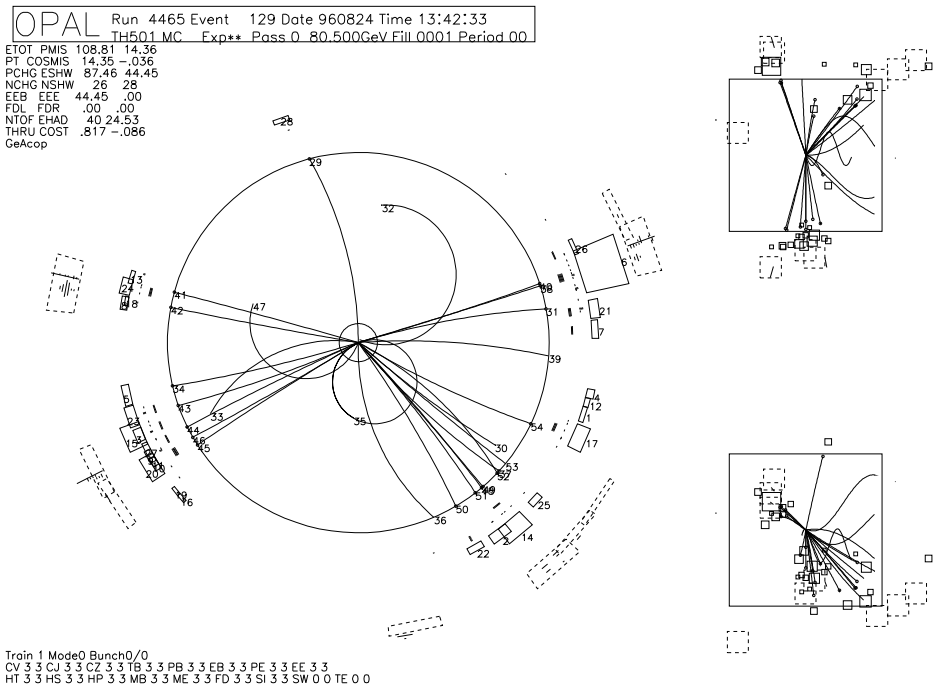

Figure 4.20: $L^+L^- \rightarrow \nu_\ell W^* \nu_\ell W^* \rightarrow \nu_\ell q q' \nu_\ell q'' q'''$ (Monte Carlo)

Chapter 5

Analysis at LEP1.5

The candidate events of heavy leptons were searched for in the following three cases:

(A) $L^0 \to \ell W^*$ via lepton flavour mixing, where ℓ is e, μ or τ, and W^* is a virtual W boson.

(B) $L^- \to \nu_L W^{*-}$, where ν_L is a stable heavy neutrino ($m_{\nu_L} > 39.5$ GeV).

(C) $L^- \to \nu_\ell W^{*-}$, where ν_ℓ is ν_e, ν_μ or ν_τ. The decay occurs via lepton flavour mixing.

For case (A) and (C), the heavy lepton was assumed to decay into a virtual W boson through the flavour changing charged current, since the ordinary V−A coupling on the heavy lepton decay was considered. In some heavy lepton models (for instance the models including 'See-Saw' mechanism [7]), the FCNC is allowed because the additional mixing with the right-handed neutrinos spoils the unitarity of the CKM matrix for the leptonic charged current, which in turn spoils the GIM cancellation and leads to off-diagonal Z^0 couplings. However in this analysis, this constraint was not considered to avoid the model dependent theoretical bias (these mixing effects are discussed in [8]).

The two W^* bosons in $L^0\bar{L}^0$ or L^+L^- event can decay either leptonically or hadronically. The analysis presented here is sensitive to all the possible combinations of the decay topologies and was designed to search for heavy leptons with masses above the current LEP1 experimental limits. In the selecting the expected candidate events, the analysis criterion have been applied separately each for $\sqrt{s} = 130$ GeV + 136 GeV data (LEP1.5) and 161 GeV data (LEP2), because the cross-section of the main background for the expected event topology is significantly different, particularly two-photon and four-fermion processes. The two-photon process backgrounds were most serious for the case (B) analysis. In order to separate this background from the expected signal, the magnitude of the missing transverse momentum is the key parameter, because the missing

momentum of the expected signal is made by missing heavy neutrinos and that of the two-photon background is generated by the recoiled high energy beams. Therefore the missing transverse momentum of this background is proportional to the beam energy. At LEP2 the background cross-sections not only of WW events but also of ZZ* and Weν processes increase compared with LEP1.5. So in order to reject these background processes, the different optimization of the cuts was tried. This chapter describes the LEP1.5 analysis in the following order:

- Monte Carlo simulation
- analysis of case (A)
- analysis of case (B) and (C)
- systematic errors

5.1 Monte Carlo Event Simulation

The $L^0\bar{L}^0$ and L^+L^- events have been generated using the TIPTOP [82] generator, which includes the effects of spin correlations in the weak decays. The generator was modified so that JETSET 7.4 [83] can be used for the hadronization, which includes gluon radiation. Initial state photon radiation was implemented in the generator based on the calculations of Berends and Kleiss [21]. The $L^0\bar{L}^0$ events were generated at six values of m_{L^0} from 40 GeV to 63 GeV for the different final states $eW^* + eW^*$, $\mu W^* + \mu W^*$ and $\tau W^* + \tau W^*$ together with other combination of leptons. The L^+L^- events were generated at 26 points in the (m_{L^-}, m_{ν_L}) plane for case (B) and at six values of m_{L^-} from 45 GeV to 65 GeV for case (C). The following background processes were simulated in this analysis:

$q\bar{q}(\gamma)$ Hadronic events with an isolated lepton coming from a heavy flavour decay, or with an isolated track misidentified as a lepton, are important backgrounds for the L^0 search. In the L^- search, the dominant $q\bar{q}(\gamma)$ background events are multijet events with one or more poorly reconstructed jet momenta. The JETSET 7.4 [83] and PYTHIA 5.7 [83] Monte Carlo generators were used for multihadron events.

$\ell\ell(\gamma)$ The KORALZ [84] event generator was used for the generation of $\tau^+\tau^-(\gamma)$ and $\mu^+\mu^-(\gamma)$ events. A sample of $e^+e^-(\gamma)$ events was generated using the BABAMC generator [86]. Radiative and non-radiative τ pairs are potential sources of background for the topology of two acoplanar jets, because neutrinos from the τ decays carry away energy and momentum.

'$\gamma\gamma$' In case (B), particularly for a small mass difference between L^- and ν_L, events from two-photon processes are the main backgrounds. Since the

visible energy is small in this case, the two-photon event topology is similar to the signal event topology. The PYTHIA 5.7 [83] Monte Carlo generator was used for generating events from two-photon processes where the Q^2 of both photons is smaller than 1.3 GeV^2 and the invariant mass of the photon-photon system ($M_{\gamma\gamma}$) is greater than 3 GeV. For events with higher Q^2 the generator TWOGEN [87] was used. Event samples for all the possible processes (final state hadrons from point-like $\gamma\gamma \to q\bar{q}$ processes and from vector meson dominance, and all $e^+e^-\ell^+\ell^-$ final states) were generated. Two-photon events were not generated in the region $Q^2 < 1.3$ GeV^2 and $M_{\gamma\gamma} < 3$ GeV. This region did not represent a serious background to the search presented here.

4-fermion Events from the four-fermion processes $\ell^+\ell^- q\bar{q}$, $\ell\nu_\ell q\bar{q}'$, $\nu_\ell\bar{\nu}_\ell q\bar{q}$ and $\nu\bar{\nu}\ell^+\ell^-$ are serious backgrounds for the $L^0\bar{L}^0$ and L^+L^- searches. The EXCALIBUR generator was used to generate all the four-fermion processes [91].

Generated signal and background events were processed through the full simulation of the OPAL detector [92], and the same event analysis chain was applied to these simulated events as to the data.

5.2 Selection of $L^0\bar{L}^0$ candidates (case A)

The expected signal topologies are discussed in Sec. 4.5. The following event selection criteria were applied. The numbers of remaining events after each cut are listed in Table 5.1, for data and for simulated background and signal samples.

(A1) The $N_{\rm ch}$ was required to be at least four, and the ratio of the number of tracks which satisfied the selection criteria to the total number of reconstructed tracks was required to be larger than 0.2 in order to reject beam-gas and beam-wall backgrounds.

(A2) In order to reduce the background from two-photon processes and multihadronic events in which one of the jet axes was close to the beam direction, the total energy deposited in each silicon tungsten calorimeter was required to be less than 5 GeV. Furthermore the energy was required to be less than 2 GeV in each forward calorimeter and less than 5 GeV in each side of the gamma-catcher. In addition, $|\cos\theta_{\rm thrust}|$ was required to be less than 0.95 in order to reduce beam-gas and beam-wall background events as well as events from two-photon processes.

(A3) The visible energy normalized to the centre-of-mass energy, $E_{\rm vis}/\sqrt{s}$, was required to be greater than 0.4 to reduce background from two-photon processes. The distributions of $E_{\rm vis}/\sqrt{s}$ after cut (A2) are shown in Fig. 5.1(a)

Table 5.1: The remained numbers of Monte Carlo events (in the $L^0\bar{L}^0$ search), normalised to the integrated luminosity, are compared with the data after each cut for various background processes. Numbers are also given for three samples of simulated $L^0\bar{L}^0$ events. The numbers of events expected from two-photon processes ('$\gamma\gamma$') do not include the region $M_{\gamma\gamma} < 3$ GeV with $Q^2 < 1.3$ GeV^2.

case (A)	data	total bkg.	$q\bar{q}(\gamma)$	$\ell\ell(\gamma)$	'$\gamma\gamma$'	4-f	$L^0\bar{L}^0$		
m_{L^0} (GeV)							50	60	60
Decay							τ	μ	e
no cuts	–	–	1645	6458	105k	20.2	1000	1000	1000
cut (A1)	43.0k	29.8k	1604	65.9	28.1k	13.6	984	984	978
cut (A2)	9581	10.7k	1219	59.7	9397	10.9	837	906	860
cut (A3)	1264	1297	1218	55.4	13.8	10.1	808	902	857
cut (A4)	124	130	127	0.21	0.78	2.48	641	781	739
cut (A5)	0	1.13	0.71	0.08	0.00	0.34	316	603	561
cut (A6)	0	0.70	0.33	0.08	0.00	0.29	295	582	537

Table 5.2: The selection efficiencies (in %) of L^0 candidates for three decay modes ($L^0 \to eW^*$, μW^* and τW^*) as a function of m_{L^0}. The errors are statistical only.

Decay	m_{L^0}=40 GeV	45 GeV	50 GeV	55 GeV	60 GeV	63 GeV
$L^0 \to eW^*$	44.2 ± 1.6	44.6 ± 1.6	50.0 ± 1.6	49.6 ± 1.6	53.7 ± 1.6	57.9 ± 1.6
$L^0 \to \mu W^*$	43.8 ± 1.6	50.7 ± 1.6	52.3 ± 1.6	53.7 ± 1.6	58.2 ± 1.6	62.5 ± 1.5
$L^0 \to \tau W^*$	21.1 ± 1.3	22.4 ± 1.3	29.5 ± 1.4	31.1 ± 1.5	30.7 ± 1.5	28.2 ± 1.4

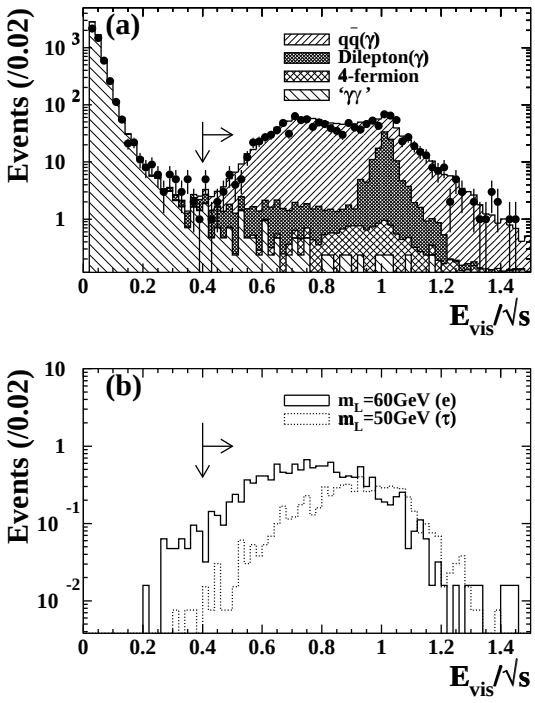

Figure 5.1: Distribution of visible energy normalized to the centre-of-mass energy before cut (A3). The arrows indicate the position of the cut and the region accepted.

for the data and the simulated background events, and in Fig. 5.1(b) for the simulated $L^0\bar{L}^0$ events.

(A4) The number of jets was required to be greater than or equal to four. The distributions of the number of jets after cut (A3) are shown in Fig. 5.2(a) for the data and the simulated background events, and in Fig. 5.2(b) for the simulated $L^0\bar{L}^0$ events.

(A5) The number of isolated leptons (e, μ or τ) was required to be at least two. The distributions of the number of isolated leptons after cut (A4) are plotted in Fig. 5.3(a) for the data and the simulated background events, and in Fig. 5.2(b) for the simulated $L^0\bar{L}^0$ events.

(A6) The invariant mass of the two isolated leptons with the largest momenta was required to be larger than 10 GeV. This cut rejected multihadron events with two lepton candidates in a single jet. The distributions of the invariant mass of the two isolated leptons just before this cut are shown in Fig. 5.4.

No events were observed in the data after the above selection. This result was consistent with the number of expected background events of 0.70. The detection efficiency for $L^0\bar{L}^0$ events was calculated for six m_{L^0} values between 40

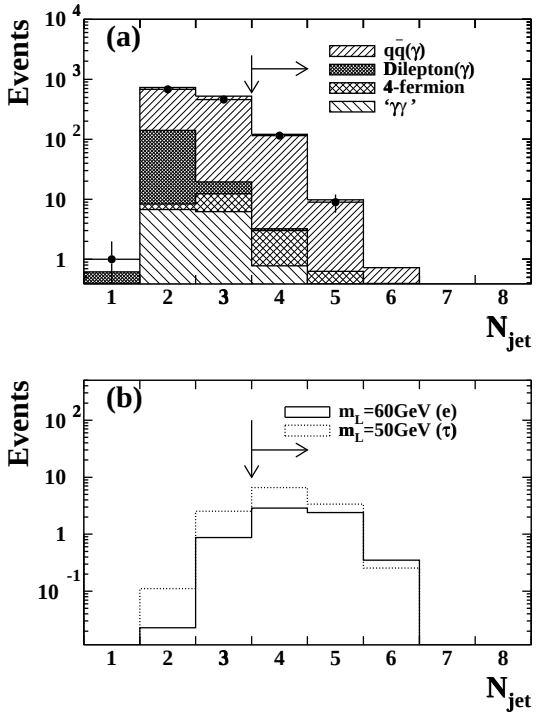

Figure 5.2: Distribution of number of jets formed by Durham algorithm with $y_{\rm cut}$ = 0.006 before cut (A4). The arrows indicate the position of the cut and the region accepted.

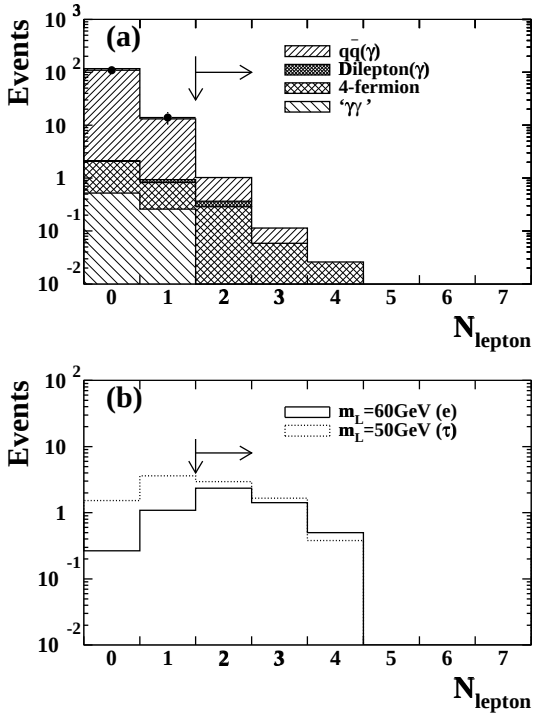

Figure 5.3: Distribution of number of isolated leptons before cut (A5).

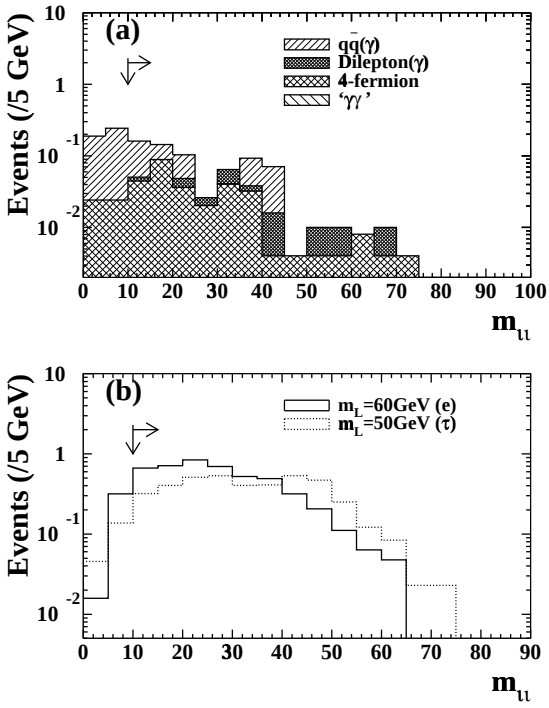

Figure 5.4: Distribution of the invariant mass of two isolated leptons with the largest momenta before cut (A6).

and 63 GeV. The efficiency for m_{L^0} in the range of 50-63 GeV was about 50-60% for $\mathrm{L}^0\bar{\mathrm{L}}^0 \to \mathrm{eW}^*\mathrm{eW}^*$ or $\mu\mathrm{W}^*\mu\mathrm{W}^*$ events, and about 30% for $\mathrm{L}^0\bar{\mathrm{L}}^0 \to \tau\mathrm{W}^*\tau\mathrm{W}^*$ events. The detection efficiencies for the expected signals are summarized in Table 5.2.

These analysis criteria have a sensitivity for tagging all light leptons (e, μ and τ). The three different final states of $\mathrm{L}^0\bar{\mathrm{L}}^0 \to \mathrm{eW}^* + \mathrm{eW}^*$, $\mu\mathrm{W}^* + \mu\mathrm{W}^*$ and $\tau\mathrm{W}^* + \tau\mathrm{W}^*$ were considered in calculating efficiencies. If the decay products of $\mathrm{L}^0\bar{\mathrm{L}}^0$ were mixed ($\mathrm{L}^0\bar{\mathrm{L}}^0 \to \mathrm{eW}^*\mu\mathrm{W}^*$, $\mathrm{eW}^*\tau\mathrm{W}^*$ or $\mu\mathrm{W}^*\tau\mathrm{W}^*$), the efficiencies would have values intermediate between the cases considered here. The efficiencies for the $\mathrm{L}^0\bar{\mathrm{L}}^0 \to \tau\mathrm{W}^*\tau\mathrm{W}^*$ case were the lowest in this analysis, and hence lead to the most conservative limit.

5.3 Selection of $\mathrm{L}^+\mathrm{L}^-$ candidates (case B, C)

The expected signal topologies are discussed in Sec. 4.5. Similar cuts were applied to select the signal events for case (B): $\mathrm{L}^- \to \nu_{\mathrm{L}}\mathrm{W}^{*-}$ and case (C): $\mathrm{L}^- \to \nu_\ell\mathrm{W}^{*-}$; however, some cut values were optimised differently for the two cases. The number of events remaining after each cut are listed in Table 5.3 for case (B) and in Table 5.6 for case (C). For comparison both tables also include the corresponding numbers of simulated background and $\mathrm{L}^+\mathrm{L}^-$ events.

The following selection criteria were applied:

(B1,C1) The $N_{\rm ch}$ was required to be at least two, and the ratio of the number of tracks which satisfied the selection criteria to the total number of reconstructed tracks was required to be greater than 0.2.

(B2,C2) The criteria for energy deposits in the silicon tungsten calorimeter, the forward calorimeter and the gamma-catcher were identical to those in the $L^0\bar{L}^0$ analysis. The $|\cos\theta_{\rm thrust}|$ was required to be less than 0.9. The $|\cos\theta_{\rm thrust}|$ cut is harder than in the L^0 analysis because the acoplanarity angle, which is discussed later, becomes unreliable if the jet axes are too close to the beam direction.

(B3,C3) Events from two-photon processes with a small visible energy were efficiently reduced by demanding the event transverse momentum (P_t), calculated excluding the hadron calorimeter clusters, to be larger than 4 GeV and the transverse momentum ($P_t^{\rm HCAL}$), calculated including the hadron calorimeter clusters, to be larger than 5 GeV in case (B) (cut B3). In case (C), the transverse momentum was expected to be larger, hence P_t and $P_t^{\rm HCAL}$ were required to be larger than 10 GeV and 12 GeV, respectively (cut C3). The distributions of $P_t^{\rm HCAL}$ after cut (B2) are shown in Fig. 5.5(a) for the data and the simulated background events, and in Fig. 5.5(b) for the simulated $L^- \to \nu_L W^{*-}$ (case (B)) events.

(B4,C4) "Radiative return" events from $e^+e^- \to Z\gamma$, where the γ escaped close to the beam direction, were rejected by requiring that the polar angle of the missing momentum direction $\theta_{\rm miss}$ satisfy $|\cos\theta_{\rm miss}| < 0.8$. The distributions of $|\cos\theta_{\rm miss}|$ after cut (B3) are shown in Fig. 5.6 for case (B).

(B5,C5) If an electromagnetic cluster was not accompanied by any track within a cone of half-angle 25° around its direction, it was defined to be an isolated photon. Events with an isolated photon of energy, E_γ, greater than 15 GeV were rejected for case (B) (cut B5). The distributions of E_γ after cut (B4) are shown in Fig. 5.7 for case (B). For case (C) the energy cut was increased to 25 GeV (cut C5). The cut values were optimized to maintain high efficiency for the signal. This cut rejects some $e^+e^- \to Z\gamma$ events.

(B6,C6) A visible energy cut was applied to reduce both multihadron and four-fermion background. The visible energy of L^+L^- events in case (B) was expected to be smaller than about 50 GeV, since the two heavy ν_L's carry away a significant fraction of the energy. The $E_{\rm vis}/\sqrt{s}$ was required to be smaller than 0.35 for case (B) (cut B6). The distributions of $E_{\rm vis}/\sqrt{s}$ after cut (B5) are shown in Fig. 5.8 for case (B). In case (C), on the other hand, the $E_{\rm vis}/\sqrt{s}$ was required to be larger than 0.3 and smaller than 0.8 (cut C6).

Table 5.3: The remained numbers of Monte Carlo events, normalised to the integrated luminosity of the data, for various background processes are compared with data after each cut for the $L^- \to \nu_L W^{*-}$ case. Numbers of expected events are also given for three samples of simulated L^+L^- events. The numbers of events expected from two-photon processes do not include the region $M_{\gamma\gamma} < 3$ GeV with $Q^2 < 1.3$ GeV^2.

case (B)	data	total bkg.	$q\bar{q}(\gamma)$	$\ell\ell(\gamma)$	'$\gamma\gamma$'	4-f	L^+L^-		
m_{L^-} (GeV)							63	60	55
m_{ν_L} (GeV)							55	45	45
no cuts	–	–	1645	6458	105k	20.2	1000	1000	1000
cut (B1)	123k	47.1k	1606	963	44.5k	18.0	965	969	975
cut (B2)	50.5k	16.4k	1142	839	14.4k	11.1	892	881	882
cut (B3)	748	780	593	168	12.2	6.58	469	749	622
cut (B4)	379	421	299	112	5.46	4.89	452	689	577
cut (B5)	289	340	231	98.5	5.46	4.76	452	687	577
cut (B6)	13	14.9	0.06	9.14	4.68	1.06	452	687	574
cut (B7)	8	7.44	0.06	2.16	4.16	1.06	452	683	569
cut (B8)	0	1.36	0.06	0.12	1.04	0.14	387	598	480
dijet	0	1.27	0.06	0.11	1.04	0.06	287	495	416
cut (B10)	0	0.35	0.00	0.03	0.26	0.06	267	437	375
monojet	0	0.09	0.00	0.01	0.00	0.08	100	103	64
(B10)+monojet	0	0.44	0.00	0.04	0.26	0.14	367	540	439

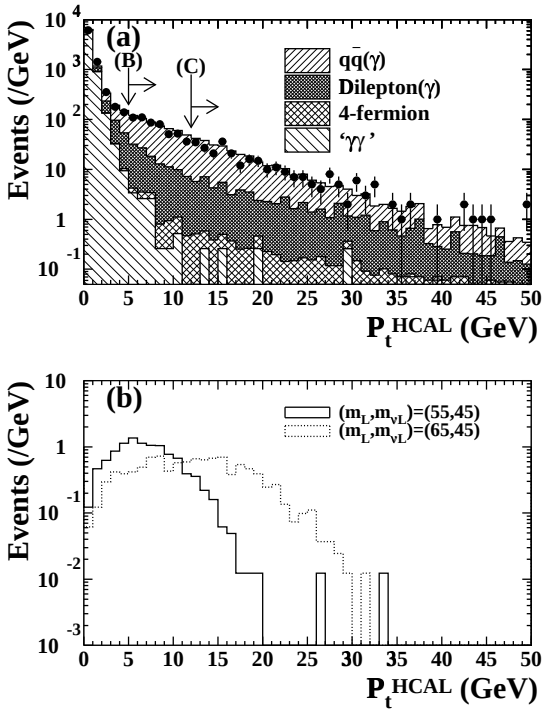

Figure 5.5: Distribution of the missing transverse momentum, $P_t^{\rm HCAL}$, before cut (B3).

(B7,C7) Events which were kinematically consistent with $\tau^+\tau^-(\gamma)$ were rejected. The tracks and the clusters in an event were divided into two hemispheres defined by the plane perpendicular to the thrust axis. Events were identified as $\tau^+\tau^-(\gamma)$ if the charged multiplicities in the two thrust hemispheres were a single track in one hemisphere and either one or three tracks in the opposite hemisphere, the sum of the charged particle momenta in one of the hemispheres was greater than 10 GeV, and the charged particle masses of both hemispheres were smaller than the τ mass. Assuming that the event was a $\tau^+\tau^-(\gamma)$, the maximum value of the acoplanarity angle was calculated from the absolute value of the charged particle momentum sum in each hemisphere. If the measured acoplanarity angle was smaller than this calculated maximum value, the event was considered to be a $\tau^+\tau^-(\gamma)$ and rejected.

(B8,C8) In order to reject events containing two back-to-back jets or leptons, the thrust of the events was required to be less than 0.9. The distributions of the thrust after cut (B7) are shown in Fig. 5.9 for case (B).

Events were classified into two different categories according to the following criteria. If one of the hemispheres had an energy smaller than 1 GeV and contained no good track, the event was categorised as a monojet event; otherwise the event was classified as a dijet event. All the events classified

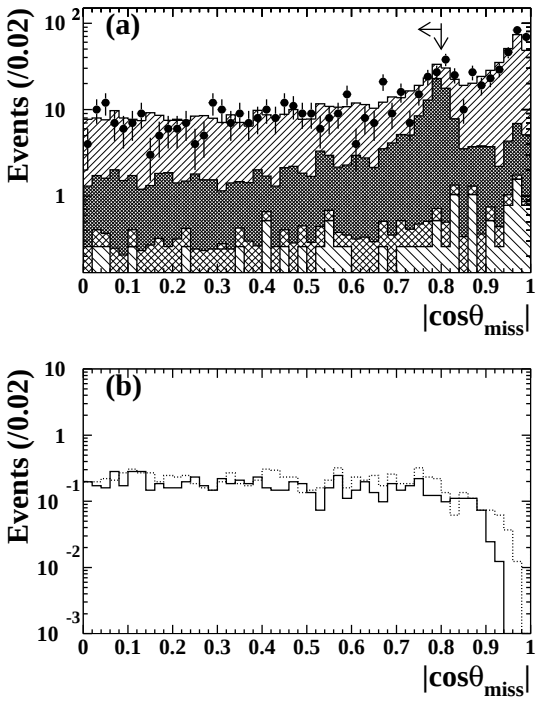

Figure 5.6: Distribution of $|\cos\theta_{\rm miss}|$ before cut (B4). The peak around $|\cos\theta_{\rm miss}| \approx 0.8$ is due to the degraded energy resolution in the region with a larger amount of material in front of the calorimeter.

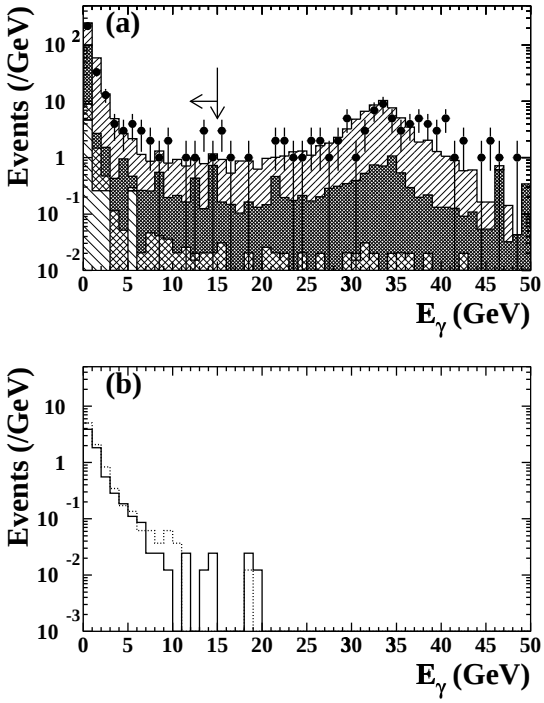

Figure 5.7: Distribution of E_γ before cut (B5).

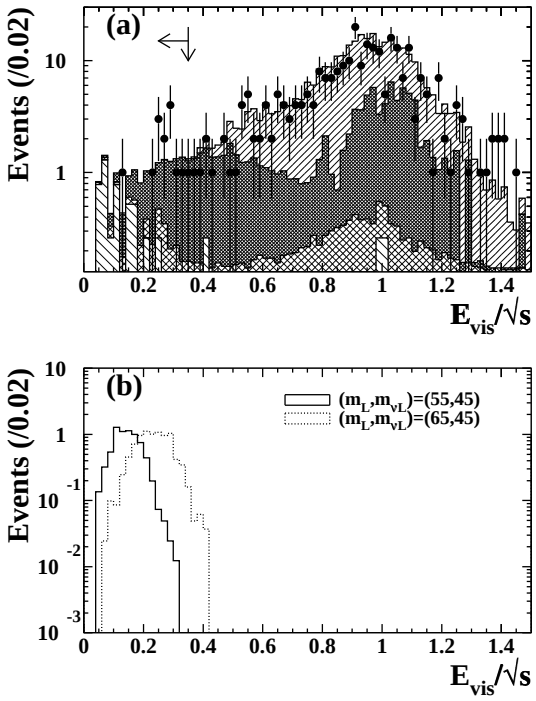

Figure 5.8: Distribution of $E_{\rm vis}/\sqrt{s}$ before cut (B6).

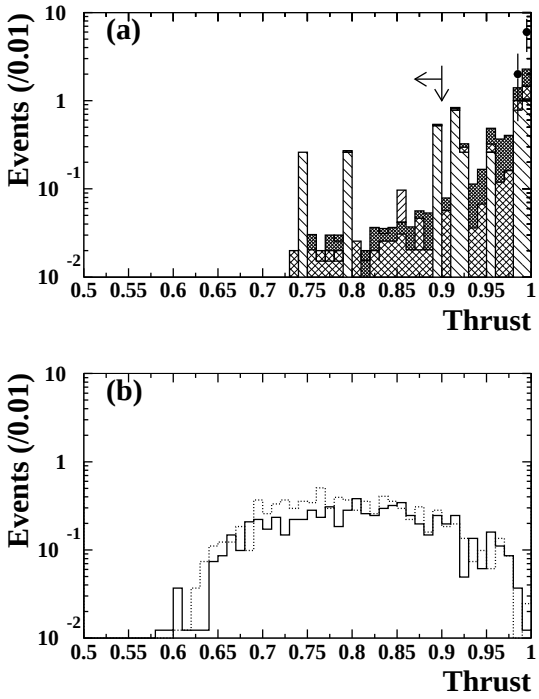

Figure 5.9: Distribution of thrust before cut (B8).

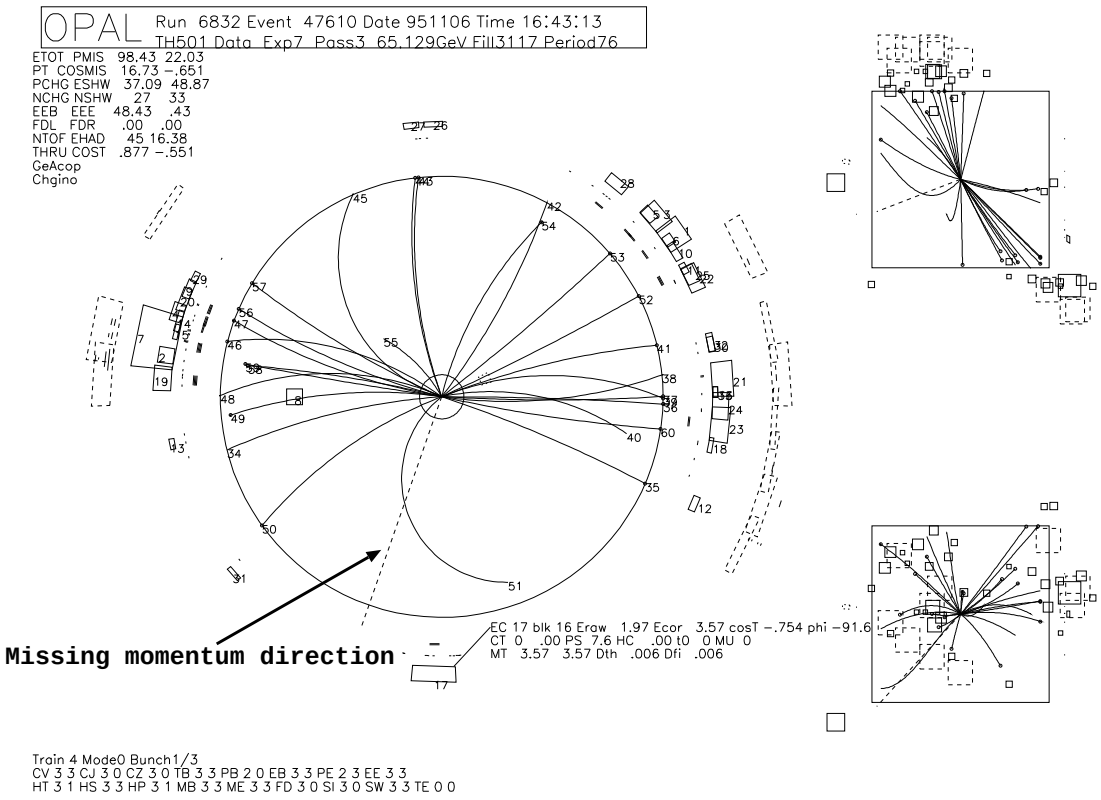

Figure 5.10: The event rejected by $E_{\rm back}$ cut (C9). The $E_{\rm back}$ energy is 3.7 GeV.

as monojet events were considered to be heavy lepton candidates.

(C9) For dijet events in case (C), The $E_{\rm back}$ within a cone of 30° half-angle around the direction of the missing momentum was calculated. In case (C) we required $E_{\rm back}$ to be less than 3 GeV. In case (B) the $E_{\rm back}$ cut was not used because multihadron events were sufficiently reduced by cut (B6). An event sample rejected by $E_{\rm back}$ is shown in Fig. 5.10.

(B10, C10) The acoplanarity angle ($\phi_{\rm acop}$) between the two jets was required to be greater than 15°. The acoplanarity angle distributions just before the cut are shown in Fig. 5.11.

No event was observed in the data after the above selections. These results were consistent with the expected background from all sources of 0.44 events for case (B) and 0.51 events for case (C).

The detection efficiencies for $\rm L^+L^-$ events were calculated at $\sqrt{s} = 130$ and 136 GeV. In case (B), the efficiency was about 55% for $(m_{\rm L^-}, m_{\nu_{\rm L}}) =$ (60 GeV, 45 GeV), and 40% for (63 GeV, 55 GeV). In case (C) the efficiency was at least 33% for $m_{\rm L^-}$ in the range 45-63 GeV. The detection efficiencies for the expected

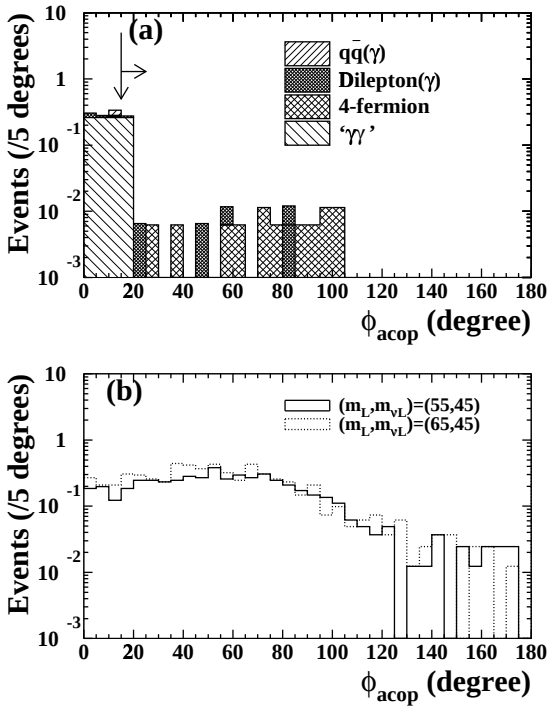

Figure 5.11: Distribution of acoplanarity angle, $\phi_{\rm acop}$, before cut (B10).

Table 5.4: The selection efficiencies (in %) for $L^+L^- \to \nu_L W^{*+} \nu_L W^{*-}$ candidates for the mass combinations between m_{L^-} and m_{ν_L} in this analysis. The errors are statistical only.

m_{ν_L}	m_{L^-} = 45 GeV	50 GeV	55 GeV	60 GeV	63.0 GeV	65 GeV
60.0	–	–	–	–	0.7 ± 0.3	13.4 ± 1.1
55.0	–	–	–	13.1 ± 1.1	36.7 ± 1.5	49.5 ± 1.6
50.0	–	–	15.5 ± 1.2	46.2 ± 1.6	53.6 ± 1.6	50.6 ± 1.6
45.0	–	16.8 ± 1.2	43.9 ± 1.6	54.0 ± 1.6	55.3 ± 1.6	56.1 ± 1.6
40.0	15.7 ± 1.2	40.4 ± 1.5	50.4 ± 1.6	49.1 ± 1.6	48.7 ± 1.6	45.2 ± 1.6

Table 5.5: The selection efficiencies (in %) of $L^- \to \nu_\ell W^{*-}$ candidates as a function of mass. The errors are statistical only.

m_{L^-} = 45 GeV	50 GeV	55 GeV	60 GeV	63 GeV	65 GeV
33.0 ± 1.5	33.2 ± 1.5	35.9 ± 1.5	38.3 ± 1.5	36.2 ± 1.5	34.8 ± 1.5

Table 5.6: The numbers of events remained, normalised to the integrated luminosity, for various background processes are compared with data after each cut for the $L^- \to \nu_\ell W^{*-}$ case. Numbers of expected events are also given for three samples of simulated L^+L^- events. The numbers of events expected from two-photon processes do not include the region $M_{\gamma\gamma} < 3$ GeV with $Q^2 < 1.3$ GeV^2.

case (C)	data	total bkg.	$q\bar{q}(\gamma)$	$\ell\ell(\gamma)$	'$\gamma\gamma$'	4-f	L^+L^-		
m_{L^-} (GeV)							45	55	63
no cuts	–	–	1645	6458	105k	20.2	1k	1k	1k
cut (C1)	123k	47.1k	1606	963	44.5k	18.0	980	985	985
cut (C2)	50.5k	16.4k	1142	839	14.4k	11.1	845	852	876
cut (C3)	237	245	195	46.5	1.04	2.95	657	691	705
cut (C4)	161	169	129	37.3	0.52	2.46	592	624	645
cut (C5)	136	138	110	25.4	0.52	2.43	581	620	641
cut (C6)	38	49.2	26.6	22.0	0.00	0.58	480	515	528
cut (C7)	20	31.1	26.6	3.95	0.00	0.58	472	514	524
cut (C8)	7	6.99	6.26	0.39	0.00	0.34	392	434	451
dijet	7	6.98	6.26	0.38	0.00	0.34	356	402	404
cut (C9)	4	4.84	4.50	0.17	0.00	0.17	326	353	367
cut (C10)	0	0.50	0.33	0.08	0.00	0.09	294	327	315
monojet	0	0.01	0.00	0.01	0.00	0.00	36	32	47
(C10)+monojet	0	0.51	0.33	0.09	0.00	0.09	330	359	362

signals are summarized in Table 5.4 for case (B) and Table 5.5 for case (C). The trigger efficiency was 100% for the selected signal events.

5.4 Systematic Errors

The expected numbers of neutral and charged heavy lepton events were estimated for various values for heavy lepton mass (or combinations of $(m_{\mathrm{L}^-}, m_{\nu_{\mathrm{L}}})$) using the detection efficiency at each centre-of-mass energy, the cross-section and integrated luminosity. In the calculation of limits the detection efficiency at arbitrary values of the heavy lepton masses was interpolated using a polynomial fit.

In this analysis, the background subtractions were not applied in order to avoid the unknown background Monte Carlo uncertainty, although the number of expected backgrounds for each analysis has been found to be less than one event. The systematic errors on the total number of expected signal events were estimated to be

- 3-6% from Monte Carlo statistics, depending on the event topology,
  The statistical uncertainty on the detection efficiency $\eta(m_{\mathrm{L}})$ is given by

$$\Delta\eta = \sqrt{\eta(1-\eta)/N_0} \quad ,$$

  where N_0 is the generated number of events (for all mass points 1000 events were simulated). The ratio $\frac{\Delta\eta}{\eta}$ for intermediate values of m_{L} was estimated by interpolation. The errors on the detection efficiencies in the case (C) analysis is summarized in the Table 5.7.

Table 5.7: m_{L}-dependence of the error on the detection efficiency η in the $\mathrm{L}^- \to \nu_{\mathrm{L}}\mathrm{W}^{*-}$ case.

m_{L} (GeV)	47	50	55	60	63	65
$\frac{\Delta\eta}{\eta}(\sqrt{s} = 136\ GeV)$	4.1%	4.0%	3.8%	3.5%	3.9%	3.7%
$\frac{\Delta\eta}{\eta}(\sqrt{s} = 130\ GeV)$	4.7%	4.0%	4.1%	3.7%	3.7%	–

- 1.2% from the interpolation of the efficiencies,
  In the calculation of limits the detection efficiency at intermediate values of m_{L} or m_{L^0} was interpolated using a polynomial fit. The systematic errors of the polynomial fit were estimated by measuring the residual between the fitted efficiencies and the weighted average values for each mass points of heavy lepton.

$$\text{Interpolation Error} = \sqrt{\frac{1}{N}\sum_{i=1}^{N}\left(\frac{F(i)-L(i)}{F(i)}\right)^2},$$

where $F(i)$ is a polynomial fitted function of a m_{L}, $L(i)$ the weighted average function of a m_{L} and i ($1 \sim$ N) is the intermediate mass between the simulated mass points.

- 0.9% from the uncertainty in the integrated luminosity, which mainly depended on the statistics of the forward luminosity monitor (FD, SW).

- 4.3% from the isolated lepton tagging uncertainty for the $\mathrm{L}^0\bar{\mathrm{L}}^0$ case;
  The e and μ identification uncertainties could be estimated track by track. The systematic uncertainty of the efficiency was estimated to be 2.5% for e and 1.2% for μ, respectively. However τ identification uncertainties depend on the jet reconstruction (in other words on the y_{cut} value on Durham algorithm) and on the uncertainty of the fragmentation parameters of the hadronic jets. The large background sources of the τ mis-identification are the semi-leptonic decay of the charmed mesons and the low multiplicity gluon jets. As the expected signals are 3-body decay of $\mathrm{L}^0 \to \ell\mathrm{W}^*$, in which may occur the low multiplicity hadronic jets, the estimation of this ambiguity is important. By using the 10000 Monte Carlo samples, this systematic error for the lepton tagging was estimated to be less than 4.3% which was dominated by the τ identification uncertainty.

- 1.5% (0.6%) from the uncertainty in the fragmentation of W^* hadronic decays for $\mathrm{L}^0\bar{\mathrm{L}}^0$ ($\mathrm{L}^+\mathrm{L}^-$).

  The fragmentation errors arose through the jet reconstruction and mainly through the uncertainty in the estimation of the acoplanarity angle and the missing momentum direction for the $\mathrm{L}^+\mathrm{L}^-$ case. The fragmentation error was estimated by varying the optimized fragmentation parameters [99] (summarized in Table 5.8) in the JETSET 7.4 Monte Carlo generator. Since the lepton tagging uncertainty was independently estimated (see before column), this systematic error for lepton tagging was not included here.

The systematic error due to trigger efficiency was estimated to be negligible for the selected signal events. In calculating the mass limits the systematic errors were treated as in Ref. [100] and were considered to be independent. For a given heavy lepton mass, a fixed number of candidates events, N, will survive the full analysis. A 95% confidence level upper limit on the expected signal level can be set using the normal Poisson statistical formula, yielding a limit of N_{95} events. The error on the sensitivity can be readily incorporated into limits by convolving

σ_S with the Poisson integrals, resulting in the substitution:

$$N'_{95} = N_{95} \times \left(1 + (N_{95} - N)\frac{(\sigma_S/S)^2}{2}\right). \quad (5.1)$$

For example, in the case of a 95% C.L. with zero observed events and a 5% error on the sensitivity, the net effect is replacing 3.00 with 3.01. Eq. 5.1 is a good approximation for the relative systematic uncertainty $(\sigma_S/S)^2$ when σ_S 10% (see Table. 1 in Ref [100]).

A 95% C.L. lower limit of 62.5 GeV is obtained for the Dirac neutral heavy lepton mass, assuming that both L^0 and $\bar{L}^0$ decay into eW* with 100% branching fraction. The mass limits for the cases of $L^0 \to \mu W^*$ and $L^0 \to \tau W^*$ are 63.0 GeV and 57.4 GeV, respectively. For Majorana L^0 the limits are reduced to 51.4 GeV for the eW* decay, 52.2 GeV for μW^* decay and 44.2 GeV for τW^* decay due to the smaller cross-section near the $L^0\bar{L}^0$ threshold.

The mass of $L^{\pm}$ was found to be larger than 64.5 GeV at 95% C.L. for case (B), if $m_{L^-} - m_{\nu_L} > 10$ GeV. The excluded region in the (m_{L^-}, m_{ν_L}) plane for case (B) is presented in Fig. 5.12. For case (C) the lower limit for m_{L^-} is 63.9 GeV at 95% C.L..

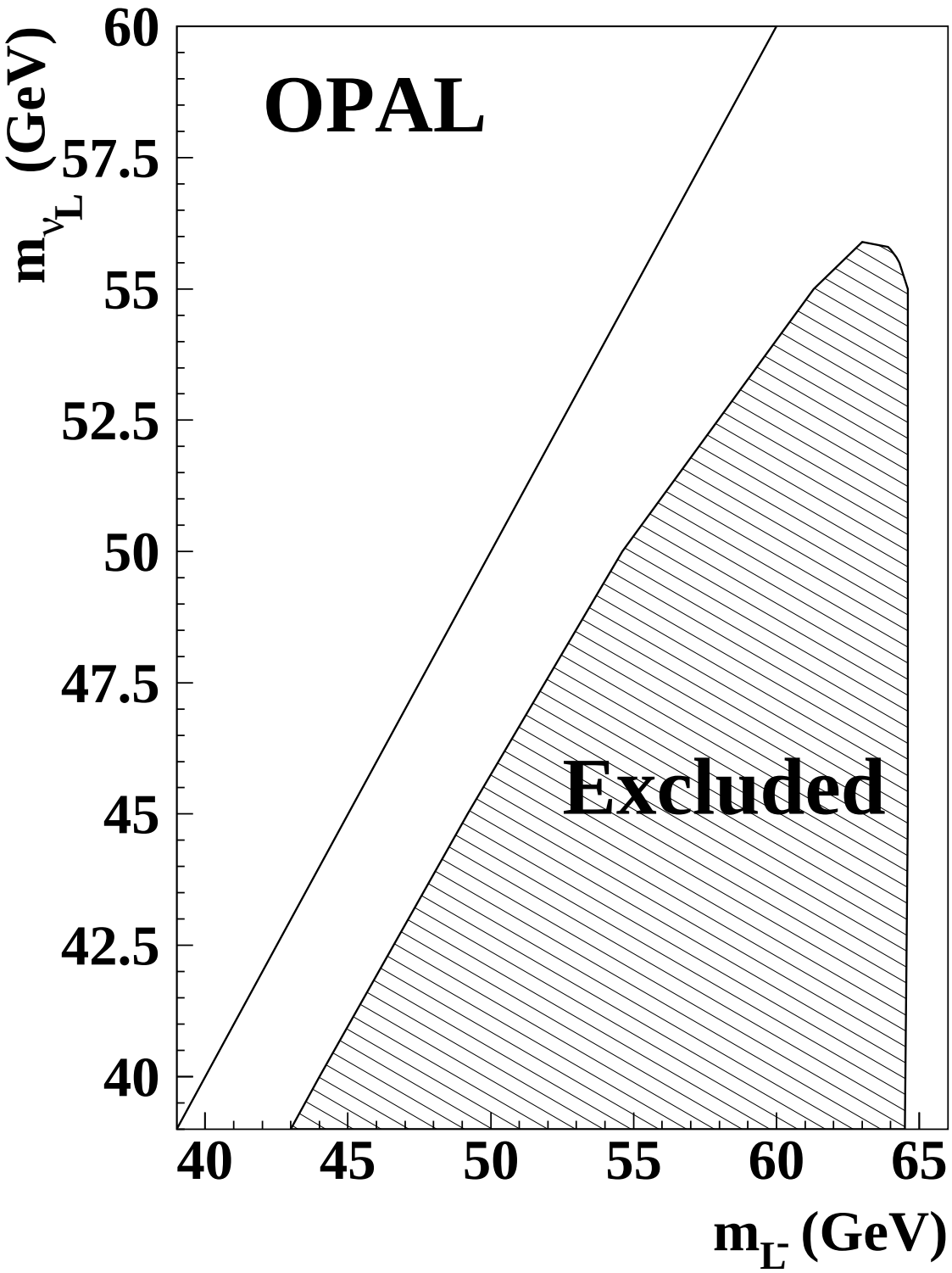

Figure 5.12: The excluded region in this analysis in the (m_{L^-}, m_{ν_L}) plane for case (B). If L^- decays into ν_L + W^{*-} and ν_L is assumed to be a stable heavy neutrino, the hatched region is excluded with more than 95% C.L. The region $m_{\nu_\mathrm{L}} < 45$ GeV is already excluded for the Dirac ν_L and $m_{\nu_\mathrm{L}} < 39.5$ GeV for the Majorana ν_L from the upper limit of the Z^0 decay width measurements at LEP [1]. The diagonal line shows $m_{\mathrm{L}^-} = m_{\nu_\mathrm{L}}$.

Parameter	Monte Carlo Name	Default value	Optimized value
Peterson Option	MSTJ(11)	4	3
qq/q	PARJ(1)	0.100	0.085 ± 0.005
s/u	PARJ(2)	0.30	0.31 ± 0.01
(us/ud)·(u/s)	PARJ(3)	0.40	0.45 ± 0.04
V_{ud}	PARJ(4)	0.050	0.025 ± 0.005
$V_{d,u}$	PARJ(11)	0.50	0.60 ± 0.10
V_s	PARJ(12)	0.60	0.40 ± 0.05
σ_q	PARJ(21)	0.36	0.40 ± 0.03
a	PARJ(41)	0.30	0.11
b	PARJ(42)	0.58	0.52 ± 0.04
ϵ_c (old value)	PARJ(54)	-0.050	-0.046
ϵ_b (old value)	PARJ(55)	-0.0050	-0.0057
Λ_{LLA}	PARJ(81)	0.290	0.250 ± 0.006
Q_0	PARJ(82)	1.00	1.90 ± 0.50
ϵ_c (updated value)	PARJ(54)	-0.050	-0.031 ± 0.011
ϵ_b (updated value)	PARJ(55)	-0.0050	-0.0038 ± 0.0010

Table 5.8: Optimized OPAL parameter set for JETSET, version 7.4. Parameters not listed were left at their default values. The parameters PARJ(41), PARJ(54) and PARJ(55) were taken from our previous parameter set for JETSET, and the other parameters listed were adjusted in a global fit. Uncertainties are given for the parameters employed in the fit. These uncertainties are the $\pm 1\sigma$ limits obtained from the χ^2 contours. Subsequent to the Monte Carlo generation with detector simulation used for the present work, the values of ϵ_c and ϵ_b were updated to those shown in the bottom part of the table in order to improve the description of our measured value for the mean scaled energy of b hadrons.

Chapter 6

Analysis at LEP2

6.1 Monte Carlo Event Simulation

The Monte Carlo generators for the $L^0\bar{L}^0$ and L^+L^- events are the same as those used for LEP1.5 analysis, which have been described in Chapter 5.1. The $L^0\bar{L}^0$ events were generated at 8 values of the heavy neutral lepton mass from 45 to 80 GeV for each of the three different final states $eW^* + eW^*$, $\mu W^* + \mu W^*$ and $\tau W^* + \tau W^*$, for Majorana and Dirac cases separately. L^+L^- events were generated at 26 points in the (m_{L^-}, m_{ν_L}) plane for case (B) and at 5 mass values of heavy leptons from 60 to 80 GeV for case (C).

The following background processes were simulated in this analysis:

$q\bar{q}(\gamma)$ The PYTHIA 5.7 [83] Monte Carlo generator was used for multihadron ($e^+e^- \to q\bar{q}(\gamma)$) events.

$\ell\ell(\gamma)$ $\tau^+\tau^-(\gamma)$ and $\mu^+\mu^-(\gamma)$ events were simulated by the KORALZ [84] program. The BHWIDE [85] generator was used for the $e^+e^- \to e^+e^-(\gamma)$ events.

'$\gamma\gamma$' The PYTHIA 5.7 and PHOJET [88] Monte Carlo programs were used for generating events from two-photon processes where the Q^2 of both photons are smaller than 1.0 GeV^2 and the invariant mass of the photon-photon system ($M^2_{\gamma\gamma}$) is greater than 4 GeV^2. For events with higher Q^2 the generators PYTHIA 5.7 and HERWIG [89] were used. Four-lepton events were simulated by the Vermaseren generator [90]. Event samples for all the possible processes (final state hadrons from point-like $\gamma\gamma \to q\bar{q}$ processes and from vector meson dominance, and all $e^+e^-\ell^+\ell^-$ final states) were generated. Two-photon events were not generated in the region where $Q^2 < 1.0$ GeV^2 and $M^2_{\gamma\gamma} < 4$ GeV^2, or $Q^2 > 1.0$ GeV^2 and $M^2_{\gamma\gamma} < 3$ GeV^2. This region did not represent a serious background to the search presented here.

4-fermion Events from four-fermion processes ($\ell^+\ell^- q\bar{q}$, $\ell^-\bar{\nu}_\ell q\bar{q}'$, $\nu_\ell\bar{\nu}_\ell q\bar{q}$, $\nu_\ell\bar{\nu}_\ell\ell^+\ell^-$), including W^+W^- events, are serious backgrounds for the $L^0\bar{L}^0$ and L^+L^-

searches. The EXCALIBUR [91] Monte Carlo program was used to simulate all four-fermion processes, including W^+W^- events. Since the event sample that we have generated using EXCALIBUR does not include $e^+e^- \to We\nu$ and $e^+e^- \to Z^*e^+e^-$ or $\gamma^*e^+e^-$ events in which one of the electrons scatters at a very small angle, these events were simulated by PYTHIA.

Generated signal and background events were processed through the full simulation of the OPAL detector [92], and the same event analysis chain was applied to these simulated events as to the data.

Jets were formed using the Durham algorithm [94] with a jet resolution parameter of $y_{\rm cut} = 0.004$.

6.2 Selection of $L^0\bar{L}^0$ candidates (case A)

The following event selection criteria were applied. The numbers of remaining events just after the applied cuts are listed in Table 6.1, for data and for simulated background and signal samples. The difference in the numbers of events between the data and the total simulated background at early stage (before cut (A4)) is mainly due to incomplete modelling of two-photon processes ('$\gamma\gamma$').

(A1) The $N_{\rm ch}$ was required to be at least four, and the ratio of the number of tracks which satisfied the quality criteria to the total number of reconstructed tracks was required to be larger than 0.2 in order to reject beam-gas and beam-wall background events.

(A2) In order to reduce the background from two-photon processes and multihadronic events in which one of the jet axes was close to the beam direction, the sum of the energies of clusters in each silicon tungsten calorimeter was required to be less than 5 GeV. Furthermore the total cluster energy was required to be less than 2 GeV in each forward calorimeter and less than 5 GeV in each side of the gamma-catcher.

(A3) The $|\cos\theta_{\rm thrust}|$ was required to be less than 0.95 in order to reduce the number of beam-gas and beam-wall background events as well as the events from two-photon processes.

(A4) The $E_{\rm vis}/\sqrt{s}$, was required to be greater than 0.45 in order to reject the background from two-photon processes. The distributions of $E_{\rm vis}/\sqrt{s}$ after cut (A3) are shown in Fig. 6.1(a) for the data and the simulated background events, and in Fig. 6.1(b) for the simulated $L^0\bar{L}^0$ events.

(A5) If the missing energy was larger than 30 GeV, the polar angle of the missing momentum direction, $\theta_{\rm miss}$, was required to satisfy $|\cos\theta_{\rm miss}| < 0.95$. One of the final states for the expected signals is $\ell\ell'{\rm qq'q''q'''}$, which has full visible

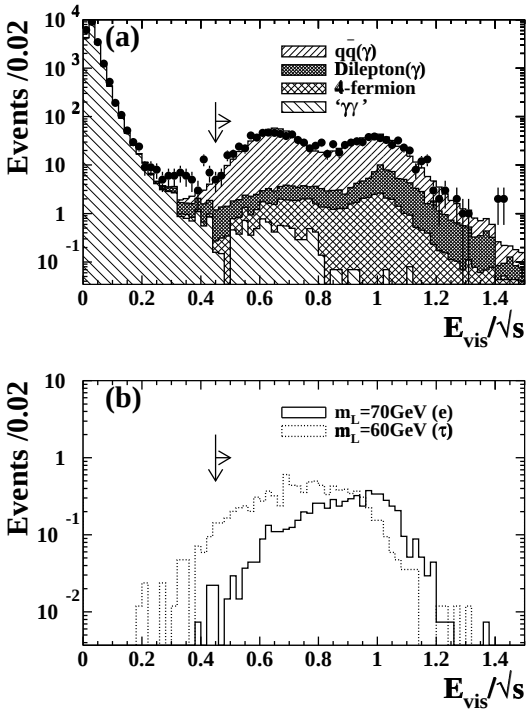

Figure 6.1: Distribution of the $E_{\rm vis}/\sqrt{s}$ before cut (A4).

energy. In this case the missing momentum direction is not meaningful, hence the missing energy threshold was applied.

(A6) The number of jets was required to be at least four. With this requirement a large fraction of the multihadron background was removed. The distributions of the number of jets after cut (A5) are shown in Fig. 6.2(a) for the data and the simulated background events, and in Fig. 6.2(b) for simulated $\mathrm{L^0\bar{L}^0}$ events. In Fig. 6.4, an event sample is shown, which is the $\mathrm{e^+e^-e^+e^-}$ four-fermion process background rejected by cut(A6).

(A7) The number of isolated leptons (e, μ or τ) was required to be at least two. The lepton identification and isolation requirements are the same as those of LEP1.5 search, except that the upper bound on the momentum of one-prong tau decay was lowered from 40 GeV to 30 GeV. The distributions of the number of isolated leptons after cut (A6) are plotted in Fig. 6.3(a) for the data and the simulated background events, and in Fig. 6.3(b) for simulated $\mathrm{L^0\bar{L}^0}$ events.

(A8) In order to reduce the $\ell^+\ell^-\mathrm{q\bar{q}}$ four-fermion background, the $E_{\rm vis}/\sqrt{s}$ was required to be smaller than 0.85 if the number of reconstructed jets was equal to four. Box distributions of the number of jets and the $E_{\rm vis}/\sqrt{s}$ after cut (A7) are shown in Fig. 6.6. In Fig. 6.5, an event sample is shown, which is the $\ell^+\ell^-\mathrm{q\bar{q}}$ four-fermion process background rejected by cut(A8).

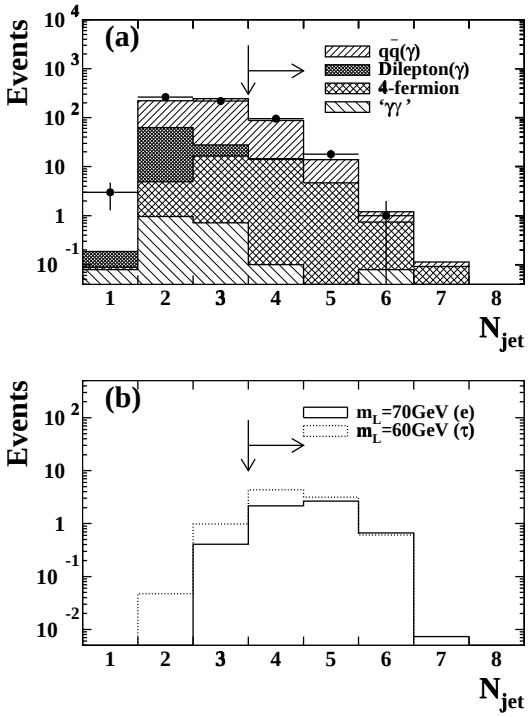

Figure 6.2: The distributions of the number of jets before cut (A6) for the data (bold circles with error bars) and for the simulated background events (a). The same distributions are shown in (b) for simulated $L^0\bar{L}^0 \to eW^*eW^*$ events with $m_{L^0} = 70$ GeV (solid line histogram) and $L^0\bar{L}^0 \to \tau W^*\tau W^*$ events with $m_{L^0} = 60$ GeV (dotted line histogram). The arrows indicate the position of the cut and the region accepted.

No event was observed in the data after the above selection. This result was consistent with the expected number of background events of 0.54. The detection efficiency for $L^0\bar{L}^0$ events was calculated for various m_{L^0} values between 45 and 80 GeV. The efficiency for m_{L^0} in the range of 50–75 GeV was between 34% and 48% for $L^0\bar{L}^0 \to eW^*eW^*$ or $\mu W^*\mu W^*$ events, and between 22% and 28% for $L^0\bar{L}^0 \to \tau W^*\tau W^*$ events. The detection efficiencies for the expected signals are summarized in Table 6.2. For the mixed decay products of $L^0\bar{L}^0$ ($L^0\bar{L}^0 \to eW^*\mu W^*$, $eW^*\tau W^*$ or $\mu W^*\tau W^*$) the efficiencies have values intermediate of the unmixed cases. The efficiencies for the $L^0\bar{L}^0 \to \tau W^*\tau W^*$ case were the lowest in this analysis.

6.3 Selection of $L^+L^- \to \bar{\nu}_L W^{*+} \nu_L W^{*-}$ candidates (case B)

The numbers of events remaining after each cut are listed in Table 6.3 for case (B). For comparison the table also includes the corresponding numbers of simulated

Table 6.1: The numbers of events remaining after each cut (in the $L^0\bar{L}^0$ search) normalised to the integrated luminosity. Numbers are also given for three samples of simulated $L^0\bar{L}^0$ events.

case (A)	data	total bkg.	$q\bar{q}(\gamma)$	$\ell\ell(\gamma)$	'$\gamma\gamma$'	4-f	$L^0\bar{L}^0$		
m_{L^0} (GeV) Decay mode							60 tau	70 muon	70 electron
no cuts	–	–	1474	8428	220k	200	1000	1000	1000
cut (A1)	108k	56.0k	1433	105.6	54.4k	62.1	990	977	978
cut (A2)	36.5k	32.4k	1063	94.4	31.2k	47.7	867	883	853
cut (A3)	21.8k	19.2k	1028	91.0	18.0k	45.9	824	841	823
cut (A4)	1048	1062	923.8	82.7	10.9	44.2	793	837	818
cut (A5)	600	569.4	459.0	69.4	1.97	39.0	767	817	806
cut (A6)	114	102.5	82.6	0.50	0.18	19.2	681	767	752
cut (A7)	1	1.10	0.21	0.09	0.00	0.80	280	531	420
cut (A8)	0	0.54	0.14	0.04	0.00	0.36	272	467	381

Table 6.2: The selection efficiencies (in %) of L^0 candidates for three decay modes ($L^0 \to eW^*$, μW^* and τW^*) as a function of m_{L^0}. The errors are statistical only.

Decay	m_{L^0}=50 GeV	55 GeV	60 GeV	65 GeV	70 GeV	75 GeV
$L^0 \to eW^*$	33.5 ± 1.5	35.8 ± 1.5	40.6 ± 1.5	42.9 ± 1.6	42.3 ± 1.6	42.5 ± 1.6
$L^0 \to \mu W^*$	36.2 ± 1.5	40.5 ± 1.6	42.2 ± 1.6	42.9 ± 1.6	46.7 ± 1.6	47.2 ± 1.6
$L^0 \to \tau W^*$	23.3 ± 1.4	26.0 ± 1.4	26.7 ± 1.4	29.1 ± 1.4	26.5 ± 1.4	24.6 ± 1.4

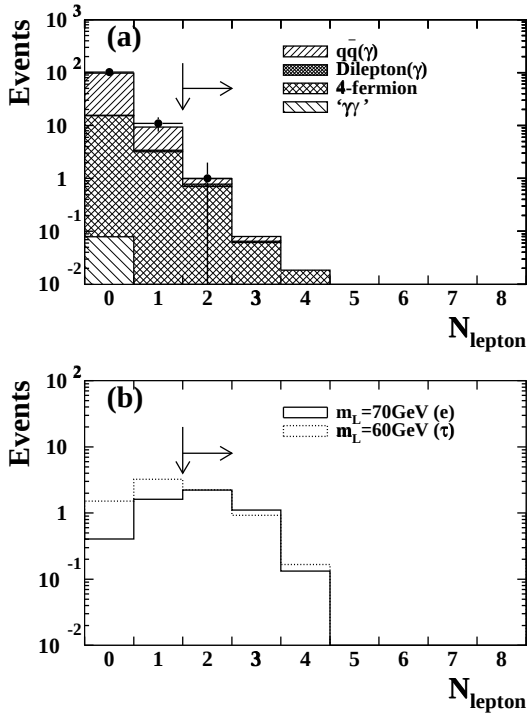

Figure 6.3: The distributions of the number of isolated leptons before cut (A7) are shown in (a) for the data and for the simulated background events. The same distributions are shown in (b) for simulated $L^0\bar{L}^0 \to eW^*eW^*$ events with $m_{L^0} = 70$ GeV (solid line histogram) and $L^0\bar{L}^0 \to \tau W^*\tau W^*$ events with $m_{L^0} = 60$ GeV (dotted line histogram).

background and L^+L^- events. The reason for the difference in the number of events between the data and the simulated background before cut (B4) is the same as in case (A).

The following selection criteria were applied:

(B1) The N_{ch} was required to be at least two, and the ratio of the number of tracks which satisfied the quality criteria to the total number of reconstructed tracks was required to be greater than 0.2.

(B2) The criteria for energy deposits in the silicon tungsten calorimeter, the forward calorimeter and the gamma-catcher were identical to those in the $L^0\bar{L}^0$ analysis (see A2).

(B3) $|\cos\theta_{thrust}|$ was required to be less than 0.9. The $|\cos\theta_{thrust}|$ cut is harder than in the L^0 analysis because the acoplanarity angle, which is discussed later, becomes unreliable if the jet axes are close to the beam direction.

(B4) Events from two-photon processes with a small visible energy were efficiently reduced by demanding P_t to be larger than 4 GeV and P_t^{HCAL} to be

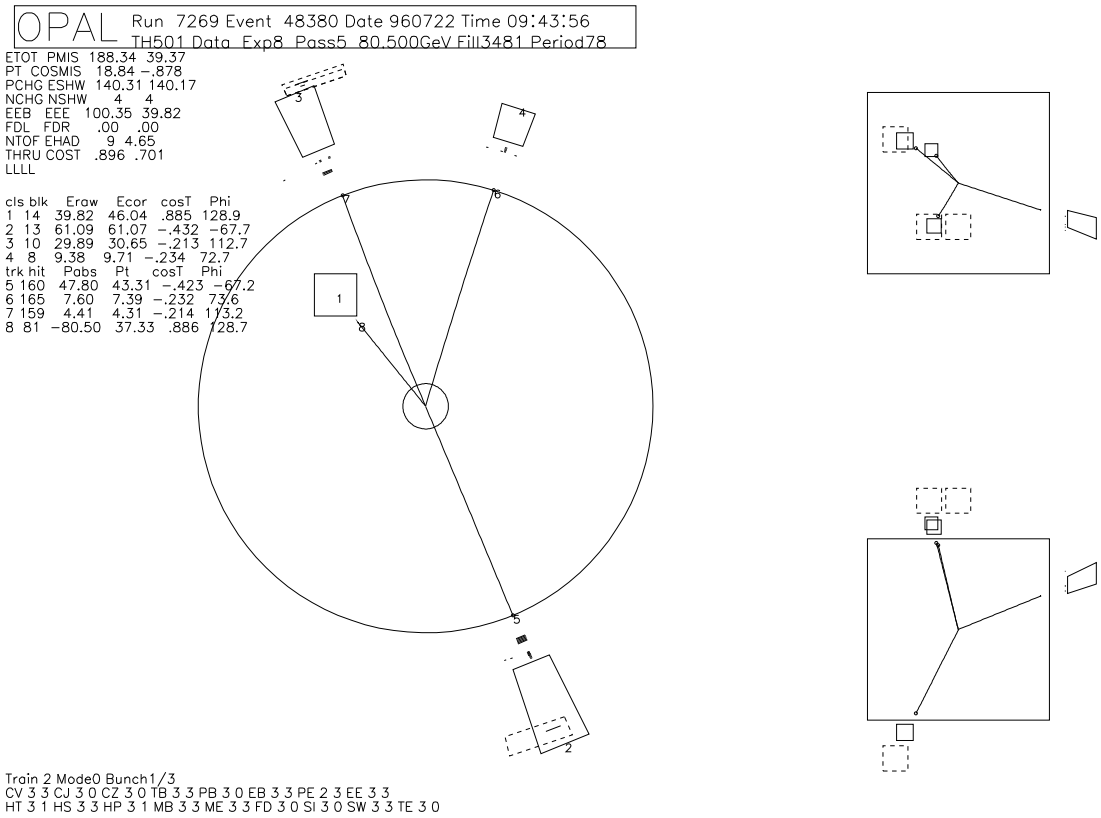

Figure 6.4: An event sample rejected by cut (A6). This event is considered as $e^+e^- \to Z^*Z \to e^+e^-e^+e^-$ process. The invariant mass of two electrons with largest momenta is 88.4 GeV, which is consistent with Z boson mass, and the invariant mass of other 2 electrons is 38.5 GeV. This event topology is similar to the expected signal, but the number of reconstructed jets for this events was three. One opening angle between the nearby clusters is less than the requirement of jet separation. Also the visible energy is too large (188 GeV) than that of the expected signals ($L^0\bar{L}^0 \to eW^*eW^* \to e^+e^-e^+e^-\nu_e\bar{\nu}_e$).

larger than 5 GeV. The distributions of $P_t^{\rm HCAL}$ after cut (B3) are shown in Fig. 6.7(a) for the data and the simulated background events, and in Fig. 6.7(b) for the simulated L^+L^- (case (B)) events.

(B5) The polar angle of the missing momentum direction $\theta_{\rm miss}$ should satisfy $|\cos\theta_{\rm miss}| < 0.7$. This reduces "Radiative return" events, in which initial state radiation results in an effective centre-of-mass energy near the Z^0 resonance, and two-photon events. The distributions of $|\cos\theta_{\rm miss}|$ after cut (B4) are shown in Fig. 6.8.

(B6) A visible energy cut was applied to reduce both multihadron and four-fermion backgrounds. The visible energy of L^+L^- events was expected

Table 6.3: The numbers of events remaining after each cut (in the $L^- \to \nu_L W^{*-}$ search) for the data and for the various background processes, normalised to the integrated luminosity. Expected numbers of events are also given for three samples of simulated L^+L^- events.

case (B)	data	total bkg.	$q\bar{q}(\gamma)$	$\ell\ell(\gamma)$	'$\gamma\gamma$'	4-f	L^+L^-		
							70	70	65
m_{L^-} (GeV)							40	65	55
m_{ν_L} (GeV)									
no cuts	–	–	1474	8428	220k	200	1000	1000	1000
cut (B1)	237k	101k	1436	1195	97.9k	83.0	981	934	968
cut (B2)	94.7k	66.6k	1063	1087	64.4k	59.1	944	915	933
cut (B3)	60.7k	37.2k	957.6	1010	35.2k	52.0	882	872	868
cut (B4)	1066	962.4	473.4	421.8	31.0	36.2	840	218	626
cut (B5)	356	344.8	170.1	140.3	11.3	23.1	630	208	520
cut (B6)	32	28.6	1.00	14.0	11.0	2.55	584	208	519
cut (B7)	18	18.7	0.83	11.0	5.29	1.60	521	136	371
cut (B8)	7	9.21	0.75	2.83	5.08	0.55	463	136	367
cut (B9)	2	1.48	0.40	0.29	0.58	0.21	412	118	304
cut (B10)	2	0.38	0.04	0.06	0.08	0.20	367	111	276

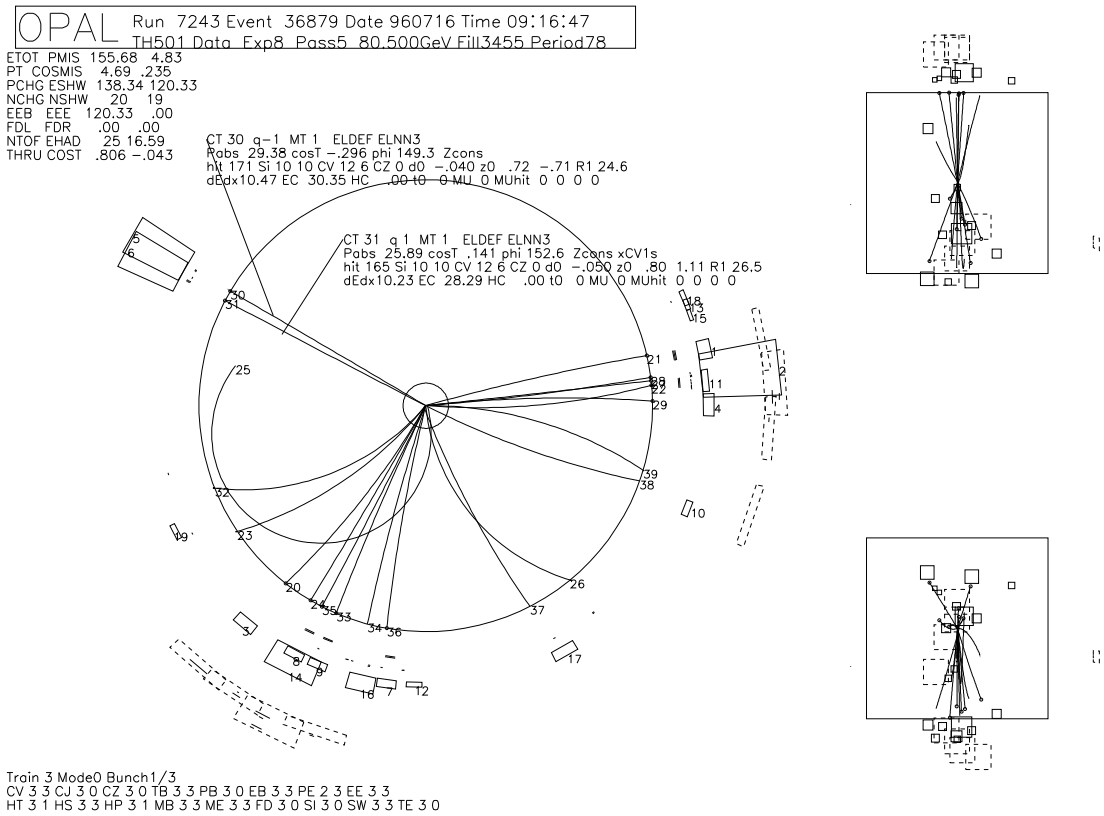

Figure 6.5: An event remaining after cut (A7). This event is considered as $e^+e^- \rightarrow Z^*Z \rightarrow e^+e^-q\bar{q}$ process. The invariant mass of 2 hadronic jets is 80.9 GeV, which is consistent with Z boson mass, and 12.9 GeV for 2 electrons.

to be smaller than about 80 GeV, since the two heavy ν_L's carry away a significant fraction of the energy. The $E_{\rm vis}/\sqrt{s}$ was thus required to be smaller than 0.45. The distributions of $E_{\rm vis}/\sqrt{s}$ after cut (B5) are shown in Fig. 6.9.

(B7) In order to reduce the remaining events from two-photon processes, two requirements were adopted: $E(|\cos\theta|{>}0.8)/\mathrm{E_{vis}} < 1.5\,E_{\rm vis}/\sqrt{s}$ and $|P_z| < 0.4\,\mathrm{E_{vis}}$, where $E(|\cos\theta|{>}0.8)$ is the visible energy in the region of $|\cos\theta| > 0.8$ and P_z is the missing momentum along the beam direction. Scatter plots showing $E(|\cos\theta|{>}0.8)/\mathrm{E_{vis}}$ vs. the $E_{\rm vis}/\sqrt{s}$ and distributions of the $|P^{\rm mis}_{(z)}|$, normalized to visible energy after cut (B6) are shown in Fig. 6.10 and Fig. 6.11, respectively.

(B8) Backgrounds from $\tau^+\tau^-(\gamma)$ and four-fermion processes were reduced by requiring that there should be no track with a momentum greater than 20 GeV. The distributions of the maximum charged track momentum after cut (B7) are shown in Fig. 6.12.

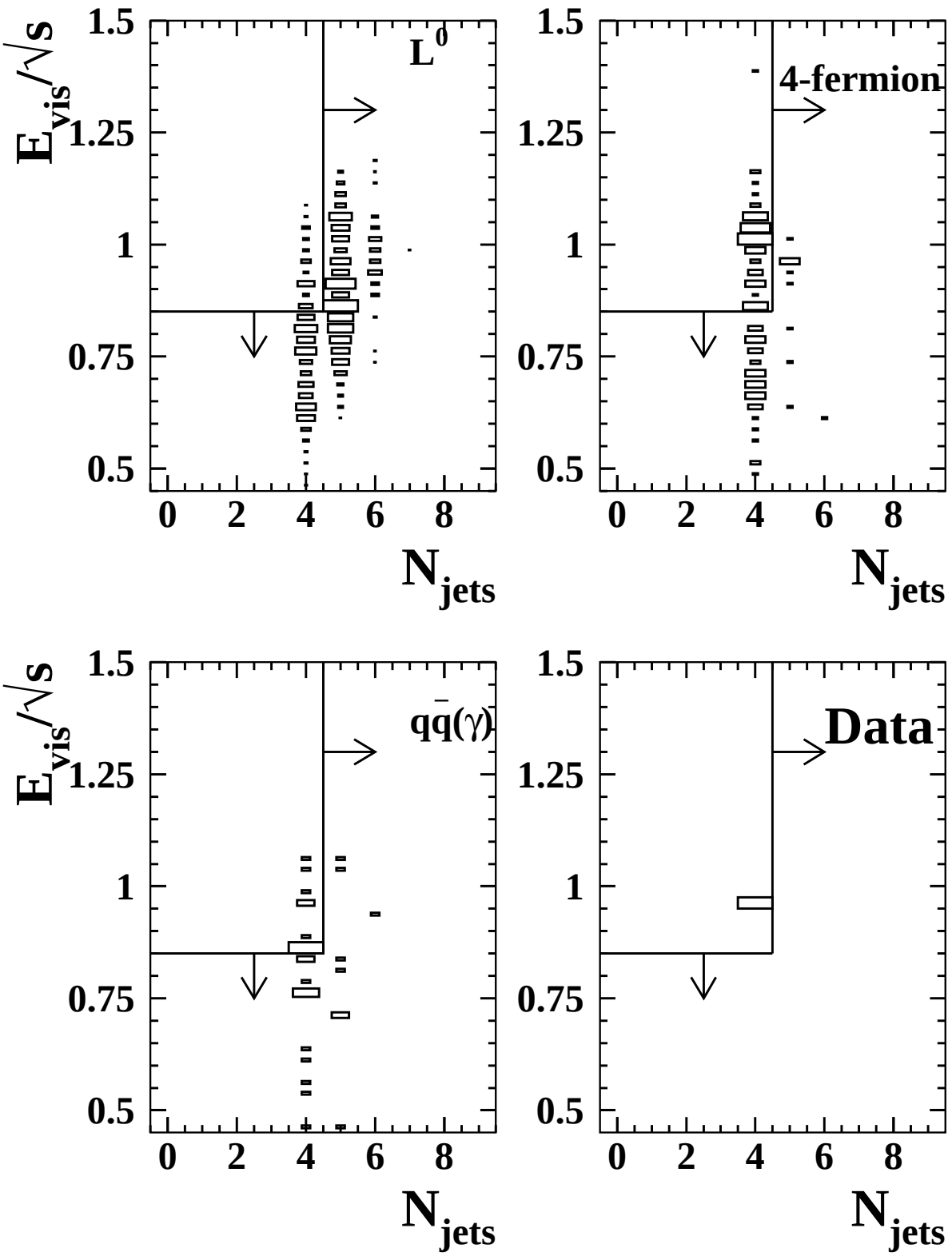

Figure 6.6: Box distributions of the number of jets and the $E_{\rm vis}/\sqrt{s}$ after cut (A7). For the expected signal events (L^0), the correlation can be seen between the visible energy and the number of jets.

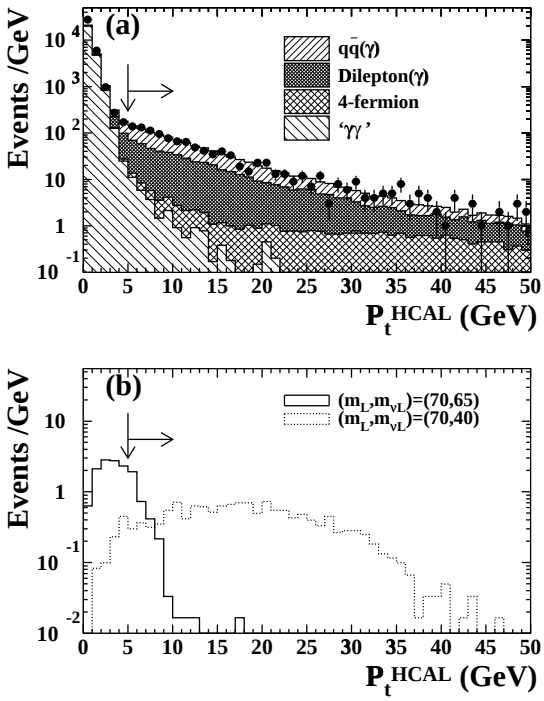

Figure 6.7: The missing transverse momentum distributions after cut (B3) are plotted in (a) for the data (bold circles with error bars) and for the simulated background events. The same distributions are shown in (b) for simulated $L^- \to \nu_L W^{*-}$ events with $(m_{L^-}, m_{L^0}) = (75, 70)$ GeV (solid line histogram) and $(m_{L^-}, m_{L^0}) = (75, 40)$ GeV (dotted line histogram). Since two-photon Monte Carlo events were generated with $M_{\gamma\gamma} > 2$ GeV, the invariant mass of visible particles was required to be greater than 2 GeV for the data.

(B9) In order to reject events containing two back-to-back jets or leptons, the thrust of the event was required to be less than 0.9. The distributions of the thrust values after cut (B8) are shown in Fig. 6.13.

(B10) The acoplanarity angle, $\phi_{\rm acop}$, was required to be greater than 15°. If all the visible decay products of L^- and L^+ happened to be in the same hemisphere, the event topology could be a monojet and $\phi_{\rm acop}$ was defined to be 180°. The distributions of the $\phi_{\rm acop}$ after cut (B9) are shown in Fig. 6.14.

Two candidate events were observed in the data after the above selection. The visible energy of one of the two candidate events was 55 GeV, and the missing momentum was 39 GeV. The event topology of this candidate event was consistent with the $ZZ^* \to \nu\bar{\nu}q\bar{q}$ process. This event was also selected as a candidate event in the searches for chargino/neutralino and scalar top/bottom quark [97]. The other candidate was considered as $e^+e^- \to \tau^+\tau^-\phi$ with ϕ decaying into $K^0_S K^0_L$, since a large energy deposit on HB was observed. This second event has a possibility of being a radiative $e^+e^- \to \tau^+\tau^-\gamma$ event. The emitted photon, however,

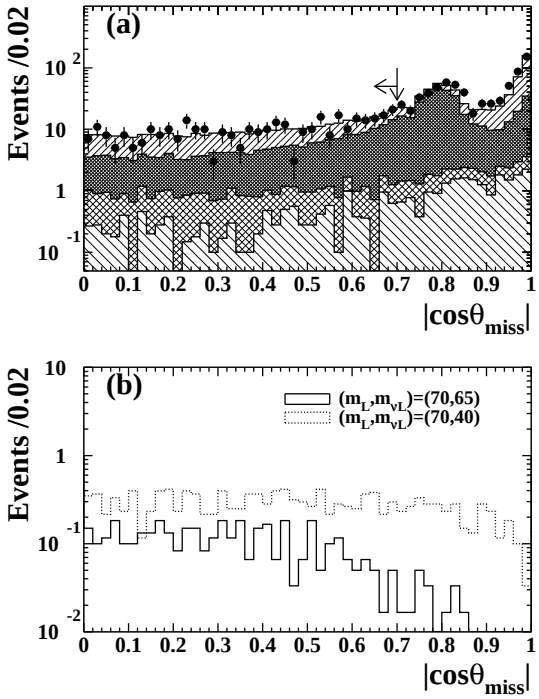

Figure 6.8: $|\cos\theta_{\rm miss}|$ distributions after cut (B4). The peak around $|\cos\theta_{\rm miss}| \approx 0.8$ is due to the degraded energy resolution in the region with a larger amount of material in front of the calorimeter.

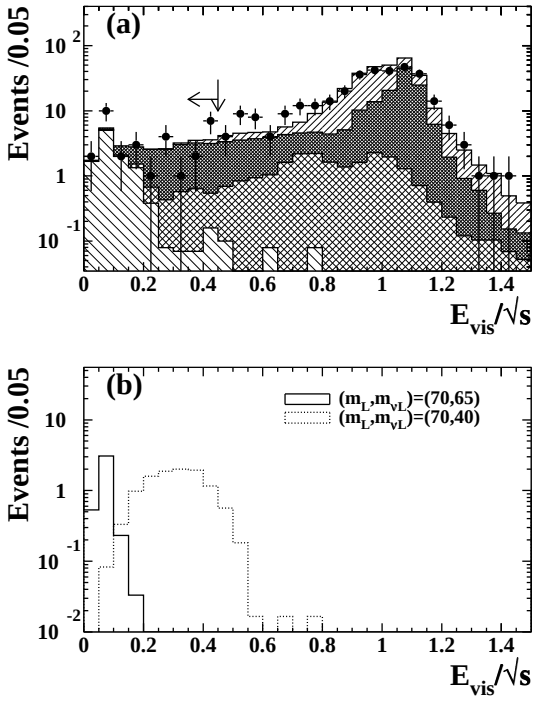

Figure 6.9: $E_{\rm vis}/\sqrt{s}$ distributions after cut (B5).

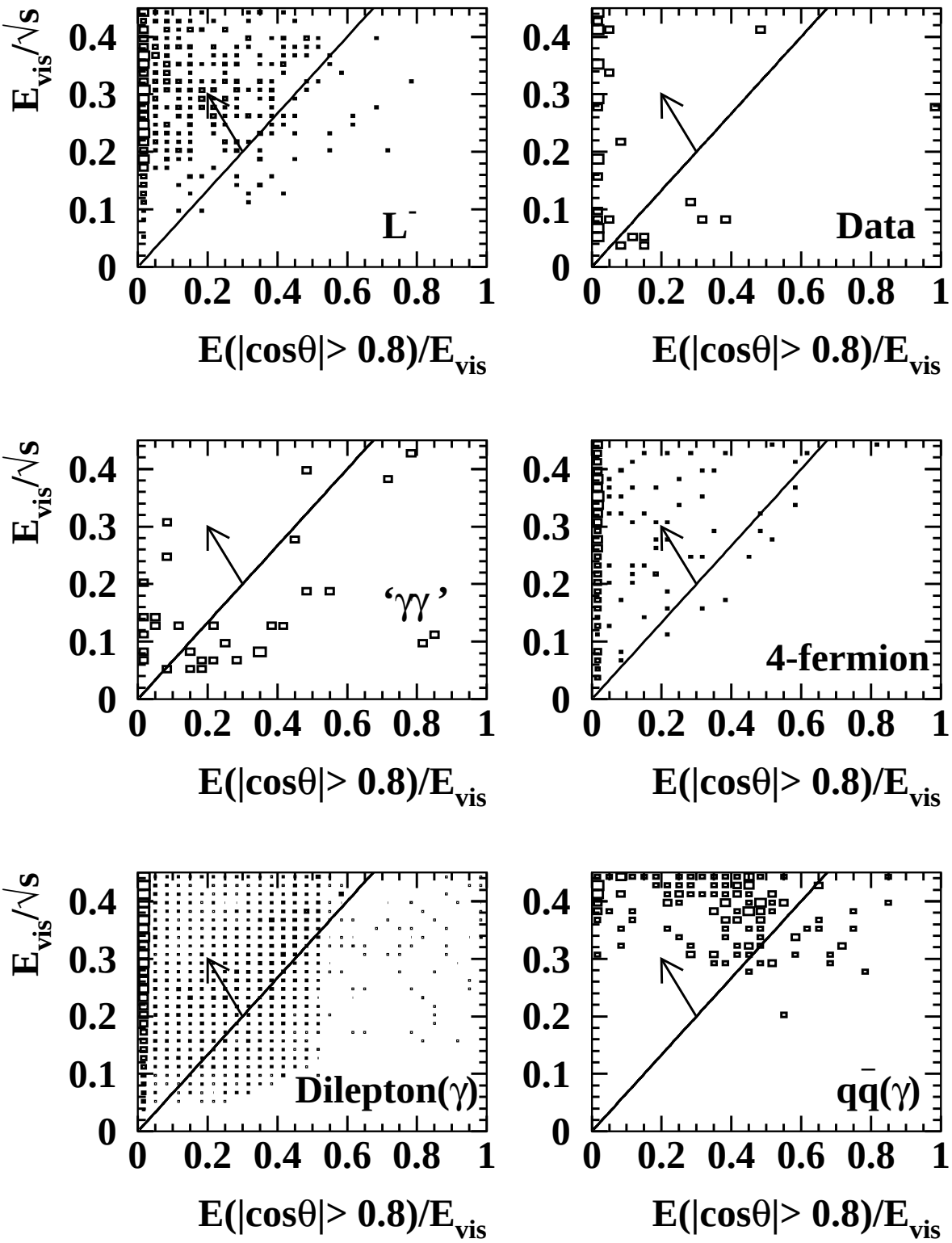

Figure 6.10: Scatter plots showing $E(|\cos\theta|{>}0.8)/\mathrm{E_{vis}}$ vs. the $E_{\mathrm{vis}}/\sqrt{s}$ after cut (B6). The diagonal line indicates cut (B7).

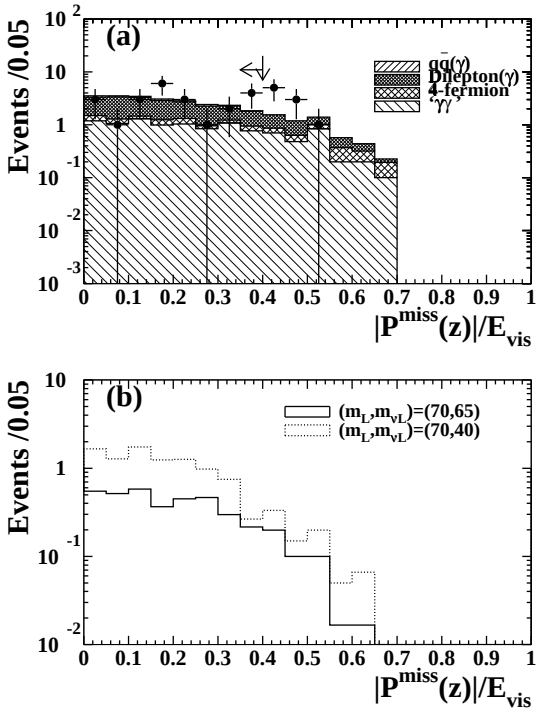

Figure 6.11: The $|P^{\mathrm{mis}}_{(z)}|$ distributions, normalized to visible energy, after cut (B6).

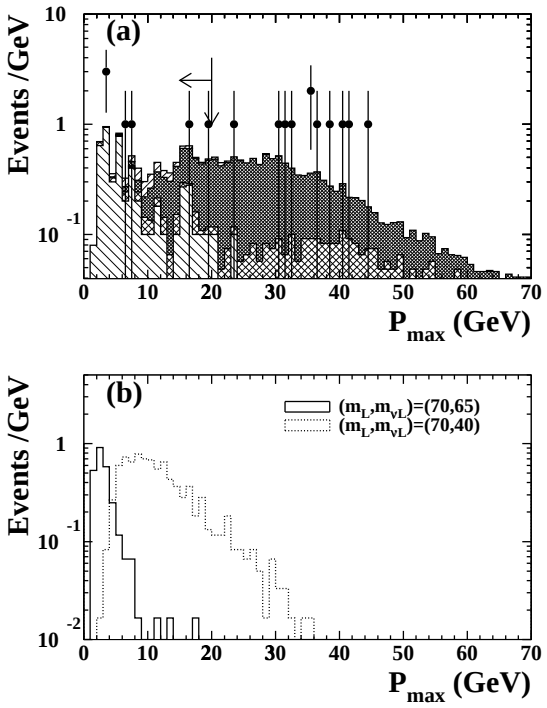

Figure 6.12: Distributions of the maximum charged track momentum after cut (B7).

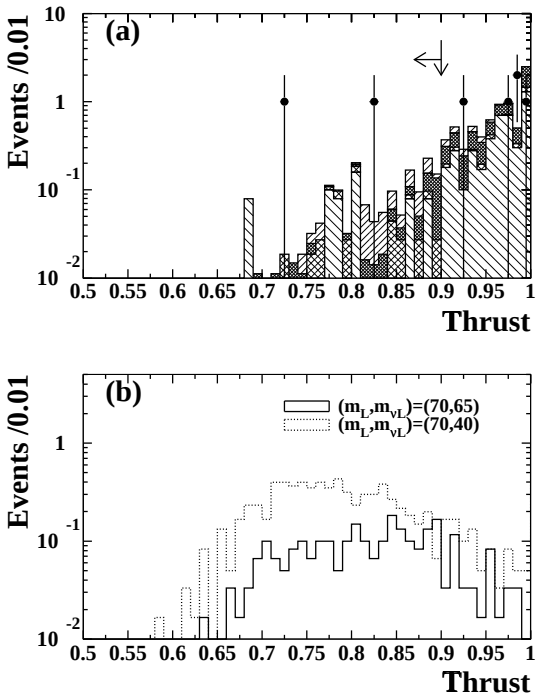

Figure 6.13: Thrust distributions after cut (B8).

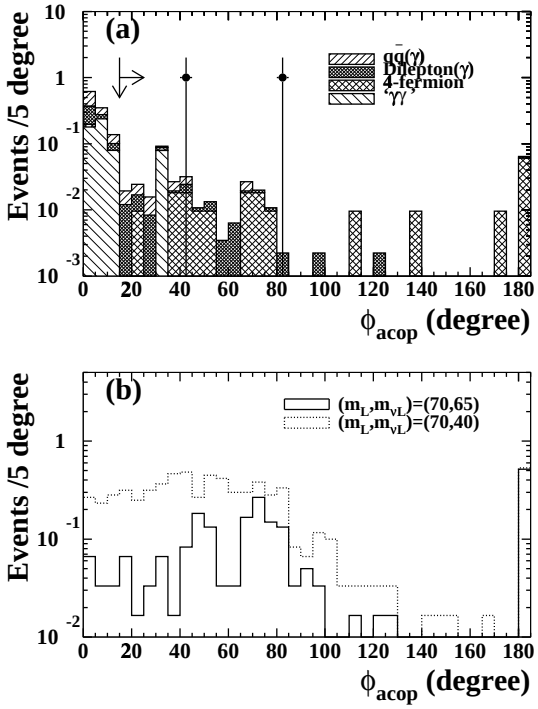

Figure 6.14: Acoplanarity angle distributions after cut (B9) for the $L^- \to \nu_L W^{*-}$ case.

Table 6.4: The selection efficiencies (in %) for $L^+L^- \to \nu_L W^{*+} \nu_L W^{*-}$ candidates for the mass combinations between m_{L^-} and m_{ν_L} in this analysis. The errors are statistical only.

m_{ν_L}	m_{L^-}= 65 GeV	70 GeV	75 GeV	80 GeV
75.0	—-	—-	—-	11.5 ± 1.0
70.0	—-	—-	11.0 ± 1.0	32.2 ± 1.5
65.0	—-	11.1 ± 1.0	31.4 ± 1.5	39.7 ± 1.5
60.0	10.6 ± 1.0	29.4 ± 1.4	36.0 ± 1.5	41.0 ± 1.6
55.0	27.6 ± 1.4	36.0 ± 1.5	39.7 ± 1.5	44.8 ± 1.6
50.0	33.3 ± 1.5	38.3 ± 1.5	41.5 ± 1.6	44.7 ± 1.6
45.0	37.6 ± 1.5	39.2 ± 1.5	40.1 ± 1.5	37.0 ± 1.5
40.0	31.8 ± 1.5	36.7 ± 1.5	32.4 ± 1.5	29.3 ± 1.4

should have been detected in the EB calorimeter with no energy deposit in HB, contrary to the observation. Thus, the possibility of being $\tau^+\tau^-\gamma$ was discarded. The two candidates are shown in Fig. 6.24 and Fig. 6.25 and measured variables are shown in Table. 6.5. The expected number of background events from all sources was estimated to be 0.38.

The efficiency of this selection was about 11% for (m_{L^-}, m_{ν_L}) = (70 GeV, 65 GeV) and 36% for (70 GeV, 40 GeV). The detection efficiencies for the ex-

Table 6.5: The measured parameters for two candidate events. In the table, $E_{\rm front}$ = $E(|\cos\theta|{>}0.8)/{\rm E_{vis}}$ and $R_{\rm vis} = E_{\rm vis}/\sqrt{s}$.

	CUT	Candidate A	Candidate B
(B1)	$N_{\rm ch} \geq 2$	15	2
(B2)	$E_{\rm FD} < 2$ GeV	0.	0.
	$E_{\rm SW} < 5$ GeV	0.	0.
	$E_{\rm GC} < 5$ GeV	0.	0.
(B3)	$\lvert\cos\theta_{\rm thrust}\rvert < 0.9$	0.15	0.072
(B4)	$P_t > 4$ GeV	35.70	13.34
	$P_t^{\rm HCAL} > 5$ GeV	39.15	23.27
(B5)	$\lvert\cos\theta_{\rm miss}\rvert < 0.7$	0.15	0.05
(B6)	$R_{\rm vis} < 0.45$	0.339	0.44
(B7)	$E_{\rm front}/R_{\rm vis} < 1.5$	0.10	0.00
	$\lvert P_z\rvert/E_{\rm vis} < 0.4$	0.11	0.02
(B8)	$P_{\rm ch}^{\rm max} < 20$ GeV	7.80	19.22
(B9)	Thrust < 0.9	0.73	0.82
(B10)	$\phi_{\rm acop} > 15°$	82.86	43.74

pected signals are summarized in Table 6.4.

6.4 Selection of $L^+L^- \to \bar{\nu}_\ell W^{*+} \nu_\ell W^{*-}$ candidates (case C)

The numbers of events remaining after each cut are listed in Table 6.6 for case (C). For comparison the table also includes the corresponding numbers of simulated background and L^+L^- events. The reason for the difference in the number of events between the data and the simulated background before cut (C3) is the same as in case (A).

The following selection criteria were applied:

(C1) The $N_{\rm ch}$ was required to be at least five, since there were WW$\to \ell\nu\ell\nu$ irreducible background and the two-lepton final state of the expected signals was not considered; one of the virtual W's was required to decay hadoronically. The ratio of the number of tracks which satisfied the quality criteria to the total number of reconstructed tracks was required to be larger than 0.2 in order to reject beam-gas and beam-wall backgrounds.

(C2) The criteria for energy deposits in the silicon tungsten calorimeter, the forward calorimeter and the gamma-catcher were identical to those in the $L^0\bar{L}^0$ analysis (see A2).

(C3) $|\cos\theta_{\rm thrust}|$ was required to be less than 0.95 in order to reduce beam-gas and beam-wall background events as well as events from two-photon processes.

(C4) The transverse momentum was expected to be large for the L^+L^- signal events, hence P_t and $P_t^{\rm HCAL}$ were required to be larger than 12 GeV and 15 GeV, respectively. With this cut the background from two-photon processes was efficiently reduced. The distributions of $P_t^{\rm HCAL}$ after cut (C3) are shown in Fig. 6.15(a) for the data and the simulated background events, and in Fig. 6.15(b) for the simulated L^+L^- (case (C)) events.

(C5) "Radiative return" events were rejected by requiring that the $\theta_{\rm miss}$ should satisfy $|\cos\theta_{\rm miss}| < 0.9$. The $|\cos\theta_{\rm miss}|$ cut was looser than in case (B) because the P_t and $P_t^{\rm HCAL}$ cuts in case (C) were tighter than in case (B). The distributions of $|\cos\theta_{\rm miss}|$ after cut (C4) are shown in Fig. 6.16.

(C6) In order to reject events containing back-to-back jets or leptons, the thrust of the event was required to be less than 0.9. The distributions of the thrust values after cut (C5) are shown in Fig. 6.17.

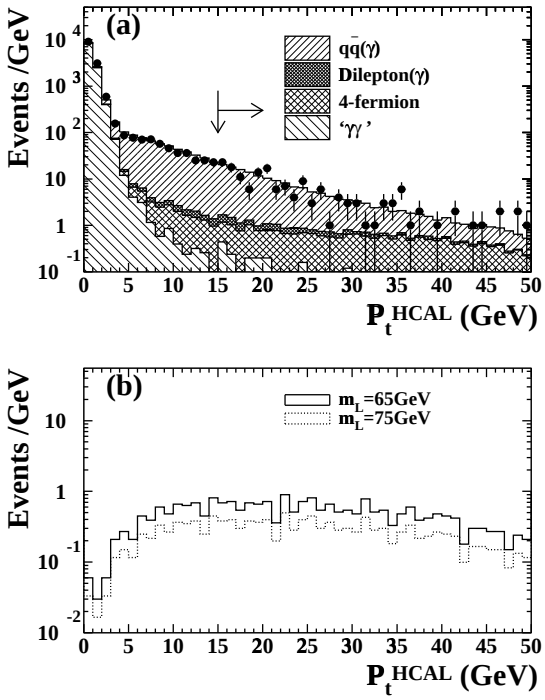

Figure 6.15: Distributions of missing transverse momentum after cut (C3) for the $L^- \to \nu_\ell W^{*-}$ case.

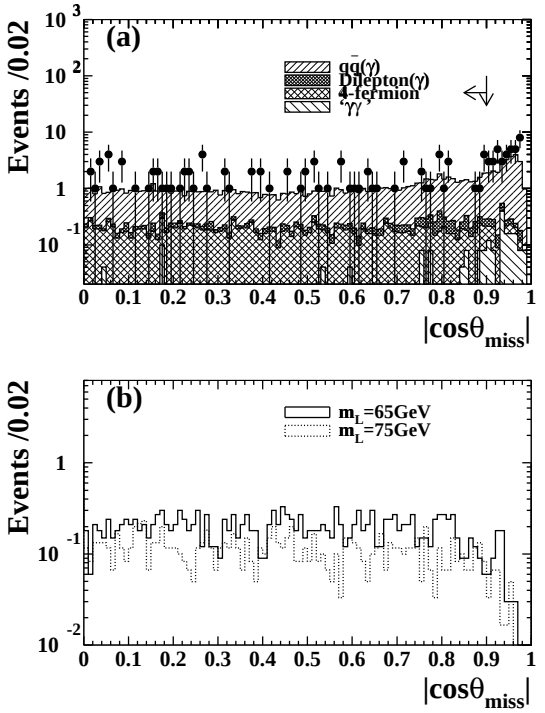

Figure 6.16: $|\cos\theta_{\rm miss}|$ distributions after cut (C4).

Table 6.6: The numbers of events remaining after each cut (in the $L^- \to \nu_\ell W^{*-}$ search) are compared with various background processes, normalised to the integrated luminosity. Expected numbers of events are also given for two samples of simulated L^+L^- events.

case (C)	data	total bkg.	$q\bar{q}(\gamma)$	$\ell\ell(\gamma)$	'$\gamma\gamma$'	4-f	L^+L^-	
m_{L^-} (GeV)							65	75
no cuts	–	–	1474	8428	220k	200	1000	1000
cut (C1)	75.4k	43.6k	1431	24.8	42.1k	59.9	900	914
cut (C2)	24.6k	23.8k	1063	21.9	22.7k	46.3	826	869
cut (C3)	13.6k	13.3k	1028	17.3	12.2k	44.6	793	831
cut (C4)	124	112.1	90.5	4.76	2.06	14.8	609	645
cut (C5)	85	88.4	69.2	4.22	0.79	14.2	589	631
cut (C6)	38	34.6	23.2	0.81	0.23	10.4	535	544
(HL)	3	6.57	2.31	0.24	0.00	4.02	173	192
cut (HL7)	0	0.56	0.28	0.07	0.00	0.21	122	133
cut (HL8)	0	0.23	0.00	0.03	0.00	0.20	111	120
(HH)	8	5.65	4.20	0.00	0.08	1.37	157	179
cut (HH9)	4	2.38	1.72	0.00	0.00	0.66	146	165
cut (HH10)	3	1.56	0.91	0.00	0.00	0.65	144	159
cut (HH11)	2	1.19	0.68	0.00	0.00	0.51	134	144
cut (HH12)	0	0.43	0.10	0.00	0.00	0.33	108	114
(HL8)+(HH12)	0	0.66	0.10	0.03	0.00	0.53	219	234

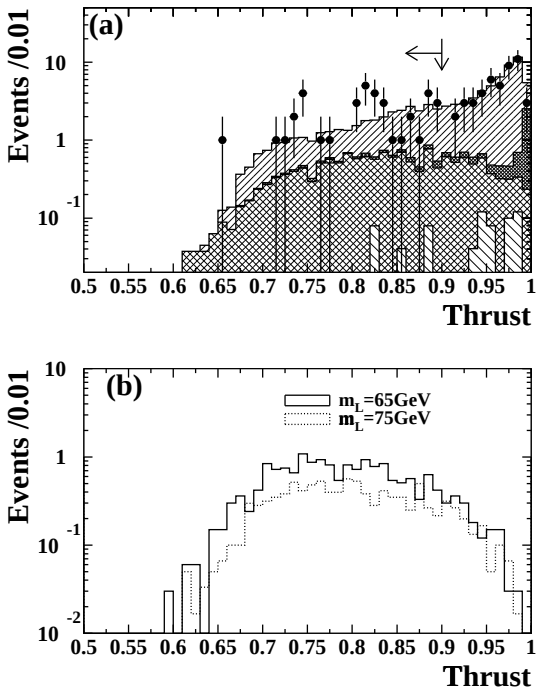

Figure 6.17: Thrust distributions after cut (C5).

The remaining events were classified into two categories, HL and HH, depending on whether they included the lepton signal or not. The same lepton identification was used as in the $L^0\bar{L}^0$ case at LEP1.5 analysis. The expected final states are $L^+L^- \to \bar{\nu}_\ell W^{*-} \nu_\ell W^{*+} \to \nu_\ell \ell' \nu_{\ell'} \nu_\ell qq'$ and $\nu_\ell qq' \nu_\ell q'' q'''$.

- (HL): If there were three reconstructed jets, including one lepton (e, μ or τ) with a momentum larger than 8 GeV, the event was classified as (HL) event, corresponding to the $\nu_\ell \ell' \nu_{\ell'} \nu_\ell qq'$ final states.
- (HH): If there was no track identified as a lepton with a momentum larger than 8 GeV and if the number of jets was equal to four, the event was categorized as (HH) event, corresponding to the $\nu_\ell qq' \nu_\ell q'' q'''$ final states.

The events which were not classified as (HL) or (HH) events were rejected in order to reduce the multihadron and four-fermion backgrounds.

The following further cuts were applied;

(HL7) For (HL) events, the visible energy was required to satisfy $0.25 < E_{\rm vis}/\sqrt{s} < 0.6$. With this cut, backgrounds from four-fermion processes and multihadron events were effectively reduced. The distributions of $E_{\rm vis}/\sqrt{s}$ for the events categorized as (HL) are shown in Fig. 6.18.

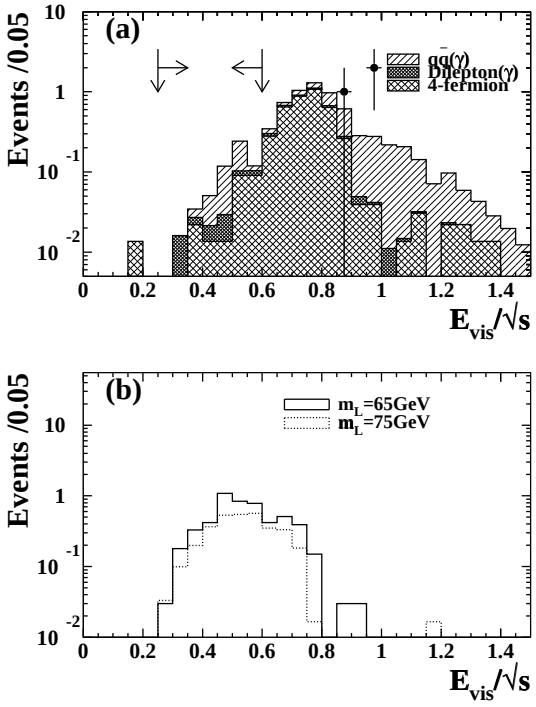

Figure 6.18: $E_{\rm vis}/\sqrt{s}$ distributions for the events categorized as (HL).

(HL8) The acoplanarity angle ($\phi_{\rm acop}$) was required to be greater than 10° to reject multihadron events. The distributions of $\phi_{\rm acop}$ after cut (HL7) are shown in Fig. 6.19.

(HH9) For (HH) events, the visible energy was required to satisfy $0.4 < E_{\rm vis}/\sqrt{s} < 0.9$. Multihadron background was reduced by this cut. The distributions of $E_{\rm vis}/\sqrt{s}$ for the events categorized as (HH) are shown in Fig. 6.20.

(HH10) The $E_{\rm back}$ was required to be less than 5 GeV in order to reduce a large fraction of the multihadron background. The distributions of $E_{\rm back}$ before cut (HH10) are shown in Fig. 6.21.

(HH11) Four-fermion processes and multihadron events were reduced by requiring that no track momentum should exceed 30 GeV. The distributions of the maximum charged track momentum after cut (HH10) are shown in Fig. 6.22.

(HH12) The acoplanarity angle ($\phi_{\rm acop}$) was required to be greater than 15° to reject multihadron events. The acoplanarity angle distributions just before the cut are plotted in Fig. 6.23(a) for the data and the simulated background events and in Fig. 6.23(b) for simulated L^+L^- events.

The detection efficiency was about 20–24% for m_{L^-} in the range 60–80 GeV. The detection efficiencies for the expected signals are summarized in Table 6.7.

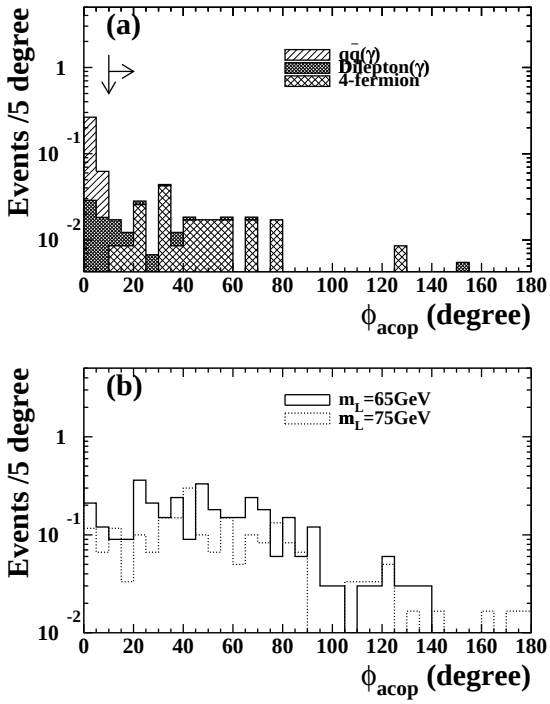

Figure 6.19: Acoplanarity angle distributions after cut (HL7).

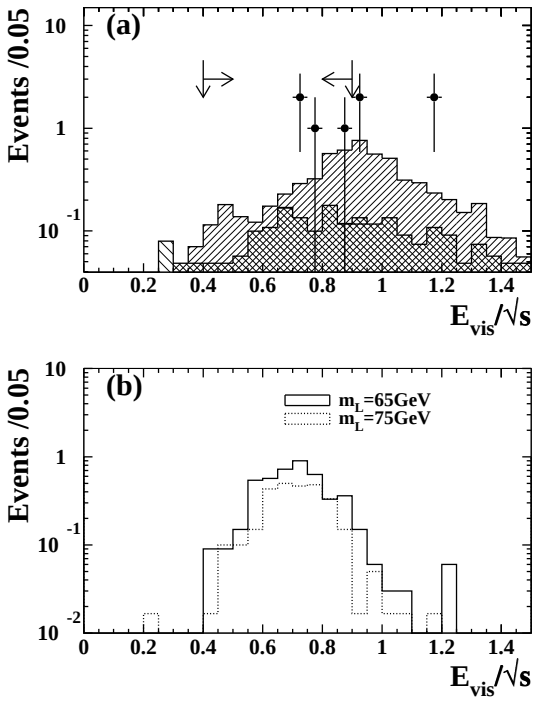

Figure 6.20: $E_{\rm vis}/\sqrt{s}$ distributions for the events categorized as (HH).

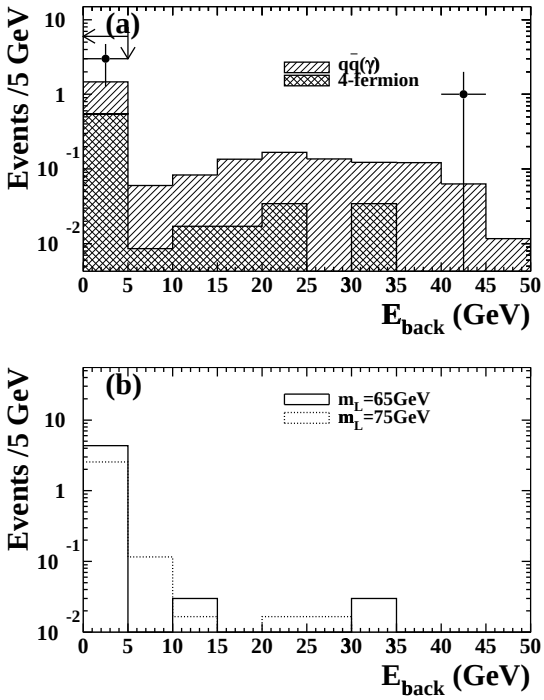

Figure 6.21: The $E_{\rm back}$ distributions after cut (HH9).

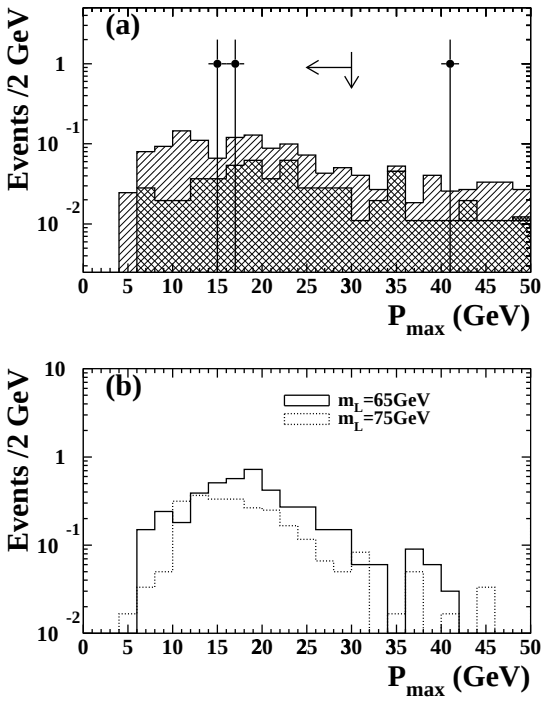

Figure 6.22: Distributions of the maximum charged track momentum after cut (HH10).

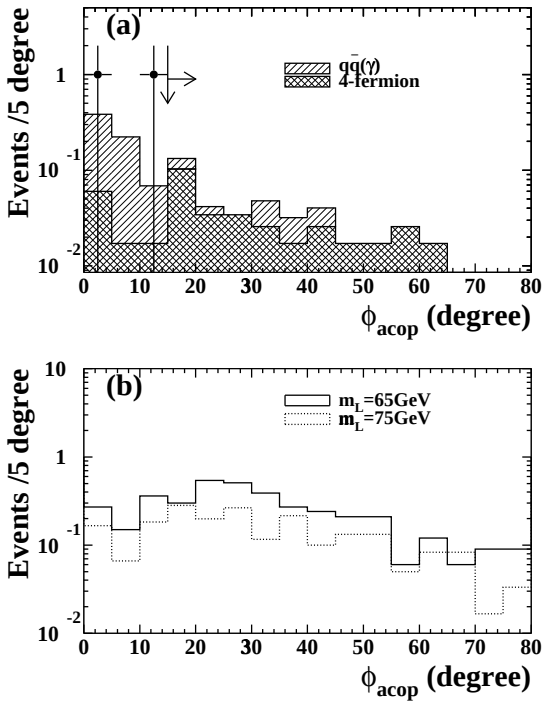

Figure 6.23: Acoplanarity angle distributions after cut (HH11).

No event was observed in the data after the above selection, consistent with the total of 0.66 background events expected.

6.5 Systematic Errors

The estimation techniques of the systematic errors are identical as the LEP15 analysis.

The systematic errors on the total number of expected signal events were estimated to be
3–6% from Monte Carlo statistics, depending on the event topology,
0.2% (1.0%) from the uncertainty on the beam energy for $L^0\bar{L}^0$ (L^+L^-),
1.3% from the uncertainty due to the detector simulation,
1.0% from the interpolation of the efficiencies,
0.6% from the uncertainty in the integrated luminosity,
3.5% from the lepton identification uncertainty, and

Table 6.7: The selection efficiencies (in %) of $L^- \to \nu_\ell W^{*-}$ candidates as a function of mass. The errors are statistical only.

m_{L^-} = 65 GeV	70 GeV	75 GeV	80 GeV
21.9 ± 1.3	24.6 ± 1.4	23.4 ± 1.3	20.0 ± 1.3

1.6% (0.9%) from the uncertainty in the fragmentation of W* hadronic decays for $L^0\bar{L}^0$ (L^+L^-). The fragmentation errors arose through the jet reconstruction and lepton isolation uncertainties for the $L^0\bar{L}^0$ case, and mainly through the uncertainty in the estimation of the acoplanarity angle and the missing momentum direction for the L^+L^- case. The fragmentation error was estimated by varying the fragmentation parameters from their optimized values [99] in the JETSET 7.4 Monte Carlo generator. The systematic error due to trigger efficiency was estimated to be negligible for the selected signal events. The individual systematic errors were considered to be independent, and the total systematic error was calculated as their quadratic sum. In calculating mass limits the systematic errors were treated as described in Ref. [100].

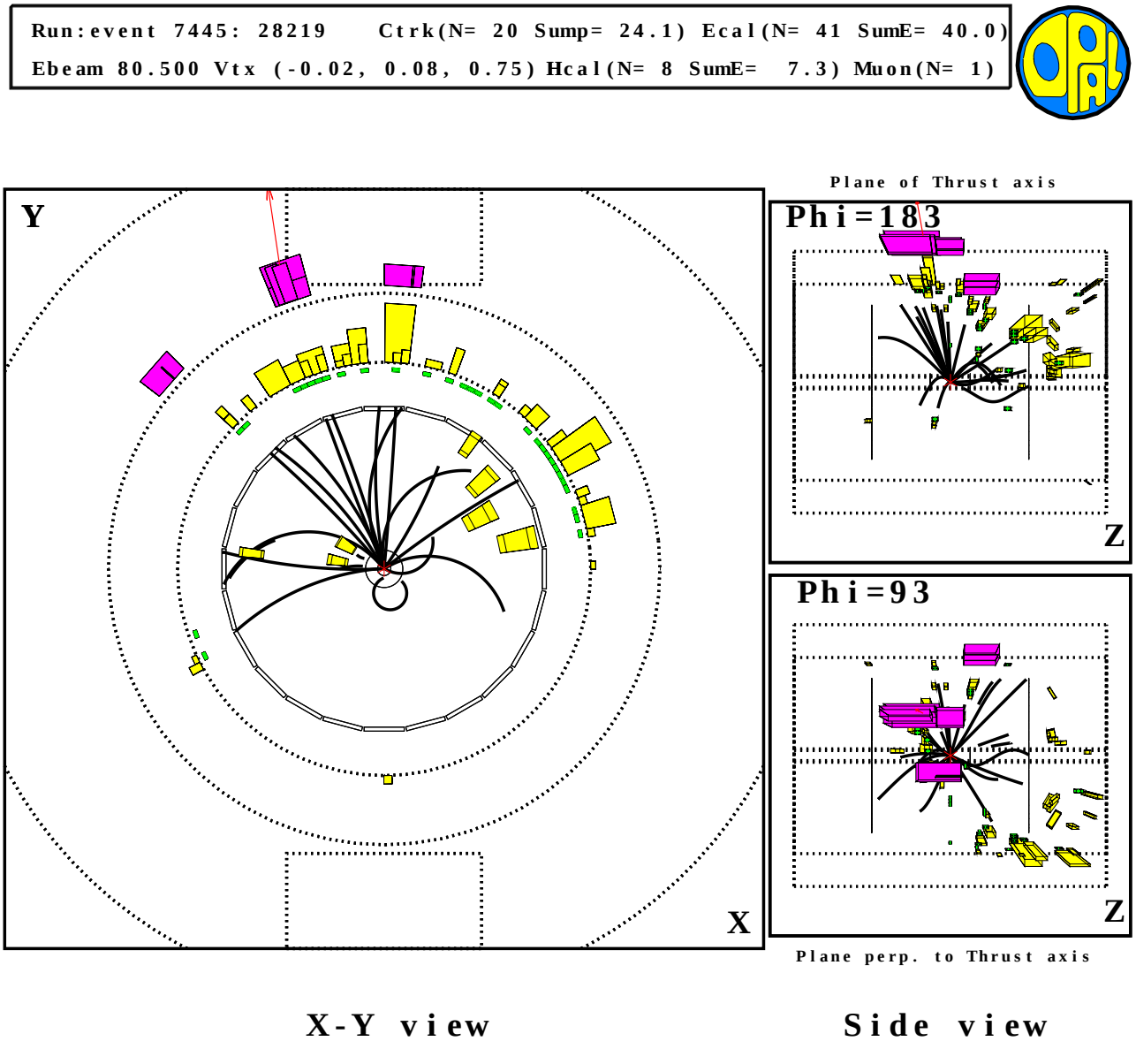

Figure 6.24: One (candidate A) of the two candidate events for case (B). The visible energy of the event is 55 GeV, and the missing transverse momentum is 39 GeV. The dark lines represent fitted charged tracks in the tracking chambers. The light grey boxes indicate the relative energies deposited in EM clusters. The dark grey boxes indicate the relative amount of energies deposited in HCAL clusters.

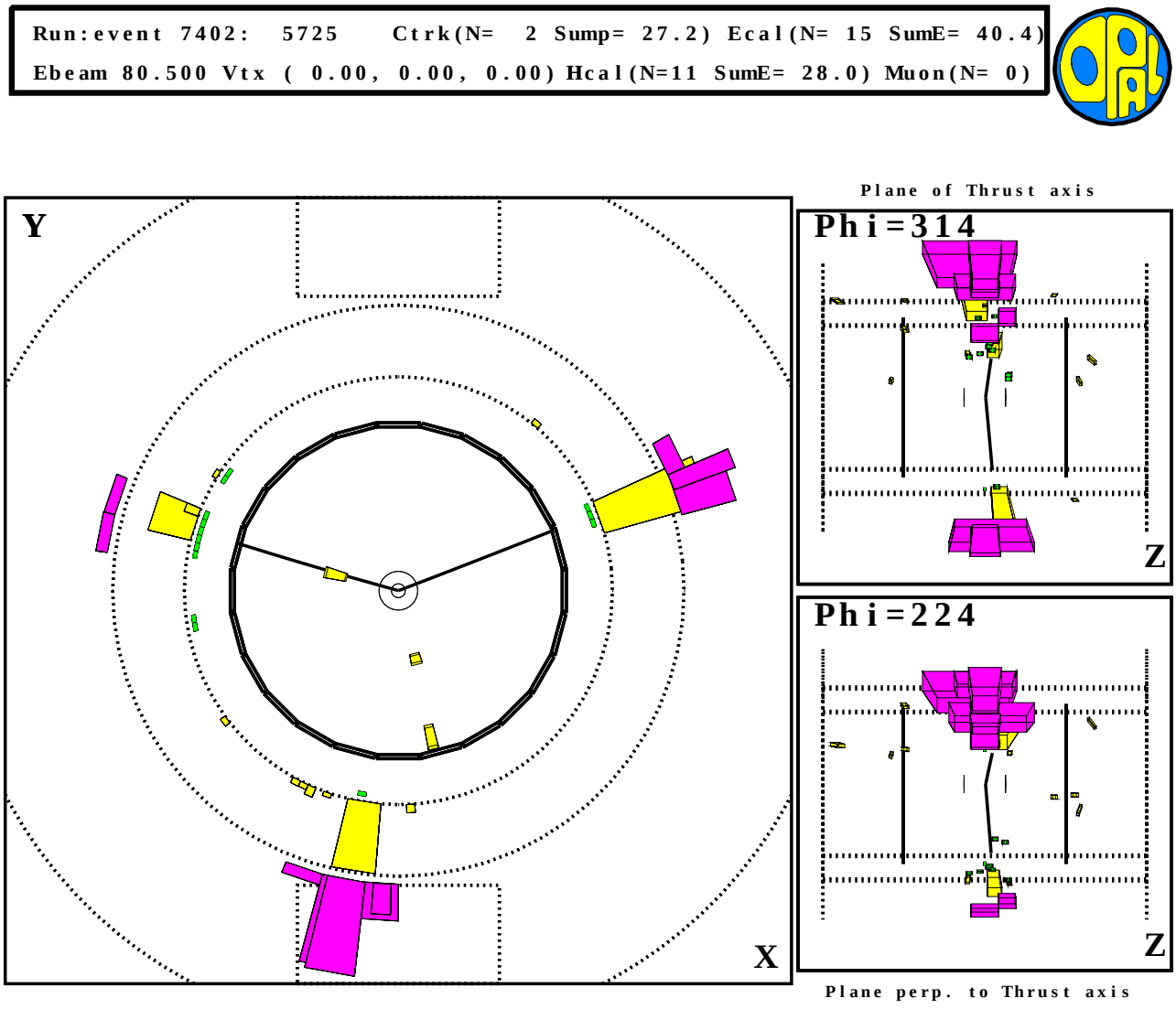

Figure 6.25: One (candidate B) of the two candidate events for case (B). The visible energy of the event is 71 GeV, and the missing transverse momentum is 23 GeV. The dark lines represent fitted charged tracks in the tracking chambers. The light grey boxes indicate the relative energies deposited in EM clusters. The dark grey boxes indicate the relative amount of energies deposited in HCAL clusters.

Chapter 7

Results

7.1 Combined results from LEP1.5 and LEP2 analyses

Lower mass limits for L^0 were calculated by combining the number of expected events both from the analysis at LEP1.5 and LEP2. On calculating the mass limits, the effect of the forward veto noise (FD, GC, SW) and the effect of inefficient subdetectors were included by reducing the signal efficiencies.

A 95% C.L. lower limit of 69.3 GeV is obtained on the mass of the Dirac neutral heavy lepton, assuming that both L^0 and $\bar{L}^0$ decay into eW* with 100% branching fraction. Corresponding limits for the cases of $L^0 \to \mu W^*$ and $L^0 \to \tau W^*$ are 72.0 GeV and 66.0 GeV, respectively. For the Majorana L^0 the limits are reduced to 59.5 GeV for the eW* decay, 60.5 GeV for the μW* decay and 55.7 GeV for the τW* decay due to the smaller cross-section near the $L^0\bar{L}^0$ threshold. For the mixed decay products of $L^0\bar{L}^0$ ($L^0\bar{L}^0 \to eW^*\mu W^*$, $eW^*\tau W^*$ or $\mu W^*\tau W^*$) the mass limits have values intermediate of the unmixed cases. Fig. 7.1 and Fig. 7.2 show the expected number of events and the limits on the cross-section as a function of m_{L^0}, respectively. The excluded region on the plane of ($|V_{L\ell}|^2$, m_{L^0}) is shwon in Fig. 7.3.

The mass of the $L^\pm$ was found to be larger than 73.5 GeV at 95% C.L. for case (B), if m_{L^-} - $m_{\nu_L} > 13$ GeV. In calculating the mass limits, the two candidate events for case (B) observed were considered as possible signals and the expected number of background events was not subtracted. The excluded region in the (m_{L^-}, m_{ν_L}) plane for case (B) is presented in Fig. 7.4.

For case (C) the lower limit for m_{L^-} is 76.7 GeV at 95% C.L. Fig. 7.5 shows the expected number of events as a function of m_{L^-}. Fig. 7.6 shows the limits on the cross-section as a function of m_{L^-}.

In summary the mass limits obtained in the LEP1.5 and LEP2 analyses are shwon in Table 7.1 and 7.2

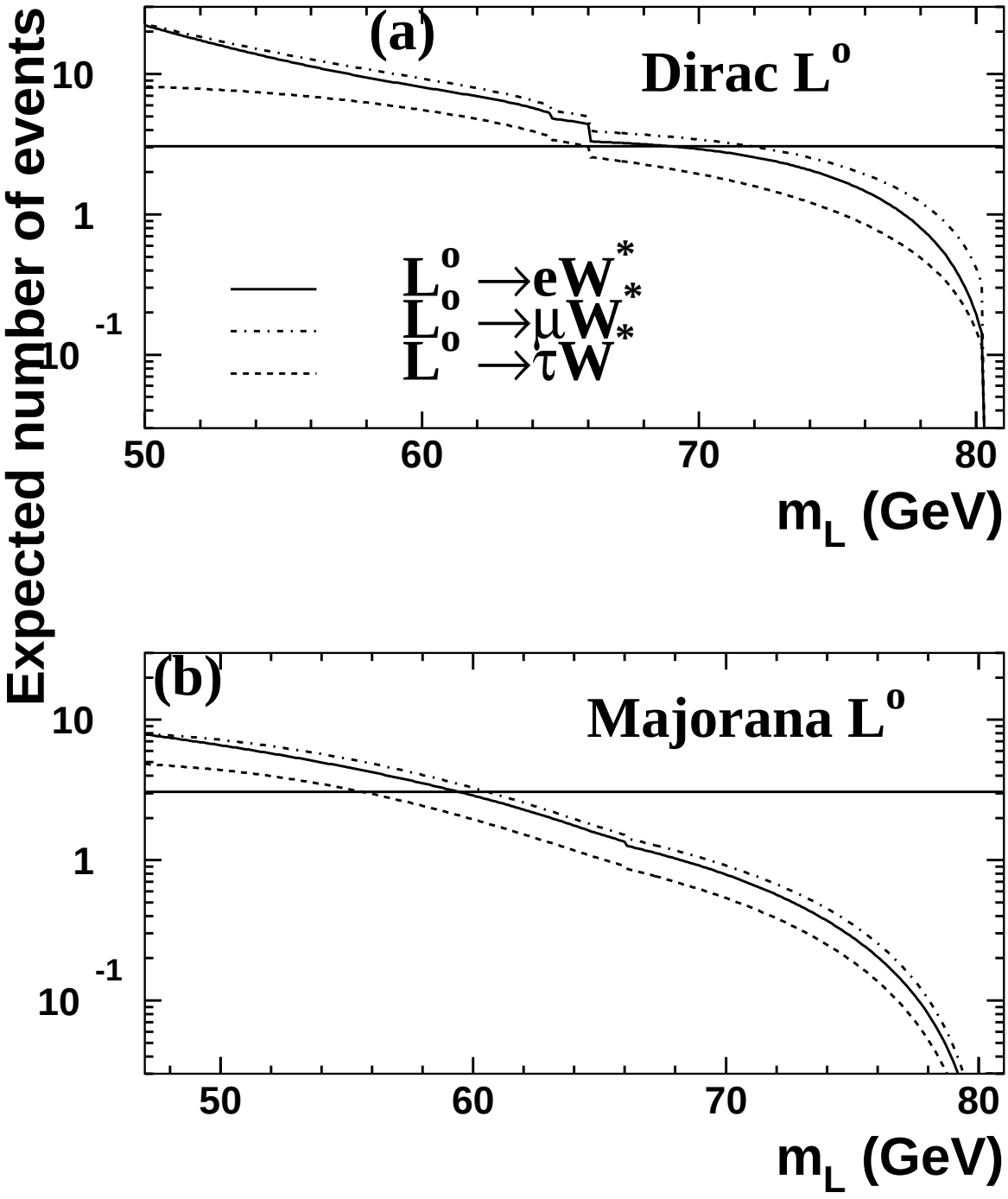

Figure 7.1: Expected number of events as a function of m_{L^0} for $\mathrm{L}^0\bar{\mathrm{L}}^0 \to \ell\mathrm{W}^*\ell\mathrm{W}^*$ (case(A)). The horizontal lines show the threshold number of expected L^0 events at the 95% C.L. limit including systematic errors.

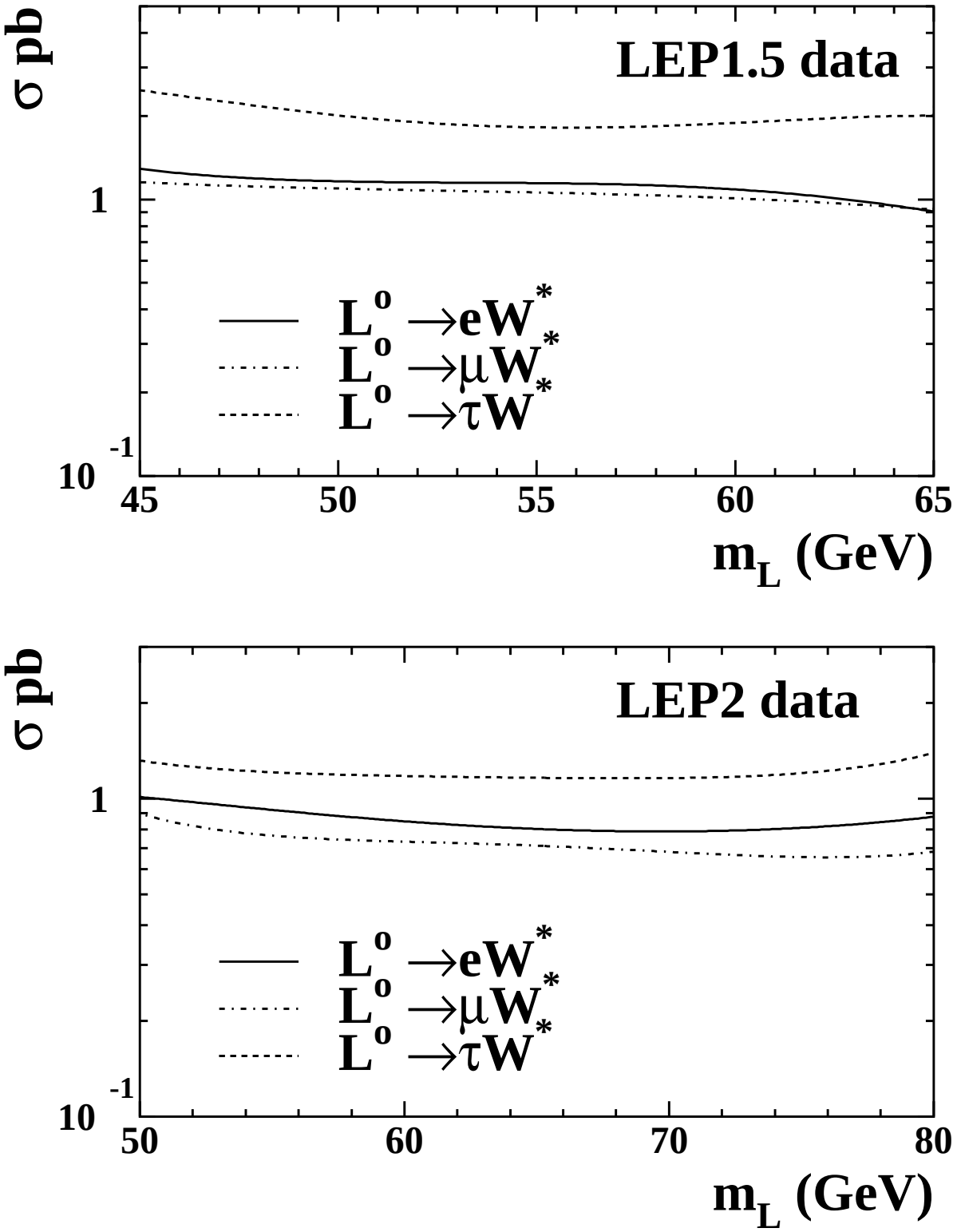

Figure 7.2: Limits on the cross-section for pair production of neutral lepton as a function of $m_{\mathrm{L^0}}$ (case (A)). Upper figure shows the LEP1.5 data and lower figure the LEP2 data.

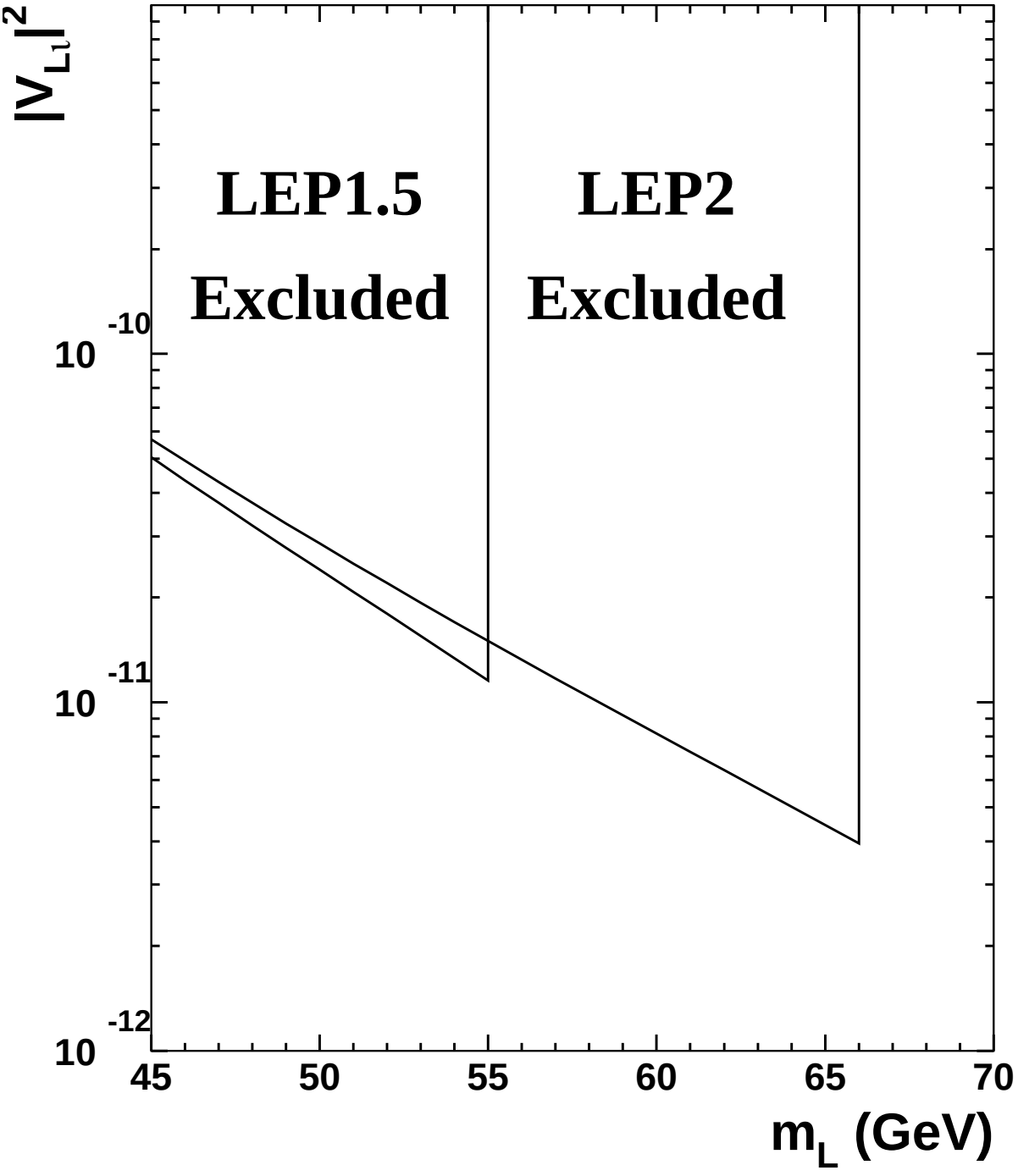

Figure 7.3: The region excluded in this analysis on the ($|V_{L\ell}|^2$, m_{L^0}) plane for the sequential Dirac L^0 (case (A)).

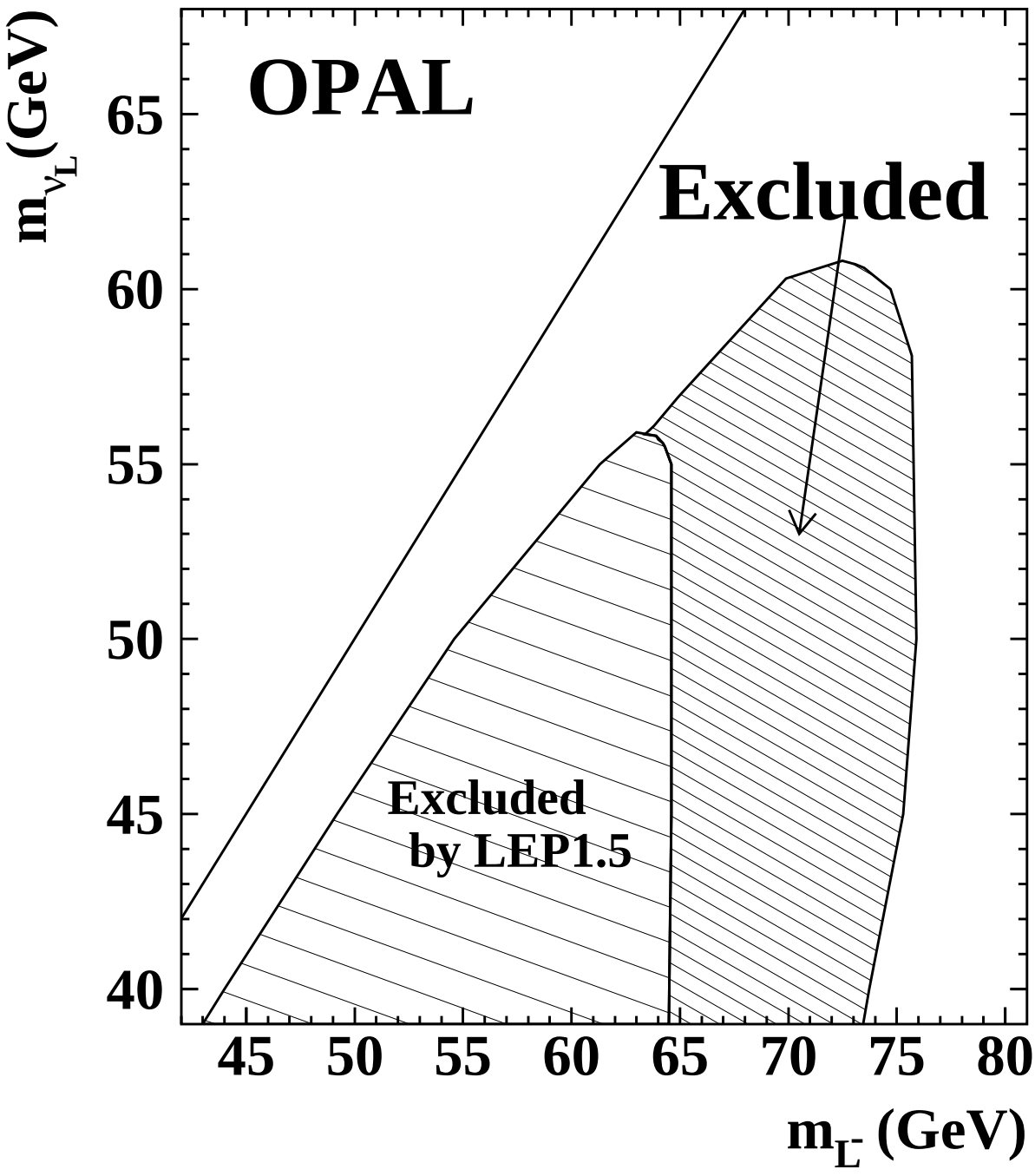

Figure 7.4: The region excluded in this analysis in the (m_{L^-}, m_{ν_L}) plane for case (B). If L^- decays into ν_L + W^{*-} and ν_L is assumed to be stable, the hatched region is excluded with more than 95% C.L. The region $m_{\nu_\mathrm{L}} < 45.0$ GeV is already excluded for the Dirac ν_L and $m_{\nu_\mathrm{L}} < 39.5$ GeV for the Majorana ν_L at LEP1 [1, 20]. The diagonal line shows $m_{\mathrm{L}^-} = m_{\nu_\mathrm{L}}$.

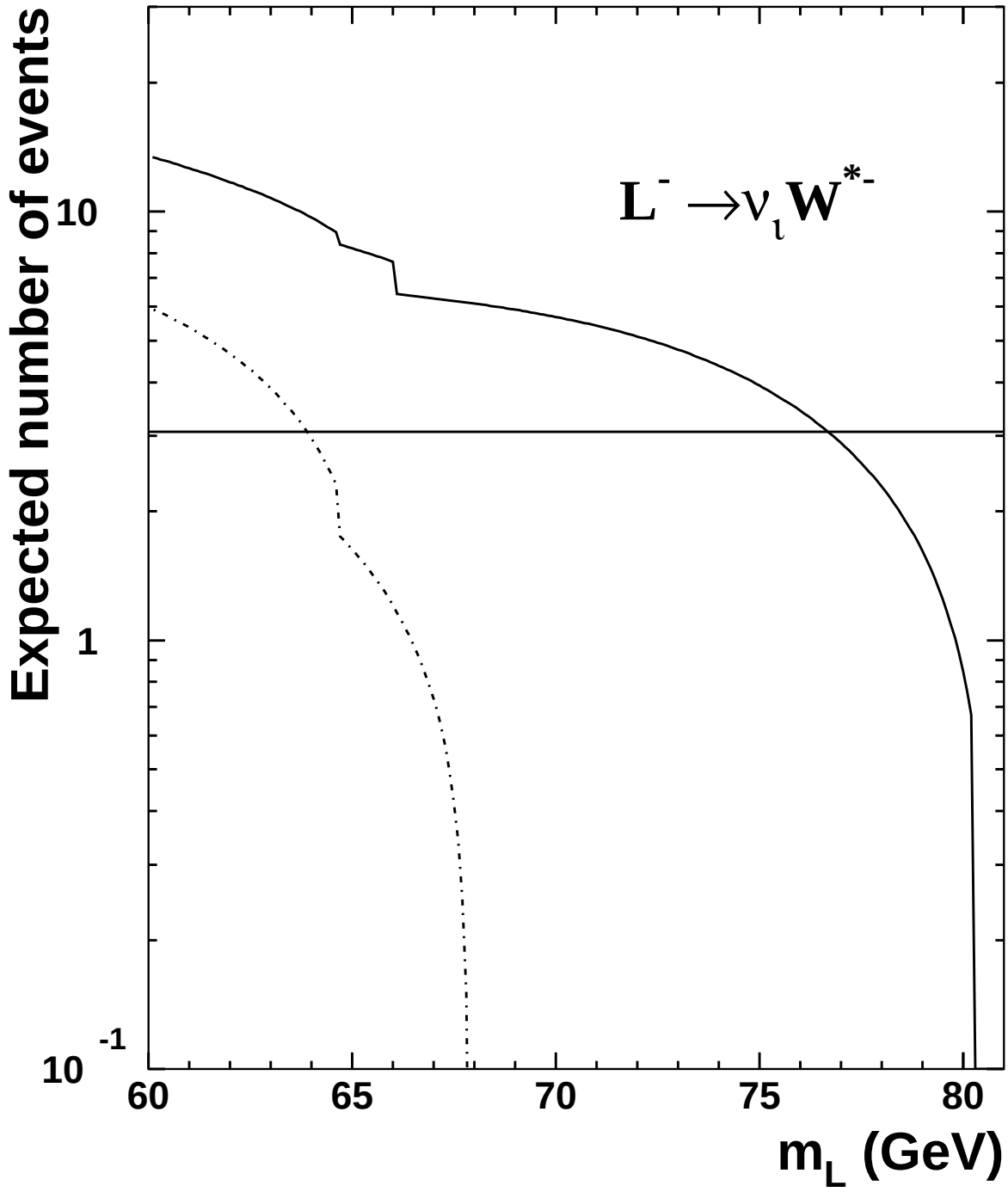

Figure 7.5: Expected number of events as a function of m_{L^-} for $\mathrm{L}^+\mathrm{L}^- \to \nu_\ell \mathrm{W}^* \nu_\ell \mathrm{W}^*$ (case (C)). The solid line indicates the combined function of LEP1.5 and LEP2. The dash-dot line indicates the function only of LEP1.5 data. The horizontal lines show the threshold number of expected L^- events at the 95% C.L. limit including systematic errors.

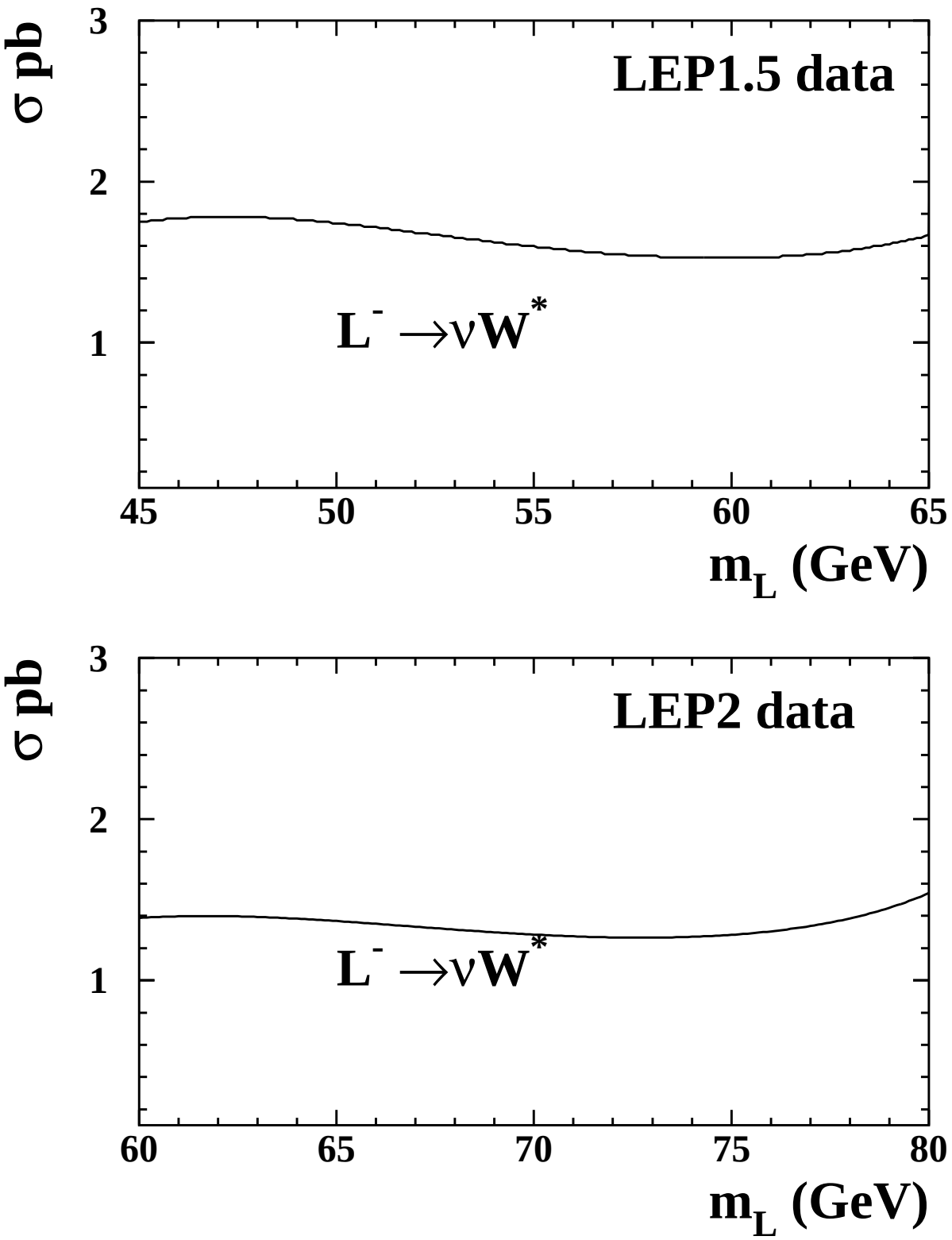

Figure 7.6: Limits on the cross-section for pair production of the charged lepton for case (C) as a function of m_{L^-}. Upper figure shows the LEP1.5 data and lower figure the LEP2 data.

Table 7.1: The lower mass limits for new unstable heavy leptons for LEP1.5 data only and LEP1.5 + LEP2 data, which are compared with LEP1 ($\sqrt{s} = M_{\mathrm{Z}}$) limits. For comparison the limits are also shown from other LEP experiments (ALEPH, L3 and DELPHI), for the mixing parameter $|V_{\mathrm{L}}\ell|^2 > 10^{10}$.

Event topology	type	LEP1	LEP1.5	LEP1.5 + 2
$\mathrm{L}^0\bar{\mathrm{L}}^0 \to \mathrm{eW}^*\mathrm{eW}^*$	Dirac	46.5 GeV	62.5 GeV	**69.3 GeV**
ALEPH limit	Dirac	45.7 GeV	63.6 GeV	–
L3 limit	Dirac	46.5 GeV	59.3 GeV	–
DELPHI limit	Dirac	46.2 GeV	–	–
	Majorana	–	51.4 GeV	**59.5 GeV**
ALEPH limit	Majorana	–	55.2 GeV	–
L3 limit	Majorana	45.5 GeV	48.6 GeV	–
DELPHI limit	Majorana	44.7 GeV	–	–
$\mathrm{L}^0\bar{\mathrm{L}}^0 \to \mu\mathrm{W}^*\mu\mathrm{W}^*$	Dirac	46.5 GeV	63.0 GeV	**72.0 GeV**
ALEPH limit	Dirac	45.7 GeV	63.6 GeV	–
L3 limit	Dirac	46.5 GeV	57.9 GeV	–
DELPHI limit	Dirac	46.2 GeV	–	–
	Majorana	–	52.2 GeV	**60.5 GeV**
ALEPH limit	Majorana	–	55.2 GeV	–
L3 limit	Majorana	45.5 GeV	47.2 GeV	–
DELPHI limit	Majorana	44.7 GeV	–	–
$\mathrm{L}^0\bar{\mathrm{L}}^0 \to \tau\mathrm{W}^*\tau\mathrm{W}^*$	Dirac	45.7 GeV	57.4 GeV	**66.0 GeV**
ALEPH limit	Dirac	45.7 GeV	63.0 GeV	–
L3 limit	Dirac	46.4 GeV	–	–
DELPHI limit	Dirac	45.7 GeV	–	–
	Majorana	–	44.2 GeV	**55.7 GeV**
ALEPH limit	Majorana	–	54.3 GeV	–
L3 limit	Majorana	46.4 GeV	–	–
DELPHI limit	Majorana	43.6 GeV	–	–

Table 7.2: The lower mass limits (with large character) for new unstable heavy leptons on LEP1.5 ($\sqrt{s} = 130$ GeV and 136 GeV data) and LEP2 ($\sqrt{s} = 161$ GeV data) for case (C), which are compared with LEP1 ($\sqrt{s} = M_{\mathrm{Z}}$) limits and ALEPH result. Even by combining LEP1.5 data with LEP2 data, the improvement of the LEP2 limit is negligible since it is mainly determined by the kinematical limit; i.e. beam energy.

Event topology	LEP1	LEP1.5	LEP2
$\mathrm{L}^- \to \nu_\ell \mathrm{W}^{*-}$	42.7 GeV	63.9 GeV	**76.7 GeV**
ALEPH limit	42.7 GeV	65.0 GeV	–

Chapter 8

Conclusion

A search has been made for pair production of unstable neutral and charged heavy leptons using a data sample corresponding to integrated luminosities of 2.4 pb^{-1} at $\sqrt{s} = 130$, 2.8 pb^{-1} at 136 GeV (LEP1.5) and 10.0 pb^{-1} at $\sqrt{s} = 161.3$ GeV (LEP2), collected with the OPAL detector at LEP. No events remained after the selection cuts for the $\mathrm{L}^0\bar{\mathrm{L}}^0$ and $\mathrm{L}^- \to \nu_\ell \mathrm{W}^{*-}$ searches. For the $\mathrm{L}^- \to \nu_\mathrm{L} \mathrm{W}^{*-}$ search, two candidate events were observed. These results were consistent with the total expected number of background events of 1.57.

The 95% C.L. lower limit on the Dirac L^0 mass, assuming that L^0 decays into eW^* with 100% branching fraction, was determined to be 69.3 GeV. The mass limits for $\mu\mathrm{W}^*$ and $\tau\mathrm{W}^*$ decays are 72.0 GeV and 66.0 GeV, respectively. For Majorana L^0 the limits were reduced to 59.5 GeV for pure eW^* decay, 60.5 GeV for pure $\mu\mathrm{W}^*$ decay and 55.7 GeV for the $\tau\mathrm{W}^*$ case due to the smaller cross-section in the region near the $\mathrm{L}^0\bar{\mathrm{L}}^0$ threshold.

The excluded region in the (m_{L^-}, m_{ν_L}) plane is presented in Fig. 7.4. If $m_{\mathrm{L}^-} - m_{\nu_\mathrm{L}} > 13$ GeV, the mass of L^- was found to be larger than 73.5 GeV at 95% C.L. If $m_{\nu_\mathrm{L}} > m_{\mathrm{L}^-}$ and L^- decays into a massless neutrino and a virtual W boson, a lower limit of 76.7 GeV at 95% C.L. was obtained for m_{L^-}. The results of these analyses have extended existing limits from the LEP experiments [1, 4, 101].

Appendix A

List of Abbreviations

CJ OPAL Jet Chamber

CV OPAL Vertex Detector

CZ OPAL Z-Chamber

EB OPAL Barrel Electromagnetic Calorimeter

EE OPAL Endcap Electromagnetic Calorimeter

EM electromagnetic calorimeter trigger

EPA Electron Positron Accumulator

FD OPAL Forward Detector

GPMH gold-plated multihadronic event selection

GTU global trigger unit

HA hadron calorimeter trigger

HB OPAL Hadron Barrel Calorimeter

HE OPAL Hadron Endcap Calorimeter

HP OPAL Hadron Pole-Tip Calorimeter

HS hadron calorimeter strip

HT hadron calorimeter tower

LSC local system crate

LTU local trigger unit

MB OPAL Barrel Muon Detector

ME OPAL Endcap Muon Detector

MU muon detector trigger

OPAL Omni-Purpose Apparatus for LEP

PAM pattern arrangement module

PB OPAL Barrel Electromagnetic Presampler

PE OPAL Endcap Electromagnetic Presampler

PS CERN Proton Synchrotron

ROPE OPAL Event Reconstruction Program

SI OPAL Silicon Microvertex Detector

SPS CERN Super Proton Synchrotron

TB OPAL Time-of-Flight Counter

TKMH Tokyo multihadronic event selection

TOF time-of-flight trigger

TT track trigger

Appendix B

Description of the event figure

The definition on upper-left side in Fig. B.1 is as follows:

ETOT	Total visible energy
PMIS	Missing momentum
PT	Missing transverse momentum
COSMIS	Cosine of the polar angle of the missing momentum direction
PCHG	Absolute sum of the momentum of the charged track
ESHW	Energy sum of the good EM clusters
NCHG	Number of good charged tracks
NSHW	Number of good EM clusters
EEB	Energy sum of the good EB clusters
EEE	Energy sum of the good EE clusters
FDL	The sum of FD calorimeter and SW energies (left-side)
FDR	The sum of FD calorimeter and SW energies (right-side)
NTOF	Number of TOF hits
EHAD	Energy sum of good HT clusters
THRU	Thrust value
COST	Cosine of the polar angle of the thrust axis

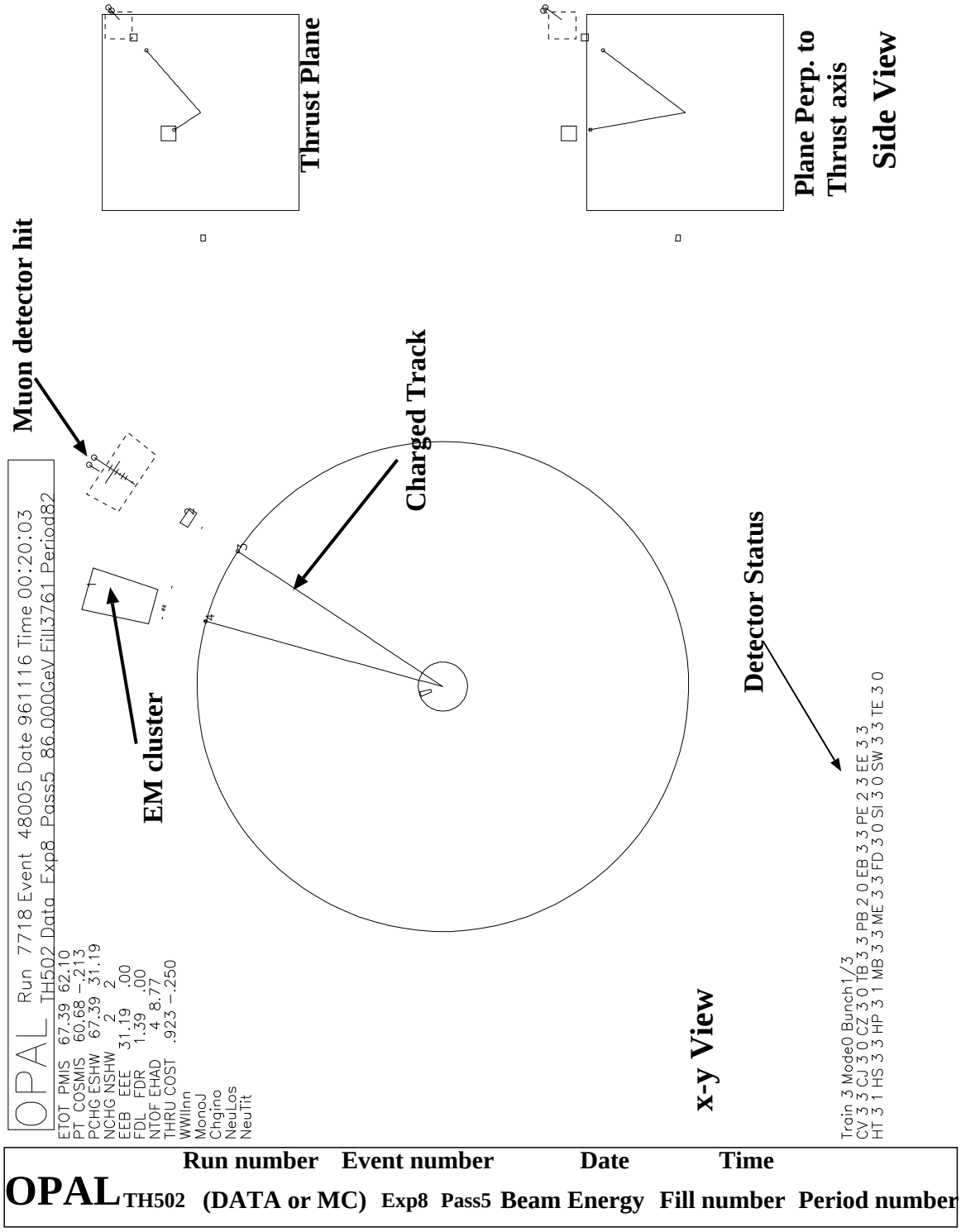

Figure B.1: An event sample of the $W^+W^- \to e\nu_e\mu\nu_\mu$.

Appendix C

The OPAL Collaboration

The OPAL detector was built and is operated by the collaboration of the following people from 34 institutes:

K. Ackerstaff[8], G. Alexander[23], J. Allison[16], N. Altekamp[5], K. Ametewee[25], K.J. Anderson[9], S. Anderson[12], S. Arcelli[2], S. Asai[24], D. Axen[29], G. Azuelos[18,a], A.H. Ball[17], E. Barberio[8], R.J. Barlow[16], R. Bartoldus[3], J.R. Batley[5], J. Bechtluft[14], C. Beeston[16], T. Behnke[8], A.N. Bell[1], K.W. Bell[20], G. Bella[23], S. Bentvelsen[8], P. Berlich[10], S. Bethke[14], O. Biebel[14], V. Blobel[27], I.J. Bloodworth[1], J.E. Bloomer[1], M. Bobinski[10], P. Bock[11], H.M. Bosch[11], M. Boutemeur[34], B.T. Bouwens[12], S. Braibant[12], R.M. Brown[20], H.J. Burckhart[8], C. Burgard[8], R. Bürgin[10], P. Capiluppi[2], R.K. Carnegie[6], A.A. Carter[13], J.R. Carter[5], C.Y. Chang[17], D.G. Charlton[1,b], D. Chrisman[4], P.E.L. Clarke[15], I. Cohen[23], J.E. Conboy[15], O.C. Cooke[16], M. Cuffiani[2], S. Dado[22], C. Dallapiccola[17], G.M. Dallavalle[2], S. De Jong[12], L.A. del Pozo[8], K. Desch[3], M.S. Dixit[7], E. do Couto e Silva[12], M. Doucet[18], E. Duchovni[26], G. Duckeck[34], I.P. Duerdoth[16], J.E.G. Edwards[16], P.G. Estabrooks[6], H.G. Evans[9], M. Evans[13], F. Fabbri[2], P. Fath[11], F. Fiedler[27], M. Fierro[2], H.M. Fischer[3], R. Folman[26], D.G. Fong[17], M. Foucher[17], A. Fürtjes[8], P. Gagnon[7], J.W. Gary[4], J. Gascon[18], S.M. Gascon-Shotkin[17], N.I. Geddes[20], C. Geich-Gimbel[3], T. Geralis[20], G. Giacomelli[2], P. Giacomelli[4], R. Giacomelli[2], V. Gibson[5], W.R. Gibson[13], D.M. Gingrich[30,a], D. Glenzinski[9], J. Goldberg[22], M.J. Goodrick[5], W. Gorn[4], C. Grandi[2], E. Gross[26], J. Grunhaus[23] M. Gruwé[8], C. Hajdu[32], G.G. Hanson[12], M. Hansroul[8], M. Hapke[13], C.K. Hargrove[7], P.A. Hart[9], C. Hartmann[3], M. Hauschild[8], C.M. Hawkes[5], R. Hawkings[8], R.J. Hemingway[6], M. Herndon[17], G. Herten[10], R.D. Heuer[8], M.D. Hildreth[8], J.C. Hill[5], S.J. Hillier[1], T. Hilse[10], P.R. Hobson[25], R.J. Homer[1], A.K. Honma[28,a], D. Horváth[32,c], R. Howard[29], R.E. Hughes-Jones[16], D.E. Hutchcroft[5], P. Igo-Kemenes[11], D.C. Imrie[25], M.R. Ingram[16], K. Ishii[24], A. Jawahery[17], P.W. Jeffreys[20], H. Jeremie[18], M. Jimack[1], A. Joly[18], C.R. Jones[5], G. Jones[16], M. Jones[6], R.W.L. Jones[8], U. Jost[11], P. Jovanovic[1], T.R. Junk[8], D. Karlen[6], K. Kawagoe[24], T. Kawamoto[24],

R.K. Keeler[28], R.G. Kellogg[17], B.W. Kennedy[20], B.J. King[8], J. Kirk[29], S. Kluth[8], T. Kobayashi[24], M. Kobel[10], D.S. Koetke[6], T.P. Kokott[3], M. Kolrep[10], S. Komamiya[24], T. Kress[11], P. Krieger[6], J. von Krogh[11], P. Kyberd[13], G.D. Lafferty[16], R. Lahmann[17], W.P. Lai[19], D. Lanske[14], J. Lauber[15], S.R. Lautenschlager[31], J.G. Layter[4], D. Lazic[22], A.M. Lee[31], E. Lefebvre[18], D. Lellouch[26], J. Letts[2], L. Levinson[26], C. Lewis[15], S.L. Lloyd[13], F.K. Loebinger[16], G.D. Long[17], M.J. Losty[7], J. Ludwig[10], M. Mannelli[8], S. Marcellini[2], C. Markus[3], A.J. Martin[13], J.P. Martin[18], G. Martinez[17], T. Mashimo[24], W. Matthews[25], P. Mättig[3], W.J. McDonald[30], J. McKenna[29], E.A. Mckigney[15], T.J. McMahon[1], A.I. McNab[13], R.A. McPherson[8], F. Meijers[8], S. Menke[3], F.S. Merritt[9], H. Mes[7], J. Meyer[27], A. Michelini[2], G. Mikenberg[26], D.J. Miller[15], R. Mir[26], W. Mohr[10], A. Montanari[2], T. Mori[24], M. Morii[24], U. Müller[3], K. Nagai[26], I. Nakamura[24], H.A. Neal[8], B. Nellen[3], B. Nijjhar[16], R. Nisius[8], S.W. O'Neale[1], F.G. Oakham[7], F. Odorici[2], H.O. Ogren[12], N.J. Oldershaw[16], T. Omori[24], M.J. Oreglia[9], S. Orito[24], J. Pálinkás[33,d], G. Pásztor[32], J.R. Pater[16], G.N. Patrick[20], J. Patt[10], M.J. Pearce[1], S. Petzold[27], P. Pfeifenschneider[14], J.E. Pilcher[9], J. Pinfold[30], D.E. Plane[8], P. Poffenberger[28], B. Poli[2], A. Posthaus[3], H. Przysiezniak[30], D.L. Rees[1], D. Rigby[1], S. Robertson[28], S.A. Robins[13], N. Rodning[30], J.M. Roney[28], A. Rooke[15], E. Ros[8], A.M. Rossi[2], M. Rosvick[28], P. Routenburg[30], Y. Rozen[22], K. Runge[10], O. Runolfsson[8], U. Ruppel[14], D.R. Rust[12], R. Rylko[25], K. Sachs[10], E.K.G. Sarkisyan[23], M. Sasaki[24], C. Sbarra[2], A.D. Schaile[34], O. Schaile[34], F. Scharf[3], P. Scharff-Hansen[8], P. Schenk[27], B. Schmitt[8], S. Schmitt[11], M. Schröder[8], H.C. Schultz-Coulon[10], M. Schulz[8], M. Schumacher[3], P. Schütz[3], W.G. Scott[20], T.G. Shears[16], B.C. Shen[4], C.H. Shepherd-Themistocleous[8], P. Sherwood[15], G.P. Siroli[2], A. Sittler[27], A. Skillman[15], A. Skuja[17], A.M. Smith[8], T.J. Smith[28], G.A. Snow[17], R. Sobie[28], S. Söldner-Rembold[10], R.W. Springer[30], M. Sproston[20], A. Stahl[3], M. Steiert[11], K. Stephens[16], J. Steuerer[27], B. Stockhausen[3], D. Strom[19], F. Strumia[8], P. Szymanski[20], R. Tafirout[18], S.D. Talbot[1], S. Tanaka[24], P. Taras[18], S. Tarem[22], M. Thiergen[10], M.A. Thomson[8], E. von Törne[3], S. Towers[6], I. Trigger[18], T. Tsukamoto[24], E. Tsur[23], A.S. Turcot[9], M.F. Turner-Watson[8], P. Utzat[11], R. Van Kooten[12], M. Verzocchi[10], P. Vikas[18], M. Vincter[28], E.H. Vokurka[16], F. Wäckerle[10], A. Wagner[27], C.P. Ward[5], D.R. Ward[5], J.J. Ward[15], P.M. Watkins[1], A.T. Watson[1], N.K. Watson[7], P.S. Wells[8], N. Wermes[3], J.S. White[28], B. Wilkens[10], G.W. Wilson[27], J.A. Wilson[1], G. Wolf[26], S. Wotton[5], T.R. Wyatt[16], S. Yamashita[24], G. Yekutieli[26], V. Zacek[18],

[1]School of Physics and Space Research, University of Birmingham, Birmingham B15 2TT, UK

[2]Dipartimento di Fisica dell' Università di Bologna and INFN, I-40126 Bologna, Italy

[3]Physikalisches Institut, Universität Bonn, D-53115 Bonn, Germany

[4]Department of Physics, University of California, Riverside CA 92521, USA
[5]Cavendish Laboratory, Cambridge CB3 0HE, UK
[6] Ottawa-Carleton Institute for Physics, Department of Physics, Carleton University, Ottawa, Ontario K1S 5B6, Canada
[7]Centre for Research in Particle Physics, Carleton University, Ottawa, Ontario K1S 5B6, Canada
[8]CERN, European Organisation for Particle Physics, CH-1211 Geneva 23, Switzerland
[9]Enrico Fermi Institute and Department of Physics, University of Chicago, Chicago IL 60637, USA
[10]Fakultät für Physik, Albert Ludwigs Universität, D-79104 Freiburg, Germany
[11]Physikalisches Institut, Universität Heidelberg, D-69120 Heidelberg, Germany
[12]Indiana University, Department of Physics, Swain Hall West 117, Bloomington IN 47405, USA
[13]Queen Mary and Westfield College, University of London, London E1 4NS, UK
[14]Technische Hochschule Aachen, III Physikalisches Institut, Sommerfeldstrasse 26-28, D-52056 Aachen, Germany
[15]University College London, London WC1E 6BT, UK
[16]Department of Physics, Schuster Laboratory, The University, Manchester M13 9PL, UK
[17]Department of Physics, University of Maryland, College Park, MD 20742, USA
[18]Laboratoire de Physique Nucléaire, Université de Montréal, Montréal, Quebec H3C 3J7, Canada
[19]University of Oregon, Department of Physics, Eugene OR 97403, USA
[20]Rutherford Appleton Laboratory, Chilton, Didcot, Oxfordshire OX11 0QX, UK
[22]Department of Physics, Technion-Israel Institute of Technology, Haifa 32000, Israel
[23]Department of Physics and Astronomy, Tel Aviv University, Tel Aviv 69978, Israel
[24]International Centre for Elementary Particle Physics and Department of Physics, University of Tokyo, Tokyo 113, and Kobe University, Kobe 657, Japan
[25]Brunel University, Uxbridge, Middlesex UB8 3PH, UK
[26]Particle Physics Department, Weizmann Institute of Science, Rehovot 76100, Israel
[27]Universität Hamburg/DESY, II Institut für Experimental Physik, Notkestrasse 85, D-22607 Hamburg, Germany
[28]University of Victoria, Department of Physics, P O Box 3055, Victoria BC V8W 3P6, Canada
[29]University of British Columbia, Department of Physics, Vancouver BC V6T 1Z1, Canada
[30]University of Alberta, Department of Physics, Edmonton AB T6G 2J1, Canada
[31]Duke University, Dept of Physics, Durham, NC 27708-0305, USA
[32]Research Institute for Particle and Nuclear Physics, H-1525 Budapest, P O Box

49, Hungary
[33]Institute of Nuclear Research, H-4001 Debrecen, P O Box 51, Hungary
[34]Ludwigs-Maximilians-Universität München, Sektion Physik, Am Coulombwall 1, D-85748 Garching, Germany

[a] and at TRIUMF, Vancouver, Canada V6T 2A3
[b] and Royal Society University Research Fellow
[c] and Institute of Nuclear Research, Debrecen, Hungary
[d] and Department of Experimental Physics, Lajos Kossuth University, Debrecen, Hungary

Department of Energy, USA,
National Science Foundation, USA,
Research Corporation, USA,
Particle Physics and Astronomy Research Council, UK,
Natural Sciences and Engineering Research Council, Canada,
Israel Science Foundation, administered by the Israel Academy of Science and Humanities,
Minerva Gesellschaft,
Japanese Ministry of Education, Science and Culture (the Monbusho) and a grant under the Monbusho International Science Research Program,
German Israeli Bi-national Science Foundation (GIF),
Bundesministerium für Bildung, Wissenschaft, Forschung und Technologie, Germany,
National Research Council of Canada,
Hungarian Foundation for Scientific Research, OTKA T-016660, and OTKA F-015089.

List of Figures

List of Tables

References

[1] ALEPH Collab., D. Decamp *et al.*, Phys. Lett. B236 (1990) 511;
OPAL Collab., M.Z. Akrawy *et al.*, Phys. Lett. B240 (1990) 250;
OPAL Collab., M.Z. Akrawy *et al.*, Phys. Lett. B247 (1990) 448;
L3 Collab., B. Adeva *et al.*, Phys. Lett. B251 (1990) 321;
OPAL Collab., G. Alexander *et al.*, Z. Phys. C52 (1991) 175;
DELPHI Collab., P. Abreu *et al.*, Phys. Lett. B274 (1992) 230.

[2] S. Tanaka and S. Asai, "Search for Unstable Charged Heavy Leptons in e^+e^- Collisions at $\sqrt{s}$ = 130 and 136 GeV", OPAL Physics Note PN216, 20th March 1996.

[3] S. Tanaka, "Search for Unstable Neutral Heavy Leptons in e^+e^- Collisions at $\sqrt{s}$ = 130 and 136 GeV", OPAL Technical Note TN377, 17th June 1996.

[4] OPAL Collab., G. Alexander *et al.*, "Search for Unstable Neutral and Charged Heavy Leptons in e^+e^- Collisions at $\sqrt{s}$ = 130 and 136 GeV", Phys. Lett. B385 (1996) 433.

[5] S. Tanaka, "Search for Unstable Neutral and Charged Heavy Leptons in e^+e^- Collisions at $\sqrt{s}$ = 161 GeV", OPAL Physics Note PN252, 8th August 1996.

[6] OPAL Collab., K. Ackerstaff *et al.*, "Search for Unstable Neutral and Charged Heavy Leptons in e^+e^- Collisions at $\sqrt{s}$ = 161 GeV", CERN-PPE/96-140 (1996), to be published in Phys. Lett. B.

[7] T. Yanagida, Proc. Workshop on "Unified Theory and Baryon Number in the Universe", eds. O. Sawada and A. Sugamoto, KEK 1979;
M. Gell-Mann, P. Ramond and R.Slanky, in "Supergravity", eds. P. van Nieuwenhuizen and D. Z. Freedman, North Holland, 1979.

[8] E. Nardi, E. Roulet and D. Tommasini, Phys. Lett. B344 (1995) 225;
G. Bhattacharyya *et al.*, Mod. Phys. Lett. A6 (1991) 2921;
G. Bhattacharyya, Phys. Lett. B331(1994) 143;
M. Tanimoto, "See-saw Enhancement of Neutrino Mixing due to the Right-handed phase", UWThPh-1994-53, HEP-PH-9503318, (1995).

[9] R. N. Mohapatra and P. B. Pal, "Massive Neitrinos in Physics and Astrophysics", World Scientific Lecture Note in Physics-Vol. 41.

[10] J. Maalampi and M. Roos, Phys. Rep. C186 (1990) 53.

[11] G.B. Gelmini and M. Roncadelli, Phys. Lett. B99 (1981) 411.

[12] R.E. Shrock, Phys. Rev. D24 (1981) 1275.

[13] B. Kayser, Phys. Rev. D39 (1984) 1023.

[14] P. Roy and O. Shanker, Phys. Rev. Lett. 52 (1984) 713;
P. Roy and O. Shanker, Phys. Rev. D30 (1984) 1949;
M. Roncadelli and D. Wyler, Phys. Lett. B133 (1983) 325.

[15] L3 Collab., O. Adriani *et al.*., Phys. Lett. B 295 (1992) 371.

[16] A. A. Natale *et al.*, "Limit on a heavy Dirac neutrino through oblique radiative corrections", IFT-P.030/95, CERN-SCAN-910052.

[17] CHARM Collab.,K. De Winter *et al.*, Nucl. Instr. Meth. A278 (1989) 670.

[18] M. Gronau *et al.*, Phys. Rev. D29 (1984) 2539.

[19] H. Baer *et al.*, in "Physics at LEP", vol. 1, eds. J. Ellis and R. Peccei, CERN 86-02 (1986) 297.

[20] L. Montanet *et al.*, Phys. Rev. D50 (1994) 1418.

[21] F.A. Berends, R. Kleiss and S. Jadach, Nucl. Phys. B202 (1982) 63;
F.A. Berends, R. Kleiss and S. Jadach, Comp. Phys. Comm. 29 (1983) 185.

[22] M. Sher and Y. Tuan, Phys. Lett. B285 (1992) 336.

[23] DELPHI Collab., P. Aarnio *et al.*, Nucl. Instr. Meth. A303 (1991) 233.

[24] T. P. R. Linnecar and E. N. Shaposhnikova, The transverse mode coupling instability and broadband impedance model of the CERN SPS, CERN-SL/94-35 (1994)

[25] M. Akrawy et al., Development studies for the OPAL end cap electromagnetic calorimeter using vacuum photo triode instrumented leadglass, Nucl. Instr. Meth. A290 (1990) 76.

[26] J. Allison et al., Diamond shaped cathode pads for the longitudinal coordinate from a drift chamber, Nucl. Instr. Meth. A236 (1985) 284.

[27] J. Allison et al., The detector simulation program for the OPAL experiment at LEP, Nucl. Instr. Meth. A317 (1992) 47.

[28] P.P. Allport et al., The OPAL silicon microvertex detector, Nucl. Instr. Meth. A324 (1993) 34.

[29] G. Altarelli et al., Nucl. Phys. B264 (1991) 219.

[30] A.K. Amundsen et al., The control system of the OPAL detector at LEP, Nucl. Instr. Meth. A293 (1990) 145.

[31] M. Arignon et al., The trigger system of the OPAL experiment at LEP, Nucl. Instr. Meth. A313 (1992) 103.

[32] M. Arignon et al., The pretrigger system of the OPAL experiment at LEP, Nucl. Instr. Meth. A333 (1993) 330.

[33] G. Arnison et al., Phys. Lett. 122B (1983) 103.

[34] G.T.J. Arnison et al., Production and testing of limited streamer tubes for the end-cap muon subdetector of OPAL, Nucl. Instr. Meth. A294 (1990) 431.

[35] G. Artusi et al., Limited streamer tubes for the OPAL hadron calorimeter, Nucl. Instr. Meth. A279 (1989) 523.

[36] J.T.M. Baines et al., The data acquisition system of the OPAL detector at LEP, Nucl. Instr. Meth. A325 (1993) 271.

[37] M. Banner et al., Phys. Lett. 122B (1983) 476.

[38] D. Bardin et al., ZFITTER, An analytical program for fermion pair production in e^+e^- annihilation, CERN-TH. 6443/92, May 1992.

[39] C. Beard et al., Thin, high gain wire chambers for electromagnetic presampling in OPAL, Nucl. Instr. Meth. A286 (1990) 117.

[40] O. Biebel et al., The laser system for calibration and monitoring of the OPAL jet chamber, Nucl. Instr. Meth. A320 (1992) 183.

[41] O. Biebel et al., Performance of the OPAL jet chamber, Nucl. Instr. Meth. A323 (1992) 169.

[42] M. Bramhall et al., A fast track trigger processor for the OPAL experiment at LEP, IEEE Trans. Nucl. Sci. NS-36(1) (1989) 380.

[43] R. Brun et al., GEANT3 user's guide, CERN DD/EE/84-1, 1984.

[44] J.R. Carter et al., The OPAL vertex drift chamber, Nucl. Instr. Meth. A286 (1990) 99.

[45] CEREN-25 lead glass, Corning France, 44 Avenue de Valvins, Avon, Cedex 77210, France.

[46] D.G. Charlton et al., The on-line event filter of the OPAL experiment at LEP, Nucl. Instr. Meth. A325 (1993) 129.

[47] CLEO Collaboration, S. Henderson et al., Phys. Rev. D45 (1992) 2212.

[48] S. Dado et al., A new high gain thin gap detector for the OPAL hadron calorimeter, Nucl. Instr. Meth. A252 (1986) 511.

[49] DELCO Collaboration, W. Bacino et al., Phys. Rev. Lett. 43 (1979) 1073.

[50] Ethernet, ISO 8802/3.

[51] H.M. Fischer et al., The OPAL jet chamber, Nucl. Instr. Meth. A283 (1989) 492.

[52] S. Glashow, Partial-symmetries of weak interactions, Nucl. Phys. 22 (1961) 579.

[53] R.L. Gluckstern, Uncertainties in track momentum and direction, due to multiple scattering and measurement errors, Nucl. Instr. Meth. 24 (1963) 381.

[54] F.J. Hasert et al., Phys. Lett. 46B (1973) 138.

[55] M. Hauschild et al., Particle identification with the OPAL jet chamber, Nucl. Instr. Meth. A314 (1992) 74.

[56] R.D. Heuer and A. Wagner, The OPAL jet chamber, Nucl. Instr. Meth. A265 (1988) 11.

[57] K. Hikasa et al., Review of particle properties, Phys. Rev. D45 (1992) S1.

[58] N. Isgur et al., Phys. Rev. D39 (1989) 799.

[59] B. Lofstedt, TPD Time Projection Digitiser F6821, CERN-EP-EL, 89.04.13 (1989).

[60] MC68020, MC68030 and MC68040 32-bit microprocessors, Motorola Inc.

[61] H. Mes et al., Design and test of the z-coordinate drift chamber system for the OPAL central detector at LEP, Nucl. Instr. Meth. A265 (1988) 445.

[62] R.P. Middleton, Proc. Int. Workshop on Software Engineering, Artificial Intelligence and Expert Systems for High Energy and Nuclear Physics, CNRS, 1990, Lyons, France, March 1990, eds: D. Perret-Gallix and W. Wojcik (CNRS, Paris, 1990) p. 349.

[63] Muon Identification Working Group, Identification of muons in hadronic Z^0 decays, OPAL Technical Note TN107, 15 July 1992.

[64] Noryl, modified polyphenylene oxide developed by General Electric Plastics Co. Profile extrusions by Copely Developments Ltd., Leicester, UK.

[65] OPAL Collaboration, OPAL technical proposal, LEPC report 83-4, CERN, 1983.

[66] OPAL Collaboration, M.Z. Akrawy et al., A measurement of global event shape distributions in the hadronic decays of the Z^0, Z. Phys. C47 (1990) 505.

[67] OPAL Collab., K. Ahmet *et al.*, Nucl. Instr. Meth. A305 (1991) 275;
P. P. Allport *et al.*, Nucl. Instr. Meth. A324 (1993) 34;
P. P. Allport *et al.*, Nucl. Instr. Meth. A346 (1994) 476;
B.E. Anderson *et al.*, IEEE Trans. Nucl. Sci. 41 (1994) 845.

[68] ORACLE, ORACLE Corporation, 20 Davis Drive, Belmont, California 94002, USA.

[69] OS9 68000 operating system, Microware Systems corporation, 1900 N.W. 114th Street, Des Moines, IA 50322, USA.

[70] C. Peterson et al., Scaling violations in inclusive e^+e^- annihilation spectra, Phys. Rev. D27 (1983) 105.

[71] R2238 photomultiplier tubes, Hamamatsu Photonics K.K., Ichino-cho, Hamamatsu, Japan.

[72] M.D. Rousseau et al., IEEE Trans. Nucl. Sci. NS-30 (1983) 479.

[73] A. Salam, in: Elementary Particle Theory, ed. N. Svartholm, (Almquist and Wiksell, Stockholm, 1968) p. 367.

[74] B. Schumm et al., Phys. Rev. Lett. 69 (1992) 3025.

[75] SF57 lead glass, Schott Glaswerke, Hattenbergstrasse 10, D-6500 Mainz 1, Germany.

[76] J.C. Stanton, A low power, low noise amplifier for a 128 channel detector read-out integrated circuit, RAL-89-009 (1989).

[77] H. Takeda, Energy Resolution of Lead Glass Counters with Materials in front, TKYLEP-50, 6/11/1985.

[78] VMEbus architecture, IEEE 1014/D1.0.

[79] S. Weinberg, Phys. Rev. Lett. 19 (1967) 1264.

[80] XP1501/FL vacuum photo triodes, Philips-RTC, 130 Avenue Ledru-Rollin, Paris XIe, France.

[81] C.N. Yang and R. Mills, Phys. Rev. 96 (1954) 191.

[82] S. Jadach and J. Kühn, preprint MPI-PAE/PTh 64/86.

[83] T. Sjöstrand, Comp. Phys. Comm. 82 (1994) 74.

[84] S. Jadach, B. F. L. Ward and Z. Wąs, Comp. Phys. Comm. 79 (1994) 503.

[85] S. Jadach, W. Płaczek and B. F. L. Ward, University of Tennessee preprint UTHEP-95-1001 (unpublished);
S. Jadach, W. Płaczek and B. F. L. Ward, in "Physics at LEP2", eds. G. Altarelli, T. Sjöstrand and F. Zwirner, CERN 96-01, vol. 2 (1996) 229.

[86] M. Böhm, A. Denner and W. Hollik, Nucl. Phys. B304 (1988) 687;
F.A Berends, R. Kleiss and W. Hollik, Nucl. Phys. B304 (1988) 712.

[87] A. Buijs *et al.*, Comp. Phys. Comm. 79 (1994) 523.

[88] R. Engel, Z. Phys. C66 (1995) 203.

[89] G. Marchesini *et al.*, Comp. Phys. Comm. 67 (1992) 465.

[90] J. A. M. Vermaseren, Nucl. Phys. B229 (1983) 347.

[91] F.A Berends, R. Pittau and R. Kleiss, Comp. Phys. Comm. 85 (1995) 437.

[92] J. Allison *et al.*, Nucl. Instr. Meth. A317 (1992) 47.

[93] OPAL Collab., G. Alexander *et al.*, Phys. Lett. B377 (1996) 181;
OPAL Collab., G. Alexander *et al.*, Phys. Lett. B377 (1996) 273.

[94] N. Brown and W.J. Stirling, Phys. Lett. B252 (1990) 657;
S. Catani *et al.*, Nucl. Phys. B269 (1991) 432;
S. Bethke, Z. Kunszt, D. Soper and W.J. Stirling, Nucl. Phys. B370 (1992) 310;
N. Brown and W.J. Stirling, Z. Phys. C53 (1992) 629.

[95] OPAL Collab., R. Akers *et al.*, Phys. Lett. B327 (1994) 411.

[96] OPAL Collab., P. Acton *et al.*, Z. Phys. C58 (1993) 523.

[97] OPAL Collab., G. Alexander *et al.*, "Search for Chargino and Neutralino Production at $\sqrt{s} = 161$ GeV", CERN-PPE/96-135 (1996), to be published in Phys. Lett. B;
OPAL Collab., G. Alexander *et al.*, "Search for scalar top and scalar bottom quarks using the OPAL detector at LEP ", CERN-PPE/96-133 (1996), to be published in Phys. Lett. B.

[98] OPAL Collab., R. Akers *et al.*, Z. Phys. C60 (1993) 199.

[99] OPAL Collab., G. Alexander *et al.*, Z. Phys. C69 (1996) 543.

[100] R.D. Cousins and V.L. Highland, Nucl. Instr. Meth. A320 (1992) 331.

[101] L3 Collab., M. Acciarri *et al.*, Phys. Lett. B377 (1996) 304, CERN-PPE/96-038 (1996);
ALEPH Collab., D. Buskulic *et al.*, Phys. Lett. B384 (1996) 439, CERN-PPE/96-080 (1996).